TUNING OF BOUNDARY CONDITIONS PARAMETERS FOR HEMODYNAMICS SIMULATION USING PATIENT DATA

Massimiliano Mercuri

School of Medicine and Biomedical Sciences

Department of Cardiovascular Science

Medical Physics Group

Submitted for the degree of PhD

Submission Date

August 2019

List of Abbreviations

AAA	Abdominal Aortic Aneurysm
AD	Aortic Dissection
AscAo	Ascending Aorta
BAV	Bicuspid Aortic Valve
BCA	Brachiocephalic Artery
CE-MRA	Contrast Enhanced Magnetic Resonance Angiography
CFD	Computational Fluid Dynamic
CFL	Courant-Friedrichs-Lewy (stability and convergence condition)
CHD	Congenital Heart Disease
CoA	Coarctation of the Aorta
CT	Computer Tomography
DBP	Diastolic Blood Pressure
DCG	Discontinuous Galerkin (resolution method for 1D models)
DescAo	Descending Aorta
DS	Degree of Stenosis
ECM	Extracellular Matrix
EVAR	Endovascular Abdominal Aortic Repair
FE	Finite Element

FEA	Finite Element Analysis
FEVAR	Fenestrated Endovascular Aortic Repair
FSI	Fluid Structure Interaction
FV	Finite Volume
IMSs	Intra Mural Stresses
ITK	Insight Segmentation and Registration Toolkit
LCA	Left Common Carotid Artery
LSUB	Left Subclavian Artery
MAP	Mean Arterial Pressure
MFS	Marfan Syndrome
MR	Magnetic Resonance
MRA	Magnetic Resonance Angiography
MRI	Magnetic Resonance Imaging
MUSCL	Monotonic Upwind Scheme for Conservation Laws
NS	Navier-Stokes
ODE	Ordinary Differential Equation
OSI	Oscillatory Shear Index
PAA	Pulmonary Artery Aneurysm
(2D)PC-MRI	Phase Contrast Magnetic Resonance Imaging
PDE	Partial Derivative Equation
PEARS	Personalized External Aortic Root Support
PVS	Peripheral Vascular Stenting

PWV	Pulse Wave Velocity
ROI	Region Of Interest
RRT	Relative Resident Time
SBP	Systolic Blood Pressure
SST	Shear Stress Transport (turbulence model)
STL	Standard Triangulation Language
TAA	Thoracic Aortic Aneurysm
TAC	Total Arterial Capacitance
TAVI	Transcatheter Aortic Valve Implantation
TAWSS	Time Average Wall Shear Stress
TEE	Transesophageal Echocardiogram
TEVAR	Thoracic Endovascular Aortic Repair
TOE	Transesophageal Echocardiogram
TT	Transit Time (method also foot-to-foot method)
TTE	Transthoracic Echocardiography
UKF	Unscented Kalman Filter
VSMC	Vascular Smooth Muscle Cells
VTK	Visualization Toolkit
WK	Windkessel (parameters)
WSS	Wall Shear Stress
0D	Zero dimensional
1D	One dimensional

1D L	One dimensional linear scheme
1D NL	One dimensional non linear scheme
3D	Three dimensional

Abstract

This thesis describes an engineering workflow, which allows specification of boundary conditions and 3D simulation based on clinically available patient-specific data. A review of numerical models used to describe the cardiovascular system is provided, with a particular focus on the clinical target disease chosen for the toolkit, aortic coarctation. Aorta coarctation is the fifth most common congenital heart disease, characterized by a localized stenosis of the descending thoracic aorta. Current diagnosis uses invasive pressure measurement with rare but potential complications. The principal objective of this work was to develop a tool that can be translated into the clinic, requiring minimum operator input and time, capable of returning meaningful results from data typically acquired in clinical practice.

Linear and nonlinear 1D modelling approaches are described, tested against full 3D solutions derived for idealized geometries of increasing complexityand for a patient-specific aortic coarctation. The 1D linear implementation is able to represent the fluid dynamic in simple idealized benchmarks with a limited effort in terms of computational time, but in a more complex case, such as a mild aortic coarctation, it is unable to predict well 3D fluid dynamic features. On the other side, the 1D nonlinear implementation showed a good agreement when compared to 3D pressure and flow waveforms, making it suitable to estimate outflow boundary conditions for subject-specific models.

A cohort of 11 coarctation patients was initially used for a preliminary analysis using 0D models of increasing complexity to examine parameters derived when tuning models of the peripheral circulation. The first circuit represents the aortic coarctation as a nonlinear resistance, using the Bernoulli pressure drop equation, without considering the effect

of downstream circulation. The second circuit include a peripheral resistance and compliance, and separate ascending and descending aortic pressure responses. In the third circuit a supra-aortic Windkessel model was added in order to include the supra-aortic circulation. The analysis detailed represents a first attempt to assess the interaction between local aortic haemodynamics and subject-specific parameterization of windkessel representations of the peripheral and supra-aortic circulation using clinically measured data. From the analysis of these 0D models, it is clear that the significance of the coarctation becomes less from the simple two resistance model to the inclusion of both the peripheral and supra-aortic circulation. These results provide a context within which to interpret outcomes of the tuning process reported for a more complex model of aortic haemodynamics using 1D and 3D model approaches.

Earlier developments are combined to enable a multi-scale modelling approach to simulate fluid-dynamics. This includes non-linear 1D models to derive patient-specific parameters for the peripheral and supra-aortic circulation followed by transient analysis of a coupled 3D/0D system to estimate the coarctation pressure augmentation. These predictions are compared with invasively measured catheter data and the influence of uncertainty in measured data on the tuning process is discussed. This study has demonstrated the feasibility of constructing a workflow using non-invasive routinely collected clinical data to predict the pressure gradient in coarctation patients using patient specific CFD simulation, with relatively low levels of user interaction required. The results showed that the model is not suitable for the clinical use at this stage, thus further work is required to enhance the tuning process to improve agreement with measured catheter data.

Finally, a preliminary approach for the assessment of change in haemodynamics following coarctation repair, where the coarctation region is enlarged through a virtual intervention process. The CFD approach reported can be expanded to explore the sensitivity of the peak ascending aortic pressure and descending aortic flow to the aortic diameter achieved following intervention, such an analysis would provide guidance for surgical intervention to target the optimal diameter to restore peripheral perfusion and reduce cerebral hypertension.

Acknowledgements

None of this would have been possible without the helps I received along the way in this long journey (more than four years!) but here we are!
I owe a huge (maybe enormous) debt of gratitude to my supervisors Andrew Narracott and Rod Hose that kindly help me and taught me so much during all the discussion we had, especially I would like to thanks my first supervisor Andrew for the patient and the unstoppable commitment he put in this project. I am very grateful to the EU Marie Curie funding that made this project possible. I want to thank also the people that welcomed me in Sheffield during my visit at the lab: John, David, Paolo, Karen, Simone F. and Simone A, thank you for the time we spent together.
To all the people that work in Therenva and to Cemil that welcomed me to his company, THANK YOU. You probably are the last person to know, but you are a great human, a great leader and a great (underground) Star!
A huge thank you goes to Dr Kerstin Wustmann and Dr Henrik von Tengg-Kobligk for giving me the opportunity to visit Bern and learn so much about their work in the clinic. I also want to thank all the people of Ansys that supported me along the way!
A huge thank you to all my friends from home and not that helped me when I needed a distraction. They all know who they are so there is no need for a detailed list.
Lastly a huge thank you goes to my family. To my mother for believing in me, betting on me, to my father that always finds a way to cheer me up, and to my brother, the rock of my life.

List of Publications

Papers

Massimiliano Mercuri, Kerstin Wustmann, Hendrik von Tengg-Kobligk, Cemil Göksu, D Rodney Hose, Andrew Narracott, Subject-specific simulation for non-invasive assessment of aortic coarctation: Towards a translational approach, Medical Engineering & Physics, Volume 77, 2020, Pages 69-79, ISSN 1350-4533. Received 2 February 2019, Revised 27 November 2019, Accepted 13 December 2019.

Conference proceedings

Mercuri M., Narracott A.J., Hose D., Göksu C. (2018) An Automatic Method for Aortic Segmentation Based on Level-Set Methods Using Multiple Seed Points. In: Tavares J., Natal Jorge R. (eds) VipIMAGE 2017. ECCOMAS 2017. Lecture Notes in Computational Vision and Biomechanics, vol 27. Springer, Cham

Contents

Listing of figures

Listing of tables

1

Literature review

In this chapter, the project background is reported. First, the cardiovascular system is presented, followed by a review of the vascular models used in the literature and aortic disease with potential for a patient-specific numerical application. Aortic coarctation is described in detail, the disease selected for development of a clinical workflow in this thesis, along with a review of previous work undertaken to simulate this pathology.

1.1 The cardiovascular system

The force that drives blood around the cardiovascular system is provided by the heart, a four chambered (two atria and two ventricles) pumping system, that contracts during systole and relaxes during diastole.

During systole, right and left ventricles contract and pump out blood into the human circulatory system. During this contraction, they generate enough energy [1] to eject blood in two different circuits: the systemic circuit (or large circulation), and the pulmonary circuit (or small circulation) made of more than 10 billion of vessels with different size, shape and function.

The systemic circuit delivers oxygenated blood from the left ventricle to the peripheral vascular system and then returns de-oxygenated blood to the right heart's chambers; while the pulmonary circuit delivers blood from the right ventricle to lungs for oxygenation, and then back to the left heart's chambers (Figure 1.1).

During the systolic phase, the pulmonary/systemic arteries receive blood from the ventricular chambers, that actively contract to eject part of the blood volume (the stroke volume) accumulated during the diastolic phase , when the valves at the pulmonary/systemic arterial sides are closed and blood fills the ventricular chambers through the atria.

Arteries are elastic and compliant[2] vessels, the mechanical properties of their walls reduces

[1] It is stated that the average power output of the heart as the product of the pressure (100 mmHg) times the flow (6 $\frac{\text{L}}{\text{min}}$) is 1.33 W, that means 115000 J in a day, the same amount of energy required to lift up by 126 m a man of 70 kg (Fay & Sonwalkar, 1996)

[2] The compliance is mathematically described as the ratio between volume and pressure (referred more precisely as transmural pressure: the difference between the internal luminal pressure and the external pressure, usually taken as zero). The compliance gives information about the ability of the vessel wall to increase and distend its internal lumen in order to accommodate the incoming blood, due to the increase/decrease of

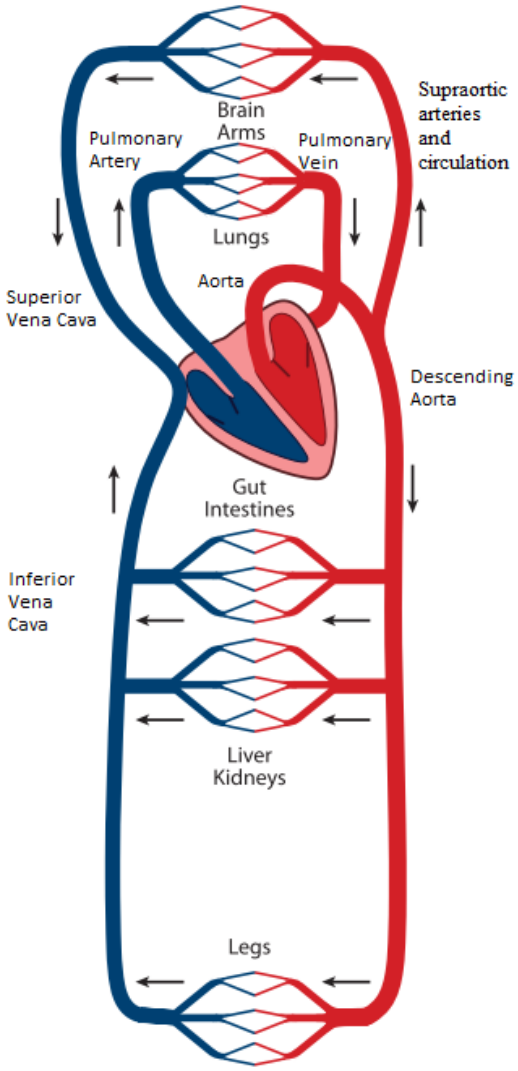

Figure 1.1: Figure illustrating the cardiovascular system comprises of a pumping heart, the pulmonary (Lungs) and systemic circulation (i.e. Brain, Arms,Gut, Intestines...). Image adapted with permission from Van de Vosse & Stergiopulos (2011)

the pulsatility of pressure and flow waveforms in the cardiovascular circulation, caused by the ventricular chambers relaxation and contraction phases, aiding blood to continuously perfuse the cardiovascular system, including the peripheral/lung vascular districts, acting as a second pump that reduces workload of the heart.

In the peripheral/pulmonary circuits, blood flows through the arterioles into capillaries. Arterioles distribute the flow to different vascular capillary beds through the relaxation and contraction of the smooth muscle cells in the vessel wall. When contracted, these muscle cells decrease the vessels diameters, causing an increase of the local vascular resistance and a reduction of blood perfusion[3]. This mechanism regulates the blood flow rate to different regions of the circulation to satisfy variation in metabolic demand and oxygen supply.

Capillaries comprise an intricate and dense network of a very small diameter vessels (less than 10 μm in diameter (Jones et al., 2014), eight times smaller than arterioles and thirty times smaller than arteries) made of a single layer of endothelial cells placed over a basement elastic membrane. Between one endothelial cell and the other there is a small gap (intercellular cleft) that allows gases, metabolic nutrients and waste products to be actively exchanged with the surrounding tissues. This exchange is only allowed by the nature of the blood flow in this circuit: steady and slow (maximum velocity less than 1.5 $\frac{cm}{s}$ (Ivanov et al., 1981)). At this point, bloods cells flow at the center of the capillary in a single-file, highly deformed and surrounded by blood plasma that acts as a lubrication layer (Fahraeus & Lindqvist, 1931). Oxygen and nutrients are effectively diffused with the surrounding tissues (which diffuse out waste products and carbon dioxide) thanks to the high number of

the transmural pressure.

[3]As described by Poiseuille and Hagen in 1840, in case of a incompressible Newtonian laminar fluid flow through a cylindrical pipe, the resistance is inversely proportional to fourth power of the pipe's radius (Batchelor, 2000).

capillaries per meter square that offer more than 5000 cm^2 of surface area available for the exchange (O'Rourke et al., 2011).

Blood flows from the capillaries to the venous system. More than 70% of total blood volume is collected in the venous system (Alastruey et al., 2012a). Acting as reservoirs, the veins can accommodate a large volume of blood that can be re-distributed during changes of the physiological state (i.e. during exercise). The natural predisposition of veins to be blood collectors is demonstrated by their high compliance and the tendency to collapsed if not filled with blood (at negative transmural pressures) (Conrad, 1969; Caro et al., 2012). Larger veins and arteries have diameters within the same range (between 0.1 and 3 cm of diameter), but pressure and velocities are lower in veins and blood flow is mostly steady and laminar. In order to prevent retrograde flow, veins contain semilunar valves that ensure unidirectional flow towards the heart [4] . Blood is passively collected from the venous circulation by the atrial chambers of the heart, and when the atrial-ventricular valves open, it flows again to the ventricular chambers ready to be ejected by a new heart contraction.

From a fluid-dynamic point of view: in the arteries, the flow is pulsatile and inertial effect predominate over viscous effects, from large arteries to capillaries and veins, the viscous effects become predominant and the flow gradually becomes steady and laminar (O'Rourke et al., 2011) as shown in Figure 1.2 where pressure and velocity waveforms are reported for each point in the circulatory system. The mean Reynolds number is in the order of 500 in the arterial tree and decreases to reach values in the region of 1 in the microcirculation (Van de Vosse & Stergiopulos, 2011).

[4] Semilunar valves and the contraction of the skeletal muscles that surround the vein help blood to flow towards the heart. When skeletal muscles are contracted, they cause a compression of the blood and increase of pressure in that area. This mechanism forces blood to flow to the heart where the venous pressure is lower.

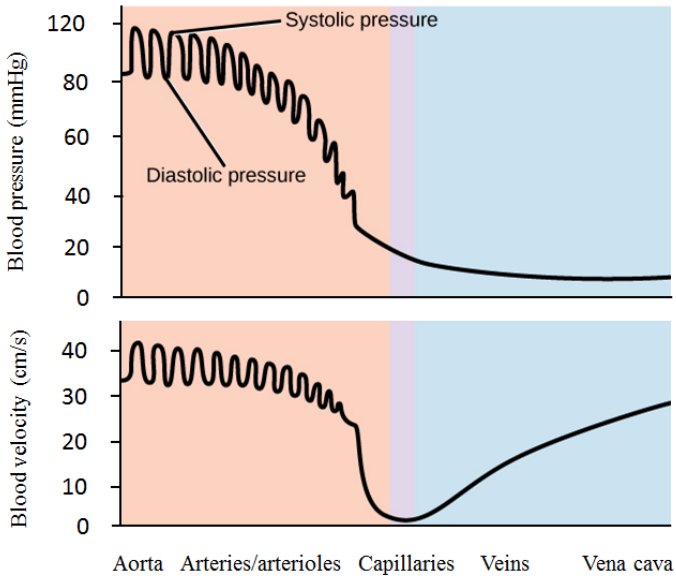

Figure 1.2: Figure illustrating pressure and velocity in the cardiovascular system at different level of the circulation, from aorta to large veins.

1.2 Modelling the Cardiovascular system

As a closed fluid system, the blood flow in the cardiovascular system is subject to the conservation laws of classical fluid mechanics, which states that mass, momentum and energy are conserved in time and space. This can be expressed as a set of mathematical expressions: the Navier-Stokes equations (Temam, 2001).

Unlike classical hydraulic pipe systems, the cardiovascular system is made of vessels that are more flexible and compliant than hydraulic tubes. The mechanical behaviour of the vessels introduces additional effects which should be considered when computing blood flow dynamics and describing the associated governing equations.

From a mathematical point of view, the cardiovascular system can be represented in the time or frequency domain using different levels of computational models. In frequency domain approaches, the continuity equations are linearized about a reference state (neglecting the nonlinear convective acceleration terms that are included in the mathematical description) and solved using the Fourier or Laplace transformation. In time domain approaches the nonlinearities are preserved, typically with an increase in the computational cost and time. The numerical descriptions can also differ in terms of the dimensionality in the model representation, from zero-dimensional (0D) through one-dimensional models (1D) to three-dimensional models (3D), as shown in Figure 1.3.

In the next section a brief review of the typical mathematical models used in the literature to describe the cardiovascular system is presented.

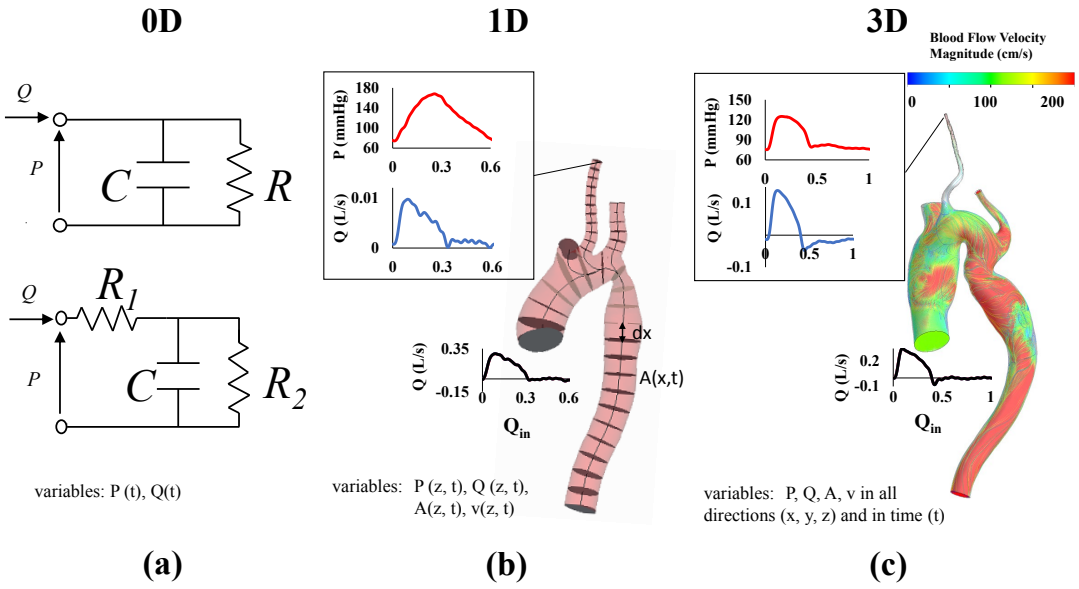

Figure 1.3: Different dimensional models used in the literature for modelling the cardiovascular system: (a) 0D models; (b) 1D models; (c) 3D models illustrating a typical detailed velocity flow field at peak systolic flow rate.

1.2.1 Zero dimensional or Lumped Parameter models

Zero dimensional (0D) or lumped parameter models provide a global description of the fundamental variables (pressure, flow and volume) for a given region or compartment of the cardiovascular system (see Figure 1.3(b)).

Depending on the clinical application, lumped models can either be used to described the entire vascular system with a single compartment (mono-compartment descriptions) or with the connection of multiple compartments (multi-compartment descriptions). Each compartment is characterized by a set of Ordinary Differential Equations (ODEs) that describes the conservation of mass, momentum balance and additional algebraic equations that relate pressure to volume (local compliance). Using an hydraulic/electrical analogy, for each compartment the mathematical relationship between voltage and current is the same relationship between pressure and flow rate. The electrical resistance, capacitance and inductance are equivalent to viscous resistance, vessel compliance and fluid inertia, respectively.

The most commonly applied zero dimensional model is the two element Windkessel, proposed by Hales in 1733 and mathematically described by Otto Frank in 1899 (Otto, 1899; Li, 2000), originally used to represent the entire cardiovascular system. The two element Windkessel model combines a resistance in parallel with a capacitance. The capacitance, C, represents the ability of the vessel wall to store blood (compliance of the large arteries) while the resistor, R, describes the vascular resistance of the peripheral circulation (capillaries and arterioles).

Westerhof et al. (1971) introduced a second resistance to improve the response of the model at high frequencies resulting in a three element Windkessel or Westkessel model (see Figure

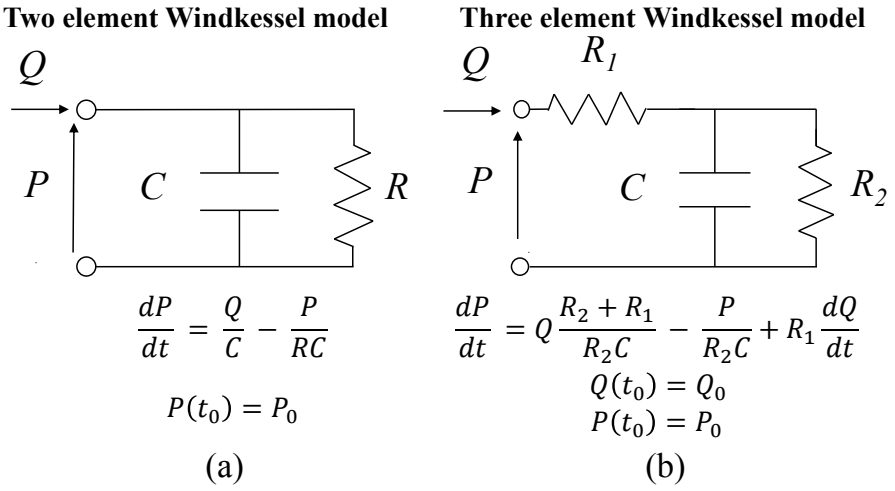

Figure 1.4: Figure illustrating Windkessel circuit schemes that relates the inlet flow Q to the pressure P with a set of ordinary differential equations (ODEs) as their electrical analogues. (a) the two element Windkessel model (RC); (b) the three element Windkessel model (RCR) also called Westkessel model. R_1 is frequently referred as the proximal resistance while R_2 is the distal resistance, their sum represent the total peripheral resistance

1.4).

The original two element Windkessel model has been significantly developed in order to increase the accuracy of the response under different physiological conditions. A fourth element was included, the inductance, in order to capture the inertial properties of the blood (the RLCR model, (Landes, 1943)). Windkessel models have, also, been used to build intricate connections of resistances, inductances and capacitances (Burattini & Natalucci, 1998; Jager et al., 1965), capable of describing in detail each single part of vascular system, in a multi-compartment modelling approach. However the introduction of more elements in the original Windkessel model description, not only increased the complexity of the model but also the computational effort. As the model parameters were no longer directly derived from anatomical vascular features and they had to be computed via iterative or optimization

schemes. Lumped models have also been used for modelling the heart chambers, valves, veins or the interaction with auto- and neuro-regulatory systems, for a more extensive description of the different zero-dimensional models used in literature see Shi et al. (2011).

1.2.2 One dimensional models

Zero-dimensional models can offer a good global description of the fluid dynamic variables in the arterial tree, but they are not able to characterize in detail pressure and flow wave propagation phenomena, which had led to the development of one-dimensional (1D) models. However, one can argue that a detailed description of the arterial tree can be obtained by using multiple linear 0D compartment models (with a multi-compartment modelling approach), as recently proved by Milišić & Quarteroni (2004), but the fundamental difference between these two numerical models arises from the capability of the 1D models to include physical nonlinearities such as convective acceleration terms together with non linear viscoelastic effects of the arterial wall.

One dimensional models are based on the mass and momentum conservation principles mathematically expressed as a set of partial derivative equations (PDEs) together with algebraic expressions to relate pressure with changes of cross sectional area. The final system of equations corresponds to a set of nonlinear hyperbolic PDEs (see the system of Equations 3.1 in Section 3.2 of chapter 3 for a more detailed insight) that can be solved using different numerical schemes (i.e., finite differences or the method of characteristics).

One dimensional models have been extensively used in the literature since they are able to accurately predict pressure and flow with low computational expense compared to two di-

mensional or three dimensional models. One dimensional models have been used to model cerebral circulation (Huang et al., 2018), coronary haemodynamics (Sun et al., 2000; Mynard et al., 2013), microvascular networks (Lee & Smith, 2008), pulmonary (Hollander et al., 2001; Lungu et al., 2016) and systemic arteries (Sherwin et al., 2003), and venous circulation (Olufsen et al., 2005). For a comprehensive review refer to (Van de Vosse & Stergiopulos, 2011; Shi et al., 2011).

1.2.3 Three dimensional models

Three dimensional (3D) models resolve the governing equations of the fluid motion, the Navier-Stokes (NS) and Continuity equations (which for an incompressible fluid are shown in Equations 1.1 and 1.2, respectively), in time and space using an iterative numerical scheme.

$$\begin{aligned}
\rho\frac{\delta u}{\delta t} + \nabla\cdot(\rho u\mathbf{U}) &= -\frac{\delta p}{\delta x} + \frac{\delta \tau_{xx}}{\delta x} + \frac{\delta \tau_{yx}}{\delta y} + \frac{\delta \tau_{zx}}{\delta z} \\
\rho\frac{\delta v}{\delta t} + \nabla\cdot(\rho u\mathbf{U}) &= -\frac{\delta p}{\delta y} + \frac{\delta \tau_{xy}}{\delta x} + \frac{\delta \tau_{yy}}{\delta y} + \frac{\delta \tau_{zy}}{\delta z} \\
\rho\frac{\delta w}{\delta t} + \nabla\cdot(\rho u\mathbf{U}) &= -\frac{\delta p}{\delta z} + \frac{\delta \tau_{xz}}{\delta x} + \frac{\delta \tau_{yz}}{\delta y} + \frac{\delta \tau_{zz}}{\delta z} \qquad (1.1)
\end{aligned}$$

$$\nabla\cdot(\mathbf{U}) = 0 \qquad (1.2)$$

Where ρ is the fluid density, u, v and w are the components of velocity in the x, y and z directions, p is the pressure, $\mathbf{U}$ is the velocity vector and τ the shear stress. The nonlinear governing equations are discretized and resolved in space by dividing the region of interest (the physical domain, i.e. the ascending aorta) into a number of finite volumes or elements

(that form the mesh), over which the governing equations are numerically solved for each time step (using a time-marching scheme) towards the end of the solution.

The numerical resolution is performed using either a finite volume (FV) or a finite element (FE) scheme. In the finite volume method the governing equations are integrated over a volume assuming a piece-wise linear variation of the dependent variables (u, v, w and p), balancing the fluxes across the boundaries of the individual volumes or cells (Versteeg & Malalasekera, 2007). In the finite element method the governing equations are integrated over an element or volume after a having been multiplied by a weight or shape function. The dependent variables are approximated over cell by the shape function and assembled into a system of algebraic equations, that is resolved using variational methods (Reddy, 2013). The choice of the piece-wise linear approximation, in the finite volume methods, and the shape function, in the finite element methods, determines the accuracy and the complexity of these methods.

Despite their computational cost, 3D models are used due to their ability to offer a more detailed insight on complex flow patterns that occur at particular locations in the arterial circulatory system such as at stenoses, bifurcations, heart valves haemodynamics or any region that can cause a separation of the fluid flow. Such complex flow phenomena are not accurately represented by analytical solutions, 0D or 1D approaches.

1.3 Model boundary conditions

Given the complexity of the fluid dynamics of blood flow, it is clear that a full subject-specific numerical model of the entire cardiovascular system is likely to be prohibitively computationally expensive even though there have been some attempts in the literature. Mynard & Smolich (2015), for example, report a 1D model of the entire human circulation including ventricular-arterial coupling and capillaries networks. The model, aside from its complexity, has the drawback that it required at least 1633 parameters, that need to be tuned with patient data in order to provide a full subject-specific model[5]. A complete tuning of all these parameters is not only challenging, but also unnecessary since cardiovascular pathologies frequently affect only a specific part of the human circulatory system.

Therefore, typically only a specific area of the cardiovascular circulation is modeled, coinciding with the region of interest for the clinical investigation. The remaining part of the cardiovascular system is integrated into the numerical solution by imposing particular conditions at the boundaries. Boundary conditions typically include an inlet, where blood mainly flows in, and a single or multiple outlets, where blood flows out.

At the inlet, inflow boundary condition are frequently applied via a time and/or spatially varying velocity (or flow rate) curve derived from clinical measurements (Gallo et al., 2012; Reymond et al., 2009) or via a lumped description of the heart coupled to the inlet boundary (Formaggia et al., 2006; Kim et al., 2009).

Outflow boundary conditions are typically more challenging to represent due to uncertain-

[5]The model comprises 396 segments, 5359 nodes and 188 junctions. Parameters were tuned based on data from healthy, young adults (20-30 years old, 75 kg weight and height 175 cm)

ties and lack of clinical measurements. Common outflow boundary conditions include:

- applying a constant or a time-varying measured pressure;
- a percentage of inlet flow rate (flow-split conditions) or flow rate provided from clinical measurements;
- 0D Windkessel models (RCR models) or 1D models representing the downstream circulation.

The choice of boundary conditions plays a crucial role in the translation of numerical blood flow models into the clinical context. Especially when the research aim is to create an *in-silico* model of the patient's pathological condition. In recent years, the *in silico* modelling community is moving towards the adoption of multiscale[6] models where 3D models, representing the clinical regions of interest, are coupled at the outlets with 0D models (RCR models) or 1D models. A recent article by Romarowski et al. (2018) confirmed the strength of three element Windkessel (RCR models) model as an outflow boundary condition against other methodologies, because of their effectiveness, ease of parametrization and low computational cost (especially when compared with 1D models).

[6]Multiscale because they represents different geometrical scales: 0D, 1D and 3D models.

1.4 Aortic diseases

The aorta is the main arterial vessel that delivers blood from the left ventricle to the systemic circulatory system. The aorta is made of three different tissue layers: the intimal, the media and the adventitia (see Figure 1.5).

The intimal layer or tunica intima is a layer of endothelial cells supported by a layer of

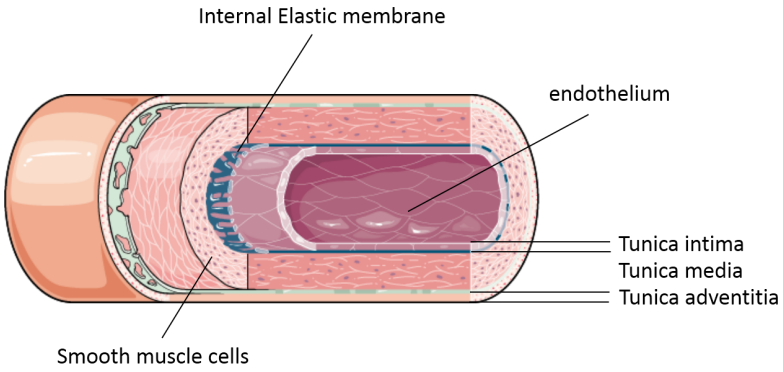

Figure 1.5: Figure illustrating aortic wall layers or tunicae: intima, media and adventitia. Figure adapted with permission from SMART SERVIER MEDICAL ART (2019)

elastic tissue (or internal elastic lamina) made of elastin and collagen fibers, populated by fibroblast and smooth muscle cells (myointimal cells). The intimal layer separates blood from the surrounding tissues and participates in the regulation of many physiological processes such as coagulation, inflammation and vascular tone.

The tunica media is composed of overlapping layers. Each layer has vascular smooth muscle cells (VSMC) embedded in an extracellular matrix (ECM) made of collagen fibers, structural glycoproteins, proteoglycans, and it is surrounded by an elastic lamina. The medial layer is the thickest of all the other layers. Because of the strong muscle cells population

and the elastic laminae (collagen and elastine), it is responsible for maintaining the vascular tone and the tubular shape even in absence of flow, and for damping the pulsatility of the blood flow generated by the ventricular pump. During the ventricular systole, part of the blood volume ejected from the heart is stored by the aortic wall, due to the vessel wall deformation following an increase of the internal pressure; during the diastolic ventricular phase, this blood is released, following the elastic recoil of the arterial wall. In this way, the peripheral district (the capillaries and veins) is continuously perfused with less energy expense.

The outer layer, the tunica adventitia, is separated from the medial layer by an elastic lamina and it is made of collagen fibers and muscle cells in an matrix that protects the vessel integrity and connects with surrounding tissues. The adventitia is also populated with lymphatic vessels, nerve fibers and vasa-vasorum (small vessels that provides nutrients to the vessel wall tissues itself).

It is clear that the particular organization of the aortic wall tissue can significantly influence its functionality and the functionality of the whole cardiovascular system. For example, it is well known that aging cause an increase of the aortic stiffness due to decrease in the production of new elastic tissue, with non-elastic, fibrotic tissues produced instead[7]. The result is an increase of blood flow resistance and pressure that may lead to hypertension and/or heart failure, for a more detail description of the aortic wall histology and its function refer to O'Rourke et al. (2011).

A range of mechanical and geometrical properties of the aortic wall are reported in Table 1.1 for the ascending and descending aorta. These measurements are derived through Magnetic

[7]Mainly fibroblast are responsible for this degenerative mechanism, since they actively regulate collagen and elastin production of different tissues, aortic wall included (Tieu et al., 2011).

Table 1.1: Table that summarize human Ascending/Descending aortic properties at different age groups and sex: before 60 years old and after 60 years old. Range of reported minimum and maximum diameters (in mm) in male and female subjects, maximum and minimum reported values for aortic wall thickness (in mm) and mean pulse wave velocity (in ms^{-1}). (M) states for males and (F) states for females.

	Ascending aorta Age <60	Ascending aorta age> 60	Descending aorta age < 60	Descending aorta age > 60
Diameter range [mm]	27-35.6 (F) 28-37.8 (M) from Mao et al. (2008)	32.2-40 (F) 35-42.6 (M) from Mao et al. (2008)	15-17.9 (F) 16-19 (M) from Joh et al. (2013)	up to 18.1 (F) up to 19.4 (M) from Joh et al. (2013)
aortic wall thickness [mm]	1.3 from Nakhleh et al. (2013)	2.38 from Nakhleh et al. (2013)	1.15-2.38 (F) 1.23-2.65 (M) from Rosero et al. (2011)	1.39-2.6 (F) 1.48-2.97 (M) from Rosero et al. (2011)
PWV [ms^{-1}]	7.9 ± 2.3 from Rogers et al. (2001)	10.6 ± 2.5 from Rogers et al. (2001)	7.9 ± 2.3 from Rogers et al. (2001)	7.1 ± 1.7 from Rogers et al. (2001)

Resonance (MR) or Computed Tomography (CT) imaging techniques at the ascending aorta at 15 mm above the left main coronary ostium or right pulmonary mid slice level (Mao et al., 2008; Nakhleh et al., 2013; Rogers et al., 2001), and at the descending aorta at the infrarenal region, between iliac arteries and renal arteries (as suggested from the International Society for Cardiovascular Surgery/Society for the assessment abdominal aortic aneurysm (Johnston et al., 1991)). The elasticity (distensibility) of the aortic wall is clinically reported in terms of Pulse Wave Velocity (PWV), measured in ms^{-1}, a high value indicates that the arterial wall has become stiff. Aortic diameter, thickness and pulse wave velocity increases with age in both female and male subjects at the ascending and descending aorta, because of the mechanism of aging that causes thickening, cystic necrosis, elastin fragmentation and plaque deposition at the intima layer, and fibrosis and medionecrosis of the tunica media and adventitia (Mao et al., 2008). In terms of aortic wall distensibility, aging affects more the ascending rather than the descending aortic regions. The progressive fragmentation of the elastin fibers has greater effect on the proximal ascending aorta region since the ratio of

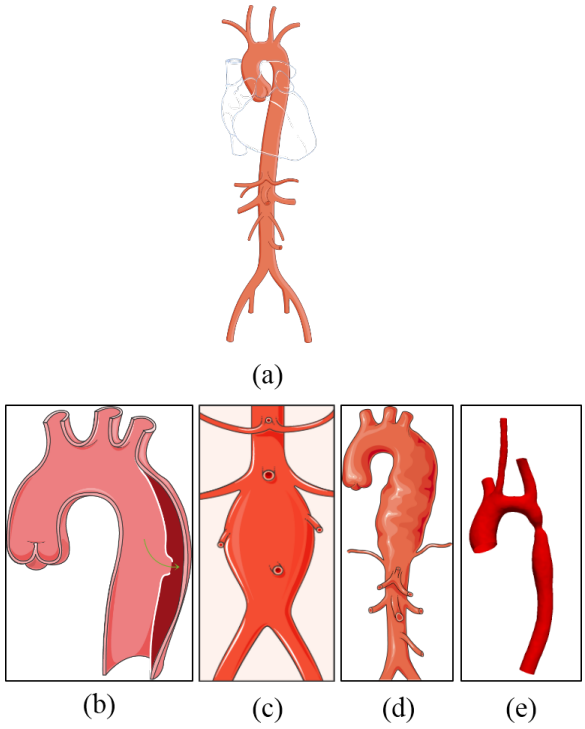

Figure 1.6: Figure (a) illustrates a physiological aorta with main branches. Figures (b), (c), (d) and (e) illustrate some of the aortic diseases that received interested from the *in-silico* model community : (b) a type III De Bakey (or type B Stanford) dissected aorta, (c)an abdominal aortic aneurysm (AAA), (d) a thoracic aortic aneurysm (TAA) and (e) a coarcted aorta. Figures (a), (b), (c) , (d) adapted with permission from SMART SERVIER MEDICAL ART (2019)

elastic to collagen fibers is 3.1:1, while at the abdominal region is 2.8:1 Apter (1967).

In this section, different pathological conditions that affect the aorta are reviewed in terms of previous analysis by the *in-silico* model community and as targets for development of predictive numerical workflows to guide clinical decision making (see Figure 1.6). Following this introduction a particular pathology has been chosen to be the target disease for the clinical toolkit: aortic coarctation. Therefore particular attention is focused on the review of numerical models that have been used to assess this disease and on their clinical application.

1.4.1 Marfan syndrome

Marfan Syndrome (MFS) is classified as an autosomal dominant inherited syndrome of the connective tissues and it is caused by a gene mutation. The results of this mutation is the production of structurally inferior collagen fibers present in the extra-cellular matrix of many organs and tissues (El-Hamamsy & Yacoub, 2012).

The estimated prevalence of the disease is approximatively 1 in 5000 individuals, and it is influenced by gender and ethnicity (caucasian males are more prone to have this disease (Groth et al., 2015)). Since most human tissues are made of collagen fibers, the effect of the gene encoding mutation is systemic. In the cardiovascular system, Marfan syndrome manifests as: aortic dilation at the sinus of Valsalva (frequently associated with aneurysm progression); pulmonary artery aneurysms (PAA) and thoracic-aortic aneurysm (TAA); aortic dissections; mitral valve prolapse and bicuspid aortic valve (BAV) syndrome.

In the clinical practice, multiple examinations are used to assess these cardiovascular degen-

erations, such as: transthoracic echocardiography (TTE); magnetic resonance (MR) or Computed tomography (CT) or an invasive transesophageal echocardiogram (TEE or TOE).

Medications and Surgical repair are the main treatments for MFS patients. Medications can slow the evolution of aortic dilation and prevent future damage only in the early phase of the pathology[8]. Despite their benefits, it has been shown that these medications neither really stop the disease progression nor preclude the eventual need for surgical intervention (Pearson et al., 2008).

The surgical procedure is usually performed when: the maximum diameter of the aortic root measured at the sinuses of Valsalva is around 5.0 cm in adults or older children (Davies et al., 2002); the aorta increases its diameter more than 1.0 cm per year during imaging follow-up examinations; or in the presence of significant aortic regurgitation (Kumar & Agarwal, 2014).

The degenerate aortic trunk can be surgically replaced by a graft (Sarsam & Yacoub, 1993; David & Feindel, 1992), and in case of valvulopathies with a graft that includes a prosthetic valve (Bentall & De Bono, 1968; Edwards & Kerr, 1970). Endovascular stent-graft replacement is commonly not performed when dealing with MFS or other connective tissue disorders, because the wall does not have sufficient mechanical properties to sustain the stent-graft positioning (Milewicz et al., 2005).

Since 2004 a novel technique, called PEARS (Personalized External Aortic Root Support), has been available as an alternative to surgery. The idea was first proposed by Tal Goleswor-thy in 2004 (Treasure, 2013; Treasure et al., 2014), and it consists of insertion of a soft and

[8]Beta blockers and Angiotensin II-receptor blockers are commonly used to control heart rate (Tahernia, 1993), minimize blood pressure (Brooke et al., 2008) and prevent excessive growth factors signaling that triggers the production of altered collagen fibers (Ramirez & Dietz, 2007)

macroporous polymeric mesh support around the ascending aorta's external wall. The problem has been investigated with CFD (Computational Fluid Dynamic) models by Singh et al. (2016) that demonstrated that the support system is able to restore the normal fluid dynamics with a reduction of the regions with high helicity and separated flow patterns at the aortic root. The simulation was performed using a rigid walled model with flow-split conditions at the supraortic vessels and a literature derived pressure waveform at the descending aortic outlet.

1.4.2 Aortic dissection

Aortic dissection (is a pathology that affects the arterial wall, caused by loss of the arterial wall integrity due to aging, aneurysm progression, hypertension or other connective tissue degenerative pathologies (i.e. Marfan's syndrome). AD occurs when a tear in the aortic intima-medial layer acts as a entry for the blood, causing the separation of the aortic layers into a false lumen (a new secondary channel) and the true lumen (the aortic lumen). The entry tear is usually localized at the zones of greatest stress (Nordon et al., 2011), see Figure 1.6(b). The incidence of aortic dissection (AD) is said to be around 30 cases per million individuals per year and the mortality rate is 25-50% at 5 years after diagnosis, especially if the disease is associated with chronic aneurysmal dilations and malperfusion of distal organs (Doyle & Norman, 2016). Dissections can be classifed based on DeBakey or Stanford classification guidelines, and into acute or chronic dissections.

Sun & Chaichana (2016) provided a review of numerical models that have been published in

the last decade focusing on AD. The AD modelling challenges are related to the capability to track each tear layer size and position and the integration of patient specific measurement inside the numerical model. More recently, Bonfanti et al. (2017) published a paper based on a patient-specific dataset of AD patient, where they adopted a multiscale approach for simulation of blood flow in the aortic geometry and evaluated the false lumen displacement, filling blood volume and WSS distribution. The multiscale approach consisted of a 3D deformable wall model (the deformation of the wall was implemented using a moving boundary technique) of the aortic geometry coupled with three element Windkessel models. The outlet Windkessel model parameters were found iteratively through the use of a lumped description of the entire dissected aorta, by matching clinical or literature derived flow rate and pressure values.

1.4.3 Thoracic Aortic Aneurysm

The Thoracic Aortic Aneurysm (TAA) results from deterioration and weakening of the aortic wall, which can lead to a permanent aortic dilatation at different levels in the chest area, see Figure 1.6(d). Thoracic aortic aneurysms occurs in approximately 6-10 per every 100000 people (Elefteriades & Farkas, 2010).

Surgery is a common procedure when the TAA diameter exceeds 5.5 cm, since it has been reported that the yearly risk of dissection or rupture rises dramatically from 3% to 7% for aneurysm diameter larger than 6 cm (Elefteriades & Farkas, 2010). Predisposing risk factors for TAA include hypertension, in combination with bicuspid aortic valve (BAV) or tissue degenerative syndromes such as Marfan's syndrome.

Diagnosis is made with the use of MRA, CTA, TEE or TTE examinations. Once the TAA has been localized, the surgeons usually replaced the aneurysmatic aorta duct with a synthetic graft. The Thoracic Endovascular Aortic Repair (TEVAR) procedure is gradually substituting the open-heart surgery technique for treating patients who suffer from Thoracic Aortic aneurysm (Bodell et al., 2018). The endograft is placed in a particular zone subject to high pressures, pulsatile flows, and radial and transverse wall motion, a combination of blood pressure and frictional forces which can significantly affects the in vivo performance of the device. Aneurysm enlargement, endograft collapse, endoleaks, and device migration are the most common drawbacks of this technique, therefore patient are due to constant screening (Matsumura et al., 2008).

In the literature, Computational Fluid Dynamics studies on TAAs are mainly focused on non-invasively estimating the distribution of wall shear stress, pressure and velocities streamlines. Investigations focus also on detecting Intra Mural Stresses (IMSs), acting on the aneurysmal walls with Finite Element Analysis (FEA) (Shang et al., 2013), or with Fluid-Structure Interaction (FSI) models (Pasta et al., 2013), prescribing literature derived pressure and/or flow rate boundary conditions. Frequently, CFD simulations on TAAs may include also models of Biscuspid Aortic Valve (BAV) (Della Corte et al., 2012; Vergara et al., 2012; Pasta et al., 2013; Rinaudo & Pasta, 2014). Figueroa et al. (2009) performed FSI simulations on a postoperative model of a descending TAA after treatment with an endograft in order to evaluate pressure and shear stress exerted by blood on the device and the risk of device migration in vivo.

1.4.4 Abdominal Aortic Aneurysm

The Abdominal aortic aneurysm (AAA, also known as triple A) is a localized enlargement (a dilation with a diameter 1.5 times or more) of the abdominal aorta, see Figure 1.6(c). AAAs are found in 4% to 8% of older men and 0.5% to 1.5% of older women . Age, smoking, sex, diet, family history, atherosclerosis, enzyme imbalances, congenital weakining of the connective tissue and rarely traumas are the most significant AAA risk factors (Lederle FA et al., 2000).

Typical tests performed to confirm the presence of Abdominal Aneurysm are: Ultrasound (similar to TEE), CT scan and MRI. Rupture of an AAA and internal bleeding is the primary cause of death in patients with triple A. The treatment of AAAs is either an open surgery or an non-invasive endo-luminal stent-graft insertion . The final goal is to reduce the risk of rupture by reducing the pressure acting at the aneurysm's wall (Rydberg et al., 2001). Despite the huge advantages introduced by these non-invasive interventions, stent migration is a well known side effects in mid-term and long-term follow-up and might lead to reintervention (Ohki et al., 2001), together with endoleaks (blood flows outside the graft in the aneurismal sac) and endotension (AAA continues to enlarge) (Chaikof et al., 2016).

Different numerical studies have focused on the hemodynamic changes in AAA with or without stent-graft or after surgical repair. These models simulated the interaction between blood flow and aneurysm wall (Di Martino et al., 2016), pre- and post-stent-graft implantation hemodynamic changes in a rigid wall configuration or a FSI simulation (Juchems et al., 2004; Prasad et al., 2013; Li & Kleinstreuer, 2016), and the risk of rupture prediction (Raghavan et al., 2000; Fillinger et al., 2002). Whilst these studies adopt relatively sim-

ple outlet boundary conditions, recently published articles have focused on getting more realistic results, with the improvement of boundary conditions (with the use of Windkessel parameters or wall displacement integration (Joly et al., 2018)), see Canchi et al. (2015) for a comprehensive review. 3D simulations offer a deeper insight into the local haemodynamics and the shared forces between stent and aortic wall, thus 3D approaches are more frequent in the literature. The modelling approach depends on the research question under investigation, for example Willemet & Alastruey (2015) published a study where the assessed the risk of rupture of an abdominal aneurysm using a one-dimensional approach instead of a three-dimensional analysis. However, when dealing with vortical or high separated flows, a one-dimensional approach could not offer a detail insight on the fluid dynamic structures at the aneurysmatic sac as a three-dimensional simulation.

1.4.5 Aortic Coarctation

Coarctation of the aorta (CoA) is a congenital cardiac defect accounting for 8-11 % of newborns with Congenital Heart Disease (CHD) in U.S. (Roger et al., 2011) and 5-8% in Europe (by the Association for European Paediatric Cardiology , AEPC). It is the fifth most common CHD (Suradi & Hijazi, 2015), more frequent in males than females, and consists on a narrowing of the lumen of the thoracic aorta distal to the ostium (opening) of the left subclavian artery at the patent ductus arteriosus location, see Figure 1.6(e).

The CoA is frequently associated with hypertension, decreased perfusion and flow disturbances at descending aorta, left ventricle hypertrophy, early onset coronary artery disease and cerebral aneurysms, right ventricular dilation and pulmonary hypertension (Agrawal

et al., 2018; Brown et al., 2013).

Patients with untreated coarctation have an average survival age of 35 years, with 75 % chance of dying by 46 years of age (Warnes et al., 2008; by the Association for European Paediatric Cardiology , AEPC).

The aortic coarctation is classified into two main categories: infantile (pre-ductal form), promixal to the ducuts arteriosus [9] a more extended and diffuse narrowing; or adult (juxta-ductal, post-ductal or middle aortic) form, where the stenosis is more abrupt and localized. The recurrent CoA can be considered the third possible form of coarctation, and typically occurs after surgical repair. The incidence of recurrent CoA is around 15% 1-5 months post-surgical intervention (Dehaki et al., 2010).

Primary symptoms of Aortic Coarctation include hypertension, therefore the first assessment consists on detecting systolic and diastolic cuff pressures at the arm and leg. The diagnosis then proceeds with the help of imaging diagnostic techniques such as: Magnetic Resonance Imaging (MRI) or Computed Tomography (CT) for detecting anatomical and geometrical features (narrowing site and its extent, minimum narrowed area or the presence of eventual dilations); transthoracic echocardiography (TTE), combined with a Color Doppler measurement can give information about peak velocity flow (generally it is the diagnostic gold standard in neonates and infants (Torok et al., 2015)); or cardiac catheterization for detecting pressure distribution across the coarctation.

There are two types of possible treatments of aortic coarctation: the endovascular repair and the surgical intervention. In the literature, there are numerous available surgical techniques.

[9] the ductus arteriosus or ductus Botalli is a vessel the connect the main pulmonary artery to the proximal descending aorta, used to bypass lung circulation during fetal development phases. This vessel normally closes at birth.

The objective of all techniques is to restore normal perfusion and the original aortic lumen cross-sectional area: via a resection of the pathological duct (Figure 1.7 A) (Dodge-Khatami et al., 2000) ; with the suture of a synthetic patch to enlarge the conduit (isthmusplastic repair or patch angioplasty, Figure 1.7 B) (Vossschulte, 1961) or with the use of a graft to replace the damaged area (graft repair, Figure 1.7 C) (Gross, 1951); or, less frequently, the narrowed section is enlarged with the sacrifice of the left subclavian's vessel used as a patch (left subclavian flap repair, Figure 1.7 D) (Hart & Waldhausen, 1983). Since most of the CoA patients are children, the resection end-to-end anastomosis (nowadays performed in the variant proposed by Amato et al. (1977)) is considered to be a more suitable surgical procedure, as it avoids the need for future re-interventions to renew the synthetic patch or graft and also it does not sacrifice supra-aortic perfusion.

Non-invasive treatments consist of balloon angioplasty or stent endovascular placement.

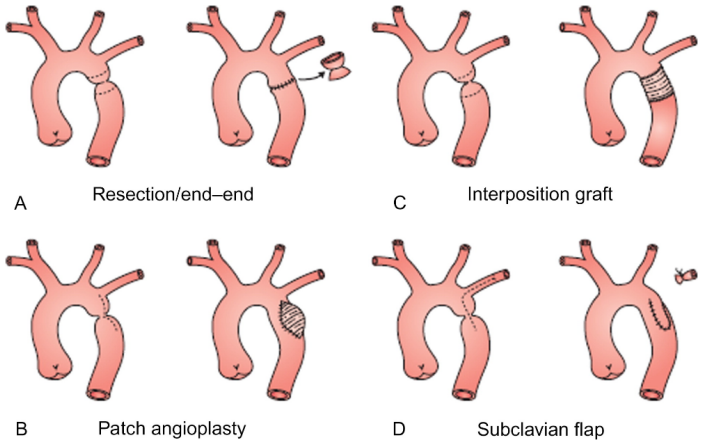

Figure 1.7: Major surgical repair techniques (Suradi & Hijazi, 2015).

Lock et al. (1983) were the first to use a balloon angioplasty in native coartaction. Recoarction and aneurysm formation are frequent side effects of a balloon angioplasty intervention

(Harris et al., 2014), for this reason balloon angioplasty is more often chosen for treating recurrent coarctations (Saxena, 2015) rather than the native coarctations.
In 1991, O'Laughlin et al. (1991) used an endovascular stent for the treatment of coarctation. When compared with balloon angioplasty, stents can decrease the rates of restenosis (or re-coarctation) and offer a better structural support. The main concern about this procedure is the risk of reintervention either due to planned dilation of a smaller stent or due to inflammatory response to the aortic wall injuries.

1.5 Assessment of aortic coarctation with a numerical model

The Coarctation of the aorta induces a pressure gradient across the narrowing similar to that associated with the Bernoulli's Venturi pipe example, used to describe the increase in the speed and the simultaneous decrease of pressure across a sudden narrowing section (Wyse et al., 1984; Baumgartner et al., 2009). The Bernoulli's principle is also used in clinical practice to assess pressure drops from Doppler ultrasound velocimetry. Peak velocity is detected by the instrumentation and the pressure drop is estimated as:

$$\Delta P = 4 \cdot (v_{vc})^2 \tag{1.3}$$

The equation is derived from:

$$P_1 + \frac{1}{2}\rho v_1^2 = P_2 + \frac{1}{2}\rho v_2^2$$

$$\Delta P = P_1 - P_2 = \frac{1}{2}\rho v_2^2 - \frac{1}{2}\rho v_1^2 = \frac{1}{2}\rho v_{vc}^2 = \frac{1060 \cdot 760}{2 \cdot 101325} v_{vc}^2 \sim 4 \cdot v_{vc}^2 \qquad (1.4)$$

used to describe how pressure distribution varies at two different points 1 and 2 of the circuit, assuming blood to have density of $1060 \frac{kg}{m^3}$ and a unit conversion factor from Pascal to mmHg of $\frac{760}{101325}$ $mmHg \cdot Pa^{-1}$. The *vena contracta* is the point where the cross section area is minimum, therefore the velocity is maximal. In the clinical practice, v_{vc} corresponds to peak velocity value, assuming that v_1 is negligible small when compared to $v_{vc} = v_2$, Equation 1.3 becomes 1.4. Where ΔP is the pressure gradient expressed in mmHg and v_{vc} is the velocity of the *vena contracta*. Equation 1.4 describes a steady state inviscid fluid flowing through a pipe, the derived pressure gradient is over-estimated by 41% when compared to catheter measurement, which is considered to be the gold standard in the clinical practice (Seifert et al., 1999). The difference is due to the fact that the Bernoulli's principle does not take into account for unsteady and viscous losses, velocity profile contribution on pressure decay and pressure recovery effects downstream of the coarctation (Wisotzkey et al., 2015; Donati et al., 2017).

Pressure drop is often clinically measured through an invasive cardiac catheterization, in order to classify the severity of the obstruction and plan for the intervention. Nowadays, with the advance in computational modeling, it has been possible to provide a CFD based assessment of this trans-coarctation pressure gradient via a numerical model representation of the fluid dynamics across the narrowed section. This assessment not only provide a clinical non-invasive measurement but can also explained most of the phenomena behind the overstimation of the pressure decay that has been observed during Doppler Ultrasound examination, giving a detail description of the local fluid flow, pressure distribution but also

velocity, since the Doppler velocimetry is higher operator dependent.

Most computational studies presented in the literature are focused on predicting and comparing pre- and post-surgical intervention pressure gradients using the cardiac catheterization data for validating the modelling assumptions. The computational problem is approached using either a fully three dimensional models, or one dimensional models.

The numerical domain is extracted from MRI or CT scan images and the governing equations are solved using patient-specific 2D/4D MR ascending flow rate data as inlet boundary conditions or a lumped model of the heart. At the outlet boundaries different approaches are used such as 0D models representing the downstream circulation, a constant zero-pressure or a percentage of the flow rate at the inlet (flow-split condition). Table 1.2 and the following section provide an overview of the modelling assumptions and strategies adopted in recent published work in the literature.

Table 1.2: Overview of different mathematical models used in the literature to assess pressure gradient across a coarctation site (y/o = years old, F = Female, M = Male, BAV= Bicuspid Aortic Valve).

3D models

Study	Patient Data	Boundary Conditions	Assumptions
Valverde et al. (2011) (cohort of 5 patients) Age: 19.6 ±3.44 y/o Sex: not stated	3D Gd CE-CMR ; 2D PC-MRI; Invasive catheter pressure waveform;	**AscAo:** 2D PC-MRI flow ; **Diaphragmatic aorta:** catheter pressure waveform; **Supra-aortic vessels:** flow split condition;	Newtonian, incompressible laminar blood flow rigid wall
LaDisa et al. (2011) (cohort of 4 patients) Age: 6.8 ±2.38 y/o Sex: 50 % F	3D Gd CE-MRA ; 2D PC-MRI; Cuff Pressure (upper/lower body);	**AscAo:** 2D PC-MRI flow and lumped heart model; **Other outlets:** 3 elements Windkessel models;	Newtonian, incompressible laminar blood flow deformable wall
Coogan et al. (2011) (1 patient) Age: 15 y/o Sex: F	3D Gd CE-MRA ; 2D PC-MRI; Cuff Pressure (upper/lower body);	**AscAo:** lumped heart model ; **Other outlets:** 3 elements Windkessel models;	Newtonian, incompressible direct numerical simulation deformable wall
Menon et al. (2012) (28 rabbits) Age: 32-36 weeks of age Sex: not stated	3D Gd CE-MRA ; 2D PC-MRI; Cuff Pressure (upper/lower body);	**AscAo:** 2D PC-MRI flow ; **Other outlets:** 3 elements Windkessel models;	Newtonian, incompressible laminar blood flow rigid wall
Wendell et al. (2013) (1 patient) Age: 34 y/o Sex: M	3D Gd CE-MRA ; 2D PC-MRI; Cuff Pressure (upper/lower body);	**AscAo:** 2D PC-MRI flow (BAV inclusion) ; **Other outlets:** 3 elements Windkessel models;	Newtonian, incompressible laminar blood flow rigid wall
Kwon et al. (2014) (1 patient) Age: 15 y/o Sex: M	3D Gd CE-MRA ; 2D PC-MRI; Cuff Pressure (only upper body);	**AscAo:** 2D PC-MRI flow **Other outlets:** 3 elements Windkessel models;	Newtonian incompressible laminar blood flow deformable wall

3D models

Study	Patient Data	Boundary Conditions	Assumptions
Pant et al. (2014) (1 patient) Age: 17 y/o Sex: M	3D Gd CE-MRA ; 2D PC-MRI; Inv. cath. Pressure;	**AscAo:** 2D PC-MRI flow; **Other outlets:** 3 elements Windkessel models;	Newtonian, incompressible laminar blood flow rigid wall
Goubergrits et al. (2015a), Goubergrits et al. (2015b) (13 patient) Age: 25 ± 14 y/o Sex: 54 % F	3D Gd CE-MRA ; 4D VEC-MRI; Invasive catheter pressure waveform;	**AscAo:** Peak 4D VEC-MRI flow; **Diaphragmatic aorta:** Peak 4D VEC-MRI flow; **Supra-aortic vessels:** flow-split condition	non-Newtonian, incompressible k-w SST turbulent blood flow rigid wall
Cosentino et al. (2015) (1 patient) Age: 19 y/o Sex: M	CT scan ; 2D PC-MRI; Invasive catheter pressure waveform; DUS velocity measurements;	**AscAo:** 2D PC-MRI flow; **Other outlets:** 3 elements Windkessel models;	Newtonian, incompressible blood flow rigid wall
Zhu et al. (2018) (25 patient) Age: 2 y/o Sex: 68 % M	CT scan ; 2D PC-MRI; Inv. cath. Pressure;	**AscAo:** 2D PC-MRI flow; **Other outlets:** 3 elements Windkessel models;	Newtonian, incompressible blood flow rigid wall
1D models			
Itu et al. (2013) (4 patients) Age: not stated Sex: not stated	3D Gd CE-MRA ; 2D PC-MRI; Invasive catheter pressure waveform;	**AscAo:** 2D PC-MRI flow; **Other outlets:** 3 elements Windkessel models;	Newtonian, incompressible blood flow
Ralovich et al. (2015) (6 patients) Age: 17.5 ± 5.62 Sex: 50 % F	3D Gd CE-MRA ; 2D PC-MRI; Invasive catheter pressure waveform;	**AscAo:** 2D PC-MRI flow; **Other outlets:** 3 Windkessel models;	Newtonian, incompressible blood flow

The computational problem has been approached using both three-dimensional (3D) models and one-dimensional (1D) models, with a range of different assumptions: rigid or deformable walls; simple BCs such as literature derived flow-split conditions; flow-split conditions together with time-varying clinically measured pressure waveforms or more complex BCs such as coupled (0D) Windkessel models to represent the circulation beyond the local aortic region.

Goubergrits et al. reported two similar studies (Goubergrits et al., 2015a,b) that evaluated post- and pre-treatment conditions with 3D CFD models. In the first study (Goubergrits et al., 2015a), they computed average cross-sectional WSS and pressure distribution along the vessel centerline at peak systolic flow in 13 patients. They used MRA images and 4D flow MRI measurements to set up the geometry and boundary flow conditions for their models. They simulated a steady state flow condition with a rigid wall assumption representing pre, post and a proposed virtual treatments. In a second study (Goubergrits et al., 2015b), they compared the pressure drop calculated from CFD models at peak systolic flow rate with a catheter derived measurement for the same cohort of patients. In both of these studies, 4D MRI Flow measurements of peak flow rate was applied at the boundaries representing the ascending and the descending aorta, assuming a flat velocity profile, the difference between these two measurements was split between the remaining outlets (the supra-aortic branches) based on their cross-sectional areas (using a flow-split boundary condition). These simulations did not consider the transient effects nor the distensibility effects of the aortic wall. Even though at peak systolic flow the storage function of the aorta is nearly zero, ascending and descending aortic flow peaks do not occur simultaneously and they show a phase lag due to the compliance of the aortic wall and the interaction with downstream peripheral

circulation. Despite these simplifications, their models showed a good accuracy when compare to the gold standard measurement. The absolute error between catheter based and CFD pressure drop was reported as 1.45 ± 0.76 mmHg. The same approach has been adopted by Brüning et al. (2018) for studying the impact of uncertainties of MR image segmentation and peak 4D flow MRI measurements on the final pressure drop calculation.

A similar rigid walled approach was previously applied by Valverde et al. (2011) but in a transient simulation. The analysis was performed on five patients assuming laminar flow, the 2D pc-MRI derived flow rate waveform was applied at the ascending aorta, the difference between MRI measured ascending and descending aortic flow rate was proportionally split between the supra-aortic branches in order to maintain a constant wall shear stress, while the catheter derived pressure measurement was applied at the diaphragmatic aorta. The analysis was performed during pharmacological stress and rest condition, the results showed an higher error when compared to Goubertis et al., reported as -4.2 ± 4.9 mmHg, at rest and -4.4 ± 21.9 mmHg, at stress. A similar study was also reported by (Sotelo et al., 2015) on a cohort of 7 patients, with 2D PC-MRI flow rate and pressure data used to inform their CFD models, including the mechanical properties adopted for the vessel wall, assumed deformable.

LaDisa et al. (2011) investigated the WSS[10] distribution in 4 patients with a native or a recurrent coarctation at rest and exercise, but instead of directly applying the peak systolic flow, they extracted the ascending aortic flow rate waveform from 2D pc MRI data and applied it at the inlet of the model, assuming a parabolic velocity profile, while at the outlets three elements Windkessel models were used to represent downstream circulation.

[10]WSS is the Wall Shear Stress, define as the tangential force per unit area exerted on a blood vessel wall as a result of flowing blood

At rest, the tuning strategy for finding the Windkessels parameters was based on previous literature studies (Vignon-Clementel et al., 2006a) and adjusted to match systolic and diastolic cuff pressure measurements, assuming a constant wall thickness and Young's modulus for the aortic wall. The tuning strategy started by finding the total arterial capacitance (TAC), which is the sum of the compliance of the 3D model and the compliances of the lumped downstream circulation models, using a three element Windkessel model, representiative of the entire cardiovascular system. The Windkessel compliance (TAC) was tuned to match cuff pressure measurement following the approach adopted by Laskey et al. (1990) [11]. The TAC is then distributed among the outlets according to their blood flow distributions (derived from mean value extracted from 2D pc MRI measurements). For each outlet the total resistance was derived by dividing the mean pressure by the mean flow rate, and then distributing this to proximal/distal resistances by adjusting proximal to total resistance ratios (starting from a ratio of 6%) in order to match systolic and diastolic cuff pressure measurements. Aortic wall thickness was set to 0.15 cm as in (Westerhof et al., 1969) and the Young's modulus was iteratively adjusted in order to match mean luminal displacements measured from PC-MRI (error within 5 %). At exercise, the resting conditions where modified in order to take into account for the increase in flow and heart rate (by 50%) and decrease of peripheral total resistances (the sum of the proximal and distal resistance of the three elements Windkessel models). The regions distal to the coarctation experienced higher values of WSS, because the velocity jet, caused by the localized cross-section reduc-

[11] The patient specific inflow flow rate curve was applied at the inlet of the three elements Windkessel. The total resistance was derived as relationship between mean pressure and mean inlet flow rate, and it was distributed to the proximal and distal resistance, assuming a proximal to total resistance ratio of 6%. As stated before, the compliance (TAC) was varied in order to match diastolic and systolic blood pressure measurements from a starting value based on the literature.

tion, impinges on the aortic wall. Peak-to-peak pressure measurements derived from the numerical model were compared with pressure drop derived from the arm and leg cuff pressure measurements, showing a good match with an error of -1.5 $\pm$ 4.94 mmHg. However, the tuning approach adopted is highly user-dependent and the constant aortic wall thickness and Young's modulus assumptions conflict with previous in vivo and experimental observations (O'Rourke et al., 2011). At supra-aortic vessels a mean flowrate value was assumed based on velocity encoded MRI measurements, which are not often evaluated during the initial or in the follow-up exams. The same tuning strategy for the outlet Windkessel models was used, in a rigid wall configuration, by Menon et al. (2012) on a cohort of 28 rabbits, by Zhu et al. (2018) on a cohort of 25 patients, by Wendell et al. (2013) for a singular subject-specific evaluation of the pre- and post-treatment cases, and by Coogan et al. (2011) for a subject-specific evaluation of pre- and post-treatment adopting also the same approach for setting the mechanical properties of the deformable aortic wall.

In a more complex way, Pant et al. (2014) used an Unscented Kalman Filter (UKF) to obtain three elements Windkessel values based on catheter pressure measurements at ascending and diaphragmatic aorta in a patient suffering from a mild-coarctation.

Computational investigations have also included stent-treated coarctation. Cosentino et al. (2015) were the first to evaluate the optimal diameter expansion of a bare metal stent in a complex case of re-coarcted aorta by using FE and CFD models. CT scan images were used to reconstruct *in silico* patient-specific 3D geometry before stent deployment. MRI flow measurements were acquired at each outlet of the 3D geometry. Stent expansion was simulated with a FE analysis four times at four different final diameters, the final 3D geometry configurations were used to characterize the hemodynamic post stent-deployment

by using a CFD modelling approach. Ascending aortic flow rate was applied at the inlet of the geometry, while each outlet was coupled with a lumped parameter model, tuned to match the acquired outlet MRI flow measurement by using a multi-compartmental 0D description of the aortic arch. To simplify the model, the aortic wall was considered rigid and blood Newtonian and incompressible. Based on safe anchoring, no flow obstruction and good coverage criteria, they eventually suggested at which final diameter the stent should be deployed during the procedure. The same WK parameters were defined for the pre- and post-stenting simulations, assuming that no significant cardiovascular changes occurred after the stenting procedure.

Kwon et al. (2014), in a similar way analyzed WSS, TAWSS and OSI index distribution in space and time over three different CFD models representing the same re-coarcted aorta virtually treated with three different commercially available stents. Geometry, ascending aortic flow waveform and outlet Windkessel parameters were set from MRA, pc MRI and previous works in the literature (Vignon-Clementel et al., 2006b). Regarding 1D models, Stergiopulos et al. (1992) were the first to consider a 1D model for representing a stenotic artery basing all the models parameters on literature data.

Later on, Itu et al. (2013) were the first to use a 1D model to evaluate pressure drop in a small cohort of 4 patients in order to assess the need of intervention. The 1D inflow boundary conditions were obtained from 2D pc-MRI flow rate data and the outlets were coupled with 0D downstream representation of the downstream circulation. The parameters for the 0D models were derived from geometrical and fluid dynamic information on patient specific available data. At the supra-aortic vessels, the total resistance was calculated as the ratio between the Mean Aortic pressure (MAP, assuming no pressure losses between ascending

aorta and supra-aortic branches) and the corresponding aortic flow (the main aortic flow, difference between measured ascending aortic flow and measured descending aortic flow, was distributed to all the supra-aortic vessel proportionally to the square of their radii). The distal resistance was then calculated as a difference between the total resistance and the proximal resistance, assumed equal to the impedance of the vessel (chosen in order to minimize the reflections). Aortic wall compliance was integrated by assuming an uniform wave speed propagation of the pressure signal, a parameter that can be easily extracted from pc-MRI and vessel geometry as in (Ibrahim et al., 2010). The total compliance parameter was derived from literature Stergiopulos et al. (1992) and it was reduced by the aortic wall compliance (the sum of the compliance of all the 1D elements in the model), it was distributed to each outlet, proportionally to the square of the radius. The model also include a nonlinear resistance representing the coarctation that included viscous , turbulent and inertial losses. The resulting error between catheter and CFD derived peak-to-peak pressure drop was 1.45 ± 0.76 mmHg.

Ralovich et al. (2015) used the same approach to evaluate pressure drop in a cohort of 9 patients. They assessed pressure drop before and after stent-graft placement, including the stent effects by locally increasing the stiffness of the aortic lumen where the device was placed. The CFD model showed a good correlation with catheter derived peak-to-peak pressure drop, the error between these two measurements was estimated to be 2.38 +/- 0.82 mmHg in the Pre-operative cases, and 1.10 +/- 0.63 mmHg after stent placement.

From the clinical point of view, these studies have demonstrated the ability of numerical models to predict pressure gradients across coarcted aorta, a parameter that indicates the need for a surgical intervention; while, from the engineering point of view, most of the

proposed models still lack capability to capture patient-specific haemodynamics due to the simplifications when dealing with applying patient specific boundary conditions. Itu et al. (2013); LaDisa et al. (2011) were the only groups who dedicated particular effort on the development of a tuning strategy for defining 0D Windkessel model parameters based on the patient available data.

1.6 Summary

Computational Fluid Dynamics simulations can offer an improvement in hemodynamics investigation for clinical patient-specific assessment of aortic pathologies. The previous section offered a brief review of several clinical research areas with potential for development of an for the engineering toolkit, which will be delivered in this work. The choice of adequate assumptions, especially in determining the boundary conditions, is essential for driving the study upon the patient-specific modelling. The engineering work-flow will improve this aspect, using all available patient data that has been already collected and accessible for setting the simulation.

From the clinical point of view, aortic coarctation seems the more intriguing application for the proposed toolkit, since towards all the possible outputs there already is one (pressure gradient) that is used in the clinic investigation. In accordance with the academic (University of Sheffield), clinical (University Hospital of Bern) and industrial supervisors (Therenva, Rennes), the engineering toolkit will be addressed for studying aortic coarctation.

2

Introduction

The aim of this work is to construct an engineering workflow, which supports specification of boundary conditions and 3D simulation based on clinically available patient-specific data. This proposed toolkit will be developed in the context of a medical software manufacturer (Therenva ®, Rennes), in order to provide additional clinical insight when treating cardiovascular diseases in the clinical environment. The host company, Therenva ®, has more than nine years of experience in designing innovative image guidance systems for minimally invasive cardiovascular surgery. Therenva's existing Endosize product targets

planning for treatments of aortic diseases such as device sizing and placement for TAVI or abdominal endovascular stents application.

A comparison of the current and proposed form of the software framework is illustrated in Figure 2.1, numbers on the right-hand side of this figure indicate the chapters of the thesis where further detail of the approach taken is reported.

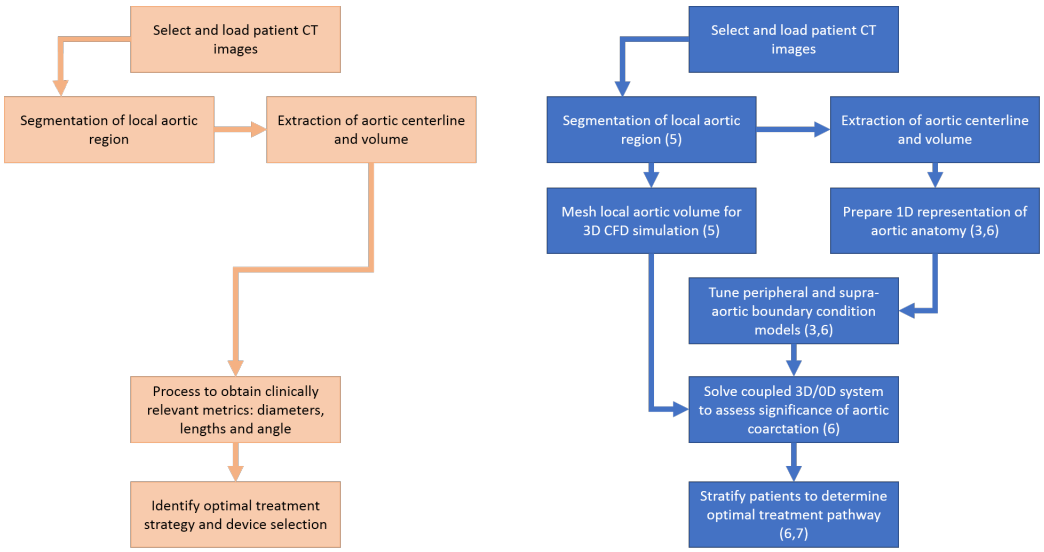

Figure 2.1: Schematic of current (left) and proposed (right) EndoSize workflow, initial steps are common in both cases. Numbers on the right indicate thesis chapters which report developments contributing to the proposed workflow. Current clinical decision making is informed using anatomical metrics to inform device selection and treatment strategy. The proposed workflow augments anatomical data with assessment of aortic haemodynamics.

Endosize is currently used to provide the clinical user with tools to load, segment and derive quantitative anatomical measures from clinical images of patients being considered for endovascular intervention. The software includes the options to select a range of device sizes and preview their deployment within the patient-specific segmented anatomical

region.

In the proposed final configuration, the segmentation provided by Endosize gives a starting point to undertake analysis of patient-specific haemodynamics to provide additional information to guide clinical decision making. In principle, this approach has potential for application across a range of aortic pathologies.

In *Chapter 3* the general system of equation that describes blood flow in a compliant tube is presented with a finite volume numerical scheme adopted for finding its solution. The system is then linearized and integrated with a finite element implementation in the frequency domain in order to analyse the effects of 1D non linearities in the modelling approaches. Both of these models are then tested on idealized geometries of increasing complexity taken from literature representing: an upper thoracic aorta, an iliac bifurcation and a full aorta geometry, concluding with analysis of a patient-specific aortic anatomy including a coarctation. This chapter details the assumptions associated with each approach and provides a discussion of their relative accuracy for the target application of this thesis. The detailed methodology of the 3D analyses reported in this chapter is provided in Chapter 6.

Chapter 4 briefly introduces the patient cohort used to inform subject-specific models for this thesis. This consists of 11 patients with aortic coarctation studied as part of a protocol approved by the local ethics committee at Bern University Hospital. This chapter presents a relatively simple analysis using several 0D models of increasing complexity to examine the sensitivity of parameters derived when tuning windkessel models of the peripheral circulation using patient-specific clinically measured pressure and flow data. The detailed methodology for processing clinical data is provided in chapter 5 and chapter 6.

Chapter 5 describes the development of novel approaches to improve 3D segmentation of

the local aortic anatomy, with particular focus on the definition of the supra-aortic branches. This development is undertaken using CT image data, as this is the current modality supported by the Endosize software framework. This chapter then describes the process undertaken for segmentation of patient anatomies acquired during the Bern study, using existing segmentation tools which support processing of MRI data. The chapter concludes with an analysis of mesh sensitivity for computation of subject-specific pressure gradients using a steady-state CFD approach for the full Bern cohort.

In *Chapter 6* the developments reported in earlier chapters are combined to enable a multi-scale modelling approach to simulate fluid-dynamics on the Bern cohort of patients. This includes the application of the nonlinear 1D model reported in chapter 3 to derive patient-specific parameters for windkessel models to describe the peripheral and supra-aortic circulation followed by transient analysis of a coupled 3D/0D system to estimate the pressure augmentation induced by the coarctation. These predictions are compared with invasively measured pressure catheter data and the influence of uncertainty in measured data on the tuning process is discussed.

Chapter 7 summarises the outcomes of previous chapters and presents a preliminary approach for the assessment of change in haemodynamics following coarctation repair for a single patient from the cohort.

Chapter 8 provides conclusions and makes recommendations for future work.

Declaration

In Chapter 3: Alessandro Melis developed the background theory for the nonlinear modelling approach as reported in his dissertation (Melis, 2017). Angela Lungu developed the background theory for the linear implementation model as reported in her dissertation (Lungu, 2015). The author implemented both models in Matlab (MathWorks Inc.) . The the 1D DCG and 3D solutions of the upper thoracic aorta and the liac bifurcation benchmark model were reported from a previous work of Boileau et al. (2015), whilst the 3D solution and the 1D DCG of the full aorta benchmark model was reported from the work of Xiao et al. (2014). The numerical calculations for the MICCAI model (3D and 1D analyses) provided by the STACOM 2013 challenge (http : //www.vascularmodel.org/miccai2013/)were performed by the author. Part of the text has been taken from the ESVB 2017 conference submitted manuscript. In chapter 6: Dr. Kerstin Wustmann and Dr. Hendrik von Tengg-Kobligk organised and ran the study and collected the data at the University Hospital of Bern. The author post-processed some of the data and ran all the numerical analyses. Part of the text has been taken from the article publication.

3

1D modelling approach

3.1 Summary

In this chapter two different 1D modelling approaches are presented. For the first approach, the general conservation form of the 1D modelling equations is presented together with the assumptions that lies behind it. Then the solution strategy, based on the work of Melis (2017) is briefly presented. This method consists of a finite volume scheme (based on the Godunov's scheme) that numerically solves the hyperbolic system of PDEs in conjunction

with the method of characteristics for setting boundary and interface conditions. For the second approach, the 1D governing equations are linearized over an initial condition (A_0, Q_0) and resolved in the frequency domain using a finite element method based on the work of Lungu (2015). Both schemes have been implemented in Matlab (MathWorks Inc.) and they have been applied to benchmark cases representative of specific aortic regions, including the upper thoracic aorta, the iliac bifurcation, an idealized aorta and a patient-specific case representative of a mild coarctation. Simulations were run on a standard workstation (Intel(R) Xeon(R) 3.50 GHz).

3.2 The governing equations of the 1D nonlinear model

The numerical approach presented in this chapter is based on the work of Melis (2017). The 1D modelling approach is based on the following system of one dimensional nonlinear hyperbolic partial differential equations (expressed in a cylindrical coordinates system (r, θ, z))[1]:

[1] one dimensional hyperbolic partial differential equations are generally in the form

$$\frac{\partial^2 \varphi}{\partial t^2} = c^2 \frac{\partial^2 \varphi}{\partial z^2}$$

where c^2 is a positive constant (c represents the wave propagation velocity) and φ is a physical quantity. This equation usually defines wave-like propagating phenomena, such as ocean wave front propagation. It needs two initial boundary conditions in order to provide a unique solution for the problem.

$$\begin{cases} \frac{\partial A}{\partial t} + \frac{\partial Q}{\partial z} = 0, \\ \\ \frac{\partial Q}{\partial t} + \frac{\partial}{\partial z}(\alpha \frac{Q^2}{A}) + \frac{A}{\rho}\frac{\partial P}{\partial z} = -2\frac{\mu}{\rho}(\gamma_v + 2)\frac{Q}{A}, \\ \\ P = P_{ext} + \beta(\sqrt{\frac{A}{A_0}} - 1),\ \beta = \sqrt{\frac{\pi}{A_0}}\frac{Eh_0}{1-\nu^2}, \\ t \in I = (t_0, t_1),\ z \in \Omega_t = (z_0, z_1) \end{cases} \tag{3.1}$$

where t refers to time, z is the longitudinal coordinate along the vessel centerline, A is the vessel cross-sectional area perpendicular to z, Q is the volumetric flow rate, P is the blood pressure, α is the Coriolis coefficient, h_0 and A_0 are respectively the reference values for the wall thickness and cross-sectional area[2], ρ is the blood density, μ is the blood dynamic viscosity, γ_v is a parameter that determines the shape of the velocity profile, P_{ext} is the external pressure, E is the vessel wall Young's modulus, ν is the Poisson's ratio (see Figure 3.1). The pulse wave speed $c(z,t)$ is related to A through

$$c = \sqrt{\frac{\beta}{2\rho}} A^{\frac{1}{4}} = \sqrt{\sqrt{\frac{\pi}{A_0}}\frac{Eh_0}{2\rho(1-\nu^2)}} A^{\frac{1}{4}} \tag{3.2}$$

This system of equations was originally formulated by Euler in 1844 (Euler, 1844) as an attempt to describe the fluid motion in a compliant circular cylinder. He presented this study as an entry in a prize competition set by the Academy of Sciences in Dijon. In his work,

[2] They refers to an unstressed condition when the acting luminal pressure is equal to 0

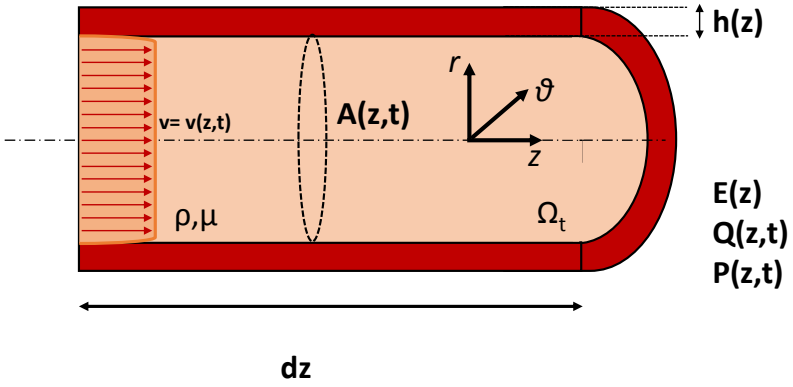

Figure 3.1: A 1D compliant arterial segment (or domain Ω) whose properties are described as a function of the axial coordinate z (vessel centerline). The density and the viscosity are denoted by ρ and μ. For each time and position, the luminal area is denoted by $A(z,t)$, the wall thickness by $h(z)$, the wall Young's modulus by $E(z)$, the cross-sectional average velocity and pressure by $v(z,t)$ and $P(z,t)$, respectively, and flow by $Q(z,t)$. The governing equations can be derived by applying conservation of mass and momentum to a control volume denoted by $dz \cdot dA$.

the governing 1D equations were derived from the equivalent momentum and continuity conservation laws written in an integral form for a control volume representing a portion of the vessel, the reader can refer to (Sherwin et al., 2003) for a complete derivation.
It can be shown that these equations can be also deduced from the linearization and integration over a generic section $A(z,t)$ of the Navier-Stokes equations that describe the fluid flow in a three-dimensional domain (Barnard et al., 1966; Formaggia et al., 2006). Nonetheless, the basic simplifying assumptions behind the system 3.1 remain the same for both derivations

- **A.1 Axial symmetry and section assumed circular.** All the physical quantities (A,Q,P,v and r) do not depend on the angular coordinate θ and the axial section $A(z,t)$ is assumed circular and remains circular for the entire cardiac cycle.
- **A.2 Wall radial displacements only.** The wall displaces only along the radial coordinate r, thus the axial wall displacements are neglected.
- **A.3 Vessel is tethered in the longitudinal direction.** The vessel cylindrical axis is fixed in time. This assumption is not valid for certain regions of the circulatory system such as the coronaries where the heart contractions cause the vessels to displace in time.
- **A.4 Pressure is constant at each axial section.** Pressure is assumed constant at each section A, therefore it depends only on z and t.
- **A.5 Body forces are neglected.** In most applications this assumption is made although gravitational forces can be added to the model by including appropriate terms in the momentum balance as showed in Sheng et al. (1995); Payne (2004). The ef-

fects of gravitational forces on the blood fluid dynamic becomes important when modelling the venous system, especially during postural changes (Brook & Pedley, 2002; Olufsen et al., 2005).

- **A.6 Velocity varies only along the axial coordinate with a fixed profile**. The vessel is long enough to consider variations of pressure, area or velocity negligible in the radial directions. It is assumed that velocity components perpendicular to the z-axis are small and can be neglected ($u = u(z,t)$ therefore $Q = Q(z,t)$, since $A = A(z,t)$ for A.1). In addition, this assumption implies that the velocity profile does not change in space. This assumption is in contrast with experimental observations and numerical results, where the blood velocity profile is highly influenced by vessel curvature and bifurcation regions. However, Azer & Peskin (2007) incorporated a local, time-dependent velocity profile function (based on the Womersley velocity profile theory (Womersley, 1957)) into a one dimensional numerical formulation, demonstrating that this assumption has small effects on the propagation of pressure and flow waveforms in the numerical domain, but more significantly affects the accuracy of wall shear stress prediction. These results have also been proved in recent works such as Čanić & Kim (2003); Bessems et al. (2007); Reymond et al. (2009); Van de Vosse & Stergiopulos (2011).

  The velocity profile affects the convective accelerations and the frictional term in the momentum balance. The velocity profile influences the convective acceleration term through the parameter α, the Coriolis coefficient (or momentum-flux correction coefficient) which accounts for the nonlinearity associated to the integral of the local velocity u_z over the cross-sectional area:

$$\alpha = \frac{\int_{S=A(z,t)} {u_z}^2 dS}{A\overline{u}^2} \tag{3.3}$$

where:

$$u_z(r, z, t) = \bar{u}(t, z)s(rR^{-1}(z)) \tag{3.4}$$

$\bar{u}$ is the mean velocity[3] for each axial section and $s(rR^{-1}(z))$ is the velocity profile function or law expressed in cylindrical coordinates (defined also as a function of y, where $y = rR^{-1}(z)$ and R is the radius at z). The profile s can be mathematically defined by a power law that depends on the value assigned to the velocity profile factor, γ_v, as:

$$s(y) = \frac{(\gamma_v + 2)(1 - y^{\gamma_v})}{(\gamma_v)} \tag{3.5}$$

In the case where the velocity profile is assumed to be parabolic (Poiseuille's flow) the value assigned to γ_v is 2, the velocity profile derived from equation (3.5) is $s(y) = 2(1 - y^2)$. The parameter α is also related to γ_v as follows

$$\alpha = \frac{\gamma_v + 2}{\gamma_v + 1} \tag{3.6}$$

Therefore from (3.6), α is equal to $\frac{4}{3}$. The velocity profile is generally flat in large arteries. The values assigned to γ_v is then equal to 9 and α is $\backsim$ 1.1. Figure 3.2 shows the effect that γ_v has on the velocity profile law. For simplicity, α was taken equal to 1 and the wall profile was assumed flat. The frictional term per unit of length, *f*, can be expressed as a function of γ_v as follows

[3]The mean velocity is defined as

$$\bar{u} = A^{-1} \int_S u_z dS$$

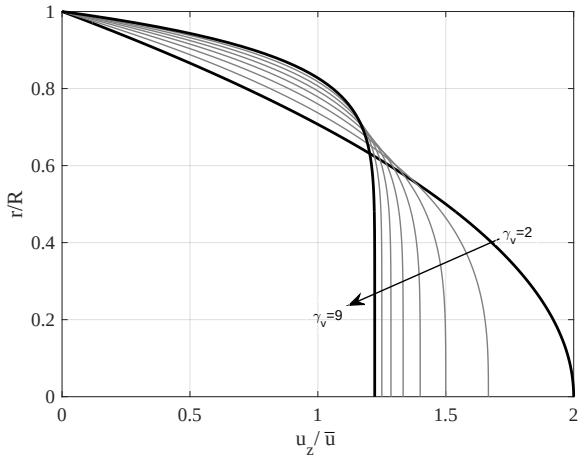

Figure 3.2: Radial velocity profiles, u_z expressed in cylindrical coordinates as a function of the mean velocity $\bar{u}$ for different values of the velocity profile factor γ_v. Note that for $\gamma_v = 9$ the velocity profile is near plug-flow with a flat region, at the center of the vessel, and a thin boundary layer; while the parabolic profile is obtained for $\gamma_v = 2$ (with $u_z(r = R) = 2\bar{u}$).

$$f = -2\mu(\gamma_v + 2)\frac{Q}{A} \tag{3.7}$$

For a parabolic profile the frictional forces are equal to $-8\mu\frac{Q}{A}$, which corresponds to the Poiseuille's resistance under laminar axial-symmetrical Newtonian flow assumptions.

- **A.7 Blood is Newtonian and incompressible.** This assumption is valid only for large arteries where the shear rate at the walls is greater than 100 s^{-1} therefore blood can be considered a Newtonian fluid (O'Rourke et al., 2011) .

- **A.8 Vessel wall is deformable.** The deformation of the wall is provided by an algebraic expression, usually referred as the *constitutive equation* or *tube law*, that links transmural pressure to the arterial wall deformation and vessel section A[4]. This equa-

[4]The constitutive law is necessary in order to close the algebraic system (3.1) and find all the three unknown

tion describes the wall behavior and in a more general form it can be expressed as:

$$P(t, z) = P_{ext} + \Psi(A(t, z); A_0(z), \beta) \tag{3.8}$$

P_{ext} is the external pressure acting on the vessel wall, usually assumed to be 0, The function Ψ is a mathematical expression that characterizes the mechanical properties of the vessel wall, it should be (at least) a $\mathcal{C}^1$ function[5], and for all values of A, A_0 and β:

$$\frac{\partial \Psi}{\partial A} > 0, \quad \text{and} \quad \Psi(A_0; A_0; \beta) = 0 \tag{3.9}$$

It can be shown that a linear elastic law for the vessel (Laplace's law) satisfies all the requirements (Olufsen et al., 2000)

$$\Psi(A; A_0; \beta) = \beta(\sqrt{\frac{A}{A_0}} - 1) \tag{3.10}$$

and β is

$$\beta = \sqrt{\frac{\pi}{A_0}} \frac{E h_0}{1 - \nu^2} \tag{3.11}$$

where E is the Young's modulus of the vessel wall, h_0 is the wall thickness, A_0 is the initial cross-section and ν is the Poisson ratio of the vessel wall. Equation 3.10 is derived assuming a thin, incompressible vessel wall undergoing axisymmetrical deformation (ε) independent for each circular cross-section. Homogeneous material

variables: P , Q and A.

[5] In order to have a realistic solution Ψ should be a continuous function and it should be differentiable with a continuous derivative (Formaggia et al., 2006).

properties are assumed in a longitudinally-tethered vessel under plane strain conditions with constant Young's modulus wall material. The circumferential (or hoop) stress σ is given by

$$\sigma = \frac{E}{1-\nu^2}\varepsilon \tag{3.12}$$

applying the Laplace's law, it reads

$$\sigma = \frac{r(P - P_{ext})}{h_0}, \quad \varepsilon = \frac{2\pi r - 2\pi r_0}{2\pi r_0} = \frac{r}{r_0} - 1 = \sqrt{\frac{A}{A_0}} - 1 \tag{3.13}$$

combining equation 3.12, 3.13, assuming small displacement for the linear elastic theory and $P_{ext} = 0$ yields

$$P = \sqrt{\frac{\pi}{A_0}}\frac{Eh_0}{1-\nu^2}(\sqrt{\frac{A}{A_0}} - 1) \tag{3.14}$$

The viscoelastic effects of the wall can be taken into account by adding to 3.12 a mathematical expression that relates stress to the first temporal derivative of strain (the reader can refer to Fung (2013); Alastruey et al. (2011)) for a complete derivation of the equivalent pressure area relation)

$$\sigma\frac{E}{1-\nu^2}\varepsilon + \varphi\frac{d\varepsilon}{dt} \tag{3.15}$$

where φ is the wall viscosity. This implementation can take into account the hysteresis and creep, stress relaxation and nonlinear behavior of the wall. For a review on the different tube laws available in literature please refer to (Absi, 2017).

The choice of the *tube law* depends on the type of circulation under study. As pre-

viously described, arterial walls are made of smooth muscle cells, elastin, collagen and glycoproteins. Smooth muscle cells, elastin and collagen fibers are responsible for the elastic behavior of the wall, while glycoproteins are responsible for the visco-elastic behavior of the wall. The high presence of elastic components in the arterial wall make the elastic assumption on the arterial wall behavior more reasonable, under physiological conditions (Alastruey et al., 2012a). Thus, in this work this assumption will be adopted.

3.2.1 Solution of the governing equations of the 1D nonlinear model

The system described in 3.1 can be solved for a given network of arterial segments using the method of the characteristics combined with a finite volume scheme. In the following subsections both methods are briefly presented for a detail explanation the reader can refer to Melis (2017).

Characteristic variables

The system of hyperbolic equations 3.1 can be written in its conservative form after few manipulations and assumptions such as a flat constant (in time and space) velocity profile ($\gamma_v = 9$ and $\alpha = 1$) and no external acting pressure ($P_{ext} = 0$)

$$\frac{\partial \mathbf{U}}{\partial t} + \frac{\partial \mathbf{F}(\mathbf{U})}{\partial z} = \mathbf{S}(\mathbf{U}) \tag{3.16}$$

where

$$\mathbf{U} = \begin{bmatrix} A \\ \\ Au \end{bmatrix} \quad \mathbf{F}(\mathbf{U}) = \begin{bmatrix} Au \\ \\ Au^2 + \gamma A^{3/2} \end{bmatrix} \quad \mathbf{S}(\mathbf{U}) = \begin{bmatrix} 0 \\ \\ f_s \end{bmatrix} \tag{3.17}$$

$$\gamma = \frac{\beta}{3\rho\sqrt{A_0}} \quad f_s = -\frac{A}{\rho}\left[\frac{\partial P}{\partial A_0}\frac{\partial A_0}{\partial z} + \frac{\partial P}{\partial \beta}\frac{\partial \beta}{\partial z} + 2\mu(\gamma_v + 2)\frac{u}{A}\right]$$

F is the flux, **S** is the source term and **U** is the solution. The characteristic analysis reported in Appendix A shows that the system is strictly hyperbolic since it is diagonalizable and has two distinct real eigenvalues $\lambda_{1,2} = u \pm c$. It follows that is possible to define two characteristic variables

$$W_{1,2} = u - u_0 \pm 4(c - c_0) = u - u_0 \pm 4\sqrt{\frac{\beta}{2\rho}}(A^{\frac{1}{4}} - A_0^{\frac{1}{4}}) \tag{3.18}$$

that are constant along certain curves, *the characteristic curves*, defined in the plane (z, t) with a slope $\lambda_{1,2} = u \pm c$. This means that, for each point in the domain, the solution can be decomposed into a forward (or entering) wave, W_1, and a backward (exiting) wave, W_2, allowing the implementation of boundary and compatibility conditions at fluid domain.

The finite volume method

The governing equations are solved in the internal cells of the numerical domain using a finite volume method. In the finite volume method, the governing equations are integrated over M cells (or finite volumes) representatives of the time-space numerical domain (denoted by $I_i = (\Delta z, \Delta t)$ in the Figure 3.3).

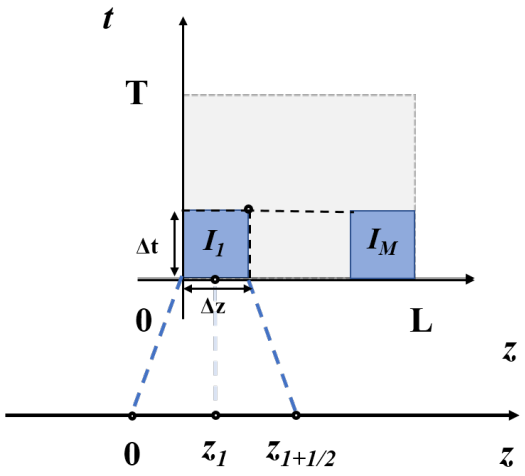

Figure 3.3: Computational numerical domain. Each cell has a dimension of $\Delta t \cdot \Delta z$ and it is centered on a node z_i with boundaries at $z_i \pm \frac{1}{2}\Delta z$.

For each cell three points are defined: z_i, the center of the cell and $z_{i\mp1/2}$, left and right boundaries. Without considering the source term $\mathbf{S}(\mathbf{U})$ in the system (3.16), the finite-volume computes the value of U_i^n at the center of the cell z_i at a given instant time t^n as a function of fluxes at the boundaries of the cell (LeVeque, 1992)

$$\frac{\partial U_i^n}{\partial t} + \frac{1}{\Delta z}(F_{i+1/2}^n - F_{i-1/2}^n) = 0 \tag{3.19}$$

The fluxes $F_{i\pm1/2} = F(U(z_{i\pm1/2}, t^n))$ can be expressed using the Lax-Friedrichs flux scheme depending on the value assigned to U. For each cell, the solution $U(z, t^n)$ can be approximated by a linear piecewise function over the cell I_i, as reported in Van Leer (1979), and solve adopting the MUSCL (Monotonic Upwind Scheme for Conservation Laws) scheme which has a first-order accuracy in time and a second order accuracy in space. The source term $\mathbf{S}(\mathbf{U})$ in (3.16) and (3.17) is then included by resolving the system $\frac{d\mathbf{U}}{dt} = \mathbf{S}(\mathbf{U})$, with the Crank-Nicholson scheme.

Time step numerical condition

The numerical scheme is stable and converges if the spatial discretization respects the Courant-Friedrichs-Lewy (CFL) condtition (Courant et al., 1967) which imposes the following limit on time-step size

$$\Delta t \leq C_{CFL}\frac{\Delta z}{S_{max}}, \quad S_{max} = \max_{i=1,\dots,M}\{\|\lambda_{1,2}\|\} \tag{3.20}$$

$$C_{CFL} \in (0, 1)$$

This ensures that the numerical speed $\frac{\Delta z}{\Delta t}$ is greater than the physical speed $\lambda_{1,2}$ of the propagating wave fronts. In this work the value for C_{CFL} was set to 0.9, to provide a compromise between stability and computational cost.

Boundary conditions

Boundary conditions must be imposed in order to close the system 3.1. The Riemann invariants W_1 and W_2 can be used to set inlet, outlet boundary conditions and interface conditions between two or more cell nodes when dealing with complex arterial networks. In general for each inlet and outlet node it is possible to identify two type of boundary conditions: reflective and non-reflecting (Quarteroni & Formaggia, 2004). Non-reflecting boundary conditions imply that the exiting characteristic variable leaves without spurious reflection and it is imposed in terms of characteristic variables ($W_{1,2}$); while reflective condition implies a partial reflection of the outgoing characteristic variables. In this section a brief description of inlet/outlet boundary conditions is provided.

Inlet boundary condition. The inlet boundary condition is applied by imposing the flow rate $Q(t)$ at the beginning of the time step. This type of boundary condition is reflective and as stated by Quarteroni & Veneziani (2003) the values (A, u) cannot be set by simply assigning $Q = Au$ at the inlet node, area and velocity should be imposed taking into account that the solution at (z_i, t_i) is composed of a forward travelling wave W_1 and backward travelling wave W_2.

The simplest choice is to set Riemann invariants at the inlet node z_1 as

$$\begin{cases} W_1(z_1, t^n) = \frac{Q_{in}(t^n)}{A_{in}(t^n)} \\ W_2(z_1, t^n) = W_2(z_1 - \lambda_2 \Delta t, t^{n-1}) + \Delta t \mathbf{l}_2^T \mathbf{S}(\mathbf{U}) \end{cases} \tag{3.21}$$

using a technique called the extrapolation of the characteristics (Peiró & Veneziani, 2009).

Outlet boundary condition. At the outlet the same procedure can be applied. However, a more realistic outflow boundary is represented by the coupling of the 1D model with a 0D model that incorporates the downstream circulation effects. The 0D model consists of a RCR / three-element Windkessel model: a proximal resistance (R_1), a compliance (C) and a distal resistance (R_2) as shown in Figure 3.4.

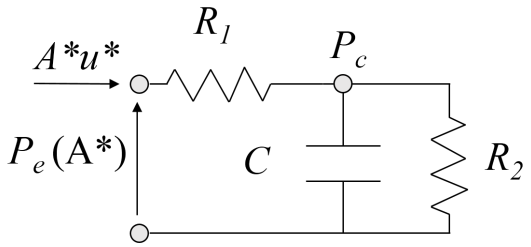

Figure 3.4: Three-element Windkessel model with a proximal resistance (R_1), a compliance (C) and a distal resistance (R_2). P_c is the pressure at the compliance, while P_e is the intermediate pressure at the 1D/0D interface.

As in the previous paragraph ((3.2.1)),the Riemann problem is solved at the end of the time-step at the 1D/0D interface following the work of (Alastruey et al., 2012a).

Interface conditions when dealing with arterial networks. The method of the characteristics lends itself to complex arterial networks, especially when defining variation of A and u at the interface between two or more vessels.

Arterial conjunction. An arterial conjunction connects together two vessels with different mechanical and geometrical properties (see Figure 3.5).

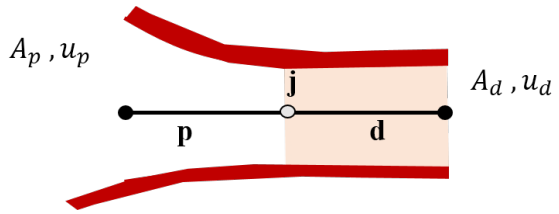

Figure 3.5: Schematic of a conjunction. The parent vessel (p) outlet is connected with the daughter vessel (d) inlet by node j

The conjunction is resolved by imposing the conservation of mass ($A_p u_p - A_d u_d = 0$) and total pressure (through the Bernoulli's principle) at the interface between the two vessels, parent and daughter vessels. Two additional relations are obtained from the Riemann variables at the outlet of the parent vessel and inlet of the daughter vessel, $W_{p,d} = u_{p,d} \pm 4c_{p,d}$. The complete system of equations is

$$F = \{fi\} = \begin{cases} u_p + 4k_p A_p^{1/4} - W_p^* = 0, \\ u_d - 4k_d u_d^{1/4} - W_d^* = 0, \\ u_p A_p - u_{d1} A_{d1} = 0, \\ \beta_p \left(\frac{u_p^2}{A_{0p}^{1/2}} - 1\right) + \frac{1}{2}\rho u_p^2 - \beta_{d1}\left(\frac{u_{d1}^2}{A_{0d1}^{1/2}} - 1\right) - \frac{1}{2}\rho u_{d1}^2 = 0, \\ \beta_p \left(\frac{u_p^2}{A_{0p}^{1/2}} - 1\right) + \frac{1}{2}\rho u_p^2 - \beta_{d2}\left(\frac{u_{d2}^2}{A_{0d2}^{1/2}} - 1\right) - \frac{1}{2}\rho u_{d2}^2 = 0, \end{cases} \tag{3.22}$$

Where $c_{p,d} = k_{p,d} A_{p,d}^{1/4}$, and $k_{p,d} = \sqrt{\frac{3}{2}\gamma_{p,d}}$. By defining the vector with unknown

variable $\mathbf{U}$ as $\mathbf{U} = \{U_i\}^T = [u_p, u_d, A_p^{1/4}, A_d^{1/4}]^T$. The system of non linear equation 3.22 is solved iteratively with the Newton's method (Press et al., 2007) by defining the Jacobian J, $J = \frac{\delta F}{\delta U}$ and resolving at each step the system

$$\begin{cases} J \cdot \delta U = -F(U), \\ U^{new} = U + \delta U. \end{cases} \tag{3.23}$$

Bifurcation A bifurcation is defined as the intersection between a parent vessel and two or more daughter vessels (see Figure 3.6).

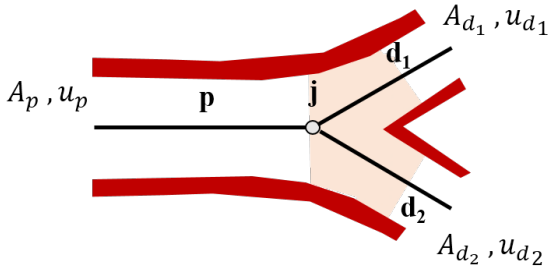

Figure 3.6: Schematic of a bifurcation. The parent vessel (p) outlet is connected with the daughter vessels ($d_{1,2}$) inlet by node j

The bifurcation is solved by imposing, at the bifurcation node, the conservation of mass, the static pressure and two additional relations obtained from the three outgoing characteristics. The unknown vector of variables $\mathbf{U}$ is defined as $\mathbf{U} = \{U_i\}^T = [u_p, u_{d1}, u_{d2}, A_p^{1/4}, A_{d1}^{1/4}, A_{d2}^{1/4}]^T$ and the system of resulting nonlinear equation F is

$$F = \{fi\} = \begin{cases} u_p + 4k_p A_p^{1/4} - W_p^* = 0, \\ u_{d1} - 4k_{d1} u_{d1}^{1/4} - W_{d1}^* = 0, \\ u_{d2} - 4k_{d2} u_{d2}^{1/4} - W_{d2}^* = 0, \\ u_p u_3^4 - u_2 u_4^4 = 0, \\ \beta_p \left(\frac{u_p^2}{A_{0p}^{1/2}} - 1\right) + \frac{1}{2}\rho u_p^2 - \beta_d \left(\frac{u_d^2}{A_{0d}^{1/2}} - 1\right) - \frac{1}{2}\rho u_d^2 = 0, \end{cases} \tag{3.24}$$

Where $c_{p,d} = k_{p,d} A_{p,d}^{1/4}$, and $k_{p,d} = \sqrt{\frac{3}{2}\gamma_{p,d}}$. The system is solved using the Newton's method as for the case of conjunction 3.2.1. In this work the conservation of only static pressure at bifurcations has been adopted, since in arterial bifurcations the pressure loss arising from the dynamic component is much smaller than the loss arising from static pressure, and such losses have also negligible effects on pressure and flow rate waveforms (Matthys et al., 2007).

The 1D nonlinear system of equations describing blood flowing in a compliant tube has been illustrated in section 3.2 with its basic assumptions. This hyperbolic system is numerically solved using a finite volume scheme illustrated in section 3.2.1 and the method of characteristics, section 3.2.1. The method of characteristics and the Riemann invariants are used to set up boundary conditions at the inlet and outlet of the numerical domain, as shown in sections 3.2.1, and interface conditions at bifurcations and conjunctions, see section 3.2.1. As previously detailed this modelling approach has been adopted based on the work of Melis (2017) and adapted for dealing with bifurcations, tapered vessels, stenosis and conjunctions, that increase the complexity of the flow patterns to be depicted.

The numerical system in 3.1 can be linearized over a reference state and re-written in the frequency domain, for which an analytical solution exists. The solution can be used as well to resolve a fluid flow in a complex arterial network with a modelling approach illustrated in the following section 3.3. The numerical methods presented in this section is based on the work of Lungu (2015).

3.3 1D linearized model

The system of equations in 3.1 can be linearized over a reference state $(A_0, 0)$, the final system (refer to (Milišić & Quarteroni, 2004) for the complete derivation) reads

$$\begin{cases} \mathcal{C}' \frac{\partial p}{\partial t} - \frac{\partial Q}{\partial z} = 0, \\ \\ \frac{\partial^2 p}{\partial t^2} - c^2 \frac{\partial^2 p}{\partial z^2} = 0 \end{cases} \tag{3.25}$$

Where $\mathcal{C}'$ is the compliance per unit of length (l) equal to $\frac{A_0}{\rho c^2}$ and c is the complex wavespeed. The first equation 3.25 refers to mass conservation while the second equation refers to momentum conservation for a 1D element. Note that, in 3.25, the viscous dissipation in the momentum equation has been neglected. The solution of this system can be expressed in the frequency domain in terms of pressure and flow waveforms. The full solution is comprised of an oscillatory and steady component. The steady component describes

the viscous dissipation term and can be treated separately.

3.3.1 Oscillatory solution

The general solution for the momentum conservation equation in 3.25 can be expressed in terms of pressure and flow rate in their forward and backward components following Womerseley's analytical solution (Womersley, 1957)

$$\begin{cases} p(\omega, z, t) = P_f e^{i(\omega t - kz)} + P_b e^{i(\omega t + kz)}, \\ \\ Q(\omega, z, t) = Q_f e^{i(\omega t - kz)} + Q_b e^{i(\omega t + kz)} \end{cases} \tag{3.26}$$

where k is the complex wave number, c is the complex wave speed, ω is the angular frequency, $P_{f,b}$ and $Q_{f,b}$ are the amplitude of the forward and backward pressure and flow waves, respectively and z is the distance along the longitudinal axis.
For an untethered, thin walled linear elastic vessel filled with an incompressible viscous fluid, the pulse wave velocity has a real and a complex component given by

$$c = \frac{\omega}{b - ia} \tag{3.27}$$

where b is the attenuation constant and a is the phase constant. The complex pulse wave

can be also expressed using the complex number k

$$k = \frac{\omega}{c} \tag{3.28}$$

Note that for an inviscid fluid flow the resulting pulse wave speed is real and equal to the Moens-Korteweg wave speed c_0

$$c_0 = \sqrt{\frac{Eh_0}{2\rho r}} \tag{3.29}$$

where E is the elastic Young's modulus of the wall, h_0 is the wall thickness, ρ is the fluid density and r is the radius of the vessel. The relationship between the viscous fluid wave speed, c, and the inviscid fluid wave speed c_0 is given by Womersley (1957)

$$\frac{c_0}{c} = \sqrt{\frac{1-\sigma^2}{1-F_{10}}} \tag{3.30}$$

and k becomes

$$k = \frac{\omega\sqrt{1-\sigma^2}}{c_0\sqrt{1-F_{10}}} \tag{3.31}$$

F_{10} is a parameter that depends on the Womersley number α, σ is the Poisson's ratio of the artery wall and they are expressed as

$$\alpha = r_0 \sqrt{\frac{\omega \rho}{\mu}} \tag{3.32}$$

$$F_{10} = \frac{2J_1(\alpha i^{3/2})}{\alpha i^{3/2} J_0(\alpha i^{3/2})} \tag{3.33}$$

where r_0 refers to the radius of the vessel at its unstressed condition, μ is the fluid dynamic viscosity, J_0 and J_1 are the Bessel functions of the first kind of order 1 and 0, respectively.

Substituting 3.28, 3.30 and 3.31 into 3.26 and separating the real and imaginary part of the complex wave number ($k = k_r + i \cdot k_i$), the pressure and flow waves, travelling in a thin elastic tube, filled with a viscous fluid are given by:

$$\begin{cases} p(\omega, z, t) = e^{-(-k_i)z} P_f e^{i(\omega t - k_r z)} + e^{(-k_i)z} P_b e^{i(\omega t + k_r z)} \\ \\ Q(\omega, z, t) = e^{-(-k_i)z} Q_f e^{i(\omega t - k_r z)} + e^{(-k_i)z} Q_b e^{i(\omega t + k_r z)} \end{cases} \tag{3.34}$$

The equation 3.34 can be expressed for a generic element (denoted as el) with a trigonometric notation (in sinus and cosinus).

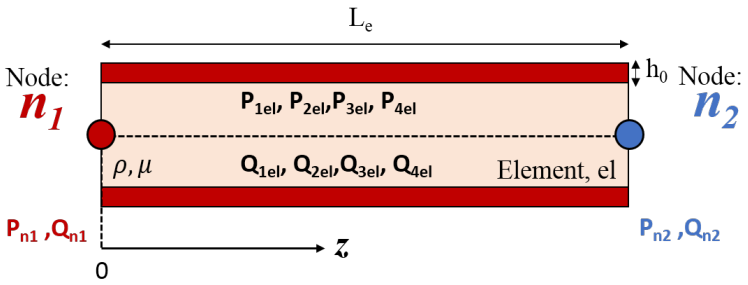

Figure 3.7: One-dimensional representation of the element in the frequency domain. For each node $n_{1,2}$ it is possible to identify nodal pressure and flow that are related to element pressure and flow, expressed as $p/Q_{1_el,2_el,3,el,4_el}$.

The real components of the forward and backward waveforms can be expressed using four components $P_{1,..4}$ and $Q_{1,..4}$. The flow components can be related to the pressure components, substituting the equation 3.34 into the continuity equation in 3.25. Re-arranging the terms and expressing the flow rate terms $\{Q_{el}\} = [Q_{1_{el}}, Q_{2_{el}}, Q_{3_{el}}, Q_{4_{el}}]$ as a function of the pressure values $\{P_{el}\} = [P_{1_{el}}, P_{2_{el}}, P_{3_{el}}, P_{4_{el}}]$ gives,

$$\{Q_{el}\} = \left[Z_c\right] \{P_{el}\} \tag{3.35}$$

where

$$\left[Z_c\right] = \frac{C'\omega}{k_{rel}^2 + (-k_{iel})^2} \begin{bmatrix} k_{r_{el}} & -(-k_{i_{el}}) & 0 & 0 \\ (-k_{i_{el}}) & k_{r_{el}} & 0 & 0 \\ 0 & 0 & -k_{r_{el}} & -(-k_{i_{el}}) \\ 0 & 0 & (-k_{i_{el}}) & -k_{r_{el}} \end{bmatrix} \tag{3.36}$$

Considering a single element with a finite length L_e, the oscillatory *pressure* component at nodes n_1 and n_2 or the nodal degrees of freedom $\{P\} = [p_{cn_1}, p_{sn_1}, p_{cn_2}, p_{sn_2}]^T$ can be related to element degrees of freedom $\{P_{el}\} = [p_{1_{el}}, p_{2_{el}}, p_{3_{el}}, p_{4_{el}}]^T$ as shown in Lungu (2015)

$$\{P\} = \left[T\right]\{P_{el}\} \tag{3.37}$$

where

$$[T] = \begin{bmatrix} 1 & 0 & 1 & 0 \\ 0 & -1 & 0 & 1 \\ e^{(k_{i_{el}})L_{el}}\cos(k_{r_{el}}L_{el}) & e^{(k_{i_{el}})L_{el}}\sin(k_{r_{el}}L_{el}) & e^{(-k_{i_{el}})L_{el}}\cos(k_{r_{el}}L_{el}) & e^{(-k_{i_{el}})L_{el}}\sin(k_{r_{el}}L_{el}) \\ e^{(k_{i_{el}})L_{el}}\sin(k_{r_{el}}L_{el}) & -e^{(-k_{i_{el}})L_{el}}\cos(k_{r_{el}}L_{el}) & -e^{(-k_{i_{el}})L_{el}}\sin(k_{r_{el}}L_{el}) & e^{(-k_{i_{el}})L_{el}}\cos(k_{r_{el}})L_{el}) \end{bmatrix} \tag{3.38}$$

This expression can be used to relates nodal degrees of fredoom $\{Q\} = [Q_{cn_1}, Q_{sn_1}, Q_{cn_2}, Q_{sn_2}]^T$ to element degrees of freedom $\{Q_{el}\} = [Q_{1_{el}}, Q_{2_{el}}, Q_{3_{el}}, Q_{4_{el}}]^T$ and from 3.35

$$\{Q\} = \left[T\right]\left[Z_c\right]\left[T\right]^{-1}\{P\} \tag{3.39}$$

Continuity dictates the net flow is zero at all internal nodes of the domain, a simple way to apply this principle is to add an F matrix to the system

$$\{Q\} = \left[F\right]\left[T\right]\left[Z_c\right]\left[T\right]^{-1}\{P\} \tag{3.40}$$

where

$$\left[F\right] = \begin{bmatrix} -1 & 0 & 0 & 0 \\ 0 & -1 & 0 & 0 \\ 0 & 0 & 1 & 0 \\ 0 & 0 & 0 & 1 \end{bmatrix} \tag{3.41}$$

Equation (3.40) returns the expression for the stiffness matrix of a singular vascular element

$$\left[k_{el}^{-1}\right] = \left[F\right]\left[T\right]\left[Z_c\right]\left[T\right]^{-1} \tag{3.42}$$

Therefore

$$\left[k_{el}\right]\left[\{P\}\right] = \left[\{Q\}\right] \tag{3.43}$$

In order to obtain the solution for the whole arterial tree, the individual elements are assembled globally following a methodology used by FEM methods (Lungu, 2015).

3.3.2 Steady solution.

Using the relationship given by the Poiseuille resistance and by imposing the steady flow component as a constraint at two boundary nodes (the inlet and the outlet node) of a vascular element, the FEM solution is equivalent to

$$\frac{1}{R_{DC}}\begin{bmatrix} 1 & -1 \\ 1 & -1 \end{bmatrix}\begin{bmatrix} P_{1DC} \\ P_{2DC} \end{bmatrix} = \begin{bmatrix} Q_{1DC} \\ Q_{2DC} \end{bmatrix} \tag{3.44}$$

In order to respect mass conservation principle the equation (3.44) is pre-multiplied with a matrix F (the sign of the flow entering the first node is changed)

$$F_{DC} = \begin{bmatrix} -1 & 0 \\ 0 & 1 \end{bmatrix} \tag{3.45}$$

The global linear system is then assembled and solved using the same methods imple-

mented for the oscillatory component system. The final solution of the linear system is found by summing up the oscillatory and the steady solutions for each node of the elements of the vascular network.

3.3.3 Boundary conditions

At the inlet of the 1D FEM network, the flowrate waveform is directly applied using a Fourier Series decomposition of the 20 frequencies of greatest magnitude. At the outlet a three element Windkessel model was applied using an equivalent impedance representation for each harmonic, which in term of sin and cosine, P_c, P_s, Q_c and Q_s responses is

$$\begin{cases} P_c(\omega) = Z_1(\omega)Q_c(\omega) - Z_2(\omega)Q_s(\omega) \\ P_s(\omega) = Z_2(\omega)Q_c(\omega) + Z_1(\omega)Q_s(\omega) \end{cases} \tag{3.46}$$

where

$$Z_1 = R_1 + \frac{R_2}{1 + (\omega R_2 C)^2} \quad Z_2 = -\frac{\omega {R_2}^2 C}{1 + (\omega R_2 C)^2} \tag{3.47}$$

and ω is the corresponding harmonic, while R_1, R_2 and C are the windkessel parameters. With the inclusion of a three-element Windkessel model at the outlets, the linear modelling approach can be integrated in the clinical simulation process for the target disease, which is an advance, since the linear approach has been used in the previous work of Lungu (2015) to evaluate pulmonary hypertension, where fluid flow is laminar and pressure propagates in straight and circular vessels.

3.4 Benchmark tests

Boileau et al. (2015) conducted a detailed numerical analysis where they tested six different numerical methods[6] used in the literature for solving 1D blood flow equations on vascular networks including the human carotid artery, the upper thoracic aorta, the aortic iliac bifurcation [7]. These 1D models were compared with 3D fluid-structure interaction simulation taken from Xiao et al. (2014). A similar approach is taken here to compare the 1D linear implementation and 1D nonlinear implementation described in the previous sections 3.2 and 3.3, respectively. Error metrics are the same as those defined by Boileau et al. (2015)

$$\epsilon_X^{RMS} = \sqrt{\frac{1}{N}\sum_{i=1}^{N}\left(\frac{x_i - X_i}{X_i}\right)^2}, \quad \epsilon_X^{MAX} = \max_i \|\frac{x_i - X_i}{X_i}\|, \tag{3.48}$$

$$\epsilon_X^{SYS} = \frac{\max x - \max X}{\max X}, \quad \epsilon_X^{DIAS} = \frac{\min x - \min X}{\min X},$$

where x and X are the waveforms computed by the 1D and 3D models, respectively. The waveforms x and X can refer either to P, Q, ΔP or Δr quantities for the 1D and 3D models, respectively. The number of time points n is equivalent to a sampling rate of 1kHz. Q, ΔP,

[6] These methods include: finite element methods (such as the Discontinuos Galerkin method, the locally conservative Galerkin method and the Galerkin least-squares method); finite volume methods ; finite difference methods (such as Lax-Wendroff and the MacCormack schemes)

[7] These schemes were also tested in more complex networks such as a 37 and ADAN56 arterial networks representing the aorta with its largest branches. The results from the 1D models were compared with in vitro pressure and flow waveforms acquired from Matthys et al. (2007) and Blanco et al. (2014), respectively.

Δr errors are normalized by the maximal Q, ΔP, Δr over the cardiac cycle to avoid division by small values, as reported in (Boileau et al., 2015). In this work all the error metrics will be reported in percentage (%). The first benchmark is a simplified model that represents the thoracic aorta as a straight tube with a constant radius, its aim is to verify the correct solution of the one dimensional governing equations. The second model, the iliac bifurcation, has been included to study the ability of the resolution schemes to include the effects due to presence of a bifurcation site, where the incoming pulse waves are reflected and trasmitted. The third and fourth benchmark tests not only include bifurcation sites but also the tapering of the aorta and as in the fourth model a mild coarctation site, the target disease. From the first benchmark to the fourth, the complexity of the phenomena depicted has been gradually increase in order to understand which one dimensional modelling approach perform the best when compared to an existing one dimensional resolution scheme (DCG scheme) and to an equivalent three dimensional FSI solution, giving an idea of which of the two modelling approaches can be used as a surrogate of a three-dimensional model to be used in the following chapter.

3.4.1 Upper Thoracic aorta model

The first benchmark evaluated represents the upper thoracic aorta (from the aortic root to the descending aorta) coupled to a three-element Windkessel model. A flow rate curve was applied at the inlet as in (Boileau et al., 2015). The thoracic aorta is modeled as straight cylinder with uniform properties with a representative diameter and length (see Figure 3.8 and Table 3.1) and was discretized using 12 elements of equal length. For both numerical

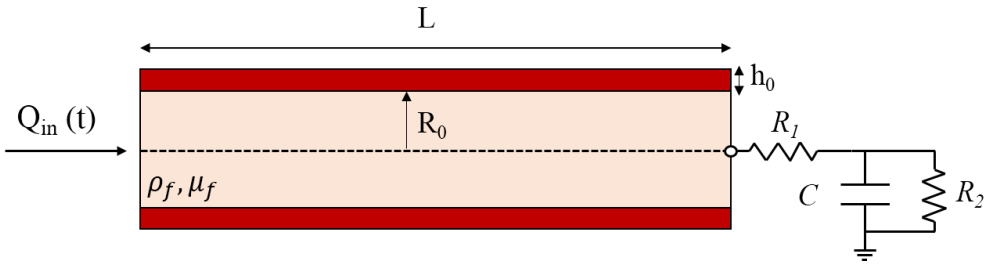

Figure 3.8: Schematic of the idealized model representing a thoracic aorta. Taken from (Boileau et al., 2015).

Table 3.1: Haemodynamic properties of the upper thoracic aorta, from the ascending to the thoracic part. Inflow flow rate curve, reference pressure values and geometrical parameters were taken from (Boileau et al., 2015). The diastolic lumen radius R_d was used as reference to compute Δr waveform. The radial velocity profile shape was set as plug-flow for the nonlinear ($\gamma_v = 9$) and DCG solution.

Property	Value
Length, L	24.2 cm
Initial radius, R_0	0.987 cm
Initial Area, A_0	3.0605 cm^2
Diastolic radius, R_d	1.2 cm
Diastolic Area, A_d	4.5239 cm^2
Thickness, h_0	0.82 mm
Elastic modulus, E	400 kPa
Systolic pressure, P_s	16.8 kPa
Diastolic pressure, P_d	9.5 kPa
Blood density, ρ_f	1060 $kg \cdot m^{-3}$
Blood viscosity, μ_f	$4 \cdot 10^{-3} Pa \cdot s$
Proximal resistance, R_1	$1.17 \cdot 10^7$ $Pa \cdot s \cdot m^{-3}$
Distal Resistance, R_2	$1.12 \cdot 10^8$ $Pa \cdot s \cdot m^{-3}$
Compliance, C	$1.0163 \cdot 10^{-8}$ $Pa \cdot s \cdot m^{-3}$

methods, the pressure (P), the volumetric flow rate (Q), the radius change (Δr) waveforms were reported along with the pressure difference ΔP between the outlet and inlet (Figure 3.9) and compared with the reference 3D solution (3D) and a finite element solution obtain through a Discontinuos Galerkin (DCG) scheme taken from the article of (Boileau et al., 2015) (see Figure 3.8 and table 3.2).

The initial area A_0 that yields the reference diastolic area A_d at $P = P_d$ was calculated for the one-dimensional schemes using

$$A_0 = A_d \left(\frac{\beta}{P_d + \beta} \right)^2 \tag{3.49}$$

This equation is derived from equation 3.10 assuming P equal to the diastolic pressure (P_d) and area A equal to the area at diastolic pressure P_d. The relative errors were determined with respect to the 3D solution, using equations in 3.48. The NL model shows the main features of the 3D simulation but underestimates by 23% the maximum ΔP needed to drive the blood flow within the vessel. At systole the peak pressure is underestimated by about 1% while at diastole about 0.5%, these errors are in line with the DCG solution published by Boileau et al. (2015). The linear model provides results comparable with the other 1D numerical methods previously reported although it overestimates the maximum ΔP value by 11%. In terms of computational time, the linear implementation required 3 second for cardiac cycle, while the nonlinear implementation required 16 seconds per cardiac cycle and both reached a stable solution in 8 cardiac cycles. In this application the linear implementation provides better results when compared to the nonlinear resolution scheme in terms of computational time (the linear implementation is five times faster) and when compared to the three-dimensional solution. However, the benchmark case detailed in this section repre-

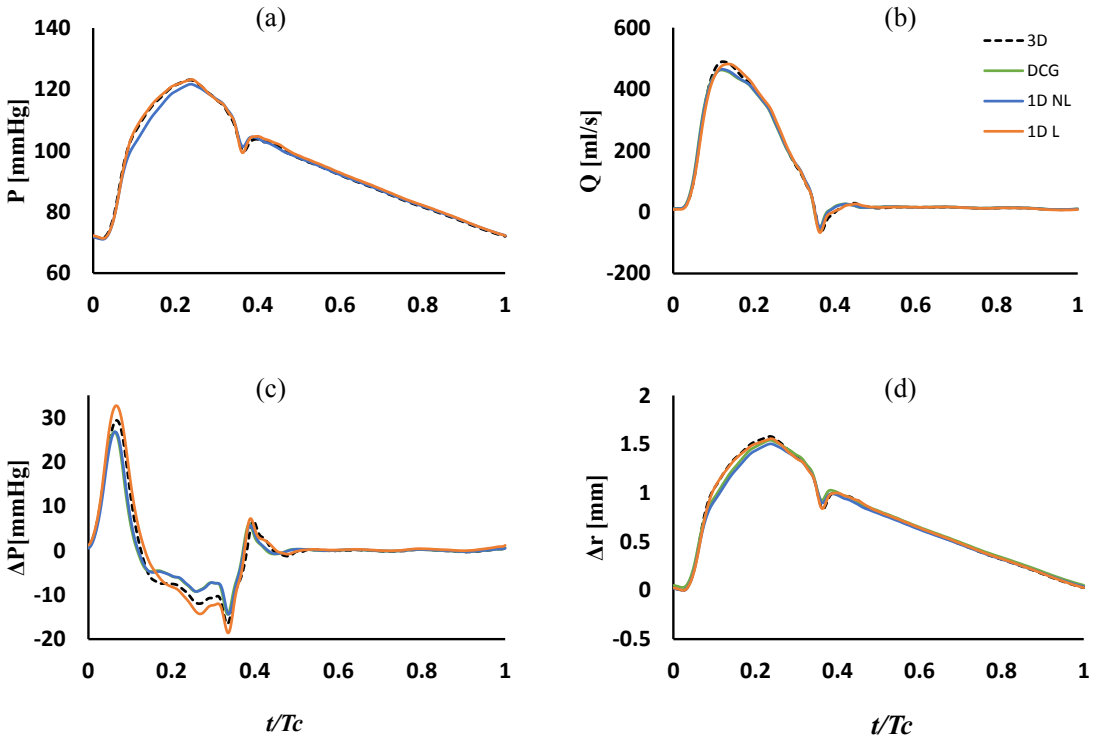

Figure 3.9: Upper thoracic aorta simulation results. (a) Pressure (b) flow (c) pressure difference between the vessel inlet and the vessel end and (d) radius change at the midpoint of the vessel. The 3D solution was taken from (Xiao et al., 2014), while the 1D DCG solution was taken from (Boileau et al., 2015)

Table 3.2: Relative errors with respect to three-dimensional solution (expressed in percentage) as defined in Equation 3.48 for the one-dimensional Discontinuos Galerkin (DCG) scheme, one-dimensional nonlinear (1D NL) scheme, one-dimensional linear (1D L) scheme at the midpoint of the upper thoracic aorta.

Error (%)	variable	DCG	1D NL	1D L
ϵ^{RMS}	P	1.09	1.33	0.65
	Q	2.55	2.90	1.28
	ΔP	7.70	7.68	4.70
	Δr	2.35	3.03	0.82
ϵ^{MAX}	P	3.54	5.38	1.26
	Q	9.13	11.78	4.38
	ΔP	31.83	23.72	13.84
	Δr	7.27	10.94	2.75
ϵ^{SYS}	P	-0.57	-1.1	0.1
	Q	-5.56	-4.99	-1.55
	ΔP	-8.92	-8.93	11.44
	Δr	-2.53	-4.82	-1.53
ϵ^{DIAS}	P	0.85	-0.5	-0.03
	Q	2.75	3.38	-0.07
	ΔP	7.32	-6.96	-6.96
	Δr	1.85	-0.07	-0.07

sents a straight cylinder with a constant radius with no bifurcations, conjunctions, tapered vessels or possible stenosis, therefore it is not representative of a patient-specific geometry of a coarcted aorta.

3.4.2 Iliac Bifurcation model

The one dimensional schemes were tested on a simplified iliac bifurcation model, a significant site of wave reflection in the cardiovascular system (Pythoud et al., 1996). This is an important benchmark as bifurcations significantly influence the form of resultant pressure and flow waveforms in complex arterial networks. The iliac bifurcation model comprises: a parent vessel, the descending aorta, and two symmetric identical daughter vessels, the iliac arteries (see Table 3.3 and Figure 3.10). Both outlet vessels were coupled with a Windkessel model while a flow waveform was imposed at the inlet as in (Boileau et al., 2015). Both models were discretized using 12 elements. The waveforms for pressure, flow rate and variations in luminal radius are shown in Figure 3.11 at three points: the midpoint of the aorta, the endpoint of the aorta and the midpoint of either iliac artery. The relative errors were determined with respect to the 3D solution, using equations in 3.48. From the results it is clear that the 1D linear and nonlinear models are capable of simulating the wave reflections caused by the presence of the bifurcation. The relative errors (with respect to the 3D solution) are within 1% for pressure and flow waveforms (see Table 3.4). In terms of computational time, the linear implementation required 12 second for cardiac cycle, while the nonlinear implementation required 47 seconds per cardiac cycle and both reached a stable solution in 9 cardiac cycles. As in the previous case the linear implementation provided

Table 3.3: Haemodynamic properties of the iliac bifurcation (aorta and two iliacs). Inflow flow rate curve, reference pressure values and geometrical parameters were taken from (Boileau et al., 2015). The diastolic lumen radius R_d was used as reference to compute Δr waveform. The radial velocity profile shape was set as plug-flow for the nonlinear ($\gamma_v = 9$) and DCG solution.

Property	Aorta	Iliac
Length, L	8.6 cm	8.5 cm
Initial radius, R_0	0.758 cm	0.549 cm
Initial Area, A_0	1.8062 cm^2	0.94787 cm^2
Diastolic radius, R_d	0.86 cm	0.60 cm
Diastolic Area, A_d	2.3235 cm^2	1.1310 cm^2
Thickness, h_0	0.90 mm	0.68 mm
Elastic modulus, E	500 kPa	700 kPa
Systolic pressure, P_s	16.8 kPa	16.8 kPa
Diastolic pressure, P_d	9.46 kPa	9.46 kPa
Blood density, ρ_f	1060 $kg \cdot m^{-3}$	
Blood viscosity, μ_f	$4 \cdot 10^{-3} Pa \cdot s$	
Proximal resistance, R_1	-	$1.17 \cdot 10^7$ $Pa \cdot s \cdot m^{-3}$
Distal Resistance, R_2	-	$1.12 \cdot 10^8$ $Pa \cdot s \cdot m^{-3}$
Compliance, C	-	$1.0163 \cdot 10^{-8}$ $Pa \cdot s \cdot m^{-3}$

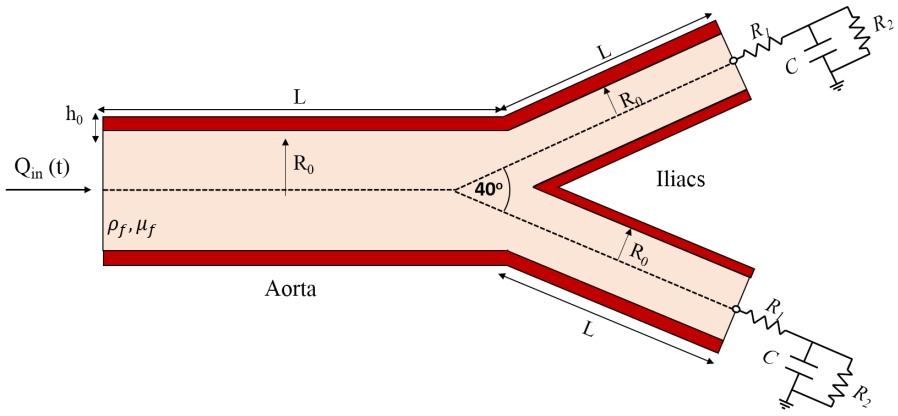

Figure 3.10: Schematic of the idealized model representing an iliac bifurcation. Taken from (Boileau et al., 2015).

similar results when compared with the nonlinear scheme but with less computational effort. However, the benchmark test is not representative of the pathology under-investigation, and simply highlight the capability of both method to resolve the main features that occur at a generical bifurcation site.

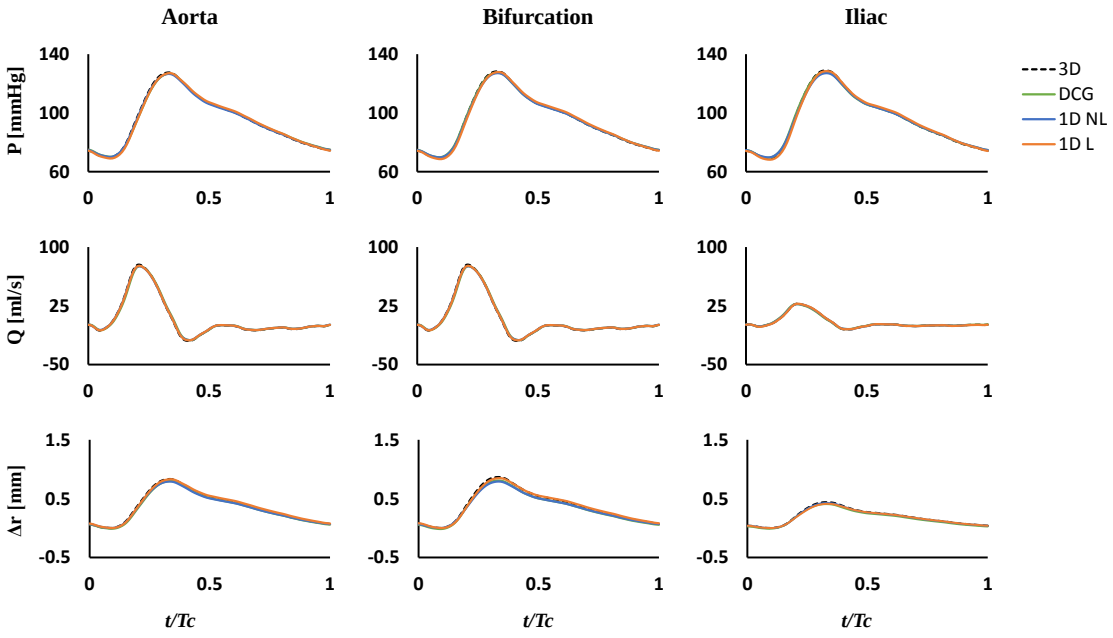

Figure 3.11: Iliac bifurcation simulation results. Pressure, flow and radius change at different locations. 3D solution taken from (Xiao et al., 2014) 1D DCG solution taken from (Boileau et al., 2015)

Table 3.4: Relative errors $(P, Q\Delta r)$ with respect to three-dimensional solution (expressed in percentage) as defined in Equation 3.48 for the one-dimensional Discontinuos Galerkin (DCG) scheme, one-dimensional Non-linear (1D NL) scheme, one-dimensional Linear (1D L) scheme at the at different points of the Iliac bifurcation test case. (Bif. = Bifurcation)

Error $(\%)$		Aorta			Bif.			Iliac		
		DCG	1D NL	1D L	DCG	1D NL	1D L	DCG	1D NL	1D L
ϵ^{RMS}	P	0.37	1.03	0.97	0.42	1.14	0.98	0.45	1.47	0.97
	Q	0.89	2.69	0.84	1.20	2.80	0.98	0.92	3.06	0.81
	Δr	2.48	2.46	1.85	4.07	4.15	1.69	4.29	1.71	2.59
ϵ^{MAX}	P	0.61	3.39	2.21	0.73	3.99	2.27	0.84	5.43	2.32
	Q	2.51	9.24	2.99	3.55	1.17	3.37	2.33	1.30	1.90
	Δr	4.05	5.55	2.61	6.87	9.37	3.68	7.29	5.72	6.64
ϵ^{SYS}	P	-0.53	-0.7	-0.3	-0.71	-0.9	-0.4	-0.83	-1.4	-0.3
	Q	-2.47	-2.5	-1.8	-3.47	-3.3	-1.9	-1.68	-1.69	0.15
	Δr	-3.96	-5.01	1.85	-6.84	-8.9	-2.2	-7.25	-2.7	-5.7
ϵ^{DIAS}	P	0.5	0.4	-1.1	0.54	0.5	-1.2	0.55	0.9	-1.4
	Q	1.16	4.8	-3.6	1.76	1.3	1.2	1.17	-3.73	-3.82
	Δr	-1.39	-0.07	-0.07	-1.93	-0.07	-0.07	-2.36	-0.07	-0.07

3.4.3 Full Aorta model

The third benchmark evaluated was an idealized aorta from the ascending to the iliac bifurcation taken from Xiao et al. (2014). This geometry includes the effect of curvature, bifurcation and tapering. The geometry is shown in Figure 3.12 and the geometrical, mechanical properties and the total number of elements are shown in Table 3.5. The thickness was chosen to be 10 % of the diastolic radius, r_d, derived from equation 3.49. The Young's modulus (E) was derived from the wall thickness and the pulse wave velocity using equation 3.2, assuming $c = c_d$ and $A = A_d$. Blood was assumed as incompressible and Newtonian with a density, ρ_f, and viscosity, μ_f, taken as 1060 kg $\cdot$ m^{-3} and $4 \cdot 10^{-3}$Pa $\cdot$ s, respectively.

Pressure and flow rate waveforms are shown in Figure 3.13 and 3.14, respectively, at five

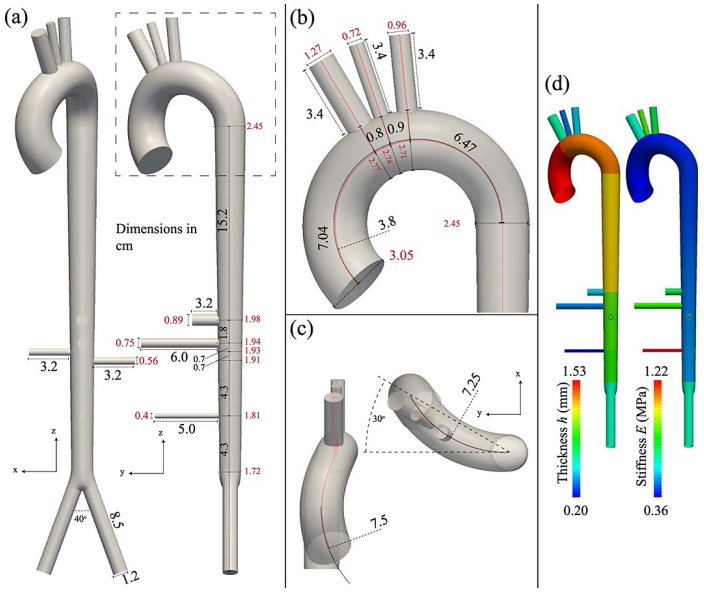

Figure 3.12: Schematic of the idealized model representing a full aorta. Taken from (Xiao et al., 2014).

Table 3.5: Haemodynamic properties of the idealized aorta. The radial velocity profile shape was set as plug-flow for the nonlinear ($\gamma_v = 9$) and DCG solution. Taken from (Xiao et al., 2014)

Arterial segment	Length cm	$r_{in} \rightarrow r_{out}$ mm	$c_{in} \rightarrow c_{out}$ m/s	R_1 $10^7 Pa \cdot s \cdot m^{-3}$	R_2 $10^8 Pa \cdot s \cdot m^{-3}$	C $10^{-10} Pa^{-1} \cdot m^3$
1. Ao I	7.0357	15.2→13.9	4.77→4.91	-	-	-
2. Ao II	0.8	13.9→13.7	4.91→4.93	-	-	-
3. Ao III	0.9	13.7→13.5	4.93→4.94	-	-	-
4. Ao IV	6.4737	13.5→12.3	4.94→5.09	-	-	-
5. Ao V	15.2	12.3→9.9	5.09→5.43	-	-	-
6. Ao VI	1.8	9.9→9.7	5.43→5.46	-	-	-
7. Ao VII	0.7	9.7→9.62	5.46→5.48	-	-	-
8. Ao VIII	0.7	9.62→9.55	5.48→5.49	-	-	-
9. Ao IX	4.3	9.55→9.07	5.49→5.57	-	-	-
10. Ao X	4.3	9.07→8.6	5.57→5.66	-	-	-
11. Brachiocephalic	3.4	6.35→6.35	6.20→6.20	5.1918	10.6080	8.6974
12. L com. carotid	3.4	3.6→3.6	7.36→7.36	19.1515	52.2129	1.7670
13. L subclavian	3.4	4.8→4.8	6.75→6.75	9.8820	13.0183	7.0871
14. Celiac	3.2	4.45→4.45	6.90→6.90	11.7617	7.5726	12.1836
15. Sup. mesenteric	6	3.75→3.75	7.27→7.27	17.4352	5.5097	16.7453
16. R renal	3.2	2.8→2.8	7.93→7.93	34.1378	5.3949	17.1017
17. L renal	3.2	2.8→2.8	7.93→7.93	34.1378	5.3949	17.1017
18. Inf. mesenteric	5	2.0→2.0	8.77→8.77	74.0167	46.2252	1.9959
19. R com. iliac	8.5	6.0→6.0	6.31→6.31	5.9149	10.1737	9.0686
20. L com. iliac	8.5	6.0→6.0	6.31→6.31	5.9149	10.1737	9.0686

outlets of the domain, the supra-aortic branches: the brachiocephalic artery (BCA), left common carotid artery (LCA), left subclavian artery (LSUB) and at one of the terminal descending aortic branches, the right iliac artery (iliac). Relative errors were derived with respect to the 3D solution, using equations in 3.48. The relative errors are shown in Table 3.6, with all models able to capture the main features of the 3D pressure and flow rate waveforms. The 1D linear implementation captures better the systolic pressure when compared to 1D nonlinear and DCG implementations: the errors are less than 3% at supra-aortic branches and at the iliac artery, while with other implementations the errors are less than 5 %. However, the linear implementation seems to underestimate the diastolic pressure with errors that reach values of 10% at right common iliac artery, while in the other models the errors remain around 1%.

When considering flow rate, the linear implementation overestimates the systolic and diastolic flow rate values with errors that reach values of 26 % at diastole, while other models show similar results with errors less than 11 %. The origin of these discrepancies is a consequence of approximations in the 1D linear formulation which calculates the viscous losses using a parabolic profile (Poiseuille's law), neglects the convective losses and does not conserve the total pressure between elements. These approximations are reasonable for application in systems with a constant lumen diameter, low pressure and flow rate such as the pulmonary arterial tree (Lungu, 2015).

When comparing the 3D results with 1D nonlinear and 1D DCG results, the 3D model is able to capture the spatial and temporal changes in velocity profile which result in additional friction losses and inertial forces in tapered and curved pipes, especially in systole. This is evidenced by the discrepancies between 1D and 3D results during systole in the inlet pres-

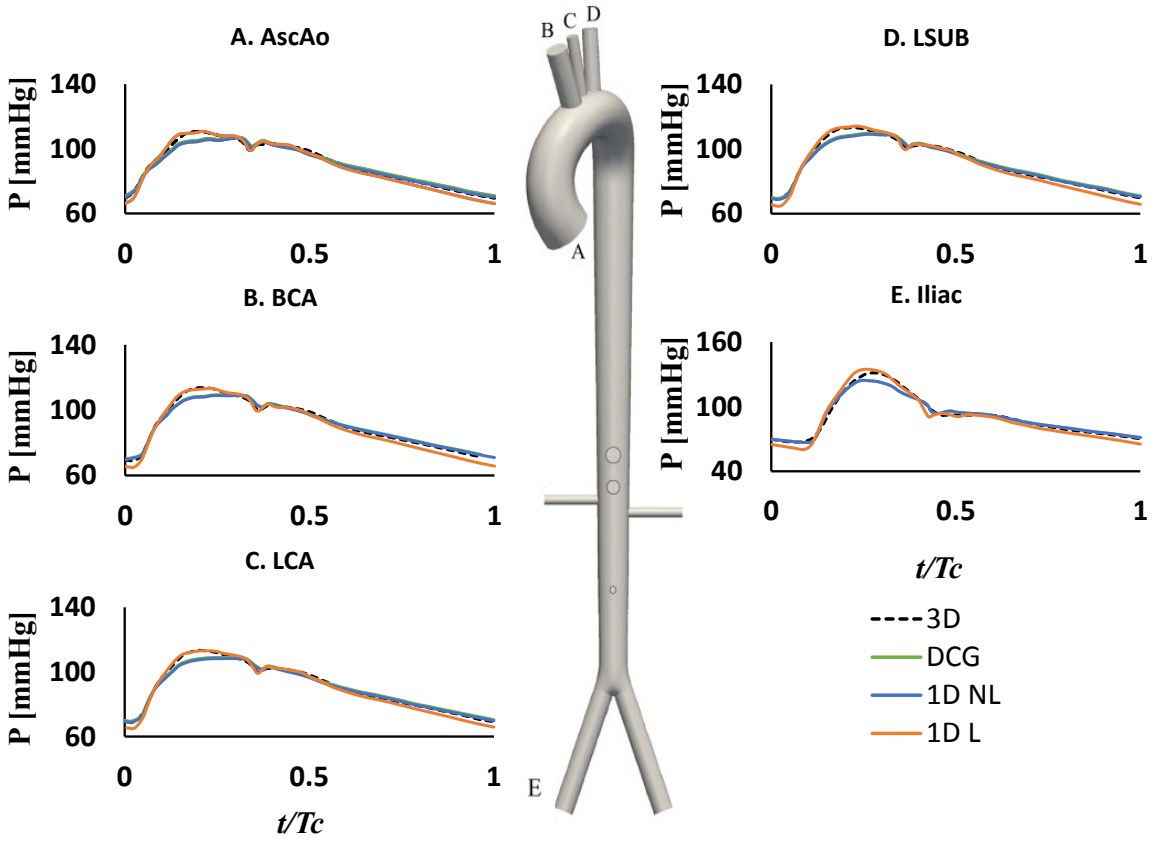

Figure 3.13: Full aorta simulation results. Pressure with time at five different locations: supra-aortic branches (BCA,LCA, LSUB) and one of the two iliac artery (the right iliac artery). 3D solution and 1D DCG solution taken from (Xiao et al., 2014)

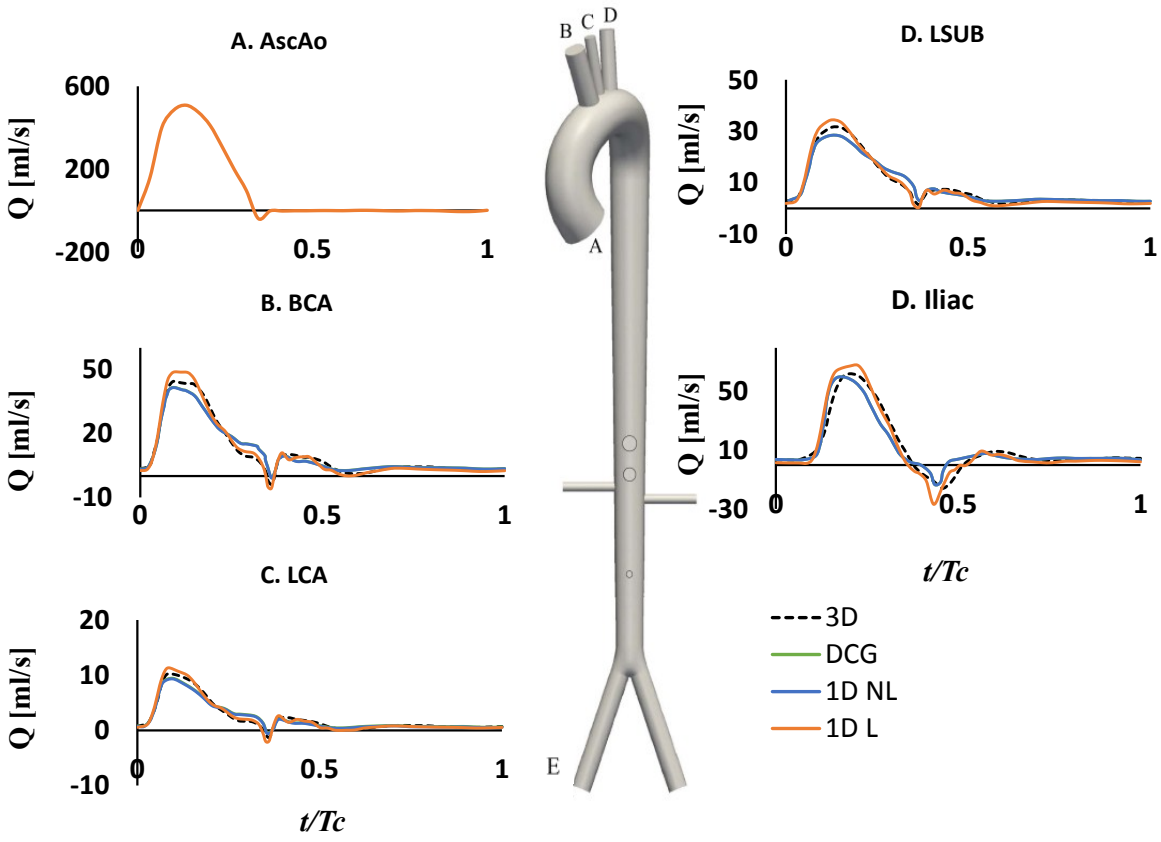

Figure 3.14: Full aorta simulation results. Flow rate with time at five different locations: supra-aortic branches (BCA,LCA, LSUB) and one of the two iliac artery (the right iliac artery). 3D solution and 1D DCG solution taken from (Xiao et al., 2014)

sure waveforms (see Figure 3.13). Xiao et al. (2014) suggested that tapering and curvatures are responsible for the differences between 1D and 3D solution at systole (at the ”shoulder” of the pressure waveform), this conclusion has been confirmed when comparing the solutions obtained from the thoracic aorta in a straight, tapered and curved configuration. Similar results have been found in a previous 1D/3D comparative study on a cerebral flow that used a rigid wall configuration (Grinberg et al., 2011). In fluid regions characterized by a velocity field with strong secondary flows with swirling and recirculation, generally at curved branches, the 1D model underestimates 3D pressure and flowrate values at systolic peak. At the outlet of the right common iliac artery one dimensional models showed a slight phase lag in the pressure and flow rate responses. This phase lag is more visible in the 1D linear formulation together with a pronounced dicrotic notch during flow reversal (see Figure 3.13and Figure 3.14).

Table 3.6: Relative errors with respect to three-dimensional solution (expressed in percentage) as defined in Equation 3.48 for the one-dimensional Discontinuos Galerkin (DCG) scheme, one-dimensional Non-linear (1D NL) scheme, One-dimensional Linear (1D L) scheme at the at different points of the full aorta test case.

Error (%)		AscAo			BCA			LCA		
		DCG	1D NL	1D L	DCG	1D NL	1D L	DCG	1D NL	1D L
	P	1.26	1.34	2.40	1.27	1.33	3.10	1.26	1.33	3.09
ϵ^{RMS}	Q	0.0	0.0	0.0	4.17	3.58	4.0	4.02	3.98	5.15
	P	5.12	5.55	3.20	4.86	4.03	2.04	4.67	4.55	2.05
ϵ^{MAX}	Q	0.0	0.0	0.0	15.0	14.8	16.0	13.4	13.5	10.04
	P	-2.90	3.01	0.1	-3.80	-3.33	0.1	-3.48	-3.55	0.1
ϵ^{SYS}	Q	0.0	0.0	0.0	-6.44	-7.0	10.0	-6.30	-6.4	10.02
	P	0.98	1.12	-5.0	0.89	1.01	-6.0	0.8	0.95	-6.0
ϵ^{DIAS}	Q	0.0	0.0	0.0	7.43	7.35	9	4.15	4.10	13.0

Error		LSUB			iliac		
		DCG	1D NL	1D L	DCG	1D NL	1D L
	P	1.21	1.35	2.0	2.06	2.4	4.0
ϵ^{RMS}	Q	3.46	4.01	4.0	4.94	5.0	13.0
	P	4.35	4.44	2.0	7.54	7.69	7.0
ϵ^{MAX}	Q	11.7	14.2	12.0	21.5	23.0	29.0
	P	-3.12	-3.01	1.0	-4.76	-5.0	3.0
ϵ^{SYS}	Q	-9.18	-10.01	12.0	-4.07	-4.24	9.0
	P	0.74	0.83	-6.0	-0.99	1.01	-10.0
ϵ^{DIAS}	Q	4.22	4.35	-12.0	0.32	0.37	26.0

3.4.4 Mild aortic coarctation case

In the following section a patient specific model is discussed. The case is representative of a moderate coarctation case and was made available by the organizers of the MICCAI CFD challenge (Project, 2013). Data provided includes the geometry, provided as STL file extracted from 3D contrast enhanced MRA (CE-MRA); flow measurements, extracted from phase contrast MRI at the ascending and descending aorta; and pressure measurement at the ascending aorta, derived from invasive catheterization. For the three supra-aortic vessels, the proportion of the total ascending aortic flow rate was specified as 17%, 8%, 10%, respectively.

Aortic fluid dynamics was computed using both 1D and 3D representations using both a non-compliant and compliant assumption for the local aortic region. For all simulations the local aortic geometry was coupled to 0D Windkessel models at the outlet branches to account for the peripheral circulation, while at the inlet, the provided flowrate waveform was applied assuming a flat velocity profile (Womersley number at the AscAo: 10.92). The network topology for both 1D models (linear and nonlinear) was defined as follows:

- Three centerlines were extracted, one for the aorta and three for the remaining supra-aortic vessels: the brachiocephalic artery (BCA), the left common carotid artery (LCA) and the left subclavian artery (LSUB);
- Thirty-five diameter measurements were taken perpendicular to the extracted centerlines, as shown in Figure 3.15. The extraction of the aortic centerlines and the sections was performed using the vmtk toolkit (Antiga et al., 2008);

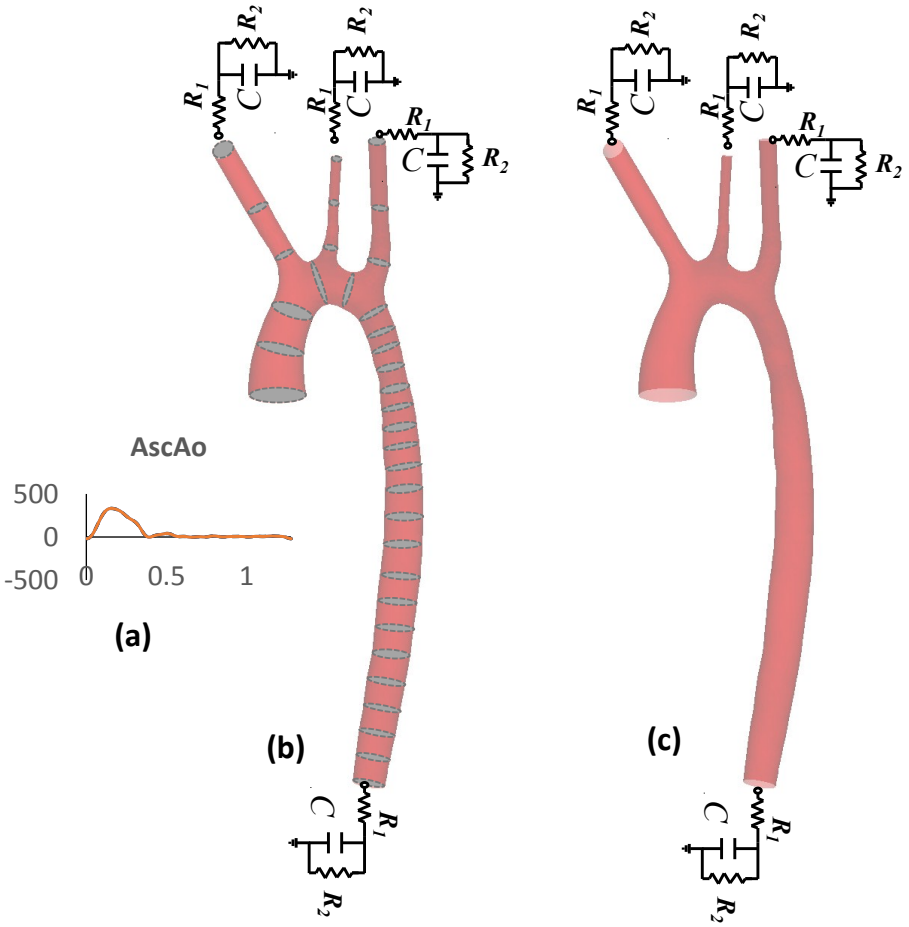

Figure 3.15: 3D and 1D modelling approach for the MICCAI simulation. (a) Ascending aortic flowrate waveform provided by the MICCAI. (b)

For 3D simulations the governing equations were solved with FLUENT 17.2 (ANSYS, PA, USA) using a laminar fluid model as prescribed by the challenge (peak Reynolds number at the coarctation site: 3660), the STL geometry was meshed using 1682026 polyhedral cells with 5 prism layers at the wall. In all the analyses the fluid was considered to be Newtonian with a viscosity 0.0040 Pa · s as prescribed by the organizers of the challenge. 3D

Table 3.7: MICCAI 2013 STACOM challenge simulation. The resulting 0D Windkessel parameters are reported for each outlet: brachiocephalic artery (BCA) left common carotid artery (LCA) left subclavian artery (LSUB) and descending aorta (DescAo)

	BCA	**LCA**	**LSUB**	**DescAo**
$R_1(10^7 Pa \cdot s \cdot m^{-3})$	1.54	16	5.55	1.32
$C(10^{-9} Pa^{-1} \cdot m^3)$	3.66	1.59	2.05	16.4
$R_2(10^8 Pa \cdot s \cdot m^{-3})$	5.83	13.2	1.49	2.13

simulations used an incompressible fluid assumption and a compressible fluid analogy to include the local aortic distensibility as in (Brown et al., 2012), this approach is described in detail in Chapter 6. In all models the blood density was set to 1000 $kg \cdot m^{-3}$, where in the compressible fluid strategy this value refers to the initial density value. The 1D models were solved using a wave-speed of $5 \cdot 10^3 m \cdot s^{-1}$ to compare with the rigid 3D analysis, an approach that was previously adopted by Grinberg et al. (2011). For the compliant case a wave speed of 7 $m \cdot s^{-1}$ was used for both the 1D and 3D approaches. The 0D Windkessel parameters used are reported in Table 3.7, derived using the methodology described in Chapter 6.

Results

For the rigid wall analysis pressure and flow rate waveforms are shown in Figure 3.16 and 3.17 at five outlets of the domain, the supra-aortic branches: the brachiocephalic artery (BCA), left common carotid artery (LCA), left subclavian artery (LSUB), ascending aorta (AscAo) and descending aorta (DescAo) with error metrics reported in Table 3.8.

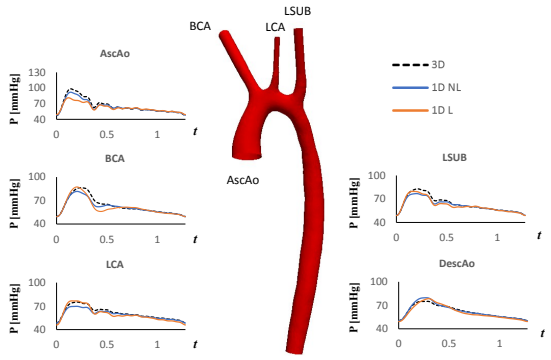

Figure 3.16: MICCAI 2013 STACOM challenge incompressible simulation results. Pressure with time at five different locations: supra-aortic branches (BCA,LCA, LSUB) and at the descending aorta (DescAo).

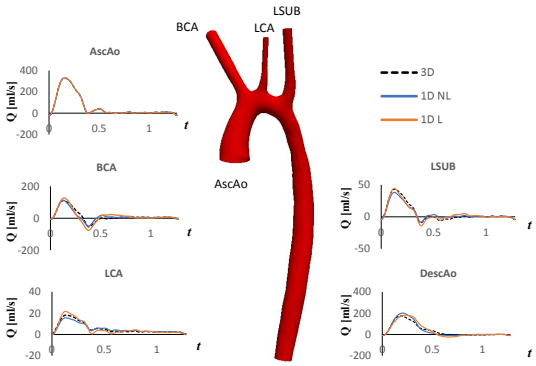

Figure 3.17: MICCAI 2013 STACOM challenge incompressible simulation results. Flow rate with time at five different locations: supra-aortic branches (BCA,LCA, LSUB) and at the descending aorta (DescAo).

Table 3.8: MICCAI 2013 STACOM challenge incompressible simulation. Relative errors with respect to three-dimensional solution (expressed in percentage) as defined in Equation 3.48 for the one-dimensional Non-Linear (1D NL) scheme, One-dimensional Linear (1D L) scheme at the at different points of the aorta.

Error (%)		AscAo		BCA		LCA		LSUB		DescAo	
		1D NL	1D L	1D NL	1D L	1D NL	1D L	1D NL	1D L	1D NL	1D L
	P	4	8	4	6	3	4	3	4	2	3
ϵ^{RMS}	Q	0	0	9	13	7	8	7	6	8	10
	P	1	4	0	4	0	5	0	2	6	6
ϵ^{MAX}	Q	0	0	16	22	7	19	11	11	20	24
	P	-7	-18	-5	1	-7	2	-7	-4	6	6
ϵ^{SYS}	Q	0	0	1	15	-14	18	-12	3	15	15
	P	1	4	0	0	0	-5	0	-1	0	0
ϵ^{DIAS}	Q	0	0	5	-19	2	-3	2	-11	-1	-1

At systolic peak, the one-dimensional linear model is not able to capture the peak aortic pressure at the ascending aorta as the nonlinear model, with an underestimation of 18 % of

the peak inlet pressure when compared to the three-dimensional solution, while the nonlinear model underestimates the peak with an error of 7%. At the same site, in the diastolic phase the error is about 4% in the linear model, whilst the nonlinear model shows an error of 1%. At the other outlets, the two models are able to capture the main features of the pressure waveforms. When considering aortic flow rate waveforms, both models shows similar results, but with a tendency of the linear model to overestimate peak flow rate and underestimate diastolic flow rate at supra-aortic branches, whilst the nonlinear model underestimates peak aortic flow rate and overestimate diastolic flow rate, but with errors that are less than the linear formulation. At descending aorta both models behaves similarly.

For the compliant aortic case the results are shown in Figures 3.18 and 3.19 with error metrics reported in Table 3.9.

As for the rigid model, at peak systolic flow the one-dimensional linear model is not able to capture the peak aortic pressure at the ascending aorta as well as the nonlinear model and underestimates peak inlet pressure by 16 % compared to the three dimensional solution. The nonlinear model underestimates the peak pressure with an error of 10%. At the same site in diastole the error is about 6% in the linear model model and 1% for the nonlinear model. At the outlets both 1D models capture the main features of the pressure waveforms. When considering aortic flow rate waveforms, both models shows similar results. The linear model tends to overestimate peak flow rate and underestimate diastolic flow rate at supra-aortic branches, whilst the nonlinear model underestimates peak aortic flow rate and overestimate diastolic flow rate, but with smaller errors than the linear formulation. At descending aorta both models behaves similarly. It worth noting that the nonlinear model is superior when reporting pressure at the coarctation site as shown in Figure 3.18, where the

peak pressure in the nonlinear model is aligned with the peak pressure measured in the three dimensional model, while the linear model not only overestimates the peak pressure value but shows more pronounced peak towards the end of the systolic phase.

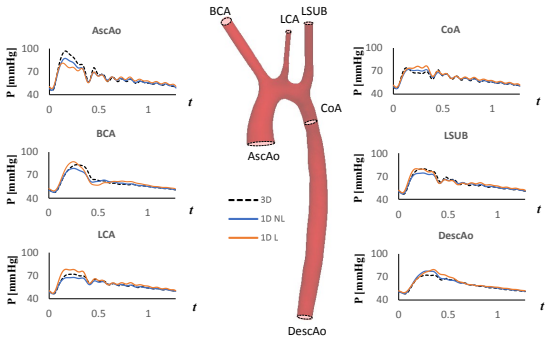

Figure 3.18: MICCAI 2013 STACOM challenge compressible simulation results. Pressure with time at five different locations: supra-aortic branches (BCA,LCA, LSUB) and at the descending aorta (DescAo).

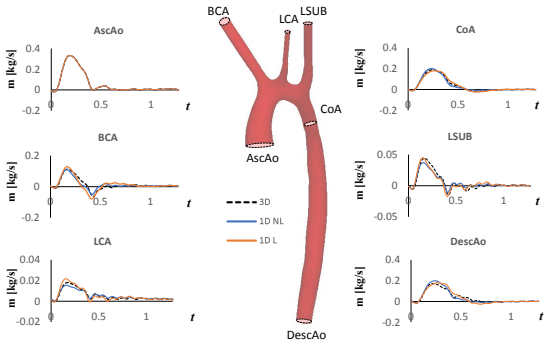

Figure 3.19: MICCAI 2013 STACOM challenge compressible simulation results. Flow rate with time at five different locations: supra-aortic branches (BCA,LCA, LSUB) and at the descending aorta (DescAo).

Table 3.9: MICCAI 2013 STACOM challenge compressible simulation. Relative errors with respect to three-dimensional solution (expressed in percentage) as defined in Equation 3.48 for the one-dimensional Non-Linear (1D NL) scheme, one-dimensional Linear (1D L) scheme at the at different points of the aorta.

Error (%)		AscAo		BCA		LCA		LSUB		CoA		DescAo	
		1D NL	1D L	1D NL	1D L	1D NL	1D L	1D NL	1D L	1D NL	1D L	1D NL	1D L
	P	4	8	4	6	3	5	3	4	3	5	3	4
ϵ^{RMS}	Q	0	0	3	5	3	5	3	3	4	4	3	4
	P	1	13	0	9	1	13	1	10	5	13	8	8
ϵ^{MAX}	Q	0	0	2	8	2	12	2	7	9	11	8	10
	P	-10	-16	-6	5	-6	9	-7	0	-3	4	7	7
ϵ^{SYS}	Q	0	0	-6	5	-6	9	-7	0	6	5	7	7
	P	1	6	0	4	0	2	1	4	0	3	0	0
ϵ^{DIAS}	Q	0	0	0	2	0	1	0	2	3	-4	0	0

Discussion

Compared to the idealised aorta case the MICCAI geometry has more complex features: supra-aortic vessels are tapered and the ascending aorta progressively reduces in area to reach a minimum at the coarctation site (aortic inlet diameter = 19.908 mm, coarctation diameter = 10.42 mm) at the descending aorta, there is a gradual increase of the aortic lumen (outlet diameter = 12 mm). These features increase the complexity of the haemodynamics providing a more challenging test of the 1D formulations proposed here. The main source of difference between the linear and nonlinear 1D models arises from the ability of the nonlinear formulation to include convective acceleration terms and preserve total pressure at conjunction sites. The main differences between the nonlinear one-dimensional model and the three-dimensional model can be attributed to the inability of the 1D model to account for secondary flow features, curvature effects and the limiting constant velocity profile assumption. Despite these limitations these results show that the nonlinear one-dimensional model can provide a reasonable representation of the form of pressure and flow waveforms within subject-specific aortic geometries which include local geometric variations arising from coarctation of the aorta.

When comparing compliant and non-compliant models it visible how the errors between one-dimensional and three-dimensional models decreased. The use of an artificially increased pulse wave velocity in the one-dimensional model limits the physics that this modelling approach is able to represent. Additionally the compliant solution showed that both models are able to capture the time delay in pressure and flow rate waveforms visible at the descending aorta (see Figures 3.18 and 3.19). A summary of the 1D benchmark modelling

output is reported in Table 3.10.

Table 3.10: Summary of the 1D benchmark modelling outputs.

Benchmark case	Computational time	Results
Upper thoracic aorta	1D L: 3 s/cycle 1D NL: 16 s/cycle	Two models shows similar features when compared to the 3D reference solution. Error metrics and computational time are slightly less in the 1D L implementation. Max absolute difference in percentage point of 9.88 between the two lists of error metrics.
Iliac bifurcation	1D L :12 s/cycle 1D NL:47 s/cycle	Two models shows similar features when compared to the 3D reference solution. Error metrics and computational time are slightly less in the 1D L implementation. Max absolute difference in percentage point of 6.85 between the six (two lists for each aortic location: aorta, bifurcation and iliac artery) lists of error metrics.
Full aorta model	1D L: 1 min/cycle 1D NL: 10 min/cycle	Two models shows similar features when compared to the 3D reference solution. 1D L model captures better the systolic pressure with error less than 1 % when compared to the 1D NL model (errors around 5%). Regarding diastolic pressure and systolic and diastolic flow rate, the 1D NL is able to capture these values with errors less than 1 % and 11 %, compared to the 1D L where the errors are equal to 11 % and 26 %. At the iliac artery (outlet of the model) the 1D L model shows spurious oscillations, especially at diastolic flow (see Figure 3.14).
MICCAI rigid	1D L: 6 min/cycle 1D NL: 22 min/cycle	Two models shows similar features when compared to the 3D reference solution. The 1D L model overestimates the systolic pressure by 18% and underestimate the diastolic pressure by 4%, when compared to the 1D NL solution where the error are less than 7% and 4%. The 1D L shows a tendency to overstimate peak flow and understimates the distolic flow rate when compared to the 1D L model.
MICCAI deformable	1D L: 4 min/cycle 1D NL: 17 min/cycle	Two models shows similar features when compared to the 3D reference solution. The 1D L model overestimates the systolic pressure by 16% and underestimate the diastolic pressure by 6%, when compared to the 1D NL solution where the error are less than 10% and 1%. The 1D L shows a tendency to overstimate peak flow and understimates the distolic flow rate when compared to the 1D L model. Spurious oscillation are visible at the DescAo (outlet of the model) in the 1D L formulation.

3.5 Conclusion

In this chapter, two different modelling approaches has been presented and tested using three benchmark test cases previously reported in the literature. The 1D non linear model is complex enough to represent the main characteristics of pulse wave propagation, despite the associated assumptions described in Section 3.2. The assumption of straight, circular and symmetric vessel geometry and ideal bifurcation geometry introduce approximations that can affect pressure losses calculations. To address this some authors have included interface conditions with loss coefficients to incorporate the effects of curvature or bifurcation angle (Yang et al., 2016; Matthys et al., 2007). However, this introduces the issue of providing appropriate loss coefficients from reported experimental measurements or 3D simulations.

Whilst the 1D linear implementation was able to represent the fluid dynamic in simple benchmarks such as in the upper thoracic aortic and iliac bifurcation cases, in more complex cases it is unable to predict well 3D fluid dynamic features. The 1D nonlinear implementation adopted in this chapter showed a good agreement with 3D pressure and flow waveforms making it suitable to estimate outflow boundary conditions for subject-specific models as described in Chapter 6.

4

Subject-specific 0D model tuning

This chapter details a preliminary analysis conducted using subject-specific data from a cohort of 11 patients with aortic coarctation (CoA) distal to the three main supra-aortic branches, except for patient 3 that represents a hypoplastic aorta, thus it has been excluded from the analysis. All data were collected at Bern University Hospital, following a protocol approved by the local ethics committee and the volunteers provided written informed consent (Swiss Adult Congenital Heart Disease Registry, SACHER, ClinicalTrials.gov Identifier NCT 02258724). The objective of this chapter is to perform a simple analysis using

0D mathematical models representative of an aortic coarctation in order to examine the sensitivity of tuning parameter to the complexity of the model used to represent the aortic region. The detailed methodology for processing clinical data used to inform the models in this chapter is provided in chapter 5 and Chapter 6.

4.1 Methods

Data used to inform the 0D models presented in this chapter was derived from patient-specific clinical measurements which includes:

- flow waveforms at the ascending (at the level of the right pulmonary artery) and descending aorta (at the diapraghmatic level) extracted from PC-MRI;
- 3D geometry extracted from a contrast-enhanced magnetic resonance angiogra- phy (CE-MRA), used to provide measures of aortic diameter;
- systolic and diastolic cuff pressures measured at the right arm;

In this chapter three levels of 0D model are considered, as shown in the schematics in Figure 4.1. Each model includes a larger number of elements to represent the aorta and peripheral circulation, the coarctation region and the supra-aortic vessels.

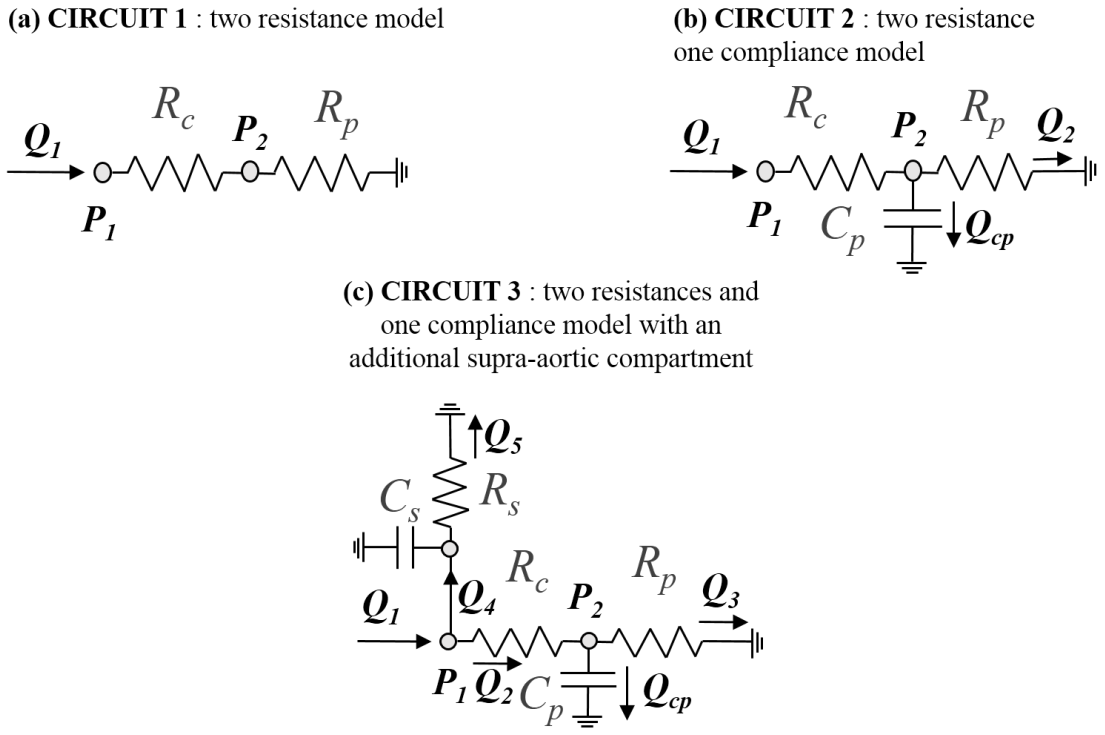

Figure 4.1: Three 0D models adopted in the analysis. (a) Circuit 1: with a resistance, R_c that represent the aortic coarctation region with the Bernoulli's equation, and a distal resistance,R_p, that represents the peripheral or distal circulation. (b) Circuit 2: two resistances and one compliance, similar to Circuit 1 but with an additional peripheral compliance. (c) Circuit 3: similar to circuit 2 but with an additional compliance, C_s, and resistance, R_s, representing supra-aortic regions. Overall, P_1 represents the ascending aortic pressure, while, P_2 the descending aortic pressure.

The resistance of the coarctation, R_c was defined based on the pressure loss associated with Bernoulli's equation 4.1 between the areas A_r, that refers to the reference descending aortic area at the descending aorta, extracted accordingly to Goubergrits et al. (2015a), and A_c, that refers to the coarctation region at the descending aorta identified by the minimum aortic area. These measures are shown for a representative aortic anatomy in Figure 4.2.

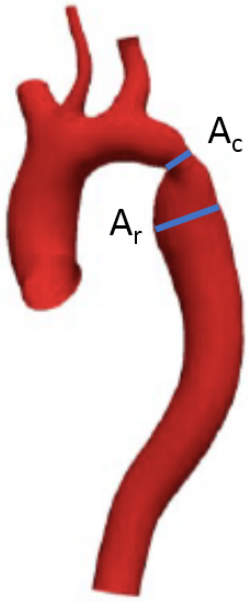

Figure 4.2: Definitions of A_r and A_c from patient-specific aortic anatomy

$$R_c = \rho \frac{A_c^{-2} - A_r^{-2}}{2} \tag{4.1}$$

where ρ is the density of blood, and the nonlinear pressure drop-flow relation is consequently

$$dP_c = R_c * Q_c^2 \tag{4.2}$$

where Q_c is the flow through the coarctation region. R_c was derived for all the 11 subjects in the cohort except for patient 3 (who presented with a hypoplastic aorta, discussed in more detail in Chapter 6). The approach for tuning the parameters for each of the 0D models is described in the following sections.

4.1.1 Circuit 1: two resistance model

In this simple model the value of R_p determines the descending aortic pressure (P_2 in Figure 4.1(a)), while the severity of the coarctation, represented by R_c, then determines the ascending aortic pressure (P_1 in Figure 4.1(a)). The ascending aortic flow rate, represented by the term Q_1 in Figure 4.1(a), is preserved throughout the circuit. The value of the nonlinear resistance R_p can be calculated directly from the peak flow and the pulse pressure for each subject as follows:

$$R_p = \frac{P_s - P_d}{Q_{1_{max}}} - R_c \cdot Q_{1^2_{max}} \tag{4.3}$$

where P_s and P_d are the systolic and diastolic pressures, $Q_{1_{max}}$ is the maximum ascending aortic flow rate.

4.1.2 Circuit 2 : two resistance one compliance model

As shown in Figure 4.1(b), in this model, the value of R_p and C_p determine the descending aortic pressure, P_2. The severity of the coarctation, represented by the nonlinear resistance R_c (computed as for circuit 1), then determines the ascending aortic pressure, P_1. The mean ascending aortic flow rate is preserved throughout the circuit, but the time varying form of the ascending and descending aortic flow is distinct. Tuning was undertaken by first keeping C_p constant and varying the value of R_p^i, from an initial value increased by 1% of

the initial value until the error metric defines as:

$$\text{Error} = ((P^i_{sys} - P_{sys_{target}})^2 + (P^i_{dias} - P_{dias_{target}})^2)^{1/2} \tag{4.4}$$

increased with change in R^i_p, the value of R^i_p associated with the minimum error was recorded as $\min(R^i_p)$. This process was then repeated with variation of C^i_p with $R_p = \min(R^i_p)$. For each value of R_p and C_p the solution of the model was found by solving the system of equations

$$\begin{cases} P_1 - P_2 = R_c \cdot Q_1^2 \\ P_2 = R_p \cdot Q_2 \\ Q_{cp} = C_p \cdot \frac{dP_2}{dt} \\ Q_1 = Q_{cp} + Q_2 \end{cases} \tag{4.5}$$

The system 4.5 can be discretised in time adopting a fixed time step of Δt as

$$\begin{cases} P_1^n - P_2^n = R_c \cdot Q_1^n \cdot Q_1^{n-1} \\ P_2^n = R_p \cdot Q_2^n \\ Q_{cp} = C_p \cdot \frac{P_2^n - P_2^{n-1}}{\Delta t} \\ Q_1 = Q_{cp} + Q_2 \end{cases} \tag{4.6}$$

where n is the value of the variable at time t^n, while $n-1$ is the value of the variable at time t^{n-1}, and $\Delta t = t^n - t^{n-1}$. The pressure drop represented by the nonlinear Bernoulli's resistance R_c has been simplified by using both value of Q_1 at time t^n and time t^{n-1} into

equation 4.2, this assumption is valid for sufficiently small values of Δt. The system in 4.6 corresponds to a set of algebraic equations where the unknown variables are P_1^n,P_2^n, Q_2^n, while Q_1^n is the measured ascending aortic flow rate Q_{AscAo}, and can be included in the algebraic system 4.6 as

$$\begin{cases} Q_1^n = Q_{AscAo}(t^n) \\ P_1^n - P_2^n = R_c \cdot Q_1^n \cdot Q_1^{n-1} \\ P_2^n = R_p \cdot Q_2^n \\ Q_{cp} = C_p \cdot \frac{P_2^n - P_2^{n-1}}{\Delta t} \\ Q_1 = Q_{cp} + Q_2 \end{cases} \tag{4.7}$$

Thus, the system 4.7 can be written in a matrix form as

$$\begin{bmatrix} Q_{AscAo}(t^n) \\ 0 \\ 0 \\ -P_2^{n-1} \\ 0 \end{bmatrix} = \begin{bmatrix} 1 & 0 & 0 & 0 & 0 \\ R_c Q_1^{n-1} & 0 & 0 & -1 & 1 \\ 0 & R_p & 0 & 0 & -1 \\ 1 & -1 & -1 & 0 & 0 \end{bmatrix} \begin{bmatrix} Q_1^n \\ Q_2^n \\ Q_{cp}^n \\ P_1^n \\ P_2^n \end{bmatrix} \tag{4.8}$$

The system in 4.8 was implemented in Matlab (MathWorks Inc.) and solved at each time point using the Matlab *mldivide* command. The matrix two-norm condition number was monitored during the solution process and results with a value superior to $1e^{-16}$ were dis-

carded.

4.1.3 Circuit 3: two resistances and a compliance model with an additional supra-aortic compartment

The circuit 3 in Figure 4.1(c) was solved in a similar way. The value of R_c was computed as for the previous 0D models. Compared to circuit 2, this model introduces an additional compliance and resistance to represent the supra-aortic vessels (the brachiocephalic artery, the left common carotid artery and the left subclavian artery). The equations that need to be solved in order to close the system are:

$$\begin{cases} R_c \cdot Q_2^2 - R_p \cdot Q_3 - R_s \cdot Q_5 = 0 \\ Q_{cp} = C_p \cdot \frac{dP_2}{dt} \\ Q_2 - Q_3 - Q_{cp} = 0 \\ Q_1 - Q_4 - Q_2 = 0 \\ Q_4 - Q_5 - Q_{cs} = 0 \\ Q_{cs} = C_s \cdot \frac{dP_1}{dt} \end{cases} \tag{4.9}$$

The system 4.9 can be discretised in time in terms of flow rates $Q_{1,2,3,4,5}^{n,n-1}$ at time t^n and t^{n-1}, pressures $P_{1,2}^{n-1}$ at time t^{n-1} and prescribed value for the ascending aortic flow $Q_{AscAo}(t^n)$ as

$$\begin{cases} Q_1^n = Q_{AscAo}(t^n) \\ R_c \cdot Q_2^n \cdot Q_2^{n-1} - R_p \cdot Q_3^n - R_s \cdot Q_5^n = 0 \\ \Delta t \cdot Q_{cp}^n - C_p \cdot R_p \cdot Q_3^n = -C_p \cdot P_2^{n-1} \\ Q_2 - Q_3 - Q_{cp} = 0 \\ Q_1 - Q_4 - Q_2 = 0 \\ Q_4 - Q_5 - Q_{cs} = 0 \\ \Delta t \cdot Q_{cs}^n - C_s \cdot R_s \cdot Q_5^n = -C_s \cdot P_1^{n-1} \end{cases} \tag{4.10}$$

where $P_{1,2}^{n}$ where written in form of flow rate $Q_{3,5}^{n}$. The system 4.10 can be written using a matrix form as

$$\begin{bmatrix} Q_{AscAo}(t^n) \\ 0 \\ -C_p \cdot P_2^{n-1} \\ 0 \\ 0 \\ 0 \\ -C_s \cdot P_1^{n-1} \end{bmatrix} = \begin{bmatrix} 1 & 0 & 0 & 0 & 0 & 0 & 0 \\ 0 & R_c \cdot Q_2^{n-1} & R_p & 0 & -R_s & 0 & 0 \\ 0 & 0 & -C_p \cdot R_p & 0 & 0 & \Delta t & 0 \\ 0 & 1 & -1 & 0 & 0 & -1 & 0 \\ 1 & -1 & 0 & -1 & 0 & 0 & 0 \\ 0 & 0 & 0 & 1 & -1 & 0 & -1 \\ 0 & 0 & 0 & 0 & -C_s \cdot R_s & 0 & \Delta t \end{bmatrix} \begin{bmatrix} Q_1^n \\ Q_2^n \\ Q_3^n \\ Q_4^n \\ Q_5^n \\ Q_{cp}^n \\ Q_{cs}^n \end{bmatrix} \tag{4.11}$$

The system in 4.11 was implemented in Matlab (MathWorks Inc.) and solved at each time point using the Matlab *mldivide* command. The matrix two-norm condition number was monitored during the solution process and results with a value superior to $1e^{-16}$ were discarded. The unknown vector of variables $[Q_1^n, Q_2^n, Q_3^n, Q_4^n, Q_5^n, Q_{cp}^n, Q_{cs}^n]^T$ and substituted into equation

$$P_1 = R_s \cdot Q_5 \tag{4.12}$$

and

$$P_2 = P_1 - R_c \cdot Q_2^2 \tag{4.13}$$

representing the ascending and descending pressures. In this 0D model, all the parameters determine the descending aortic pressure, P_2. The severity of the coarctation and the

parameters in the supra-aortic circulation (C_s and R_s) then determine the ascending aortic pressure, P_1. Both the mean flow and flow waveforms are distinct in the ascending and descending aorta. The parameters C_s, R_s, C_p, R_p were found by iteratively solving the system 4.11, starting from tuning the total compliance value C_{tot} (sum of C_s and C_p) and then the total resistance value R_{tot} (sum of R_s and R_p) in order to match systolic and diastolic pressures at the ascending aorta. In this stage the total compliance and resistance value are split evenly between the supra-aortic and descending aortic circuits. In a second stage , the values to assign to C_s, R_s, C_p, R_p are found by varying the ratios $t_c = C_s/C_p$ and $t_R = R_s/R_p$ to match the maximum value of the descending aortic flow Q_2 with

$$R_p = R_{tot} \cdot \frac{t_R + 1}{t_R}, \quad R_s = t_R \cdot R_p \tag{4.14}$$

$$C_p = \frac{C_{tot}}{1 + t_c}, \quad C_s = C_{tot} - C_p \tag{4.15}$$

where the parameter t_R in 4.14 was varied from 0.7 to 3.7, while t_c in 4.15 was varied from 0.8 to 2.3, both were sampled with a granularity of 0.05.

4.2 Results

In the following sections the results obtained from the 0D models are reported, commented and compared.

4.2.1 Circuit 1 analysis

The relevant patient-specific anatomical, pressure and flow parameters are reported in Table 4.1, along with the values of R_p computed for the circuit. Values are not reported for subject

Table 4.1: Patient specific anatomical, pressure and flow parameter used for the circuit 1.

	Pressure (mmHg)		Diameter (mm)					
Subject	Systolic	Diastolic	Inlet	Ref	CoA	$R_c(Pa \cdot s \cdot m^{-6})$	$Q_{1_{max}}(m^3 \cdot s^{-1})$	$R_p(Pa \cdot s \cdot m^{-3})$
1	152	85	45	21	18	$0.37 \cdot 10^{10}$	$5.78 \cdot 10^{-4}$	$1.33 \cdot 10^{7}$
2	125	75	29	29	23	$0.18 \cdot 10^{10}$	$3.29 \cdot 10^{-4}$	$1.96 \cdot 10^{7}$
4	134	66	21	23	15	$1.38 \cdot 10^{10}$	$5.64 \cdot 10^{-4}$	$0.82 \cdot 10^{7}$
5	147	95	29	27	14	$2.06 \cdot 10^{10}$	$4.59 \cdot 10^{-4}$	$0.56 \cdot 10^{7}$
6	150	83	26	23	13	$2.68 \cdot 10^{10}$	$3.89 \cdot 10^{-4}$	$1.25 \cdot 10^{7}$
7	138	69	23	20	16	$0.76 \cdot 10^{10}$	$6.33 \cdot 10^{-4}$	$0.96 \cdot 10^{7}$
8	167	75	27	18	10	$7.70 \cdot 10^{10}$	$2.75 \cdot 10^{-4}$	$2.32 \cdot 10^{7}$
9	130	100	32	26	16	$1.11 \cdot 10^{10}$	$4.18 \cdot 10^{-4}$	$0.49 \cdot 10^{7}$
10	125	60	24	14	8	$18.56 \cdot 10^{10}$	$4.56 \cdot 10^{-4}$	$-6.56 \cdot 10^{7}$
11	144	48	24	17	15	$0.66 \cdot 10^{10}$	$4.91 \cdot 10^{-4}$	$2.28 \cdot 10^{7}$

3 as this subject involved a hypoplastic aorta and did not result in a focal narrowing of the aorta. It is also notable that the value of R_p computed for subject 10 is negative. Clearly this is non-physical and arises from the high value for R_c associated with the large change in diameter between the reference and coarctation diameters for this subject. Figure 4.3 shows both P_1 and P_2 pressures computed for each subject, illustrating the contribution of the coarctation to the pressure reported in the ascending aorta.

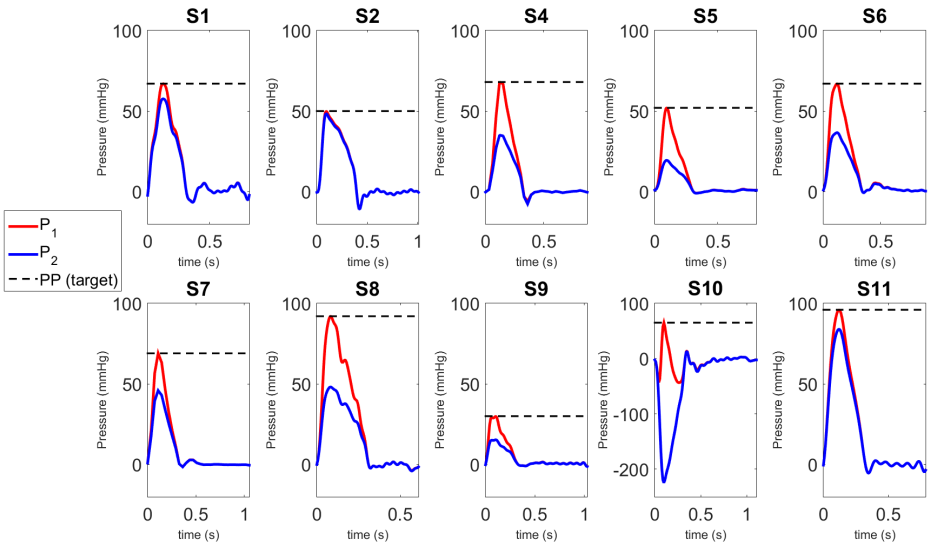

Figure 4.3: Results from the 0D circuit 1 model, reported for all 11 subjects: P_1 (in red) is the pressure at the ascending aorta, P_2 (in blue) is the pressure at the descending aorta, while PP (dashed in black) is the target pulse pressure.

This simplified model does not take into account the aortic compliance, thus, peak pressure drop across the coarctation corresponds with the instant of peak flow in the aorta. Using this crude representation of aortic anatomy predicts a pressure gradient across the coarctation that is higher than the recommended threshold for clinical intervention (20 mmHg) for subjects 4, 5, 6, 8 and 10.

4.2.2 Circuit 2 analysis

The values computed for R_p and C_p following the tuning process for circuit 2 are reported in Table 4.2 along with the value of R_p for circuit 1 for comparison. In Figure 4.4 the surface

response at different R_p and C_p is reported.

Table 4.2: Patient specific parameters used for the circuit 2 and compared to circuit 1. The notation [1] indicates the values used for circuit 1, while [2] indicates the values used for circuit 2.

Subject	$R_c(Pa \cdot s \cdot m^{-6})$	$R_p^1(Pa \cdot s \cdot m^{-3})$	$R_p^2(Pa \cdot s \cdot m^{-3})$	$C_p^2(Pa \cdot m^{-3})$
1	$0.37 \cdot 10^{10}$	$1.33 \cdot 10^{7}$	$1.18 \cdot 10^{8}$	$0.775 \cdot 10^{-8}$
2	$0.18 \cdot 10^{10}$	$1.96 \cdot 10^{7}$	$3.29 \cdot 10^{8}$	$0.776 \cdot 10^{-8}$
4	$1.38 \cdot 10^{10}$	$0.82 \cdot 10^{7}$	$5.64 \cdot 10^{8}$	$0.972 \cdot 10^{-8}$
5	$2.06 \cdot 10^{10}$	$0.56 \cdot 10^{7}$	$4.59 \cdot 10^{8}$	$0.820 \cdot 10^{-8}$
6	$2.68 \cdot 10^{10}$	$1.25 \cdot 10^{7}$	$3.89 \cdot 10^{8}$	$0.606 \cdot 10^{-8}$
7	$0.76 \cdot 10^{10}$	$0.96 \cdot 10^{7}$	$6.33 \cdot 10^{8}$	$0.997 \cdot 10^{-8}$
8	$7.70 \cdot 10^{10}$	$2.32 \cdot 10^{7}$	$2.75 \cdot 10^{8}$	$0.281 \cdot 10^{-8}$
9	$1.11 \cdot 10^{10}$	$0.49 \cdot 10^{7}$	$4.18 \cdot 10^{8}$	$1.608 \cdot 10^{-8}$
10	$18.56 \cdot 10^{10}$	$-6.56 \cdot 10^{7}$	$4.56 \cdot 10^{8}$	$1.436 \cdot 10^{-8}$
11	$0.66 \cdot 10^{7}$	$2.28 \cdot 10^{7}$	$2.28 \cdot 10^{8}$	$0.446 \cdot 10^{-8}$

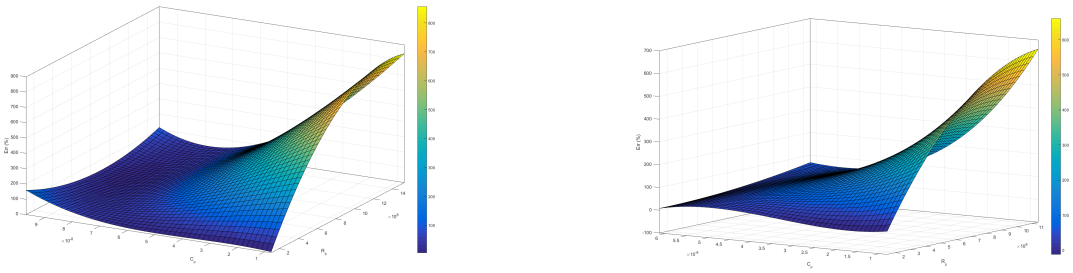

Figure 4.4: Surface response reported for the Circuit 2 analysis for patient 1 and patient 5.

It is notable that in all cases the value of R_p increased significantly by an order of magnitude from circuit 1 to circuit 2. Figure 4.5 shows both P_1 and P_2 pressures computed for

each subject, illustrating the contribution of the coarctation to the pressure reported in the ascending aorta.

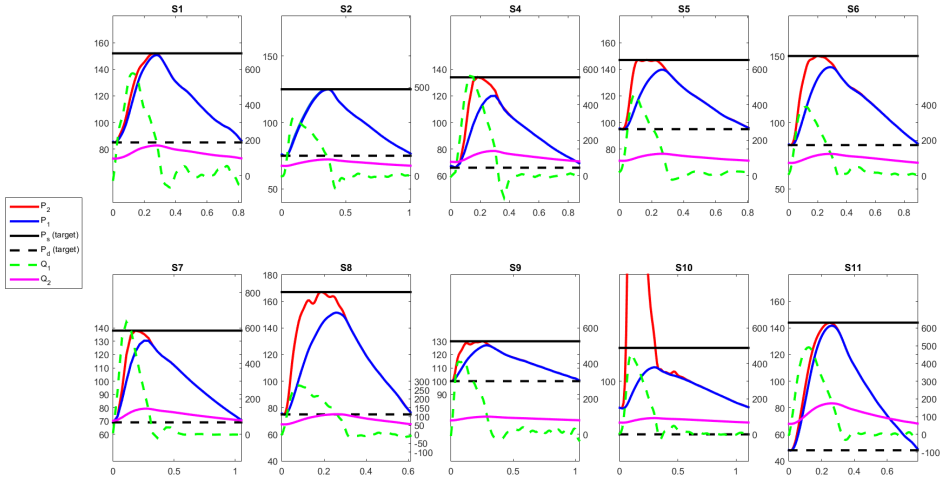

Figure 4.5: Results from the 0D circuit 2 model, reported for all 11 subjects: P_1 (in red) is the pressure at the ascending aorta; P_2 (in blue) is the pressure at the descending aorta; P_s(solid black) and P_d (dashed in black) are the is the target systolic and diastolic pressures, respectively; Q_1 (dashed in green) is the ascending aortic flow and Q_2 (in magenta) is the descending aortic flow.

The addition of peripheral compliance in the model reduces the significance of the coarctation in determining the ascending aortic pressure, as a result the pressure gradient across the coarctation is higher than 20 mmHg only for patient 10. The inclusion of peripheral compliance reduces peak flow in the descending aorta significantly, but mean flow is maintained, and so descending aortic flow overestimates the values measured using PC-MRI (discussed in more detail in Chapter 6). The peak pressure gradient across the coarctation typically occurs after peak flow in the ascending aorta.

4.2.3 Circuit 3 analysis

The values computed for R_p, C_p and R_s, C_s following the tuning process for circuit 3 are reported in Table 4.3 along with the values of R_p and C_p for circuit 2 for comparison in Table 4.4. In Figure 4.6 the surface response at different R_p and C_p is reported.

Table 4.3: Tuned parameters and error metrics for circuit 3 analysis. C_{tot} is the total compliance; R_{tot} is the total resistance; R_s is the supra-aortic resistance; R_p is the peripheral resistance; C_s is the supra-aortic compliance and C_p is the peripheral compliance.

Subject	C_{tot} (10^{-7}Pa · m^{-3})	Error C_{tot} (Pulse Pressure)	R_{tot} (10^{8}Pa · s · m^{-3})	Error R_{tot} (both pressures)	Rs/Rp	Cs/Cp	Error Total	Error P_s	Error P_d	Error Q_{DescAo}
1	0.0744	0.8525	1.1804	0.7769	0.85	2.25	0.0038	0.0359	0.7526	-0.3922
2	0.0761	0.5474	1.8178	0.6060	2.50	1.50	0.0005	-0.6374	-0.0747	-0.0687
4	0.0759	0.5874	1.2137	0.5566	3.55	1.35	0.0022	-1.3213	0.0170	0.5369
5	0.0705	0.4414	1.5494	0.7448	1.05	1.35	0.0082	-0.6021	-0.2900	-0.4881
6	0.0528	0.4639	1.5833	0.3928	0.80	1.25	0.0051	-0.0007	0.2444	0.4272
7	0.0878	0.3282	1.2374	0.3648	1.15	1.10	0.0090	-0.4211	0.0371	2.2584
8	0.0228	0.7436	1.8832	0.9208	1.45	1.25	0.0031	-1.0216	0.5920	-0.1974
9	0.1416	0.6941	1.7066	0.4955	0.85	1.70	0.0038	-0.2233	0.3163	0.5865
10	0.0790	0.6771	1.4479	0.5938	0.65	1.80	0.0168	7.4232	0.4609	0.6808
11	0.0424	0.5788	1.0905	0.4935	1.95	1.15	0.0019	-0.7139	0.2286	0.0044

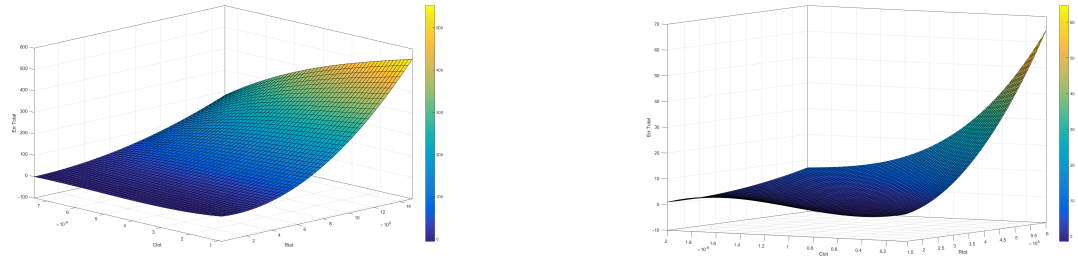

Figure 4.6: Surface response for the Circuit 3 analysis reported for patient 1 and patient 5.

Figure 4.7 shows P_1 and P_2 pressures for each subject and the ascending and descending aortic flow.

Table 4.4: Comparison of tuned parameters between circuit 2 and circuit 3 analysis.

Subject	R_c ($Pa \cdot s \cdot m^{-6}$)	R_p^2 ($Pa \cdot s \cdot m^{-3}$)	C_p^2 ($Pa \cdot m^{-3}$)	R_{tot}^3 ($Pa \cdot s \cdot m^{-3}$)	C_{tot}^3 ($Pa \cdot m^{-3}$)	C_{tot}^3/C_p^2	R_{tot}^3/R_p^2
1	$3.73 \cdot 10^{9}$	$1.18 \cdot 10^{8}$	$7.75 \cdot 10^{-9}$	$1.18 \cdot 10^{8}$	$7.44 \cdot 10^{-9}$	0.96	1.00
2	$1.84 \cdot 10^{9}$	$1.82 \cdot 10^{8}$	$7.76 \cdot 10^{-9}$	$1.82 \cdot 10^{8}$	$7.61 \cdot 10^{-9}$	0.98	1.00
4	$1.38 \cdot 10^{10}$	$1.14 \cdot 10^{8}$	$9.72 \cdot 10^{-9}$	$1.21 \cdot 10^{8}$	$7.59 \cdot 10^{-9}$	0.78	1.06
5	$2.06 \cdot 10^{10}$	$1.50 \cdot 10^{8}$	$8.20 \cdot 10^{-9}$	$1.55 \cdot 10^{8}$	$7.05 \cdot 10^{-9}$	0.86	1.03
6	$2.68 \cdot 10^{10}$	$1.54 \cdot 10^{8}$	$6.06 \cdot 10^{-9}$	$1.58 \cdot 10^{8}$	$5.28 \cdot 10^{-9}$	0.87	1.03
7	$7.67 \cdot 10^{9}$	$1.20 \cdot 10^{8}$	$9.97 \cdot 10^{-9}$	$1.24 \cdot 10^{8}$	$8.78 \cdot 10^{-9}$	0.88	1.03
8	$7.70 \cdot 10^{10}$	$1.78 \cdot 10^{8}$	$2.81 \cdot 10^{-9}$	$1.88 \cdot 10^{8}$	$2.28 \cdot 10^{-9}$	0.81	1.06
9	$1.11 \cdot 10^{10}$	$1.69 \cdot 10^{8}$	$1.61 \cdot 10^{-8}$	$1.71 \cdot 10^{8}$	$1.42 \cdot 10^{-8}$	0.88	1.01
10	$1.86 \cdot 10^{11}$	$1.70 \cdot 10^{8}$	$1.44 \cdot 10^{-8}$	$1.45 \cdot 10^{8}$	$7.90 \cdot 10^{-9}$	0.55	0.85
11	$6.62 \cdot 10^{9}$	$1.08 \cdot 10^{8}$	$4.46 \cdot 10^{-9}$	$1.09 \cdot 10^{8}$	$4.24 \cdot 10^{-9}$	0.95	1.01

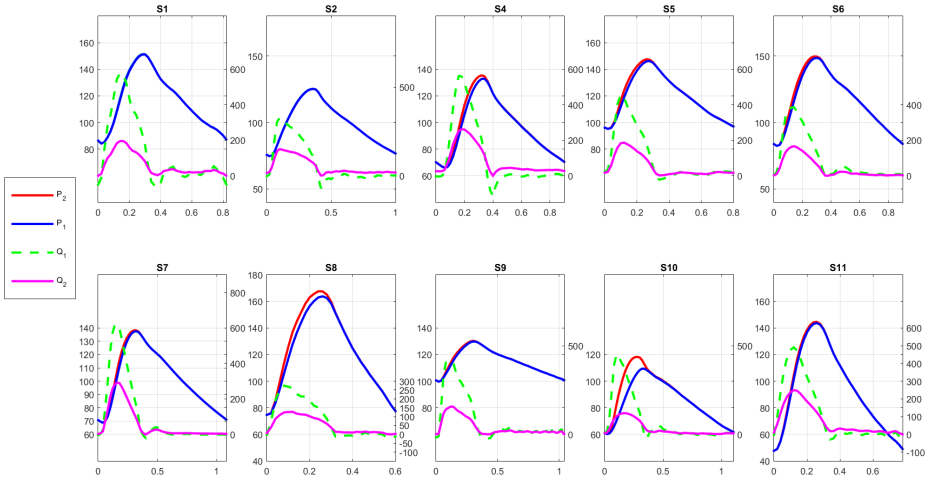

Figure 4.7: Results from the 0D circuit 3 model, reported for all 11 subjects: P_1 (in red) is the pressure at the ascending aorta; P_2 (in blue) is the pressure at the descending aorta; Q_1 (dashed in green) is the ascending aortic flow and Q_2 (in magenta) is the descending aortic flow.

With the adopted tuning strategy the compliances and resistances have been successfully tuned to match diastolic pressure in all the subjects in the cohort, with an error that is less than 1%. When considering the systolic pressure, the adopted strategy has been able to match the prescribed value in all cases except for subject 10, where the error was higher than 7%. However, the total error defined by the Equation 4.4 remains under the tuning threshold of 1%, as imposed by the tuning strategy threshold definition. Regarding the maximum descending aortic flow rate, all models were successfully tuned to match this value, except for subject 7 where the error was higher than 2%.

It is notable that the derived total compliance C_{tot} in circuit 3 is lower than the single value C_p derived for circuit 2. On the other side, the total resistance R_{tot} in circuit 3 is very close to the value derived for circuit 2, except for subject 10. As in the previous case the introduction of a supra-aortic circulation improves the accuracy of tuning to descending aortic flow rate, but as a results, the influence of the aortic coarctation is decreased, even for subject 10, where the predicted peak-to-peak pressure drop becomes lower than the clinical threshold for intervention (20mmHg).

4.3 Discussion

The first circuit represents the aortic coarctation as a nonlinear resistance, using the Bernoulli pressure drop equation, without considering the effect of downstream circulation. The second circuit include a peripheral resistance and compliance, and separate ascending and descending aortic pressure responses, a two element Windkessel model was adopted instead

of a three-element for limiting the number of unkown parameters that the algorithm needs to be found. In the third circuit a supra-aortic two elements Windkessel model was added and represent the supra-aortic circulation as one single circuit for the sake of simplicity and since no information regarding the flow at each of these branches was provided. In circuit 1 the amount of flow that passes through the coarctation site directly determines the pressure drop across the coarctation, this is expected to overestimate the actual pressure drop for two reasons. Firstly, the full ascending aortic flow passes through the coarctation without any flow diverted to the supra-aortic circulation. Secondly, the simple coarctation resistance model assumes that none of the Bernoulli pressure drop is recovered distal to the coarctation. In circuit 2 the form of the ascending and descending aortic flow are separate and the peak flow that passes through the coarctation site changes significantly. The peripheral resistance Rp also increased to match diastolic measured pressure, resulting in a good representation of peak to peak pressure variation for all subjects except for case 10, were the peak to peak pressure increased with respect to the previous case from 52 mmHg to 264 mmHg. However, this form of model does not consider the contribution of supra- aortic vessels on the descending aortic flow and preserves the mean ascending aortic flow rate through the model. In the third model the supra-aortic vessel circulation introduces variation between ascending and descending aortic mean flow and allows the model to be tuned to match not only systolic and diastolic pressure values but also peak descending aortic flow. It is notable that as the form of the model becomes more complex the peak-to-peak pressure gradient between the ascending and descending aorta tends to reduce.

4.4 Conclusion

The analysis detailed in this chapter represents a first attempt to assess the interaction between local aortic haemodynamics and subject-specific parameterization of windkessel representations of the peripheral and supra-aortic circulation using clinically measured data. From the analysis of these 0D models, it is clear that the significance of the coarctation becomes less from the simple two resistance model to the inclusion of both the peripheral and supra-aortic circulation. These results provide a context within which to interpret outcomes of the tuning process reported for a more complex model of aortic haemodynamics using 1D and 3D model approaches reported in Chapter 6.

5

Pre-processing steps

This chapter describes development of the pre-processing steps to support geometry extraction of anatomical features such as the aortic geometry. Therenva has more than ten years experience in the development of software solutions for the extraction of anatomical features from CT scan images for the planning of endovascular surgery. The Endosize software framework is able to automatically extract the aortic wall and centerlines from pre-operative CT images in only a few seconds using an intuitive and adaptable interface. The current segmentation procedure implemented within Endosize is optimized for the extrac-

tion of the main anatomical structures in the thoracic and abdominal aorta, but is not well suited for segmentation of the smaller supra-aortic vessels which are especially important when the segmentation step is used as the starting point for 3D CFD simulation. This chapter describes the implementation of an alternative segmentation methodology implemented within Endosize to improve supra-aortic vessel extraction. At the current time the Endosize framework does not support processing of MR images such as those provided by collaborators at the University of Bern to provide a cohort of patients for assessment of the proposed CFD workflow. Therefore, the second part of this chapter details segmentation of aortic geometry from MR images for the Bern cohort using existing tools. The pre-processing steps to generate suitable meshes for CFD analysis are outlined along with a steady-state mesh sensitivity analysis for the identification of the optimal mesh density to adopt for the transient CFD simulations described in Chapter 6.

5.1 Patient specific geometry extraction

5.1.1 Introduction

The segmentation methodology presented here has been implemented inside an existing FDA-approved and CE marked medical software device: Endosize (Therenva, Rennes). Endosize is commercially available software used for planning minimally invasive endovscular techniques such as EVAR (Endovascular Abdominal Aortic Repair), TEVAR (Thoracic Endovascular Aortic Repair), FEVAR (Fenestrated Endovascular Aortic Repair), Periph-

eral Vascular Stenting (PVS) and TAVI (Transaortic Valve Implant). Starting from CT scan images, clinicians are provided with tools to automatically reconstruct the aortic centerline, take anatomical measurements and choose the interventional strategy to adopt for a specific patient.

The new segmentation method has been compared with the existing segmentation method adopted by Endosize (based on the region growing approach). Whilst, the existing method provides an excellent definition of the internal lumen of the aortic trunk (especially in the case of AAA), it does not capture the small supra-aortic vessels (brachio- cephalic trunk, left carotid artery and subclavian artery) well, which are not only crucial for defining boundary conditions to be used for fluid-dynamic simulations, but also determine local haemodynamics.

The workflow of the new segmentation method is outlined in Figure 5.1

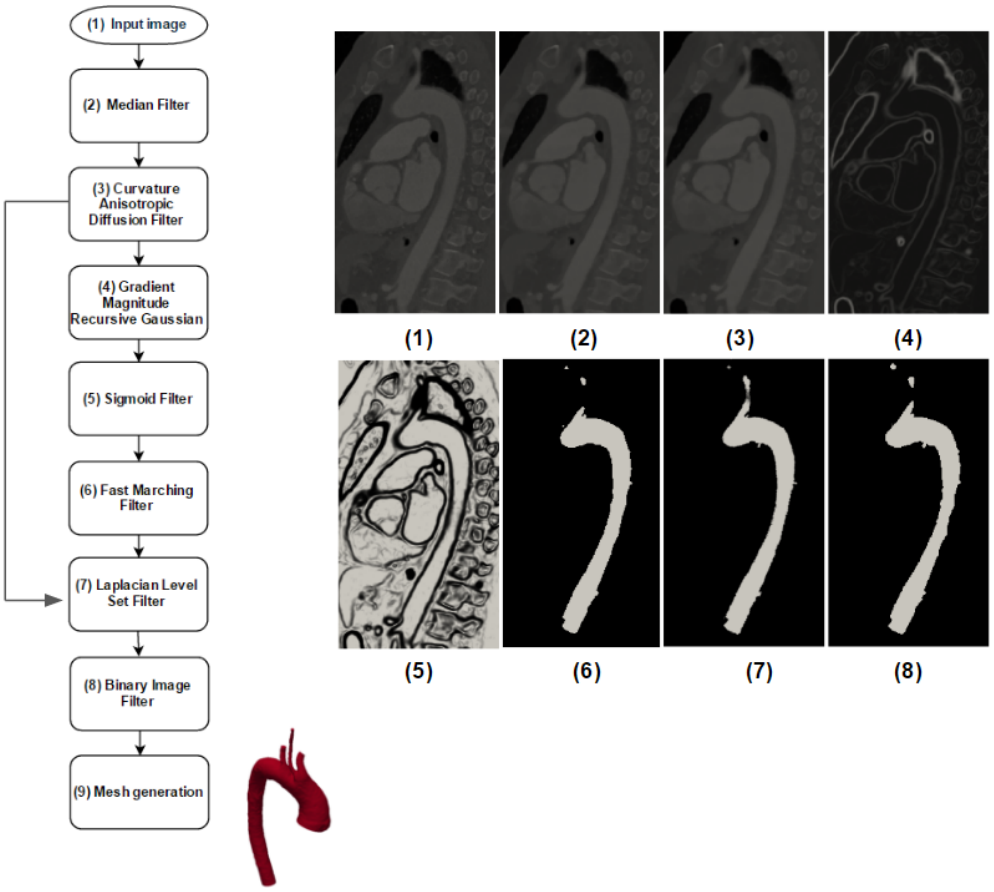

Figure 5.1: Flowchart describing the filter steps used for the novel segmentation method.

5.1.2 Methods

CT images were initially denoised in a preprocessing (enhancing) stage. The algorithms used for both the pre-processing (enhance) phase, shown in Figure 5.1(1-3), and extraction of the final geometry, shown in Figure 5.1(4-9), have been taken from available algorithms

in two open source libraries: ITK (Insight Segmentation and Registration Toolkit (Johnson et al., 2015)) and VTK (Visualization Toolkit (Avila, 2006)); and imported into the Endosize library. For testing the segmentation method, CT contrast-enhanced anonymized scan images were used from an open source data file system (Osirix Advanced Imaging in 3D, 2016). This data represents a case of a Dilated Thoracic Aorta. Geometry extraction without denoising is difficult since the intensity distribution of the raw images is irregular due to noise. At first, a median filter (Figure 5.1(2)) was used to remove salt-and-pepper noise without biasing the contour of the structures. In the second enhancement phase a curvature-based anisotropic diffusion filter (Figure 5.1 (3)) (Whitaker & Xue, 2001) implemented in ITK was employed. This anisotropic diffusion filter reduces the effect of additional disturbing artifacts while preserving the boundaries and fine details of the organs and tissues even on weaker contrast CT images. For this specific case a numerical time step of 6 msec (used for solving the iterative scheme) was imposed, for guaranteeing the convergence of the finite difference scheme, 5 iterations were adopted, with a conductance value of 1.5 (Johnson et al., 2015).

Multiple points were selected as seed points over the centerline of the aortic region that needed to be extracted: ascending, descending and supra-aortic vessels. A total of 200 points were automatically chosen along the extracted aortic centerlines at different CT slices, by using the pre-existing algorithms already implemented inside Endosize (Therenva, Rennes). The seed points were equally spaced along the vessel centerline which is extracted in the preliminary phase when the user is asked to define two points, one at the ascending and the second at the descending aortic region in order to extract the region of interest (ROI), via a adapted region growing algorithm.

A fast-marching level-set method (Sethian, 1996) implemented in ITK was customized to extract an initial aortic region using the intensity information of the selected seed points. The fast-marching level set method consists of four steps: (1) calculation of the CT image gradient magnitude at each voxel, (2) calculation of the contour propagation speed based on the gradient magnitude at each voxel, (3) calculation of the arrival time of the propagation contour at each voxel and (4) generation of the initial aortic region based on calculated arrival time by using a binary image filter implemented in ITK (Whitaker & Xue, 2001).

The gradient magnitude recursive gaussian filter (Deriche, 1992) implemented in ITK was used to perform a first derivative and a smoothing, via the convolution of the gaussian filter, on the CT image dataset voxels. The contour propagation speed for the fast-marching level set method was calculated based on the CT image gradient magnitude using a sigmoid function implemented in ITK as

$$S = \frac{1}{1 + e^{-\frac{G-\beta}{\alpha}}} \tag{5.1}$$

where G is the gradient magnitude, α and β are the parameters which magnify the intensity differences between the aortic lumen and the non-aortic lumen in each CT slice. The parameter β was taken as

$$\beta = \frac{2}{l_{max}} \tag{5.2}$$

where l_{max} is the maximum of all the intensity values measured along the vessel centerline, at the seed points, in the gradient magnitude image, while α is the average value of all the intensity values measured along the vessel centerline, at the seed points, in the gradient magnitude image.

The arrival time of the propagating front is calculated by solving the wave-front Eikonal

equation

$$\|\nabla T_i\| S = 1 \tag{5.3}$$

The extraction of the vessel geometry via the fast-marching algorithm is based on the computation of the arrival time T_i for each CT slice of propagating fronts from different initial seed points. The arrival time is a function of the position and the speed function S, is taken as sigmoid filtered image. The Eikonal equation is solved using the upwind, viscosity-s scheme (Prados et al., 2006). Lastly, an initial binary aortic region was generated based on the calculated arrival times. The voxels with their arrival times in a certain threshold value (taken as 50) were considered as the initial aortic region.

In the final step of the segmentation method a laplacian level set algorithm (Osher & Sethian, 1988) implemented in ITK was used. The laplacian filter resolve a level set equation by finding the solution , called also the zero level set solution, of the implemented partial derivative equation

$$\varphi_t + F(x)\|\nabla\varphi\| + \alpha_1 H(x)\|\nabla\varphi\| + \beta_1 P(x) \cdot \nabla\varphi = 0 \tag{5.4}$$

Where the first term is the derivative in time of φ, the second term is the inflation term, the third term is the penalization term, where H(x) is equal to

$$H(x) = \nabla \cdot \frac{\nabla\varphi}{\|\nabla\varphi\|} \tag{5.5}$$

and the fourth term is the attraction potential term, P(x) equal to

$$P(x) = -\|\nabla I(x)\| \tag{5.6}$$

where $I(x)$ is the intensity map value of the image. The inflation term controls the propagation of the surface along the gradient with a velocity expressed by the term $F(x)$. The penalization term is added to ensure the smoothness of the surface and it is controlled by the term α_1 (taken as 10). The attraction potential is a convective term that drives the surface of the front towards the edges and it is controlled by the term β_1 (taken as 60). The extracted contour of the aortic region was slightly dilated using a binary dilatation method (Nodes & Gallagher, 1982) implemented in ITK.

5.1.3 Results

Figure 5.2 shows a comparison of the new segmentation and the previous segmentation algorithm used within Endosize, based on the region growing algorithm. The extraction time with the new method is 956 sec (around 15 minutes), while the existing method requires 0.318 seconds with an Intel(R) Xeon(R) 3.50GHz.

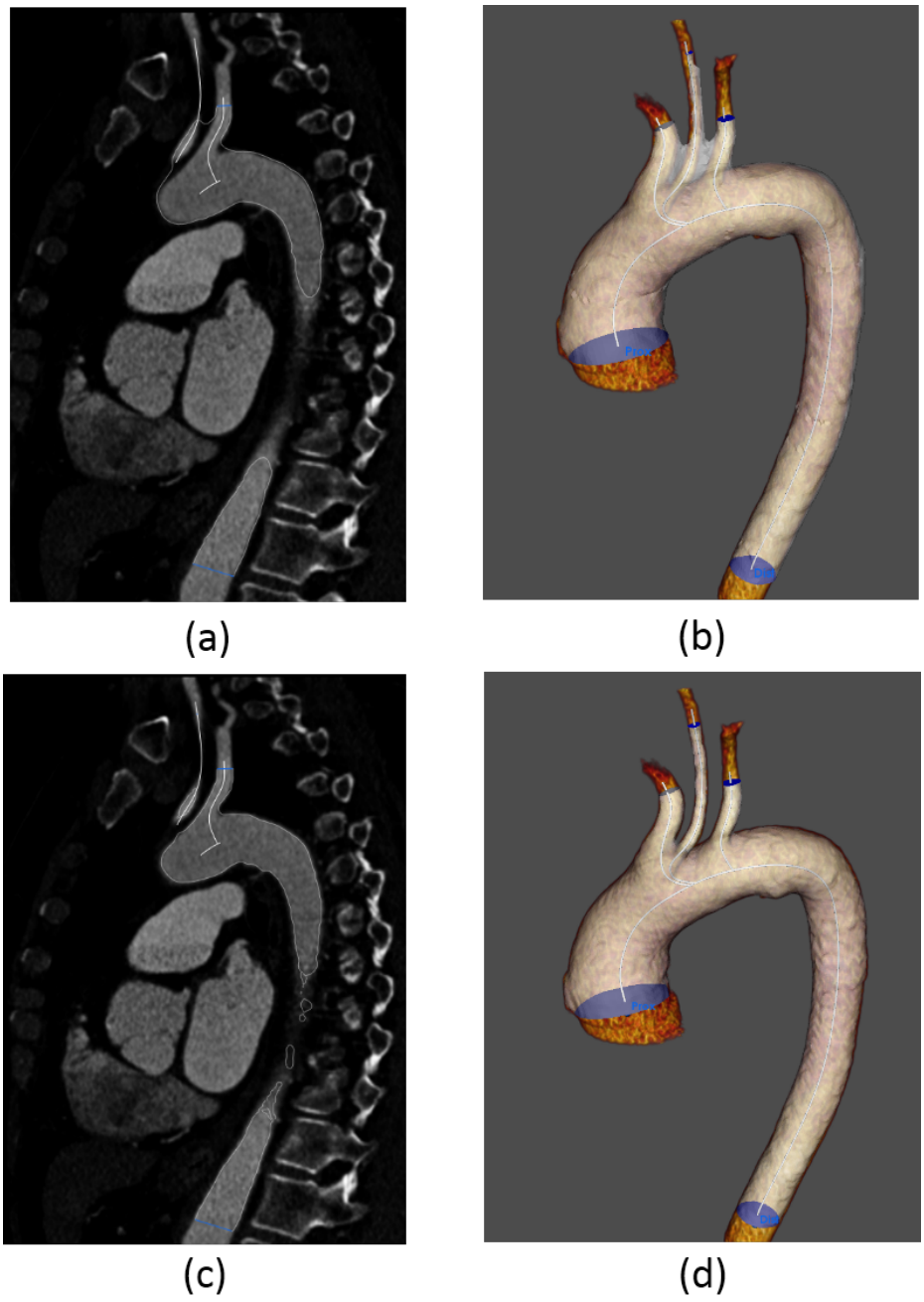

Figure 5.2: Visual representation of the segmentation accuracy of the aortic region: Existing segmentation procedure based on the region growing method, (a) sagittal slice-highlighted segmented region, (b) extracted 3D geometry with centerlines. New segmentation procedure, (c) sagittal slice-highlighted segmented region, (d) extracted 3D geometry with centerlines.

5.1.4 Discussion

The implementation of the new segmentation methodology provided a good result for the test CT dataset. In particular, the supra-aortic vessels were accurately delineated, and the overall geometry was in good agreement with the aortic geometry present in the CT images. When compared to the existing region growing method, the proposed methodology provided better results especially in the region of the aortic arch. Comparison of the cross-sectional area outside this region is a good agreement between the methods with a maximum difference of 1%. However, the improved segmentation significantly increased the time required for geometry extraction. Similar segmentation procedures have been used in literature by Yang et al. (2014) for segmenting liver structures from CT scan images, and Antiga et al. (2008) for extracting aortic vessel structures from MRI images. Yang et al. (2014) performed a pre-processing phase by using the same anisotropic filter for denoising CT scan images then applied the fast-marching algorithm with different seed points. The seed points were manually chosen by the operator, therefore, the segmentation is an hybrid form between a manual and an automatic segmentation procedure. The pre-existing algorithm implemented within Endosize (Therenva, Rennes) allows seeds points to be automatically selected on the centerline of the aorta. Antiga et al. (2008) were the first to use a coupling of a fast-marching algorithm with a level set algorithm to perform an automatic segmentation of the aortic trunk and collaterals. In their methodology they only used two seed points (one in the suprarenal aorta and the other at the iliac bifurcation) for segmenting the entire geometry, which may be inferior to this approach where multiple initial seed points are provided. Figure 5.3 shows that the segmentation it is not as accurate when only

two seed points are used for segmenting the entire aortic geometry.

It worth notice that Computer Tomography is not an imaging technique commonly used when dealing with coarcted patient, even though it can provide excellent anatomic detail of the aorta, the coarctation segment and collateral circulation as well as other associating aortic and cardiac abnormalities (such as left ventricle hypertrophyor bicuspid aortic valve) due to its high spatial resolution (0.5-0.625 mm full width at half maximum (Lin & Alessio, 2009)). In addiction, CT scan is less susceptible to artifacts due to the present of the stent. However, CT scan has some common drawbacks that are linked to the quantitave of radiation at which the patient is subjected at each examination that can lead to a potential cumulative exposure damages, especially in pediatric patients where a constant follow-up is needed, potential contrast allergy or chronic kidney disease. Therefore cardiac MRI and MRA are frequently preferred over the CT imaging, not only because is ionizing radiation–free, but also because the contrast used to enhance the vasculature (Gadolinium based contrast) can be used to evaluate safetly patients with mild or moderate renal insufficiency. In addition, the use of cine phase contrast sequences allows the detection of aortic flow rate and other hemodynamic features at different levels of the aorta. However, when compared to CT scan image MRI has a lower spatial resolution (1-2 mm in full width at half maximum (Lin & Alessio, 2009)), that may question the accuracy of the reconstruction of stenotic regions. This section explored the possibility to integrate CT scan in the simulation workflow through a developed segmentation process that allows the automatic extraction of the geometrical of the aortic geometry. The segmentation can be easily integrated inside Endosize, since it has been adapted for dealing with CT images, in order to complete the simulation process, inlet and descending aortic flow rates or velocity information needs to

be provided through PC-MRI or eco-doppler measurements.

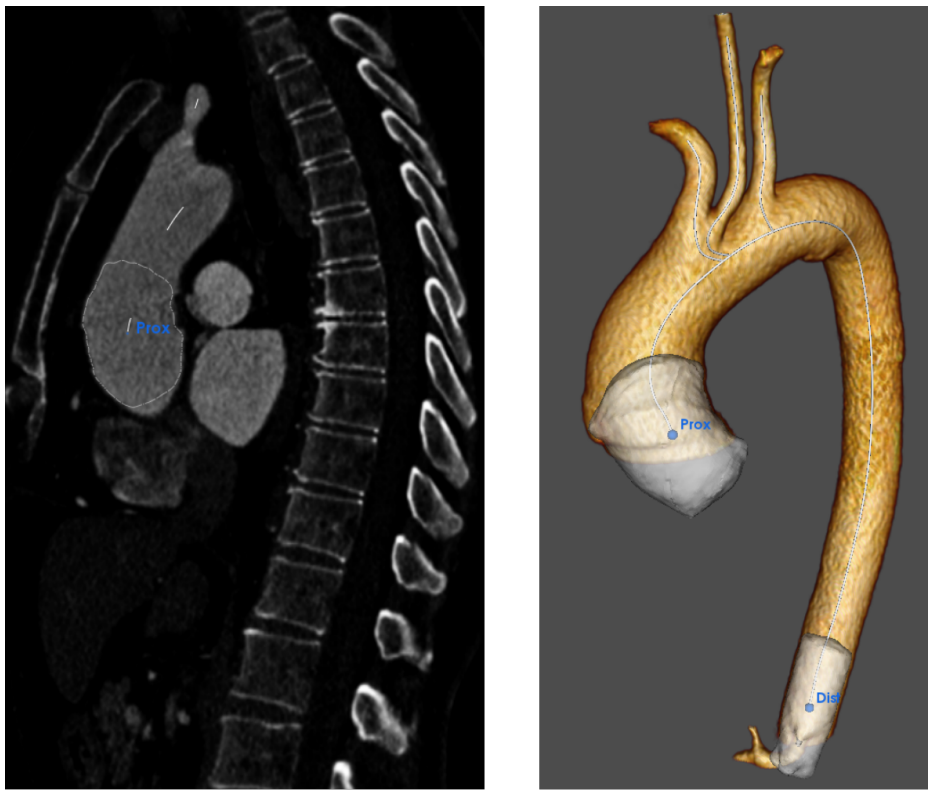

(a) (b)

Figure 5.3: Visual representation of the segmentation accuracy of the aortic region when only two seed points are considered along the vessel centerline (at the proximal and distal aorta). (a) Sagittal slice - highlighted segmented region (b) Extracted 3D geometry with centerlines, in the case when Fast Marching Filter threshold is equal to 50.

5.1.5 Conclusion

This section reports successful application of a novel image processing chain applied to representative clinical data. This processing chain has been implemented directly within En-

dosize (Therenva, Rennes), a commercially available software used for planning minimally invasive techniques. The performance of the algorithm has been compared with the existing Endosize segmentation method (based on the region growing approach). The new method produced a more accurate aortic segmentation, particularly in the region of supra-aortic branches. Further work to examine the efficacy of the proposed method should include a statistical study of performance across many datasets.

5.2 3D geometry extraction for Bern cohort

A detailed description of data processing associated with the Bern patient cohort is provided in Chapter 5. In this section the specific steps associated with segmentation of the 3D aortic geometry for CFD analysis are described. In this patient cohort contrast-enhanced magnetic resonance angiography was performed as a first assessment for clinical suspicion of aortic coarctation or as a follow-up exam after previous surgical intervention for all 11 patients. The subjects were scanned in the supine position using a 1.5T MAGNETOM Aera scanner (Siemens Healthcare, Erlangen, Germany) using a T1 weighted, k-space, spoiled gradient recalled echo sequence (echo time: 1.1ms , repetition time: 3.17ms , flip angle: 30 , field of view: $370-420\text{mm}$, slice thickness: $1-1.2\text{mm}$, acquisition matrix: $384\text{x}250$ reconstructed to $512\text{x}512$) and intravenous gadolinium-based contrast medium injection with optimal contrast timing to enhance the thoracic aorta (contrast flow at $3.5\text{ml}\cdot\text{s}^{-1}$) using the test-bolus technique.

The 3D geometry was then reconstructed using semi-automatic segmentation software (Philips

Intellispace, Philips, Koninklijke, Netherlands) to provide the aortic geometry in the form of an STL file. The STL file was post processed manually using the open source software Autodesk MeshMixer (Autodesk, Inc). The final STL was truncated to obtain four outlets (cutting the surface perpendicular to the extracted centerline) using the vmtk toolkit Antiga et al. (2008).

5.2.1 Results

The typical geometry processing time is less than 15 minutes for each patient. The final results are shown in Figure 5.4 for all the patients in the cohort.

5.3 Mesh sensitivity analysis

Mesh resolution and design are two important factors that can affect the results of a numerical simulation. A mesh sensitivity analysis is frequently performed in order to assess whether the obtained solution is independent of the resolution of the numerical grid. Generally, the mesh sensitivity analysis starts by setting up at least three identical simulations with same boundary conditions, resolution scheme and material properties but with a different mesh density: a coarse, medium and a fine mesh. The evaluation of the mesh quality is affected by the output parameter under investigation, a physical parameter that can be derived from the simulation, such as Pressure, Flow or Wall Shear Stress distribution. An appropriate mesh density provides a good compromise between the accuracy of the results,

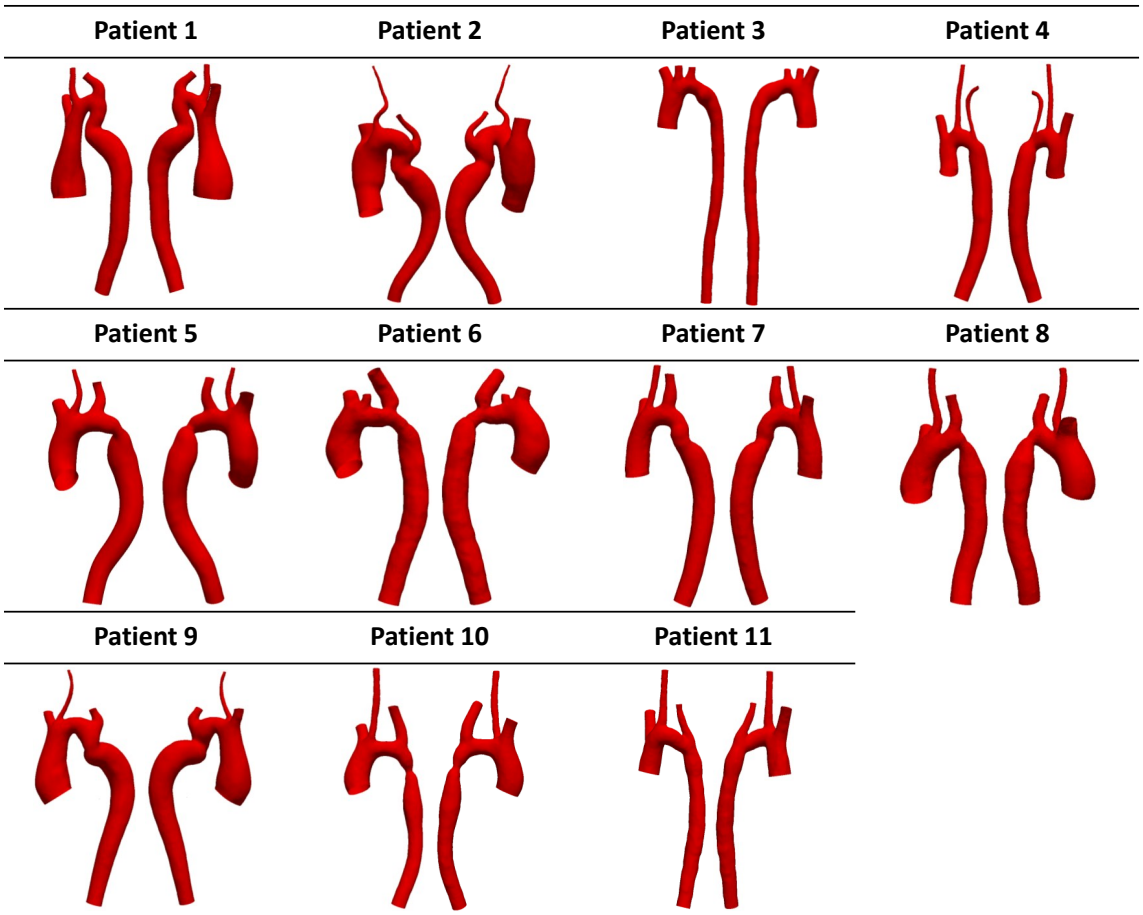

Figure 5.4: Post-processed 3D geometries adopted in the mesh sensitivity analysis.

Table 5.1: Mesh densities adopted in the studies presented in the introductory chapter of the thesis.

CoA Study	Number of elements
LaDisa et al. (2011)	$2 - 3 \cdot 10^6$ tetrahedral elements
Coogan et al. (2011)	$2 \cdot 10^6$ tetrahedral elements
Menon et al. (2012)	$4 \cdot 10^6$ tetrahedral elements
Wendell et al. (2013)	$3 \cdot 10^6$ tetrahedral elements
Kwon et al. (2014)	more than $8 \cdot 10^6$ tetrahedral elements
Pant et al. (2014)	$0.29 - 3.75 \cdot 10^6$ tetrahedral elements
Goubergrits et al. (2015a)	$2 \cdot 10^6$ tetrahedral elements
Cosentino et al. (2015)	$1 \cdot 10^6$ tetrahedral elements
Zhu et al. (2018)	$1 - 2 \cdot 10^6$ tetrahedral elements

when compared to an equivalent experimental set-up or a known analytical solution, and the computational cost of the simulation. Most studies reported in the introductory chapter, provided information on the number of elements used to discretize the fluid domains. The number of elements used in previous studies are reported in Table 5.1 in terms of the number of cells of a medium size grid designed for the mesh sensisitivity analysis. In all of these studies, the 3D geometries were discretized using tetrahedral elements. The mesh densities vary from 0.29 to $8 \cdot 10^6$ tetrahedral cells. Kwon et al. (2014) used the highest cell density to discretize their models, since they aimed to adequately resolve flow features towards stent structures. On the other way, Pant et al. (2014) demonstrated that a mesh density of 300 000 elements can adequately resolve the fluid domain in terms of flow and pressure field, with negligible difference when compared to a finer mesh of more $1 \cdot 10^6$ tetrahedral elements. It is worth noting that in these studies no information was reported regarding the

maximum or minimum element volume, length or any other parameter to provide a more detailed insight into the spatial resolution of these meshes.

In this study all the geometries have been discretised using polyhedral elements. Polyhedral elements were first introduced by (Oaks & Paoletti, 2000) and the meshing algorithm was officially release in 2005 by CD-adapco (Melville,NY) into their CFD based solver named STAR-CCM+. In the literature, few groups have used this type of mesh for haemodynamic simulations (Lotfi et al., 2016; Spiegel et al., 2011; Karmonik et al., 2012). Spiegel et al. (2011) conducted a comparative study between polyhedral and tetrahedral-based meshes, evaluating velocities and Wall Shear Stress distribution at different points in two cerebral aneurysm geometries: a saccular carotid aneurysm and a terminal basilar tip aneurysm. This comparison was conducted for both steady and transient flow, using the same analysis settings for all mesh densities. The results showed that polyhedral elements were able to resolve complex WSS pattern with around 60% less elements compared to tetrahedral mesh types. In addition, polyhedral elements showed improved convergence of the solution in terms of number of iterations to achieve the residual convergence threshold, and consequently the computational time required for the simulation. Peric (2004) had already investigated the advantages of polyhedral meshes over the existing meshing technques in many CFD engineering applications, demostrating that polyhedral grid cells not only improve convergence, stability and computational time but also they are less sensitive to stretching (especially in restricted regions), providing a better approximation of velocity gradients and recirculation zones. The latter is explained by the topoloogy of the polyhedral cell itself. Unlike tetrahedral meshes, in polyhedral meshes a single cell could have at least ten neighbors (while tetrahedral only a couple of neighbors), improving the computation of the gradient at

cell centers with the associated linear shape functions, especially near the boundaries where automatic meshing approaches can lead to a single tetrahedral cell touching the boundary with its corner, while a polyhedral cell is able to touch this surface with its entire face.

This section reports a mesh sensitivity analysis performed on the 3D domain for all 11 patients in the cohort, in order to define the minimum mesh density required to perform the simulations reported in Chapter 6.

The geometries were automatically meshed in ANSYS classic (ANSYS, Canonsburg, PA, USA) by means of a parameterised script file with the final mesh densities reported in Table 5.3. The geometries were meshed using polyhedral elements with five prism layers at the wall, using an expansion ratio of 1.2, in order to improve the resolution of the boundary layer at the wall. The number of boundary layers and the expansion ratio (ratio between the first and last element of the boundary layer) were chosen to ensure that the mesh does not become overly distorted at the supra-aortic vessels (BCA, LCA, LSUB) where the radius is small. Figure 5.5 shown a detailed view of the medium size mesh generated for Patient 1.

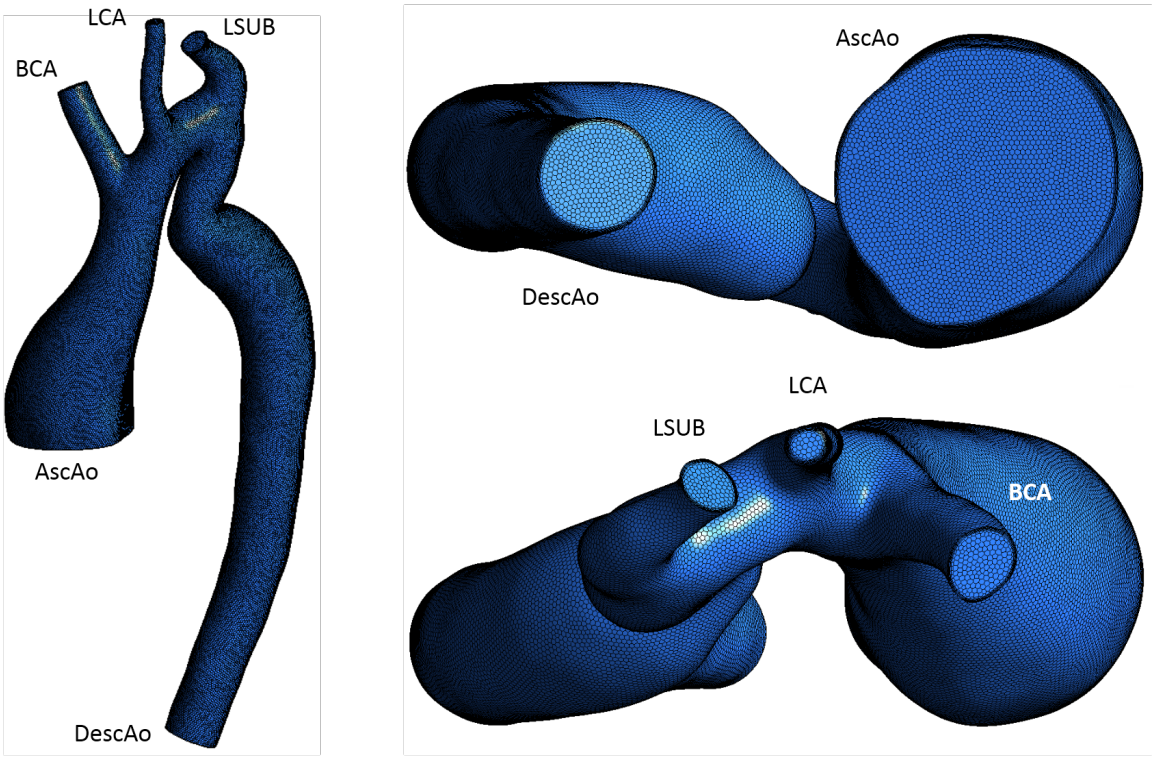

Figure 5.5: A detail of the medium size mesh adopted for Patient 1. The geometry was meshed using polyhedral elements in the core fluid region together with a five prism boundary layer near the wall.

5.3.1 Boundary conditions

The simulations were performed in steady state. At the inlet, the peak flow, measured from Phase Contrast MRA (see Chapter 6 for further information), was applied using a flat velocity profile. A constant pressure was applied at each outlet of the numerical domain using outlet-specific pressure values taken from the transient simulations reported in Chapter 6, at peak systolic flow (see Table 5.2). A no-slip condition was applied at the wall and the

simulation convergence criteria for momentum and continuity residuals were set at $1e^{-5}$. Blood was assumed to be an incompressible Newtonian fluid (the density, ρ, was set to $1060 kg \cdot m^{-3}$ while the viscosity, μ, was set equal to $4.5\ Pa \cdot s^{-3}$).

Table 5.2: Boundary conditions adopted for the mesh sensitivity analaysis.

	Peak Mass	Pressure (mmHg)			
	flow rate (kgs^{-1})	BCA	LCA	LSUB	Descao
Patient 1	0.61	133	131	132	119
Patient 2	0.35	117	112	114	110
Patient 3	0.29	119	119	118	103
Patient 4	0.61	112	118	116	134
Patient 5	0.49	157	154	156	154
Patient 6	0.41	146	145	136	127
Patient 7	0.69	135	134	130	111
Patient 8	0.29	130	129	129	110
Patient 9	0.44	166	157	160	149
Patient 10	0.48	185	179	180	126
Patient 11	0.52	146	142	124	126

5.3.2 Assessment of mesh convergence

As explain in the introduction of this chapter, in all numerical studies it is important to assess the ability of the computational mesh to adequately resolve the governing equations, producing an acceptably small variation in the parameters under investigation. In this case

the primary output under investigation is the pressure distribution along the vessel centerline which determines the pressure gradient across the coarctation. For the patient-specific analyses reported here no analytical solution or experimental result is available for comparison so the independence of the results to cell grid size is based on the comparison with an extrapolated solution equivalent to the case when the cell grid size is zero. For this purpose, the Richardson's extrapolation method was adopted to estimate the exact solution and predict the error of the numerical solution at each mesh size (Roache, 1994; Stewart et al., 2009). Richardson's method requires at least three meshes and a reference length (h_i), the maximum element length, for each mesh and the numerical solution (f_i), which is, in this case, the pressure distribution along the aortic centerline. The refinement ratio is defined as

$$r_{mesh} = \frac{h_2}{h_1} = \frac{h_3}{h_2} \tag{5.7}$$

where $i = 3$ is the finest mesh density. The order of the numerical solution is equal to

$$p_{sol} = \frac{In\frac{f_3 - f_2}{f_2 - f_1}}{In(r_{mesh})} \tag{5.8}$$

And the Richardson extrapolation predicts the value at $h = 0$ (to return an estimate of the exact solution)

$$f_{h=0} = f_{fine} + \frac{f_1 - f_2}{r^{p_{sol}} - 1} \tag{5.9}$$

The relative error is defined as the absolute difference between Richardson's solution and the numerical solution for each mesh and is normalised relative to the mean amplitude of

pressure in order to avoid division by zero

$$\text{Error} = \frac{f_i - f_{h=0}}{\frac{1}{n}\sum_{j=1}^{N} f_{h=0}} \cdot 100 \tag{5.10}$$

Where N is the number of points (along the vessel centerline). The mesh densities used in this study are reported in Table 5.3 for all the 11 patients in the cohort.

Table 5.3: Patient mesh densities used in the sensitivity study from the coarser (NA1) to the finer mesh (NA3).

	Type	Number of Elements	Min Element Edge Length (m)	Max Element Volume (m^3)
Patient 1	NA1	241476	$1.62 \cdot 10^{-3}$	$4.26 \cdot 10^{-9}$
	NA2	564822	$1.15 \cdot 10^{-3}$	$1.51 \cdot 10^{-9}$
	NA3	1237944	$8.33 \cdot 10^{-4}$	$5.97 \cdot 10^{-10}$
Patient 2	NA1	200221	$2.14 \cdot 10^{-3}$	$9.85 \cdot 10^{-9}$
	NA2	465929	$1.17 \cdot 10^{-3}$	$1.60 \cdot 10^{-9}$
	NA3	1037420	$8.43 \cdot 10^{-4}$	$5.99 \cdot 10^{-10}$
Patient 3	NA1	55462	$1.45 \cdot 10^{-3}$	$3.02 \cdot 10^{-9}$
	NA2	105205	$1.09 \cdot 10^{-3}$	$1.31 \cdot 10^{-9}$
	NA3	230951	$7.97 \cdot 10^{-4}$	$5.06 \cdot 10^{-10}$
Patient 4	NA1	123156	$1.52 \cdot 10^{-3}$	$3.54 \cdot 10^{-9}$
	NA2	243057	$1.16 \cdot 10^{-3}$	$1.54 \cdot 10^{-9}$
	NA3	544991	$1.61 \cdot 10^{-4}$	$4.14 \cdot 10^{-12}$
Patient 5	NA1	197287	$1.57 \cdot 10^{-3}$	$3.88 \cdot 10^{-9}$
	NA2	414011	$1.12 \cdot 10^{-3}$	$1.41 \cdot 10^{-9}$
	NA3	923975	$8.26 \cdot 10^{-4}$	$5.64 \cdot 10^{-10}$
Patient 6	NA1	126724	$1.55 \cdot 10^{-3}$	$3.76 \cdot 10^{-9}$
	NA2	257415	$1.20 \cdot 10^{-3}$	$1.71 \cdot 10^{-9}$
	NA3	603176	$8.42 \cdot 10^{-4}$	$5.96 \cdot 10^{-10}$
Patient 7	NA1	124557	$1.63 \cdot 10^{-3}$	$5.34 \cdot 10^{-9}$
	NA2	276698	$1.14 \cdot 10^{-3}$	$1.47 \cdot 10^{-9}$
	NA3	621294	$8.12 \cdot 10^{-4}$	$5.34 \cdot 10^{-10}$
Patient 8	NA1	103723	$1.57 \cdot 10^{-3}$	$3.90 \cdot 10^{-9}$
	NA2	220962	$1.11 \cdot 10^{-3}$	$3.90 \cdot 10^{-9}$
	NA3	508201	$8.09 \cdot 10^{-4}$	$5.30 \cdot 10^{-10}$
Patient 9	NA1	167679	$1.60 \cdot 10^{-3}$	$4.06 \cdot 10^{-9}$
	NA2	364572	$1.16 \cdot 10^{-3}$	$1.55 \cdot 10^{-9}$
	NA3	1003314	$8.26 \cdot 10^{-4}$	$5.63 \cdot 10^{-10}$
Patient 10	NA1	215597	$1.11 \cdot 10^{-3}$	$3.92 \cdot 10^{-9}$
	NA2	445133	$8.72 \cdot 10^{-4}$	$1.38 \cdot 10^{-9}$
	NA3	97066	$1.58 \cdot 10^{-3}$	$6.63 \cdot 10^{-10}$
Patient 11	NA1	102533	$1.57 \cdot 10^{-3}$	$3.86 \cdot 10^{-9}$
	NA2	218617	$1.16 \cdot 10^{-3}$	$1.58 \cdot 10^{-9}$
	NA3	489772	$8.24 \cdot 10^{-4}$	$5.60 \cdot 10^{-10}$

5.3.3 Results

The mean (Err_{mean}) and maximum (Err_{max}) errors are reported in Table 5.4 for each mesh density (NA1, NA2 and NA3) for all patients in the cohort. The NA1 solution was found to have largest deviations from Richardson's solution for each patient in the cohort. For Patient 3,7,11 NA1 failed to produce a converged solution. NA2 and NA3 exhibit lower error values and produce solutions that were converged for all patient geometries. The centerline pressure for all mesh densities and the resulting solution using Richardson's extrapolation method are compared in Figure 5.6.

Table 5.4: Mean and maximum errors reported for different meshes: NA1, NA2 and NA3.

		NA1	NA2	NA3
Patient 1	Err_{mean}	0.77	0.55	0.01
	Err_{max}	1.72	1.21	0.02
Patient 2	Err_{mean}	1.08	0.14	0.04
	Err_{max}	1.58	0.29	0.07
Patient 3	Err_{mean}	4.39	1.79	1.01
	Err_{max}	6.56	2.63	1.50
Patient 4	Err_{mean}	1.06	0.93	0.03
	Err_{max}	3.76	3.19	0.1
Patient 5	Err_{mean}	0.3	0.07	0.03
	Err_{max}	0.71	0.11	0.05
Patient 6	Err_{mean}	0.29	0.26	0.1
	Err_{max}	0.91	0.81	0.32
Patient 7	Err_{mean}	2.2	1.47	0.78
	Err_{max}	5.92	3.95	1.49
Patient 8	Err_{mean}	0.11	0.06	0.01
	Err_{max}	0.25	0.11	0.01
Patient 9	Err_{mean}	0.23	0.07	0
	Err_{max}	0.58	0.24	0
Patient 10	Err_{mean}	0.38	0.13	0
	Err_{max}	1.11	0.49	0.02
Patient 11	Err_{mean}	3.45	1.45	0.64
	Err_{max}	4.53	1.91	1.21

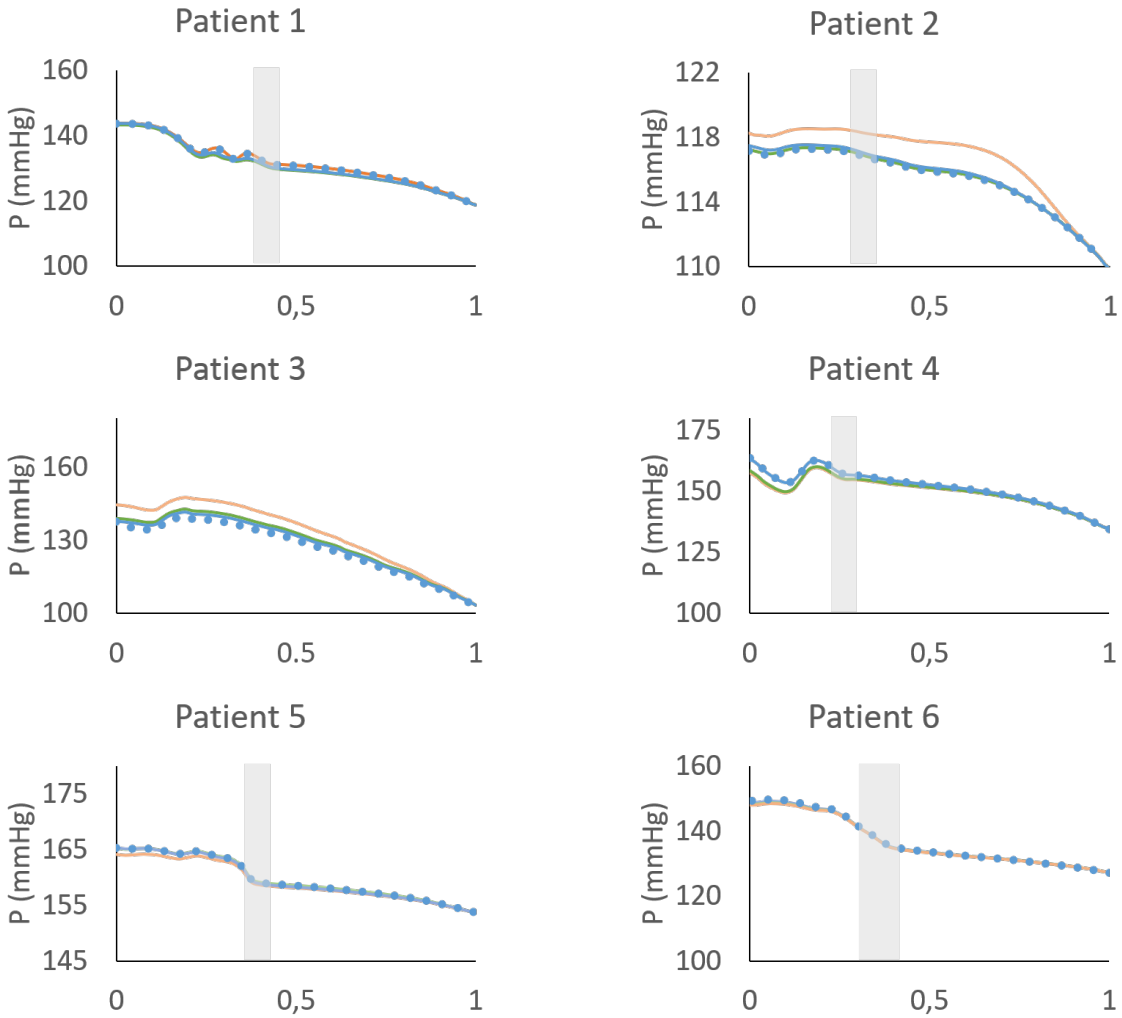
Patient 1
P (mmHg)
160
140
120
100
0
0,5
1
Patient 2
P (mmHg)
122
118
114
110
0
0,5
1
Patient 3
P (mmHg)
160
130
100
0
0.5
1
Patient 4
P (mmHg)
175
150
125
100
0
0,5
1
Patient 5
P (mmHg)
175
165
155
145
0
0,5
1
Patient 6
P (mmHg)
160
140
120
100
0
0,5
1

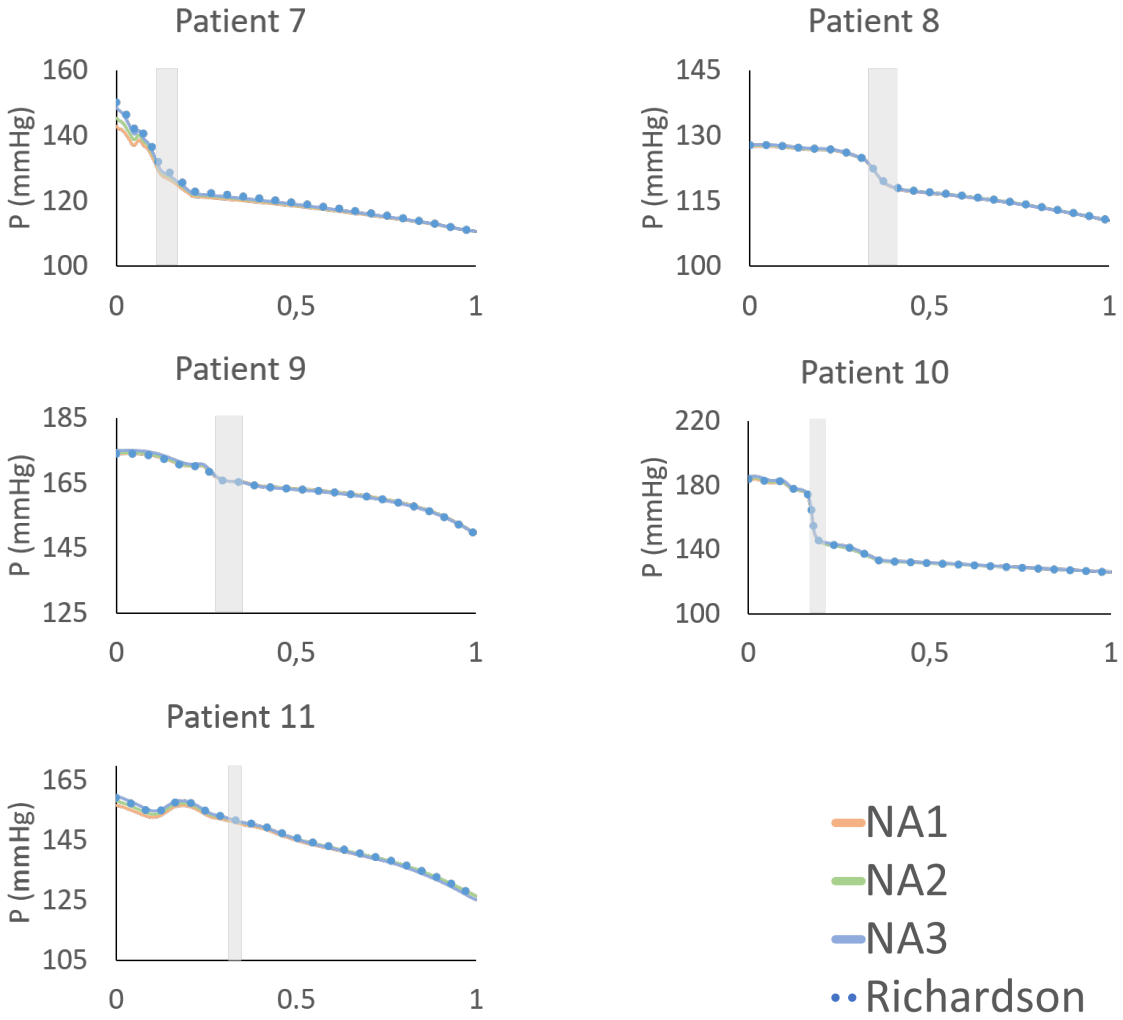

Figure 5.6: Centerline pressure graphs reported for all the patients in the cohort. The coarctation region has been highlighted for all the patients except for patient 3 since it represents a hypoplastic aorta.

5.3.4 Discussion

As explained in the previous section, the topological assumption behind the formulation of the polyhedrical elements gives a reasonable explanation about why the maximum number of elements reported in Table 5.3 used to discretize all the patient specific geometries are far less then those reported in the literature (see Table 5.1). As no mesh size parameters were provided in these works, a direct comparison of spatial resolution is more difficult. All the meshes reported here have been generated using a script file that takes as input the smoothed STL geometries and returns the meshed grid volume, reducing sensitivity to operator-dependent mesh definition and making the process well suited to integration within an automated software workflow such as EndoSize. The results showed that for all patient geometries the medium size mesh (NA2) provided a good compromise between accuracy of the pressure profile along the centerline and computational time required by the simulation. As a result the NA2 mesh density was used for all analyses reported in Chapter 6 to set up 3D transient simulations.

5.4 Summary

In this chapter different segmentation strategies has been presented. All these solutions has been adopted in order to provide 3D geometries that will be used in the numerical analysis adopted in the following chapter (chapter 6). The first strategy was developed inside Endosize and precisely studied to increase the accuracy during the exctraction of

supra-aortic vessel during the exctraction of the aortic geometry for the CFD simulations. It implies a combination of available filters that help to pre-process, enhance and extract the aortic region from a CT scan data set. Unfortunately the data that have been provided by the University Hospital of Bern for this study did not make possible to use this segmentation. Therefore an alternative strategy has been proposed to overcome this limitation. The 3D aortic geometry for the given Bern data have been presented together with a CFD mesh sensitivity steady steate analysis with the final to provide the optimal mesh density that will be used in the following chapter (chapter 6).

6

Clinical application: Aortic coarctation

This chapter details the analysis of clinical data obtained from 11 patients undergoing assessment of severity of coarctation. The cohort was heterogeneous and included patients who had already undergone coarctation repair. The clinical data collected included MR images of aortic geometry, MR phase contrast measurements of aortic flow rate in the ascending and descending aorta (proximal and distal to the coarctation site) and cuff pressure measurements from the right arm and at the foot.

All data were collected at Bern University Hospital, following a protocol approved by the

local ethics committee and the volunteers provided written informed consent (Swiss Adult Congenital Heart Disease Registry, SACHER, ClinicalTrials.gov Identifier NCT 02258724). The chapter is organized as follows: first, clinical patient-specific data collection and processing is described, from the acquistion of the subject-specific geometries and flow rate waveforms with MRI techniques to the pressure measurements acquired during the clinical assessment or follow-up examination; then, two geometrical multi-scale models are presented (0D/1D models and 3D/0D models) and the tuning process used to derive patient-specific outflow boundary conditions is introduced toghether with the strategy used to include vessel wall deformability. Data processing of model outputs is described followed by results, including comparison between predicted and measured pressure gradient across the coarctation and the descending aortic flow rate; the discussion focusses on potential future application of the workflow within the clinical setting and comparison with previously reported approaches.

6.1 In vivo data: acquisition and model generation

Contrast-enhanced magnetic resonance angiography (CE-MRA) was performed as a first assessment for clinical suspicion of aortic coarctation or as a follow-up exam after previous surgical intervention for all 11 patients. As stated before, the cohort included patients who already underwent to a surgical intervention with a patch repair or end-to-end anastomosis, with an average age of 32.89 $\pm$14.66 years old, and 55% of males, as reported in Table

6.1. Patient 3 presented with a case of hypoplastic aortic arch, where, due to an abnormal embryological development, the narrowing of the aorta is not localized but it is extended to the thoracic and abdominal segments (Langley et al., 2013). In terms of number of patients, this study is similar to other computational studies reported in the literature, whilst in terms of average age the patients in the cohort were older (see Table 1.2 in chapter 1). The heterogeneity of the classification of the cohort is similar to variability reported in other studies (Itu et al., 2013; Ralovich et al., 2015; Goubergrits et al., 2015b,a; LaDisa et al., 2011; Valverde et al., 2011; LaDisa et al., 2011).

Table 6.1: Patient cohort classification: native, surgically repaired or hypoplastic descending aorta. Information about sex and age are reported for each case (average age: 32.89 $\pm$14.66 years old, 55 % of males)

	Sex	**Age**	**Type**
Patient 1	Male	28	native
Patient 2	Female	59	native
Patient 3	Female	20	hypoplastic descending aorta
Patient 4	Male	21	surgically repaired (end-to-end anastomosis)
Patient 5	Male	58	surgically repaired (patch repair)
Patient 6	Female	34	surgically repaired (end-to-end anastomosis)
Patient 7	Male	36	native
Patient 8	Female	41	surgically repaired (end-to-end anastomosis)
Patient 9	Female	25	native
Patient 10	Male	22	native
Patient 11	Male	18	surgically repaired (end-to-end anastomosis)

6.1.1 Aortic geometry

The 3D aortic geometry was extracted from contrast-enhanced magnetic resonance angiography (CE-MRA) images and described in the previous chapter. It is notable that the length of each supra-aortic branch varied due to loss of signal towards the borders of the volume (as shown in Figure 5.4), which may result in a reduced accuracy of the segmentation in these regions (Ralovich et al., 2015). An overview of this process for a single patient is illustrated in Figure 6.1.

For all patients the severity of the coarctation was quantified from the geometrical 3D extracted shape, using the measure reported in Goubergrits et al. (2015b), the degree of stenosis (DS)

$$\mathrm{DS} = \left(1 - \frac{\mathrm{A_{st}}}{\mathrm{A_d}}\right) \tag{6.1}$$

Where $\mathrm{A_{st}}$ is the cross-sectional area at the stenosis (the minimum reported value along the vessel's centerline) and $\mathrm{A_d}$ is the cross-sectional area of the descending aorta 150 mm downstream of the model inlet. For patient 3 the DS value was not reported as this case represents a hypoplastic descending aorta. The mean value of DS was $48 \pm 23\%$ in line with previous published works such as Goubergrits et al. (2015b) $54.8 \pm 19.21\%$, Itu et al. (2013) $48.2 \pm 7\%$, Ralovich et al. (2015) $41 \pm 9.5\%$.

Table 6.2: Degree of Stenosis reported for each of 11 patients in the cohort study. For patient 3 geometrical values were not reported as this case represents a hypoplastic descending aorta.

	Inlet diameter (mm)	**Reference diameter (mm)**	**Stenosis diameter (mm)**	**DS (%)**
Patient 1	45	21	18	10
Patient 2	29	29	23	36
Patient 4	21	23	15	59
Patient 5	29	27	14	79
Patient 6	26	23	13	68
Patient 7	23	20	16	22
Patient 8	27	18	10	69
Patient 9	32	26	16	45
Patient 10	24	14	8	72
Patient 11	24	17	15	23

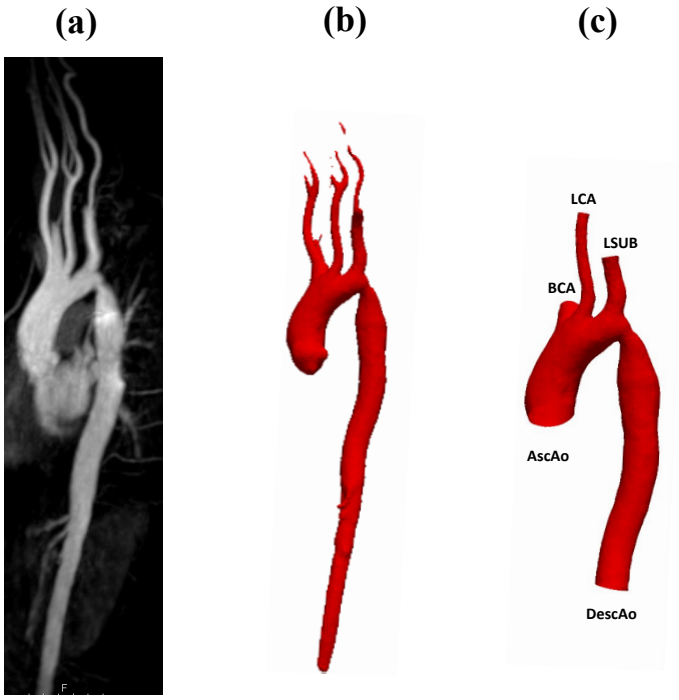

Figure 6.1: Patient-specific one dimensional and three-dimensional model construction. (a) Maximum intensity projection of the thoracic aorta from the contrast-enhanced magnetic resonance images (CE-MR). (b) 3D reconstructed geometry. (c) Post-processed 3D geometry (including surface smoothing) with truncation to obtain four outlets representing the ascending aorta and diaphragmatic aorta (truncated at the plane where MRI measurements were taken), brachiocephalic artery (BCA), left common carotid artery (LCA), left subclavian artery (LSUB).

6.1.2 Aortic flow rate

Volume flow rate waveforms were obtained at two planes perpendicular to the aortic centerline: the ascending aorta at the level of the right pulmonary artery and in the descending aorta at diaphragmatic level, using retrospectively ECG-triggered 2D phase contrast flow

velocity-MRI (echo time: 2.47 ms , repetition time: 37.12 ms , flip angle: 20 , field of view: 320-370 mm, slice thickness: 6 mm, acquisition matrix: 192 x 119, velocity encoding 150-200 cm $\cdot$ s^{-1}, temporal resolution 30 phases/cardiac cycle). The flow waveform in the ascending and descending aorta for all patients is shown in Figure 6.2.

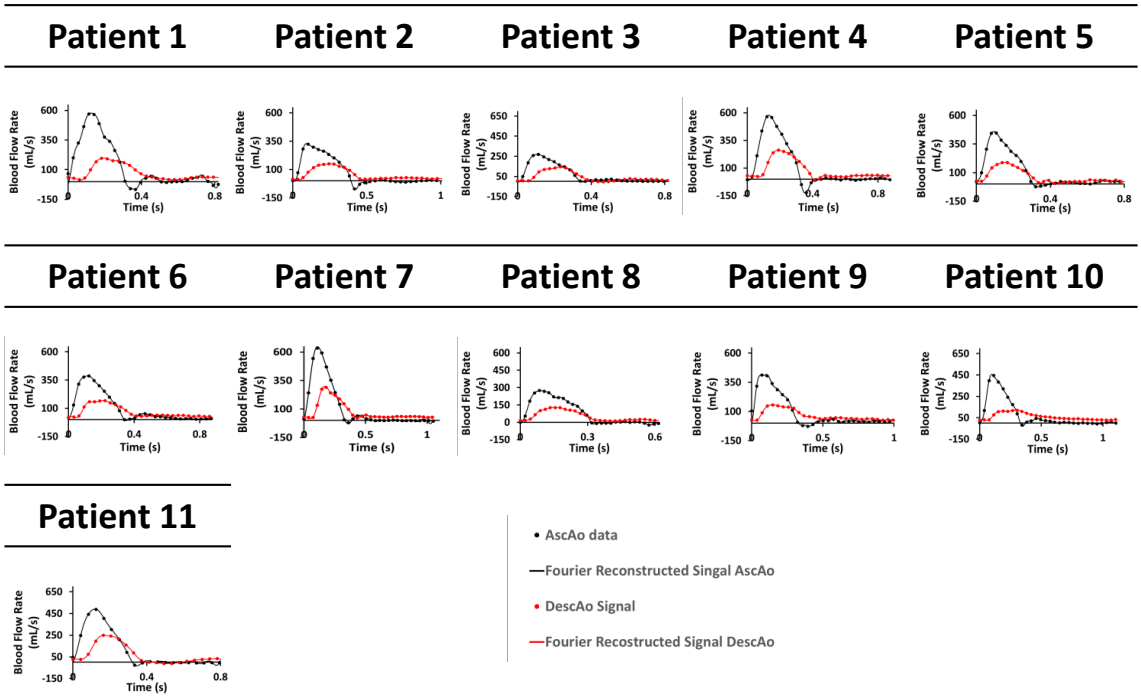

Figure 6.2: Aortic flow rates extracted from 2D-PC MRA data at the aortic root plane and diaphragmatic aortic plane, the original data had a temporal resolution of 20-30 phases per cardiac cycle, for the modelling approach the signal's temporal resolution was increased through a Fourier Series transformation.

For patient 11 the temporal resolution of the acquired 2D-PC MRA was equal to 20 phases per cardiac cycle with an equivalent signal time around 40 ms. For the remaining patients the 2D PC-MRA temporal resolution was equal to 30 phases/cardiac cycle with an

equivalent signal time between 30 and 40 ms.

6.1.3 Patient-specific pressures

In coarcted patient, intra-arterial blood pressure is monitored via the insertion of a catheter with a radial or a femoral access. The pressure measurement using catheterization is the gold standard for the pressure monitoring and it has been shown to have an accuracy of 4% or 4 mmHg if the measured pressure is below 100 mmHg (Commission et al., 2010).

In the current work, blood pressure measurements were taken by an expert cardiologist 0-35 days after the MR examination with six of the patient cohort measured on the same day. Resting blood pressure cuff measurements were taken at the right arm and at the leg as reported in Table 6.3 using an appropriately sized sphygmomanometer cuff. Right cubital blood pressure was measured using an automatic oscillometric method (Dinamap Procare 300, GE Healthcare) after resting for more than 5 minutes. Systolic blood pressure in one of the legs (dorsalis pedis artery or posteria tibial artery) was measured by an appropriately sized cuff placed around the lower calf and using a Doppler probe (Huntleigh dopplex D900, Huntleigh Healthcare Ltd, Cardiff, UK).

Mostly, blood pressure measurements were performed either simultaneously at the arm and the leg, or within 3 minutes of each other. Blood pressure difference was calculated between the proximal (arm) and distal (leg) systolic blood pressure. All non-invasive blood pressure data were obtained during routine clinical follow-up visit in a centre for congenital heart disease. For patient 8 the systolic pressure at the leg was not available.

Table 6.3: Cuff pressure measurements for the 11 reported patients, systolic blood pressure, SBP, and diastolic blood pressure, DBP (NA = not available).

	SBP right arm	**DBP right arm**	**SBP leg**
Patient 1	152	85	130
Patient 2	125	75	95
Patient 3	131	60	100
Patient 4	134	66	120
Patient 5	147	95	120
Patient 6	150	83	115
Patient 7	138	69	110
Patient 8	167	75	NA
Patient 9	130	100	95
Patient 10	125	60	95
Patient 11	144	48	130

Diagnostic catheterization to assess invasive aortic pressure gradients was performed in order to evaluate the need for intervention. Invasive blood pressure curves in the ascending and descending aorta were obtained either simultaneously with the insertion of two catheters (5 French, Cordis, Cardinal Health, US) using a radial and femoral arterial access or by pull-back technique using one catheter. All measurements were collected over 5 cardiac cycles and the peak-to-peak pressure gradient was calculated by the integrated pressure monitoring system (Siemens Healthcare, Erlangen, Germany). The computational models were not informed by catheter-based pressure measurements and the peak-to-peak measurement was

used only for validation to compare with the simulation results.

6.2 Numerical formulations

Two multi-scale models were informed by the available clinical dataset. The first model was a 1D/0D nonlinear numerical model, presented in Chapter 3, section 3.2 and the second a 3D/0D numerical model. In this section the formulation of these two models is provided, together with a description of the required physical and geometrical input parameters and the simulated quantities that are relevant for this study.

6.2.1 One dimensional formulation

In the 1D/0D modelling framework, the aortic geometry was divided into a series of interconnected segments. For each segment a system of one dimensional nonlinear hyperbolic equations was defined, derived from the continuity and Navier-Stokes equations for incompressible flow within a deformable elastic vessel, as previously shown in Chapter 3, section 3.2.

The frictional losses were computed by assuming a flat velocity profile based the corresponding Womerlsey numbers derived at the inlet of the aorta (see table 6.4). The Womersley numbers were calculated based on the extracted ascending aortic cross sections and

peak flow rate values derived from the 2D PC-MRI examinations, as

$$\alpha = \sqrt{\frac{\omega R^2}{\nu}} \tag{6.2}$$

where ν is the kinematic viscosity ($\nu = \frac{\mu}{\rho}$) measured in $\frac{m^2}{s}$, ω is the angular velocity derived as $2\pi f$ where f is the frequency. The resulting average value was 17 ± 5.01, which justify the

Table 6.4: Table reporting the Womersley numbers derived at the inlet for each patient in the cohort. The average value was 17 ± 5.01

	Womersley number
Patient 1	30
Patient 2	17
Patient 3	11
Patient 4	14
Patient 5	19
Patient 6	17
Patient 7	14
Patient 8	21
Patient 9	19
Patient 10	14
Patient 11	16

assumption of a plug profile (O'Rourke et al., 2011) which corresponds to a one dimensional polynomial velocity profile of 9 ($\zeta = 9$) with

$$f = -2 \cdot (\zeta + 2) \cdot \mu \cdot \pi \cdot u(x, t) \tag{6.3}$$

where μ is the blood viscosity. This assumption provides best fitting when compared to experimental results in a human arterial tree (Matthys et al., 2007). Following this assumption the momentum correction factor α (or Coriolis coefficient) was set constant in time and space and equal to 1 (Stergiopulos et al., 1992).

The system of one dimensional nonlinear equations was solved using a finite-volume numerical scheme formulation provided in 3, section 3.2. For all the simulations blood density and viscosity were assumed constant ($\mu = 4.5$ mPa $\cdot$ s (Itu et al., 2013) and $\rho = 1060$ kg $\cdot$ m^{-3}).

The stability of the scheme was guaranteed by the computation of the time step for each iteration in all vessels depending on their maximum local wave speed c_{max} and the element length Δx as

$$\Delta t = C_{cfl} \frac{\Delta x}{c_{max}} \tag{6.4}$$

where the Courant number was set to $C_{cfl} = 0.9$ and Δt was set to the smallest computed value over all elements.

Three dimensional formulation

The Navier-Stokes (NS) and continuity equations were solved in 3D over time using a transient analysis with the finite volume CFD-based solver ANSYS-FLUENT 17.2 (ANSYS Inc., PA, USA). Local aortic distensibility was included using a compressible fluid strategy as in (Brown et al., 2012). Blood density changes were related to pressure changes via an ideal gas with the fluid wave speed, c, as input. The inflow boundary condition was provided by imposing the time-varying mass flowrate waveform at the inlet (assuming a flat

velocity profile and an initial density of 1060 $kg \cdot m^{-3}$). Blood viscosity was set equal to $\mu = 4.5\ mPa \cdot s$ using a Newtonian model. The simulation was run with a laminar flow model, the cases were peak Reynolds numbers at the coarctation site exceeded the limit imposed by the classical turbulence analysis (3500) were recomputed using an SST turbulence model. The solution was performed using a double precision solver with a second order discretization coupled scheme for pressure-velocity coupling and a time step of 10^{-4}s to ensure convergence over the entire cardiac cycle. Simulations were run for three to five cardiac cycles until the flow rate and pressure fields yielded consistent solutions over successive cycles (change in peak pressure and flow rate less than 1 %).

Three dimensional and one dimensional meshes

For the three dimensional model, the mesh was generated with FLUENT automatic mesh library starting from the STL file using polyhedrycal elements with 5 prism lay- ers at the wall using the approach described in Chapter 5 with mesh density chosen based on the sensitivity analysis previously reported.

For the 1D model formulation the vessel centerlines were extracted from the STL files using vmtk libraries and tools (Antiga et al., 2008). Four centerlines were extracted: through the aorta itself and the three supra-aortic vessels: the brachio-cephalic artery (BCA), the left common carotid artery (LCA) and the left-subclavian artery (LSUB). Along these vessel centerlines the perpendicular vessel cross-section was computed every 5 mm (see Figure 6.1 (e)), defining the vessel segments for the 1D formulation. For each vessel segment the finite volume mesh was defined with an element length of 1 mm. The 1D/0D model

was initialized with the cross-sectional area extracted from the CE-MRA geometry as the luminal area A_d at diastolic pressure P_d, and the initial area A_0 found using the pressure-area relationship (or tube-law) in 3.1. The wall thickness (h_0) was defined as function of lumen radius (R_0) Avolio (1980) , as follows

$$\frac{h_0}{R_0} = ae^{bR_0} + ce^{dR_0}, \tag{6.5}$$

Where a, b,c and d are constants. Other authors have adopted a value of 10 % of the measured diastolic luminal radius r_d Alastruey et al. (2016), while LaDisa et al. (2011); Coogan et al. (2011) set a wall thickness of 0.15 cm for their models. The Young's modulus was defined to reproduce the measured pulse wave velocity (c) derived as described in section 6.2.2, through the equations

$$c = \sqrt{\frac{\beta}{2\rho\sqrt{A_0}}} A_d{}^{\frac{1}{4}}, \tag{6.6}$$

and

$$\beta = \sqrt{\frac{\pi}{A_0}} \frac{Eh_0}{1-\nu^2} \tag{6.7}$$

Assuming a constant pulse wave velocity within the aortic geometry.

6.2.2 Mechanical properties

As shown in the introductory chapter of this thesis different assumptions have been made on the elastic properties for the aortic wall in CFD models representing coarcted aortas. Mostly

the aortic wall was assumed rigid (Valverde et al., 2011; Menon et al., 2012; Goubergrits et al., 2015a,b; Wendell et al., 2013; Brüning et al., 2018; Pant et al., 2014; Zhu et al., 2018; Cosentino et al., 2015), deformable with a constant Young's Modulus (LaDisa et al., 2011; Coogan et al., 2011; Kwon et al., 2014) or deformable with a constant pulse wave-speed or pulse wave velocity (PWV or c) derived from the velocity-encoded cardiovascular magnetic resonance as in (Itu et al., 2013; Ralovich et al., 2015).

The aortic wall distensibility or arterial stiffness is a parameters that has been increasingly used in clinical practice for the evaluation of altered mechanical properties of arteries in many cardiovascular diseases, including aortic coarctation (Cavalcante et al., 2011; Juffermans et al., 2019). CMR images and Doppler ultrasound offer the opportunity to derive this parameter non-invasively [1]. CMR is generally preferred over Doppler ultrasound, as CMR provides visualization of the entire vessel whereas ultrasound reproducibility and accuracy is dependent on the acoustic window, vessel depth or curvature, transducer placement and operator expertise (Bolster Jr et al., 1998; Lehmann et al., 1993; Wright et al., 1990).

The aortic stiffness can be assessed via the calculation of the pulse wave velocity (PWV), the velocity at which the flow or pressure waves propagates along the vessel. PWV can be derived from measured changes in cross-sectional area and/or flow rate waveforms instead of using a direct pressure measurement, a method that has been already validated in vivo and in phantoms (Macgowan et al., 2002; Grotenhuis et al., 2009). The assessment of PWV has been performed using different methods such as the transit-time (TT) or foot-to-foot method (Mohiaddin et al., 1993), flow-area (QA) method (Vulliémoz et al., 2002) and the cross-correlation (XC) method (Fielden et al., 2008). In the TT method, the PWV

[1] The invasive estimation implies the use of pressure catheters (Kilic et al., 2013)

is assessed from the flow rate curves computed at two distant cross-sections along the aortic vessel, and corresponds to the ratio between the distance of the two locations along the vessel centerline, Δx measured in meters, and the time interval in seconds between the two onset (foot) of the flow rate curves, Δt, as

$$\mathrm{PWV} = \frac{\Delta x}{\Delta t} \tag{6.8}$$

The QA method asses the local PWV as the ratio between the changes in blood flow and the vessel cross-sectional area at upslope of the flow rate curve (early systole) as

$$\mathrm{PWV} = \frac{\Delta Q}{\Delta A} \tag{6.9}$$

The XC method derive the PWV value from a first-order linear interpolation of the phase shift between different flowrate curves selected along the vessel centerline and the distance along the vessel centerline.

Ibrahim et al. (2010) investigated the reproducibility and repeatability of these techniques, focusing on the inter-observer, intra-observer, and inter-scan variabilities in six normal volunteers and fifty cardiovascular patients. The TT method resulted as the most reproducible and repeatable measurement and required less processing time followed by the XC method, which required a data set with a high temporal resolution, and the QA method, which, on the contrary, required a data set with a high spatial resolution. The QA method is highly operator dependent, since it requires the definition of the aortic cross section for the first frames of the registered images (approximatively from ten to fifteen frames) and provides just a local measure of the PWV, whilst XC and TT methods provide an estimate of the

PWV along the vessel centerline. For the 11 patients in this cohort velocity-encoded MR images were available at two different planes, at the aortic arch at the pulmonary artery level and at the descending aorta at the diaphragmatic level, thus limiting the applicability of the XC and QA methods for the calculation of the aortic PWV.

In both the 3D and 1D models, the mechanical properties for the arterial wall were derived from the estimation of the pulse wave velocity, c. The value of c was assumed to be uniform over the aortic geometry and was derived from the 2D PC-MRI data using the transit-time method (or foot-to-foot method). The PWV value was determined from the calculation of the foot of the flow rate curves at the ascending and descending aorta. For each flow waveform, the foot is derived from the intersection between the gradient during initial flow increase, defined by a line connecting points at 20% and 80% of the maximum flow rate, and the minimum flow rate (also referred as baseline).

The values of pulse wave velocity obtained are reported in Table 6.5. For patients 1,4,6 and 7 the resulting pulse wave velocity generated instability in the solution of the 1D model, as a result the pulse wave velocity was increased to ensure convergence of the model over the entire cardiac cycle (see Table 6.5).

Table 6.5: Foot-to-foot method parameters and resulting pulse wave velocity (PWV) derived for the 11 patients and the PWV used in the simulations.

	Δx **(m)**	Δt **(s)**	**PWV derived** $(m \cdot s^{-1})$	**PWV simulation** $(m \cdot s^{-1})$
Patient 1	0.359	0.0845	4.68	7
Patient 2	0.290	0.0263	11	11
Patient 3	0.231	0.0475	4.87	4.87
Patient 4	0.250	0.0538	4.64	6
Patient 5	0.296	0.0254	11.65	11.65
Patient 6	0.250	0.0501	4.99	6.5
Patient 7	0.280	0.0689	4.06	5.0
Patient 8	0.19	0.0218	8.70	8.70
Patient 9	0.3	0.0351	8.55	8.55
Patient 10	0.238	0.0218	10.9	10.9
Patient 11	0.250	0.0445	5.61	5.61

6.2.3 Boundary conditions

The same inflow and outflow boundary conditions were imposed for the 1D and 3D solutions (see Figure 6.3 (b) and Figure 6.3(c)). At the inlet, the aortic flow waveform $Q_{asc}(t)$ measured by phase-contrast MRI was applied using a Fourier Series reconstruction to increase the time resolution. At each of the four outlets, a three-element Windkessel model, representing the downstream vasculature, was coupled as reported in Brown et al. (2012); Alastruey et al. (2012a). These 0D models consist of a proximal resistance R_1, in series with a parallel combination of a distal resistance, R_2 and a compliance, C. These parameters were found using an iterative scheme proposed in Xiao et al. (2014) (see Figure 6.3 (a)).

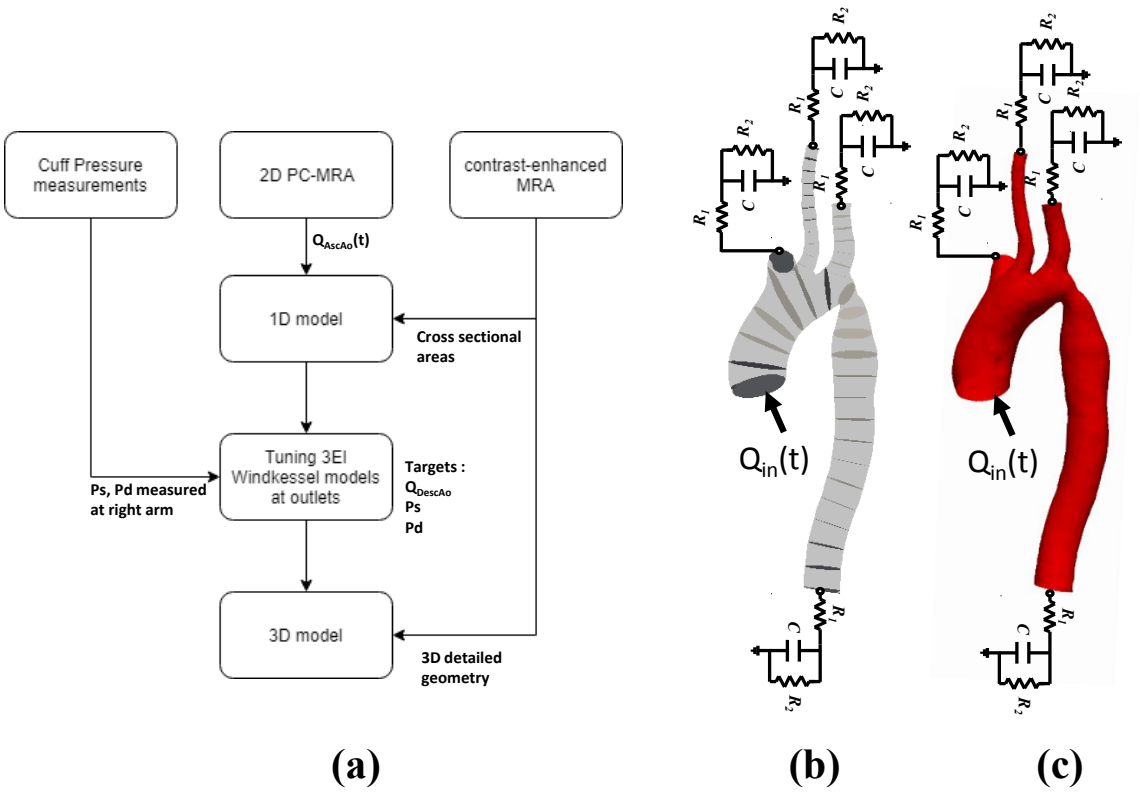

Figure 6.3: Schematic representing the multi-scale model domain and tuning process used to find the boundary conditions (BCs). (a) Flow chart representing the procedure used to find the WK parameters of the outflow BCs. (b) Schematic of the one-dimensional modelling approach: time-varying flow rate derived from 2D-PC MRA (Qin(t)) is directly applied at the inlet of the model and three-element Windkessel models are coupled at the outlets. The tuning process using the 1D model computes outflow Windkessel parameters for BCs based on mechanical properties derived from patient-specific available data. These parameters are then directly applied to the three-dimensional model imposing the same time-varying flow rate (Qin(t)) at the inlet and the same mechanical properties used for the one-dimensional model.

The scheme starts from estimating the total peripheral compliance, C_T, and the total peripheral resistance, R_T, representing the equivalent resistance and compliance of the whole

1D/0D system. Following the process described in 6.2.3 and 6.2.3 below, the values for the Windkessel parameters were derived for all the outlets (ie, BCA, LCA, LSUB and DescAo) of the 1D/0D domain.

To tune the 1D/0D model the coupled system was solved with iterative adjustment of C_T and R_T to match the pressure at the aortic inlet to the measured systolic and diastolic cuff pressures, P_s and P_d respectively, assuming that the pressure measured at the right arm is equal to the pressure at the ascending aortic root (see Figure 6.3 (a)).

Calculating the peripheral resistances of the outflow 0D models

The total resistance, R_T, at the outlet of the 1D/0D network was defined as

$$R_T = \frac{P_m}{\bar{Q}_{in}}, \; P_m = P_d + \frac{1}{3}(P_s - P_d) \tag{6.10}$$

where P_m is the mean aortic pressure, P_s and P_d are the systolic and diastolic cuff pressures, respectively, while $\bar{Q}_{in}$ is the mean aortic flow rate measured at the ascending aorta from 2D PC-MRI data. The total resistance is then distributed over the outlets of the model as follows

$$R^j_{tot} = R^j_1 + R^j_2 = R_T \frac{\bar{Q}_{in}}{\bar{Q}^j_{out}} \tag{6.11}$$

where $j = 1, 2, 3, 4$ refers to the four outlet interfaces of the 1D/0D multiscale model

(BCA, LCA, LSUB and DescAo), while $\bar{Q}^{j}_{out}$ is the mean aortic flow rate at the outlet j. The values for $\bar{Q}^{j}_{out}$ were assumed to be proportional to the square of the radius Zamir et al. (1992) of each the supra-aortic vessels as follows

$$\bar{Q}^{j}_{out} = \bar{Q}_i \cdot \frac{r_i^2}{\sum_{i=1}^{i=3} r_i^2} \tag{6.12}$$

where r_i is the radius of the supra-aortic branch $i = 1, 2, 3$ (ie, BCA, LCA and LSUB) and $\bar{Q}_i$ is the total mean flow rate for the supra-aortic branches, obtained from the difference between the mean aortic flow of the inlet and the mean aortic flow of the descending aorta, derived from the time average of the 2D PC-MRI flow waveform measurement taken at the diaphragmatic aortic plane.

The relationship adopted in 6.12 is a frequently assumed to compensate the lack of information for individual supra-aortic branches and implies that the mean velocity of the flow is approximatively the same for each vessel. The proximal resistances, R^{j}_{1} , at the four outlets (ie, BCA, LCA, LSUB and DescAo) were assumed to match the characteristic impedance of the terminal vessel j, in order to minimize artificial wave reflections, as described in Alastruey et al. (2008). For a new iteration $n + 1$, R_T is updated via a first-order Taylor expansion of (6.10) around the measured diastolic pressure P_d as follows

$$R_T^{n+1} = R_T^n + \frac{\Delta P_m^n}{\bar{Q}_{in}}, \ \Delta P_m^n = P_d - P_d^n \tag{6.13}$$

Calculating the the peripheral compliances of the outflow 0D models

The total compliance,C_T, was calculated as in Alastruey et al. (2012b), based on the approximation $C_T = \frac{dV}{dP}$

$$C_T = \frac{Q_{max} - Q_{min}}{P_s - P_d}\Delta t \tag{6.14}$$

where Q_{max} and Q_{min} are the maximum and minimum ascending aortic flow rate values, Δt is the time delay between Q_{max} and Q_{min}, and P_s and P_d are the systolic and diastolic cuff pressures measured at the right arm, respectively. Following the work of Alaustrey et al. Alastruey et al. (2012b) the total compliance, C_T, is equivalent to the sum of the compliance 0D Windkessel elements, C_p, and the compliance that given by the sum of all the 1D model segments, C_c, as

$$C_T = C_c + C_p, \tag{6.15}$$

From Equation (6.15) the total peripheral compliance of the outflow models can be derived and distributed to the outflow branches in proportion to the flow distribution as in Stergiopulos et al. (1992). For a new iteration $n+1$, C_T is updated via a first-order Taylor expansion of (6.14) around the measured diastolic pressure P_{pulse} as follows

$$C_T^{n+1} = C_T^n + \frac{Q_{max} - Q_{min}}{(P_{pulse}^n)^2}\Delta t \Delta P_{pulse}^n, \quad \Delta P_{pulse}^n = P_{pulse} - P_{pulse}^n \tag{6.16}$$

The Windkessel parameters for the outlets compliances and resistances found via the 1D/0D models are then applied to the 3D/0D counterparts. The results obtained from the 3D/0D model were compared to the measured data in terms of 2D PC-MRI measured descending

aortic waveforms and catheter derived peak-to-peak pressure gradient. All 1D simulations were solved on an Intel Xeon E5-1620, 8 cores, 16 GB RAM and took maximum 30 minutes per cardiac cycle. 3D simulations were run using a workstation with 3 processor Intel E5-620 and 12 GB of RAM and took a minimum of 12 hours to a maximum of 22 hours, typically running for three to five cardiac cycles until the flow rate and pressure fields yielded consistent solutions over successive cycles (change in peak pressure and flow rate less than 1 %).

6.2.4 Pressure gradients

Coarctation pressure gradients were reported using the 3D/0D model strategy to capture the nature of the complex haemodynamics in the region of the coarctation. A single value was used for clinical assessment, reported as the difference in peak pressure between the waveform measured in the ascending aorta and that measured in the proximal descending aorta. As the simulation provides the pressure waveform simultaneously at all locations the following values were reported for comparison with the clinical value:

- Difference in peak pressure between ascending (inlet) and descending (outlet) aorta ($\mathrm{Max}_{\mathrm{AscAo}} - \mathrm{Max}_{\mathrm{DescAo}}$);
- Maximum instantaneous pressure gradient across the full computational domain over the full cardiac cycle ($\mathrm{Max}_{\mathrm{gradient}}$);
- Pressure gradient across the full computational domain at peak systole ($\mathrm{Sys}_{\mathrm{gradient}}$);

- Pressure gradient over the coarctation region at peak systole ($CoA_{gradient}$).

6.3 Results

6.3.1 Effectiveness of the tuning process

The effectiveness of the 1D/0D tuning process is detailed for the 11 patients in Table 6.6. The errors between the 1D/0D and 3D/0D laminar solutions and the systolic (SBP) and diastolic (DBP) cuff pressure measurements are reported as a percentage.

When solving using the 1D model, the tuning process resulted in errors less than 10% for eigth to eleven patients, with larger discrepancies for cases 5,9 and 10. The highest relative errors were observed in tuning the systolic pressure, while for patient 9 significant error was observed in both systolic and diastolic values. When the solution was re-computed using the 3D approach, the error increased in most cases but remained below 10% for 6 of the 11 cases. For an example of comparison between the 1D and 3D model see Figures 6.4,6.5, 6.6, 6.7, 6.8, 6.9, 6.10, 6.11, 6.12, 6.13,6.14 where errors between 0D/1D and 0D/3D models where calculated as in 3.48.

The resulting Windkessel parameters are reported in Table 6.7.

Table 6.6: Effectiveness of the 1D/0D tuning strategy when compared with systolic and diastolic cuff pressure measurements and correspondence between the 1D/0D model and 3D/0D model in predicting ascending aortic pressures for the 11 cases. SBP refers to the systolic blood pressure, DBP refers to the diastolic blood pressure. Errors are reported in percentage (%).

	Measured		**1D/0D Tuned**		**No. iterations**	**Errors (%)**		**3D/0D Simulation**		**Errors (%)**	
	SBP	**DBP**	**SBP**	**DBP**		**SBP**	**DBP**	**SBP**	**DBP**	**SBP**	**DBP**
Patient 1	152	85	151	84	7	-1	-1	150	84	-1	-1
Patient 2	125	75	128	75	60	+2	0	130	77	+4	+3
Patient 3	131	60	131	60	3	0	0	128	60	-2	0
Patient 4	134	66	139	63	34	+4	-5	158	65	+18	+2
Patient 5	147	95	161	95	25	+10	0	166	100	+13	+5
Patient 6	150	83	150	83	4	0	0	162	78	+8	-6
Patient 7	138	69	138	69	8	0	0	142	70	+3	+1
Patient 8	167	75	167	75	5	0	0	169	79	+1	+5
Patient 9	130	100	156	81	35	+20	-19	177	86	+36	+14
Patient 10	125	60	164	61	34	+31	+2	195	69	+56	-15
Patient 11	144	48	145	48	9	-1	0	160	39	+11	-19

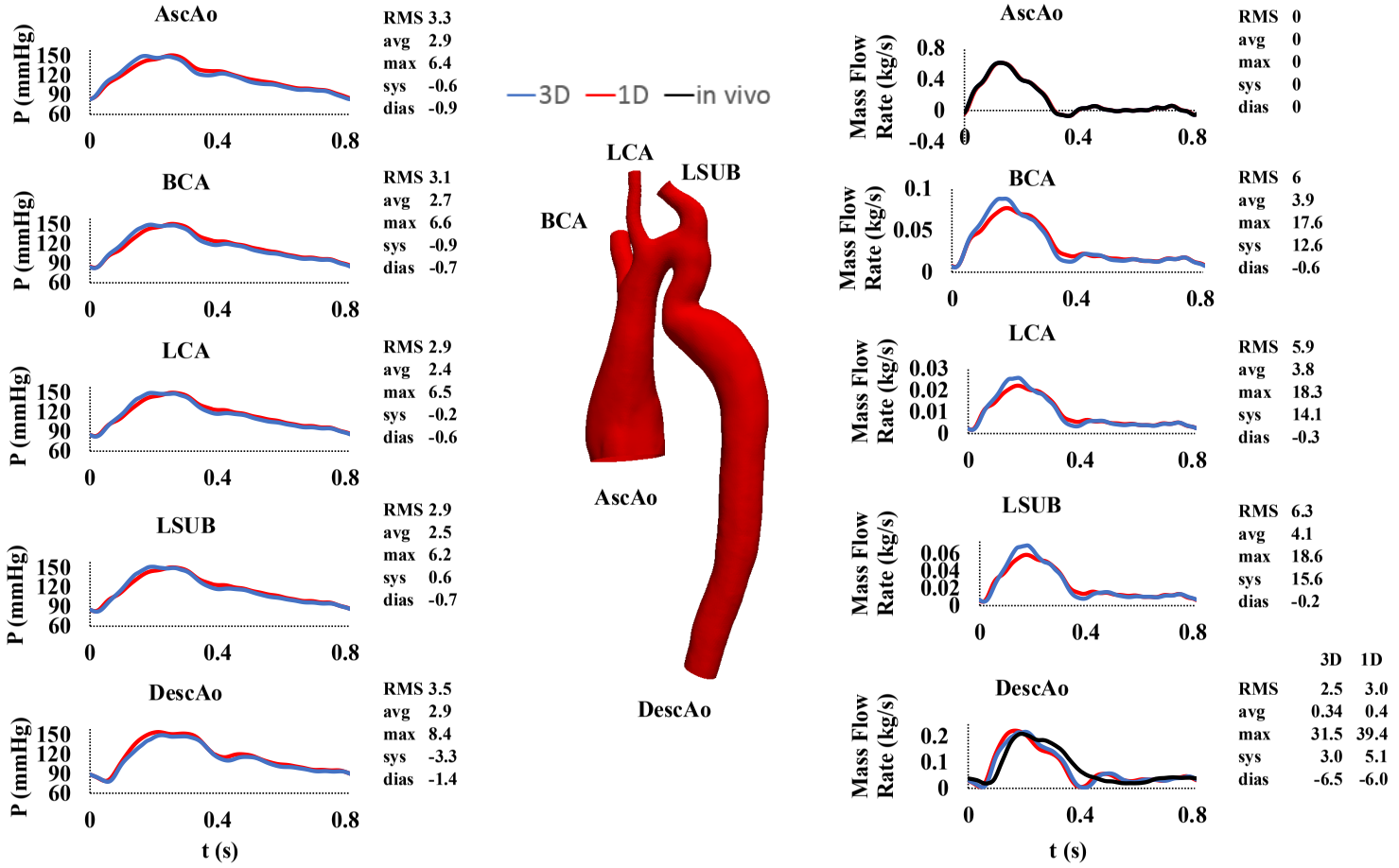

Figure 6.4: Blood flow (Mass Flow Rate) and Pressure (P) waveforms computed using the 1D (red lines) and 3D (blue lines) models in five arterial sites: ascending aorta (AscAo) Brachiocephalic artery (BCA) left common carotid artery (LCA) left subclavian artery (LSUB) and descending aorta (DescAo) and comparison with available in-vivo data for Patient 1

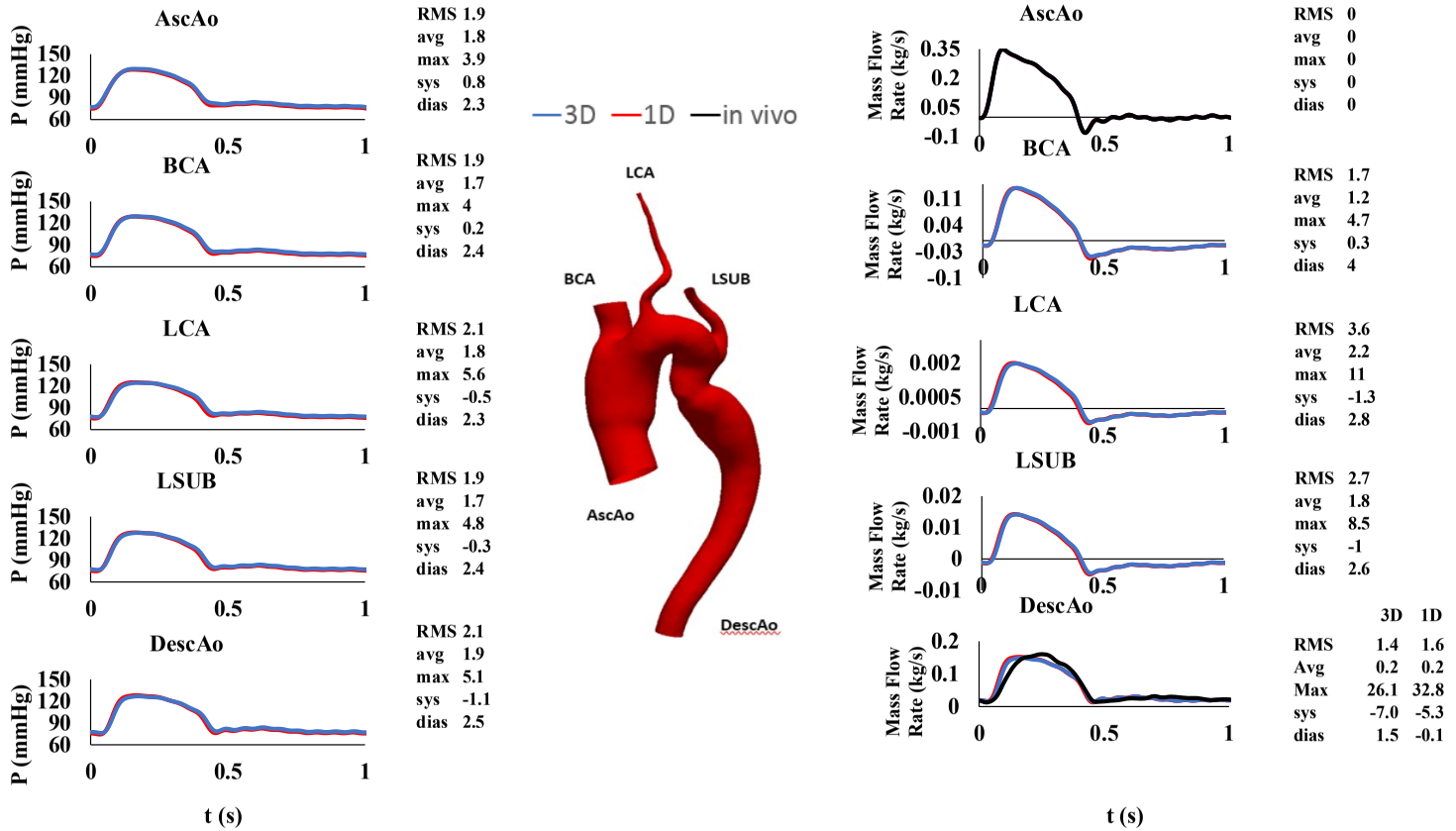

Figure 6.5: Blood flow (Mass Flow Rate) and Pressure (P) waveforms computed using the 1D (red lines) and 3D (blue lines) models in five arterial sites: (a) ascending aorta (b) Brachiocephalic artery (c) left common carotid artery (d) left subclavian artery (e) descending aorta with comparison with available in-vivo data for Patient 2

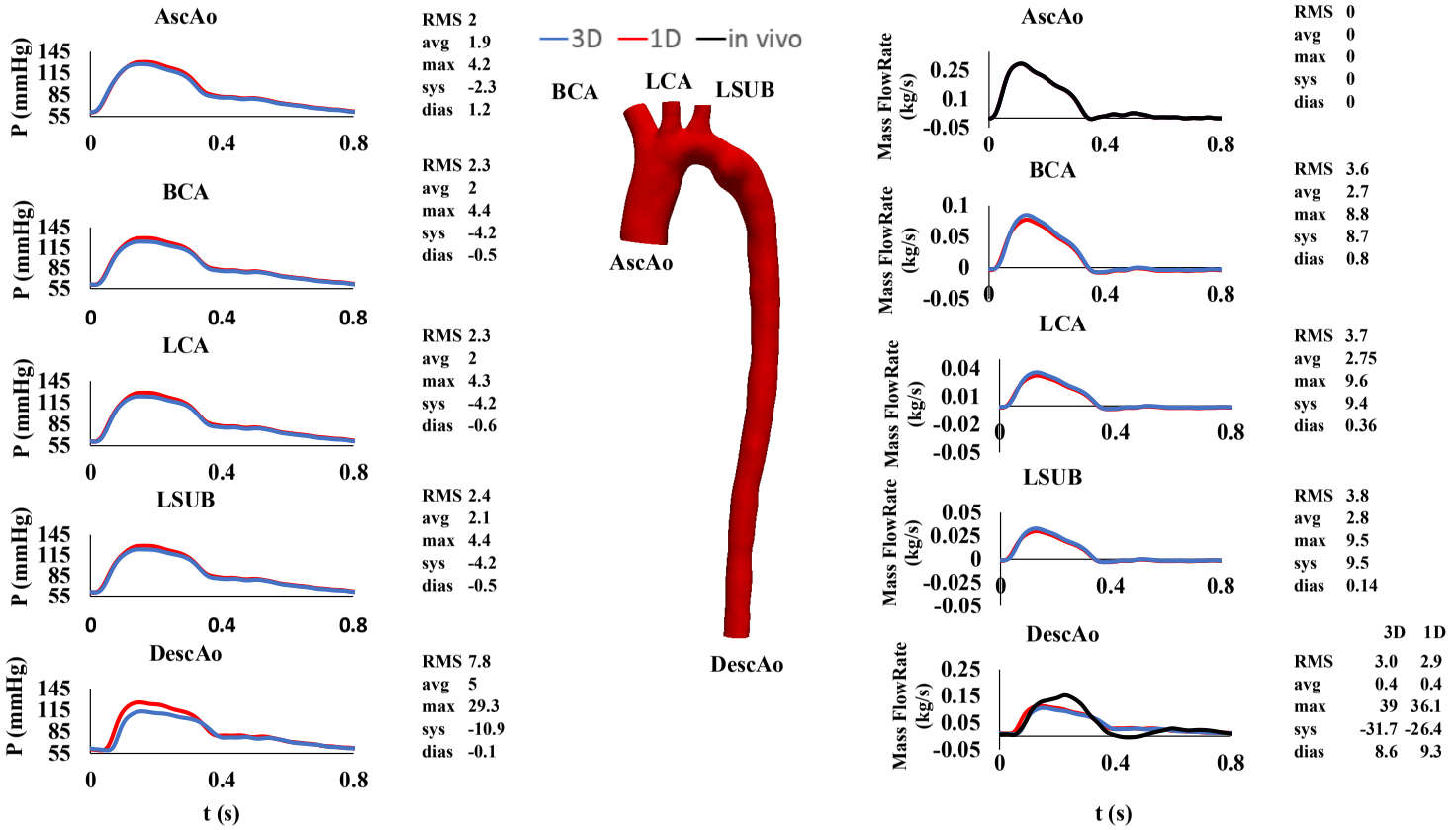

Figure 6.6: Blood flow (Mass Flow Rate) and Pressure (P) waveforms computed using the 1D (red lines) and 3D (blue lines) models in five arterial sites: ascending aorta (AscAo) Brachiocephalic artery (BCA) left common carotid artery (LCA) left subclavian artery (LSUB) and descending aorta (DescAo) and comparison with available in-vivo data for Patient 3

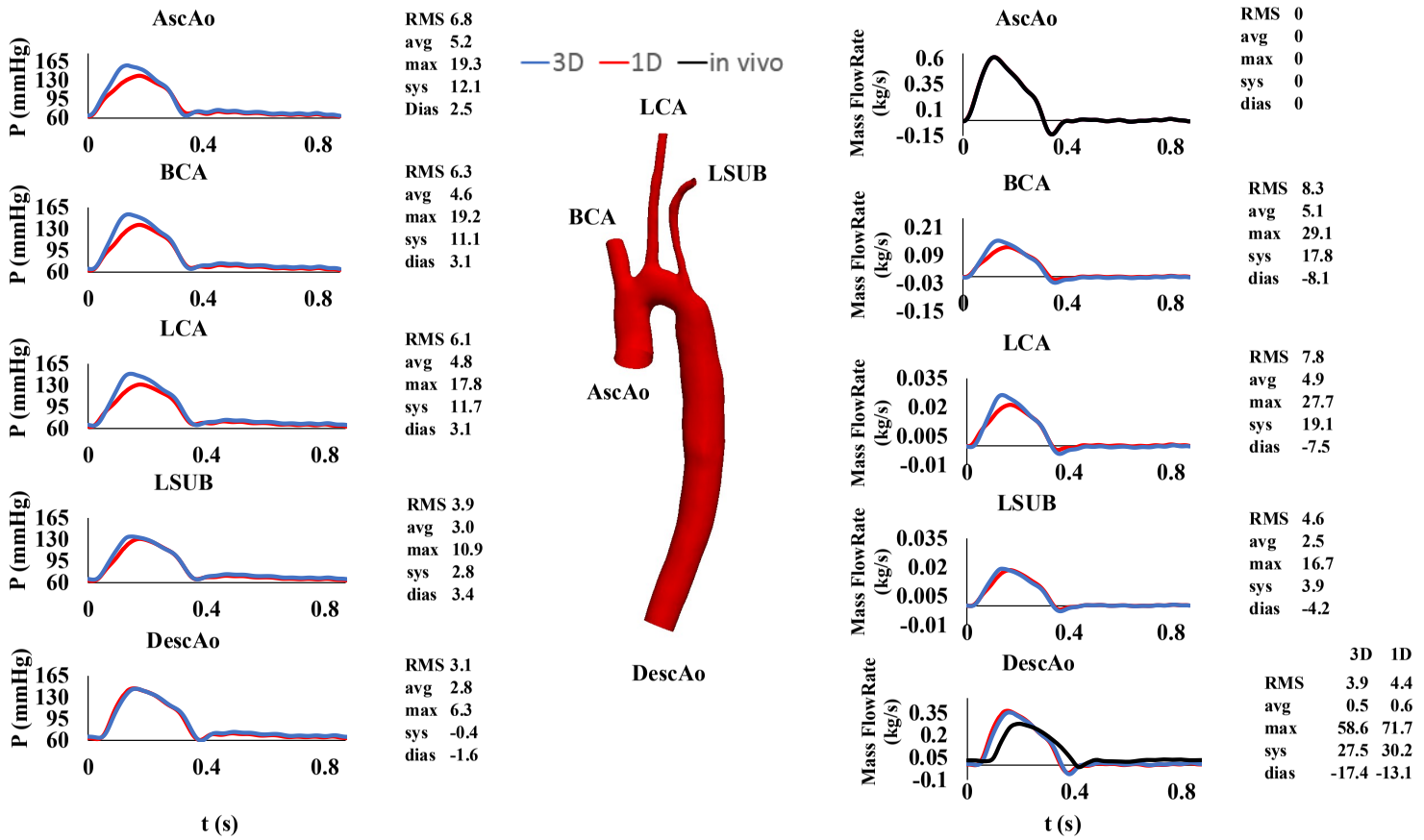

Figure 6.7: Blood flow (Mass Flow Rate) and Pressure (P) waveforms computed using the 1D (red lines) and 3D (blue lines) models in five arterial sites: ascending aorta (AscAo) Brachiocephalic artery (BCA) left common carotid artery (LCA) left subclavian artery (LSUB) and descending aorta (DescAo) and comparison with available in-vivo data for Patient 4

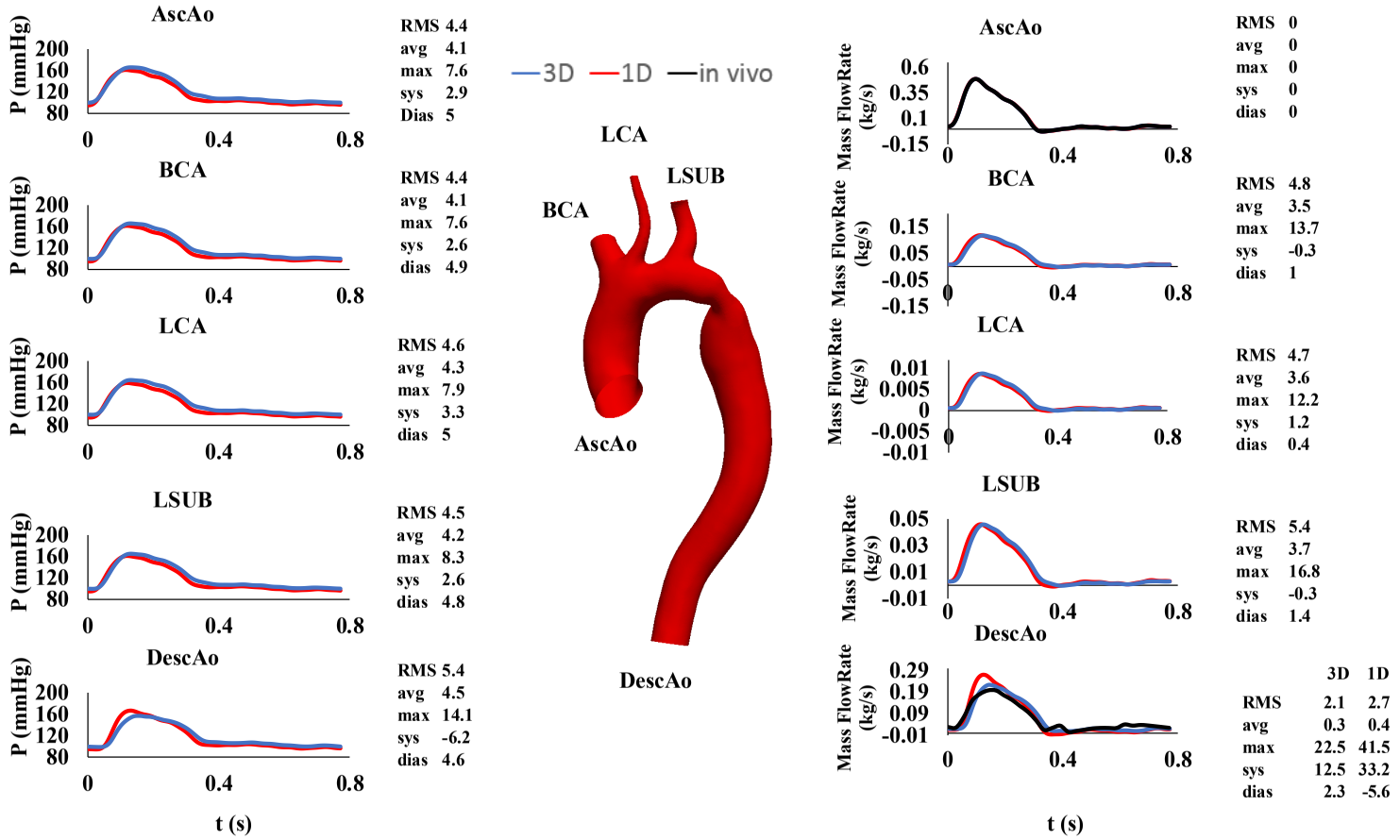

Figure 6.8: Blood flow (Mass Flow Rate) and Pressure (P) waveforms computed using the 1D (red lines) and 3D (blue lines) models in five arterial sites: ascending aorta (AscAo) Brachiocephalic artery (BCA) left common carotid artery (LCA) left subclavian artery (LSUB) and descending aorta (DescAo) and comparison with available in-vivo data for Patient 5

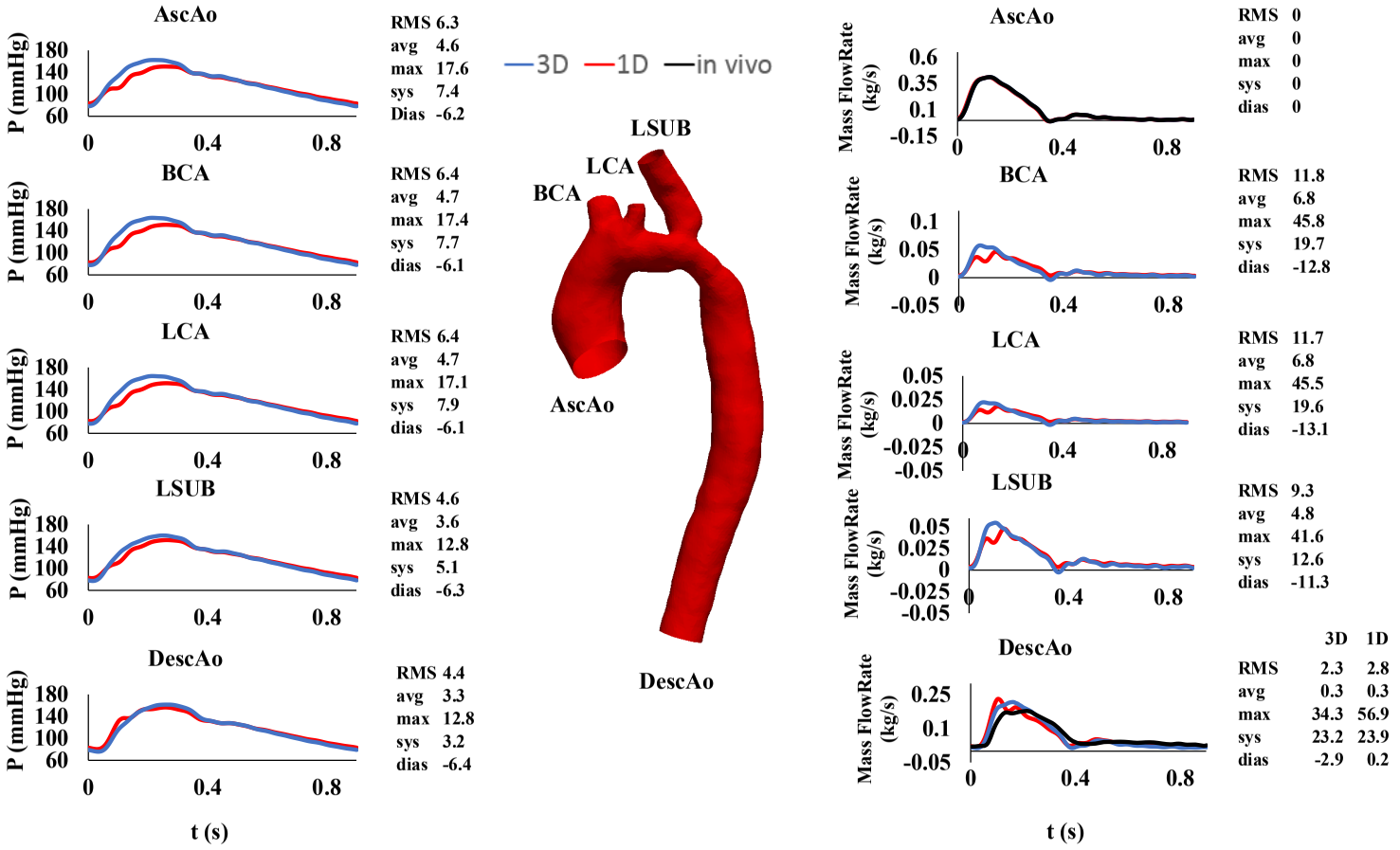

Figure 6.9: Blood flow (Mass Flow Rate) and Pressure (P) waveforms computed using the 1D (red lines) and 3D (blue lines) models in five arterial sites: ascending aorta (AscAo) Brachiocephalic artery (BCA) left common carotid artery (LCA) left subclavian artery (LSUB) and descending aorta (DescAo) and comparison with available in-vivo data for Patient 6

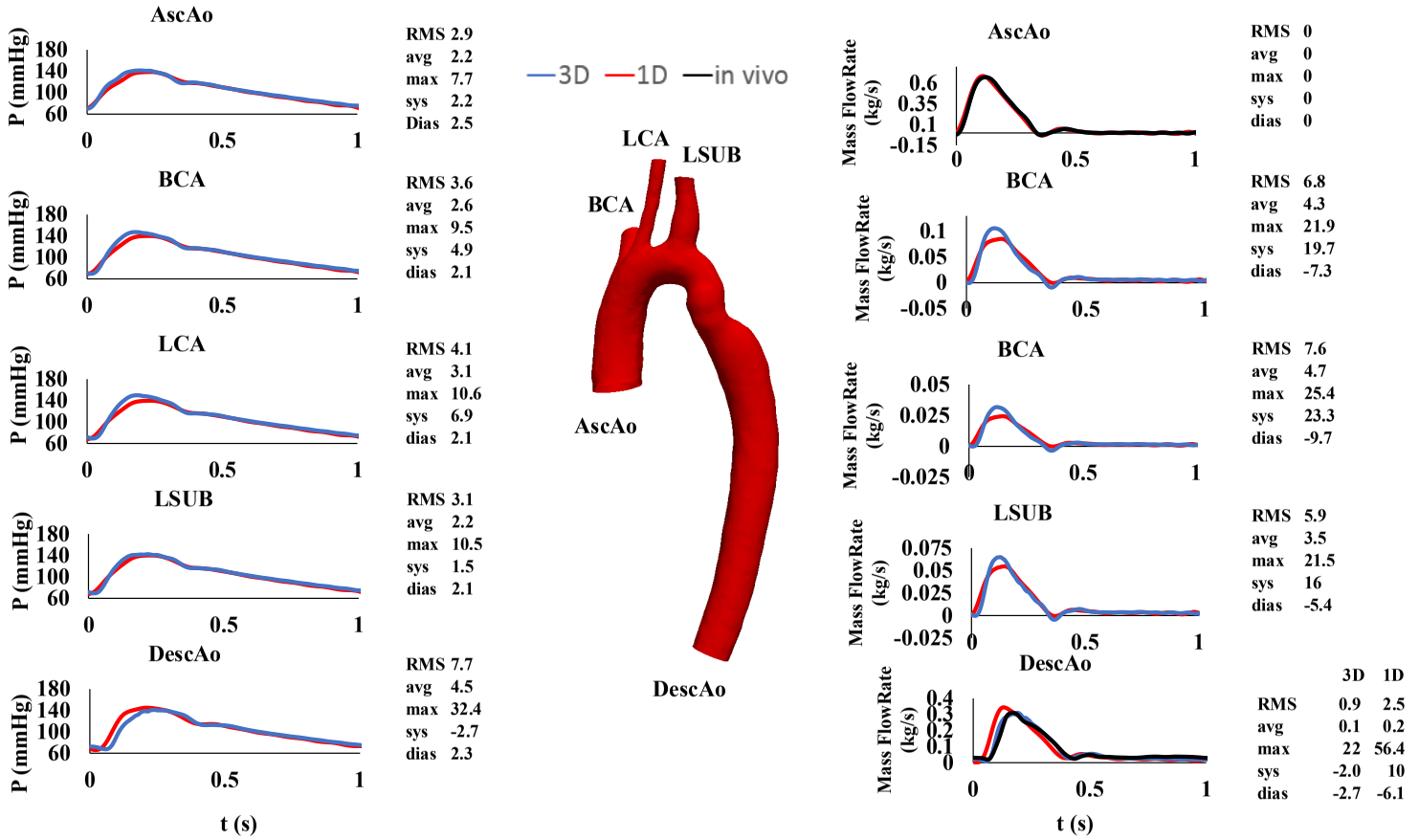

Figure 6.10: Blood flow (Mass Flow Rate) and Pressure (P) waveforms computed using the 1D (red lines) and 3D (blue lines) models in five arterial sites: (a) ascending aorta (b) Brachiocephalic artery (c) left common carotid artery (d) left subclavian artery (e) descending aorta with comparison with available in-vivo data for Patient 7

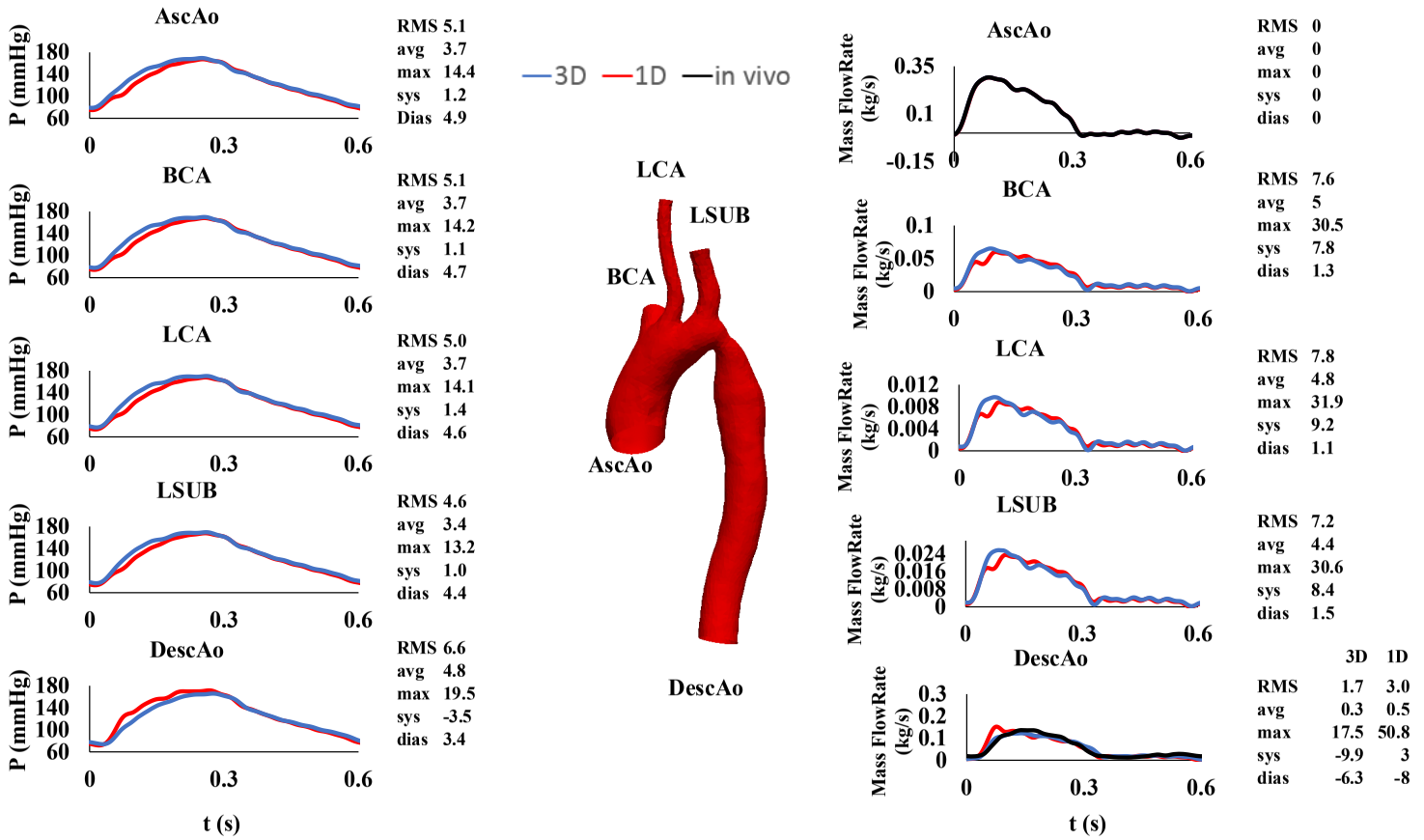

Figure 6.11: Blood flow (Mass Flow Rate) and Pressure (P) waveforms computed using the 1D (red lines) and 3D (blue lines) models in five arterial sites: ascending aorta (AscAo) Brachiocephalic artery (BCA) left common carotid artery (LCA) left subclavian artery (LSUB) and descending aorta (DescAo) and comparison with available in-vivo data for Patient 8

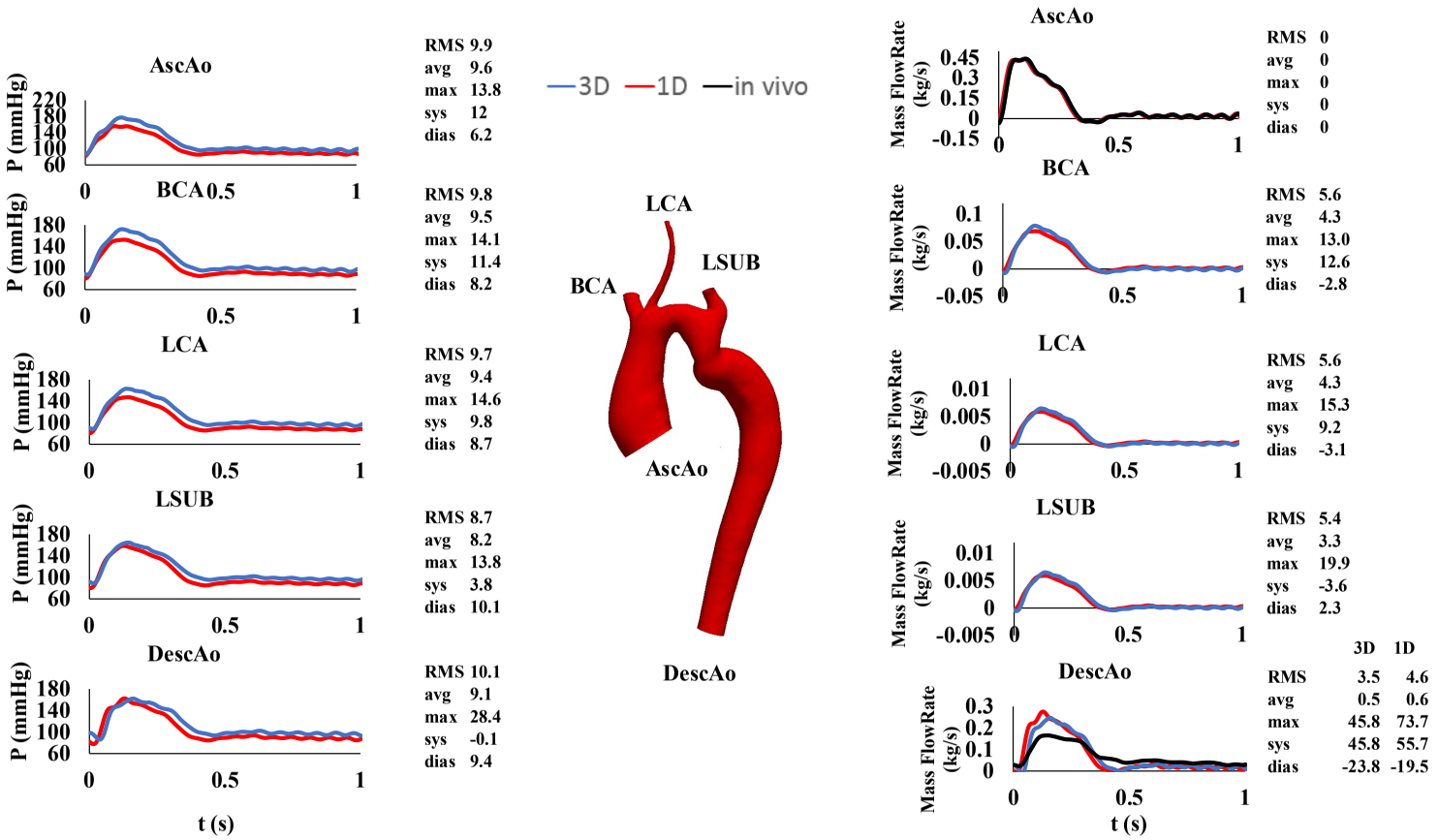

Figure 6.12: Blood flow (Mass Flow Rate) and Pressure (P) waveforms computed using the 1D (red lines) and 3D (blue lines) models in five arterial sites: ascending aorta (AscAo) Brachiocephalic artery (BCA) left common carotid artery (LCA) left subclavian artery (LSUB) and descending aorta (DescAo) and comparison with available in-vivo data for Patient 9

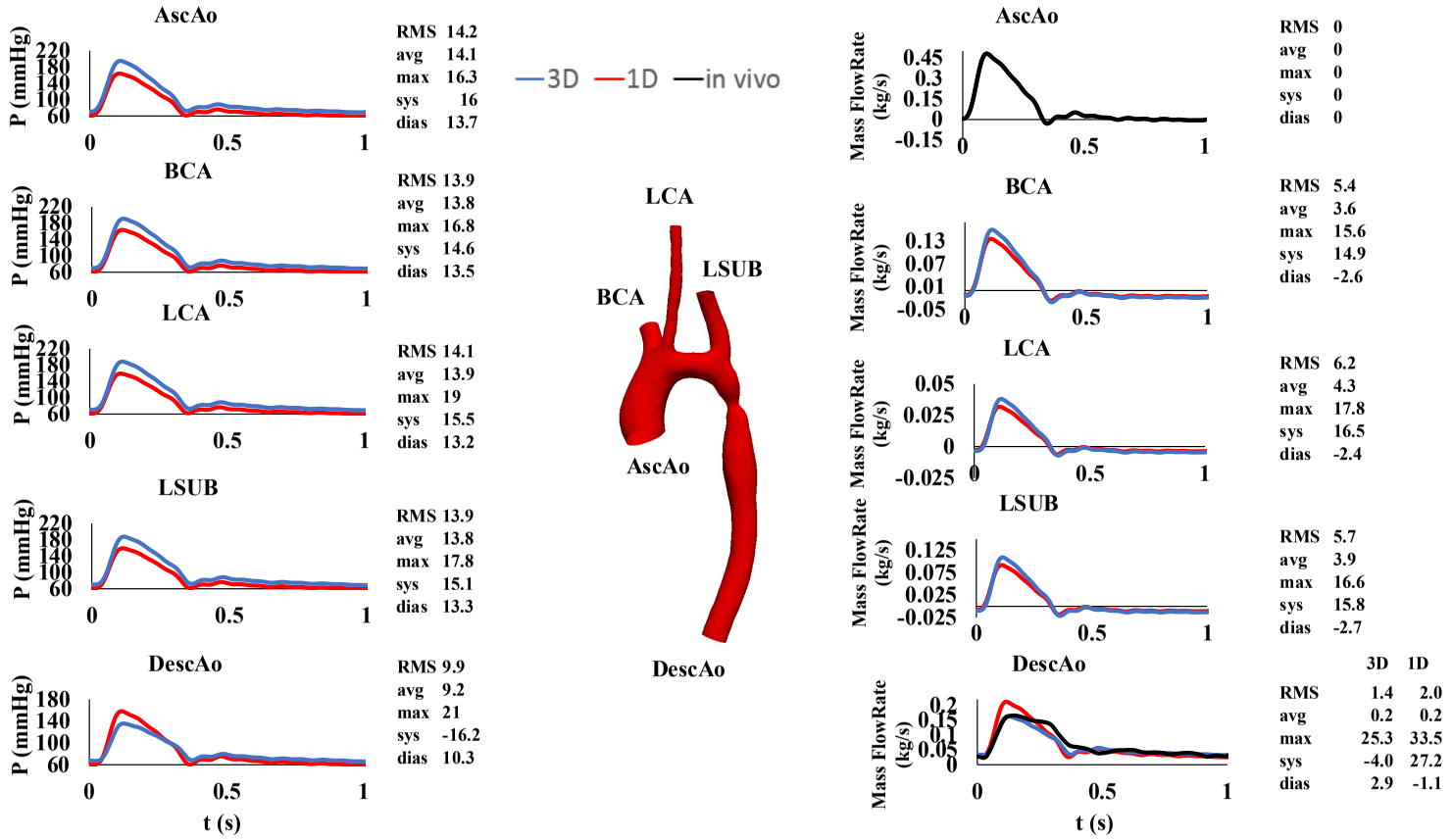

Figure 6.13: Blood flow (Mass Flow Rate) and Pressure (P) waveforms computed using the 1D (red lines) and 3D (blue lines) models in five arterial sites: ascending aorta (AscAo) Brachiocephalic artery (BCA) left common carotid artery (LCA) left subclavian artery (LSUB) and descending aorta (DescAo) and comparison with available in-vivo data for Patient 10

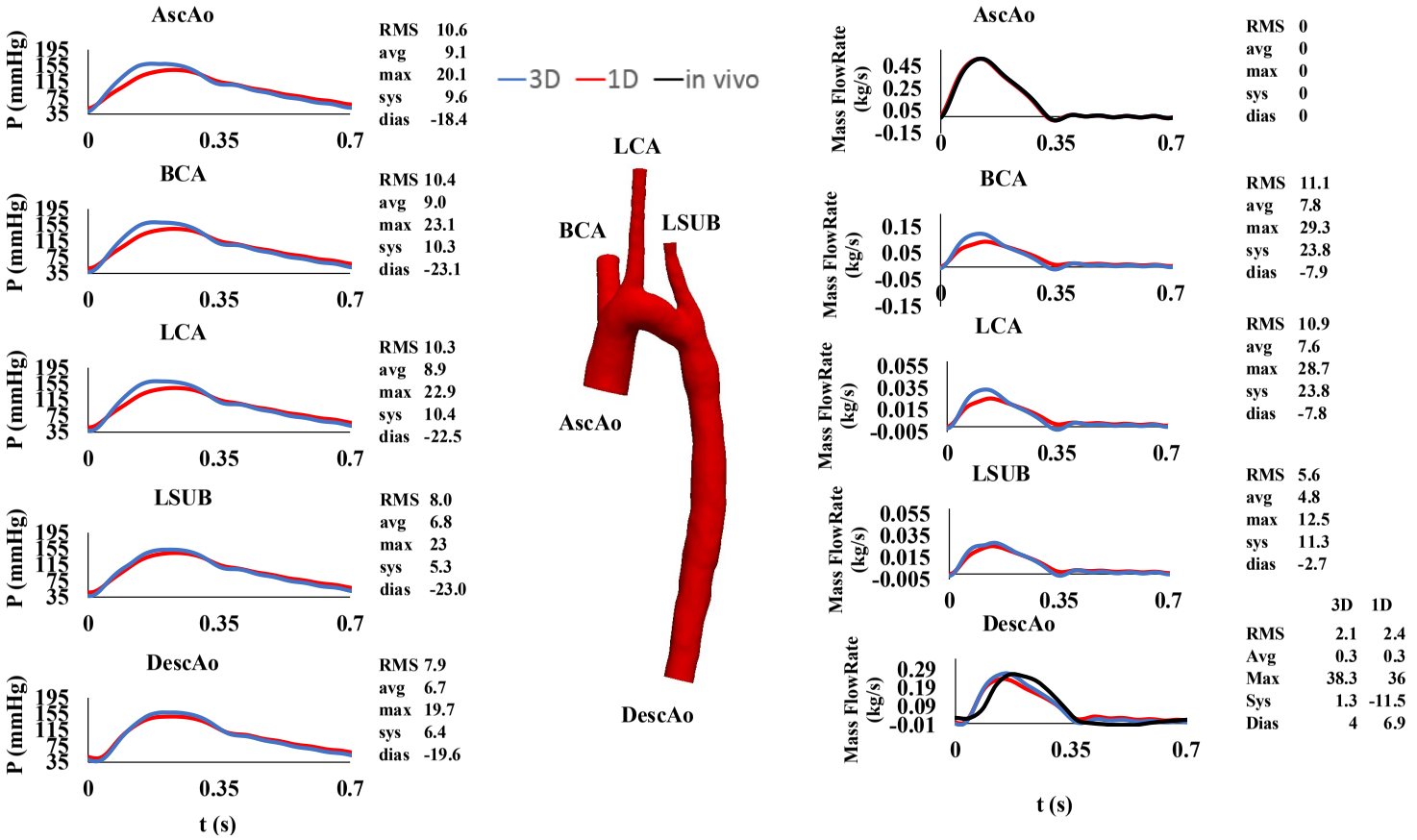

Figure 6.14: Blood flow (Mass Flow Rate) and Pressure (P) waveforms computed using the 1D (red lines) and 3D (blue lines) models in five arterial sites: ascending aorta (AscAo) Brachiocephalic artery (BCA) left common carotid artery (LCA) left subclavian artery (LSUB) and descending aorta (DescAo) and comparison with available in-vivo data for Patient 11

Table 6.7: Resulting Windkessel paramaters R_1 (expressed in $10^8 Pa \cdot s \cdot m^{-3}$) , R_2 (expressed in $10^9 Pa \cdot s \cdot m^{-3}$) and C (expressed in $10^{-10} Pa^{-1} \cdot s \cdot m^3$) obtained from the tuning strategy reported for each outlet: brachiocephalic artery (BCA) left common carotid artery (LCA) left subclavian artery (LSUB) and descending aorta (DescAo).

		BCA	**LCA**	**LSUB**	**DescAo**
	R_1	6.32	22.2	8.55	2.55
Patient 1	C	3.88	10	30.54	13.6
	R_2	3.88	13.6	5.28	1.73
	R_1	4.59	290	43.7	5.51
Patient 2	C	116	1.83	12.2	456
	R_2	6.76	428	64.4	1.72
	R_1	9.74	23.1	25	8.77
Patient 3	C	24.5	10.3	9.57	94.3
	R_2	6.96	16.5	17.8	1.81
	R_1	7.52	42.0	48.4	3.05
Patient 4	C	10.1	18	15.7	307
	R_2	3.64	20.3	23.4	1.19
	R_1	7.83	103	20	3.74
Patient 5	C	58.5	4.46	22.9	129
	R_2	4.67	61.3	11.9	2.12
	R_1	6.44	16.6	6.29	2.66
Patient 6	C	5.25	2.03	5.37	26.4
	R_2	10.9	28.2	10.7	2.17
	R_1	5.05	17.7	7.99	2.22
Patient 7	C	13.4	3.83	8.50	59.8
	R_2	6.79	23.8	10.7	1.53
	R_1	5.31	36.6	13.6	3.73
Patient 8	C	4.64	0.673	1.80	10.7
	R_2	6.69	46	17.2	2.89
	R_1	13.4	146	18.5	4.07
Patient 9	C	182	16.7	133	829
	R_2	9.29	101	12.8	2.05
	R_1	9.48	39	13.5	7.50
Patient 10	C	117	28.5	81.9	1110
	R_2	9.74	40.1	13.9	1.03
	R_1	5.98	21.9	22.5	3.52
Patient 11	C	9.36	2.55	2.49	25.4
	R_2	3.89	14.3	14.6	1.43

6.3.2 Pressure gradients

Pressure gradient measures are reported in Table 6.8 from the 3D/0D model along with the pressure catheter measurement. From these results it is observed that the CFD derived metric in best agreement with the measured pressure is the CoA gradient catheter data, MB, of -9 mmHg and standard deviation from the mean difference (LOA, upper limit = 10 mmHg, lower limit = -28 mmHg). The absolute error is 10 ± 8 mmHg. However, direct comparison of the peak-to-peak difference in pressure between the ascending and descending aorta is in poor agreement between the CFD derived metric and the catheter reported values. It worths noting that the clinical measurement has been provided in terms of solely peak-to-peak pressure, which has been derived with the use of two different techniques (simultaneous and pullback). No information has been provided regarding the mean pressure drop across the coarctation neither the agreement with systolic and diastolic cuff pressures.

These results have been compared with further additional simulation scenarios, as reported in Table 6.9. The peak-to-peak pressure gradient has been reported for the 3D/0D compliant model (referred as 3D transient simulation same of Table 6.8) and averaged over the cardiac cycle (3D simulation cycle averaged). The same pressure measurement has been reported for the 1D/0D transient case (1D transient simulation) and averaged over the cardiac cycle (1D simulation cycle averaged); for a steady state 3D rigid case where the MRI peak flow rate has been applied at the inlet, while at the outlets of the numerical domain a sensible flow split between the head vessels based on their areas (3D steady state peak flow rate), and, finally, the same setting has been used but a mean-flow rate has been applied at

Table 6.8: Pressure gradients computed in the 3D/0D model, measured using the cuff arm-leg method and obtained from catheterization (NA= not available) reported in mmHg. Peak Reynolds number are reported at the coarctation site. Laminar (L) and turbulence SST model (T) are reported for the cases where the peak Reynolds number exceeds the limit imposed by the classical turbulence analysis (3500).

	peak Re	$\mathrm{Max}_{\mathrm{AscAo}} - \mathrm{Max}_{\mathrm{DescAo}}$		$\mathrm{Max}_{\mathrm{gradient}}$		$\mathrm{Sys}_{\mathrm{gradient}}$		$\mathrm{CoA}_{\mathrm{gradient}}$		Cuff arm-leg	Cath
					Native						
		L	T	L	T	L	T	L	T		
Patient 1	3405	1	-	35	-	18	-	9	-	22	32
Patient 2	1861	3	-	18	-	9	-	7	-	30	20
Patient 3	2948	15	-	39	-	20	-	20	-	31	31
Patient 7	5554	1	1	43	43	20	20	14	17	28	14
Patient 9	4341	15	16	47	48	24	24	22	18	35	34
Patient 10	5969	59	59	67	66	59	61	41	42	30	38
					Surgically Repaired						
		L	T	L	T	L	T	L	T		
Patient 4	6824	14	14	37	37	22	23	18	18	14	19
Patient 5	4617	9	9	33	33	24	23	23	22	27	23
Patient 6	4848	1	1	29	29	18	15	20	23	26	21
Patient 8	3482	4	-	23	-	20	-	21	-	NA	42
Patient 11	5031	2	1	38	36	23	16	8	12	14	30

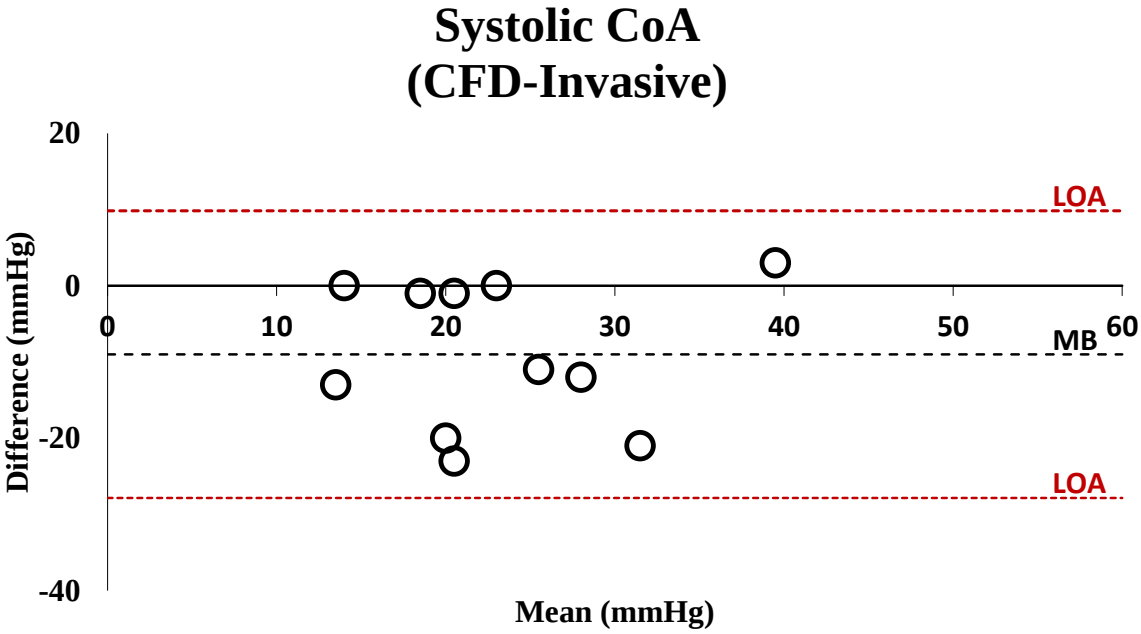

Figure 6.15: Bland-Altman plot: comparison of the invasive catheter measurement and computed CFD pressure gradient (mmHg) across the aortic coarctation for each case. Dashed red lines represent two standard deviations from the mean difference (LOA, 95 % limits of agreement) while the black dashed line represents the mean difference between the CFD and invasive data (MB).

the inlet of the 3D domain (3D steady state mean flow rate). All these measurement has been compared to the peak-to-peak catheter pressure gradient (Cath) and with the derived Doppler pressure estimation in equation 1.3, where the peak velocity has been derived from the MRI peak descending aortic flow rate and the measured area at the coarctation site.

Table 6.9: Pressure gradients computed in the 3D/0D model, 1D/0D model and Doppler equation 1.3 compared to catheter peak-to-peak data.

	3D steady state peak flow rate	3D steady state mean flow rate	3D transient simulation	3D simulation cycle averaged	1D transient simulation	1D simulation cycle averaged	Doppler derived from equation 1.3	Cath
Patient 1	23	16	1	3	1	3	2	32
Patient 2	13	1	3	1	3	1	1	20
Patient 3	33	7	15	6	14	3	1	31
Patient 4	30	2	14	4	13	3	3	19
Patient 5	17	1	9	3	8	2	1	23
Patient 6	16	2	1	1	1	1	1	21
Patient 7	54	2	1	1	1	1	4	14
Patient 8	20	1	4	2	4	2	1	42
Patient 9	23	1	15	3	14	2	1	34
Patient 10	200	8	59	14	50	12	4	38
Patient 11	40	2	2	1	3	1	5	30

The results showed a good agreement between 1D/0D and 3D/0D transient models, confirming the ability of the reduced 1D nonlinear model to provide a surrogate for the tuning of 3D models. The 3D steady state results overestimate the peak-to-peak pressure gradient when compared to other modelling approaches and catheter data, while the pressure decay derived from the doppler equation underestimate the catheter provided measurement.

6.4 Discussion

This study takes advantage of recent developments in modelling methods to build an engineering workflow for subject-specific modelling of the haemodynamics in a cohort of 11 patients who were assessed both before and after aortic coarctation repair. Key factors for successful clinical translation of such technologies include the ability to inform the workflow using non-invasive routinely collected clinical data and the feasibility for robust, repeatable application in a clinical environment.

By exercising the workflow on retrospective data acquired using standard clinical protocols, this study demonstrates the feasibility of using only CE-MRA images, flow rate waveforms acquired via 2D PC-MRI and systolic and diastolic cuff pressure values from the right arm, to construct two levels of model with a relatively low level of user interaction. Compared to previous work, the compressible fluid strategy adopted for the 3D/0D multiscale model allows aortic distensibility to be included without the use of a full FSI model, saving computational cost, simulation time and reducing the level of user interaction required to set-up the model.

This is an advance in the current state of 3D model simulation of CoA patients compared with the approach of Goubergrits et al. (2015b,a) where, despite the good agreement with catheter data, aortic distensibility and transient effects were neglected. A similar approach has been adopted in the previous section showing as sensisble overstimation of the peak-to-pak pressure drop, when compared to the provided data (see Table 6.9).

This study includes patient-specific aortic distensibility informed by PC-MRI data assuming the elastic properties of the aorta were uniform over the 1D/3D region. This is supported

by evidence that the use of non-uniform properties may lead to overestimation of the aortic stiffness (Alastruey et al., 2016) and it is well suited to deployment of this approach with existing clinical workflows, where PC-MRI flow rate waveforms are typically available at two locations (aortic root and diaphragmatic aorta).

Compared to previous published reports of 3D/0D approaches this study provides a more patient-specific assessment than LaDisa et al. (2011) and Coogan et al. (2011) who both used mechanical properties derived from literature-based data.

Ralovich et al. (2015) and Itu et al. (2013) used the same approach proposed here (foot-to-foot method) to inform the deformability of a 1D/0D model from 2D-PC MRI. Their model represented the coarctation site with a time constant nonlinear resistance that incorporated the effect of energy dissipation due to turbulence but did not capture the influence of 3D anatomical features such as curvature, bending, bifurcation and tapering. The importance of such effects, especially at systolic phases, where recirculation and helical flow clearly occurs (Xiao et al., 2014). Furthermore, it is possible that including a nonlinear resistance may result in artefactual pressure/flow wave reflections due to compliance mismatch.

Despite the limitation of 1D approaches to fully capture geometric effects, a 1D/0D multi-scale model provides a useful tool for tuning outflow boundary conditions and mechanical properties for the 3D model. The automatic tuning process adopted in this study offers the advantages of requiring only systolic and diastolic cuff pressures, diaphragmatic mean flow rate, and pulse wave velocity from 2D PC-MRI as input data. This avoids manual operator tuning that has been adopted in previous studies (LaDisa et al., 2011; Coogan et al., 2011; Wendell et al., 2013; Kwon et al., 2014). Alternative approaches have been proposed such as the use of the peak velocity flow rate value extracted from 4D flow MRI (Goubergrits

et al., 2015b,a) or UDS (Zhu et al., 2018), or a detailed catheter-derived pressure waveform applied at the domain boundaries (Valverde et al., 2011; Sotelo et al., 2015), but these require data are often not routinely collected in the clinical.

The 1D model showed some instabilities at lower values of measured wave speed, which limits the robustness of the tuning process. However, it should be noted that the aortic mechanical properties are derived from the wave speed calculation informed by both 2D PC-MRI and geometrical features, both associated with measurement uncertainties. The 1D/0D tuning process was successful in most cases and the 3D/0D models, with the tuned Windkessel parameters, captured the systolic and diastolic cuff pressure measurements reasonably well. Tuning through iterative solution of the coupled 3D/0D system is possible but introduces very highly computational costs.

The computational method underestimates measured catheter gradients compared with previous published studies Valverde et al. (2011); Goubergrits et al. (2015b); Itu et al. (2013); Ralovich et al. (2015). These increased errors may partially arise from the clinical data acquisition process, as data were processed retrospectively and not specifically for this computational study.

The pressure gradient across the coarctation at peak flow provides an assessment of the potential for reduction of the flow limiting effect of the coarctation following treatment, an advantage of the computational approach is the ability to examine this effect in isolation. Due to delayed augmentation in pressure in the descending aorta predicted by the CFD approach in several cases agreement between peak-to-peak measures of pressure gradient is poor. This suggests that, in addition to measurement errors previously discussed, assumptions made in the general nature of the tuning approach (i.e. distribution of resistance

and compliance based on generic relationships based on vessel radius) may lead to poor representation of patient-specific pressure transmission between the local 3D domain and the windkessel outlet conditions. A more detailed understanding of these effects would be provided by analysis of the time varying form of the pressure catheter measurements used to provide the clinical peak-to-peak pressure gradient, which was not available during this study.

Several limitations are associated with routine imaging and pressure measurement as aortic imaging by MR, non-invasive blood pressure measurements and invasive measurements by catheterization are typically not performed simultaneously. Furthermore, catheter measurements were performed at rest but without sedation and the location of PC-MRI measurements may be different from that at which the catheter data were obtained. All these limitations may contribute to variability between the model and measured results.

In this study, the effects of collateral flow (due to vertebral, internal mammary, intercostal or collateral arteries that join the descending aorta distal to the coarctation site) have been neglected because it has not been possible to segment these vessels for all patients, due to the small size of these vessels and limited spatial resolution of MR angiography. Some studies have included such vessels in their models LaDisa et al. (2011); Coogan et al. (2011) but only starting from the native supra-aortic branch point to the conjunction at the coarctation site without the need for supplementary BCs.

At supra-aortic branches (BCA, LCA, LSUB arteries) no PC-MRI flow rate (as inLaDisa et al. (2011)) nor catheter/tonometry derived blood pressure measurements (as in Alastruey et al. (2016)) were available therefore the mean flow rate was imposed based on vessels radii as in Zamir et al. (1992). This may introduce some limitations in this study, but the

automatic process described here can be simply adapted for future applications if such measurements are routinely acquired.

It should be noted that the same uniform aortic compliance was used for both patients after coarctation repair and unrepaired cases. The possible interaction between the rigid patch (in one patient) and the end-to-end anastomosis and the native aortic wall is expected to increase the number of reflected waves towards the proximal aorta, thus increasing the pressure gradient. In literature, this mechanism has been investigated for CoA patients treated with an aortic stent placement, by increasing the mechanical stiffness of the stented region up to 15 times the normal aortic compliance Coogan et al. (2011); Ralovich et al. (2015).

This study was conducted using retrospectively collected data obtained from patients at rest, which is likely to increase the uncertainty associated with comparison between CFD and measured data, in previous research studies under stress conditions the pressure gradient has been shown to reach values above 40 mmHg Sotelo et al. (2015). However, the rest condition represents the clinical protocol for assessment of coarctation patients under current guidelines Warnes et al. (2008).

6.5 Conclusion

This study has demonstrated the feasibility of constructing a workflow using non-invasive routinely collected clinical data to predict the pressure gradient in coarctation patients using patient specific CFD simulation, with relatively low levels of user interaction required. The results showed that the model is not suitable for the clinical use at this stage. The uncer-

tainties is too large in comparison to clinical decision making, thus further work is required to enhance the tuning process to improve agreement with measured catheter data. Part of this uncertainty can be addressed to provided catheter data, where only the peak-to-peak pressure has been provided, which has been measured with two different techniques (pull-back with insertion of one catheter or simultaneously with the use of two catheters), without any information regarding the mean pressure drop across the coarctation region neither the agreement with the measured systolic and diastolic pressure at the arm.

7

Virtual repair of aortic coarctation

This chapter describes a preliminary approach to simulate virtual surgical treatment for a single patient from the Bern cohort, reported in Chapter 6. This analysis was conducted on patient 10 as this case presented the most significant pressure gradient associated with the coarctation geometry.

7.0.1 Methods

Treatment of coarctation typically involves the placement of a stent or surgical intervention to restore the aortic lumen. As for previous studies reported in the literature Goubergrits et al. (2015a); Ralovich et al. (2015); Kwon et al. (2014); Cosentino et al. (2015) the approach taken here is not to directly simulate intervention, but to assume the intervention is able to remove the local stenosis associated with the coarctation region. To represent the intervention, the coarctation region was removed and the regions proximal and distal to the coarctation were joined together assuming a constant diameter that approximates the reference aortic diameter reported in chapter 4. These steps were taken using the open source software Autodesk MeshMixer (Autodesk, Inc.). An illustration of the pre- and post-treated geometry of the aorta is shown in figure 7.1.

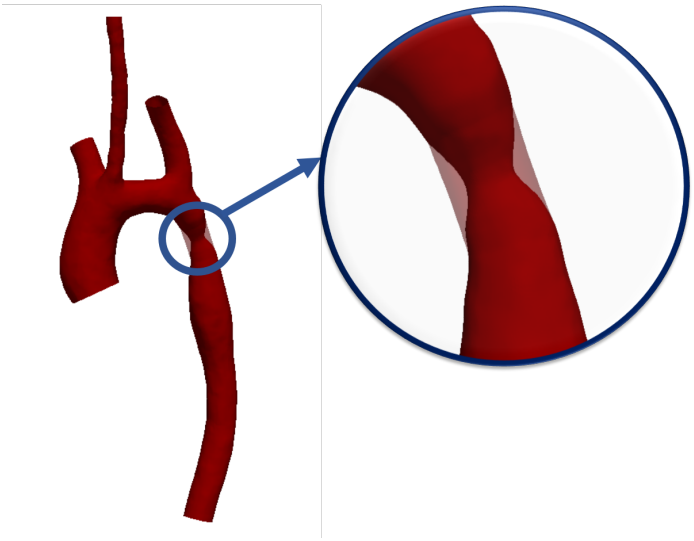

Figure 7.1: Workflow of the virtual treatment procedure using MRI data of patient 10. The detailed repaired geometry is presented and compared to the pre-treatment case.

The post-treated geometry was automatically meshed in ANSYS classic (ANSYS, Canonsburg, PA, USA) using polyhedral elements with five prism layers at the wall by means of a parameterised script file, using the same approach as for the pre-treated anatomy, with the final mesh density that is similar to the previous reported NA2 value in chapter 5, in terms of number of elements and length. The simulation was run using a laminar fluid model and the same boundary conditions derived using the tuning strategy described in chapter 6. At the inlet the ascending aortic flow rate measured in the pre-treatment condition was applied, assuming no change in the cardiac output between pre and post-treatment (repaired) conditions. At the model outlets the same parameters for the windkessel models were applied, assuming no changes in the response of the peripheral circulation.

7.0.2 Results

The pre-treatment aortic region presented a minimum diameter of 8 mm, while the repaired geometry had a diameter of 12 mm, which was close enough to the reference diameter, 14 mm. The pressure and flow waveforms obtained using the pre-treatment and post-treatment geometry are compared in Figure 7.2. From pre-treatment to post-treatment the peak-to-peak pressure gradient was reduced from 59 mmHg to 12 mmHg, while peak systolic pressure was reduced in the ascending aorta and supra-aortic vessels and increased in the descending aorta. The perfusion of each supra-aortic branch did not vary significantly although a noticeable increase in descending aortic flow was observed increased, with a significant reduction of the diastolic tail, a phenomena that is visible in pre-treatment case and characterized the descending aorta. Because of the presence of the coarctation descending

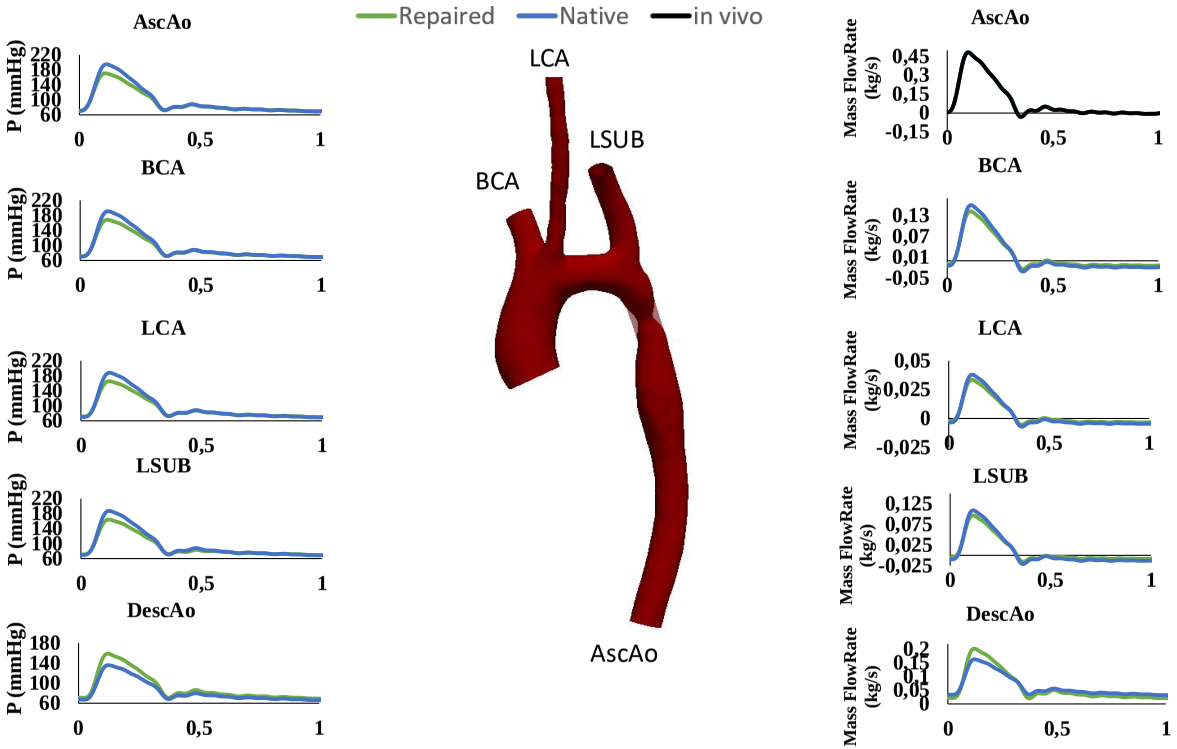

Figure 7.2: Blood flow (Mass Flow Rate) and Pressure (P) waveforms computed using the 3D native geometry (blue lines) and 3D virtual repaired geometry (green dashed lines) models in five arterial sites: ascending aorta (AscAo) Brachiocephalic artery (BCA) left common carotid artery (LCA) left subclavian artery (LSUB) and descending aorta (DescAo) and comparison with available in-vivo data for Patient 10

aortic flow does not reach negative value but has a constant perfusion .

7.0.3 Discussion

The preliminary study conducted in this section highlights a potential application of the CFD analysis to directly quantify the potential to reduce hypertension in the ascending aorta and improve perfusion to the peripheral circulation through treatment of coarctation. This approach has been adopted in previous works Goubergrits et al. (2015a); Ralovich et al. (2015); Kwon et al. (2014); Cosentino et al. (2015) using both 1D and 3D models. In most of these works, the treatment simulated a stent insertion by simply increasing the section of the coarctation region, except for Cosentino et al. (2015) who performed a 3D mechanical and fluid dynamics analysis, simulating the full stenting procedure. In his 1D numerical study Ralovich et al. (2015) increased the mechanical properties of the aortic wall in the post-treated region, assuming a wave-speed 15 times higher than the normal aortic region. Kwon et al. (2014) virtually placed the stent without performing a mechanical analysis, whilst Goubergrits et al. (2015a) simulated the surgical treatment by locally increasing the diameter of the aortic region, using a rigid wall assumption and performing a steady state CFD analysis.

7.0.4 Conclusion

This analysis demonstrates how improved haemodynamics can be achieved when the coarctation region is enlarged through a virtual intervention process. The CFD approach reported here can be expanded to explore the sensitivity of the peak ascending aortic pressure and descending aortic flow to the aortic diameter achieved following intervention, such an analysis would provide guidance for surgical intervention to target the optimal diameter to restore peripheral perfusion and reduce cerebral hypertension.

8

Discussion & Conclusion

The aim of this work was to develop an engineering workflow, which allows specification of patient-specific boundary conditions and 3D simulation based on clinically available patient-specific data. In chapter 1 a general overview of the potential modelling approaches used to describe the cardiovascular system was presented, together with an overview of potential target diseases where CFD has been applied to add value in the evaluation of patients. In this thesis the target disease chosen for the toolkit was aortic coarctation.

Nonlinear and linear 1D modelling approaches were presented in chapter 3 and applied

to idealized geometries of increasing complexity, benchmarked against 3D simulations to characterise their relative accuracy for simulation of aortic haemodynamics in general and patient-specific aortic coarctation in particular. From this analysis the nonlinear one-dimensional model was chosen for its ability to reproduce the main features of the 3D model with a reduced computational cost as the basis for the tuning approach reported in chapter 6. In chapter 4 the patient cohort consisting of 11 patients with aortic coarctation (studied as part of a protocol approved by the local ethics committee at Bern University Hospital) was used to examine the sensitivity of windkessel parameters for the peripheral circulation to the level of complexity of 0D models when tuning such models to patient-specific clinically measured pressure and flow data. It was observed that the effects of the coarctation became less significant with increasing model complexity. Chapter 5 described implementation of a novel approach to 3D pre-processing of clinical imaging data, with a particular focus on the segmentation process that has been developed inside Endosize for increased accuracy of supra-aortic vessel segmentation. As Endosize currently only supports processing of CT images an alternative segmentation approach was adopted for the Bern cohort MRA images to produce 3D geometries for CFD simulation. In the final part of this chapter a mesh sensitivity analysis was performed in order to select the optimal parameters for the automatic meshing strategy adopted in the 3D simulations. In chapter 6 the 1D nonlinear approach presented in chapter 3 was used to provide a tuning strategy for selecting haemodynamic properties and outflow boundary conditions to use in 3D aortic analysis, with reduced computational cost. The definition of 1D model parameters can be easily integrated inside Endosize, which already provides an automatic approach for the definition of the aortic centerline and perpendicular cross sectional area. The proposed 1D tuning strat-

egy would be straightforward to integrate within the Endosize framework once CE-MRA data processing is supported.

When compared to the solely clinical measurement provided, the peak-to-peak pressure gradient, the modelling strategy showed a poor agreement, which make it not directly translatable in the clinical evaluation process. However, the analysis of the curve flow rate at the descending aorta revails a good agreement with the measured descending aortic flow rate measured via 2D PC-MRI, especially for the prediction of the positive diastolic flow-rate (diastolic tale) which is one of the metrics that cardiologist uses to evaluate patient's condition.

8.1 Limitations and future works

The aortic wall has been assumed as homogoneaous, isotropic and linear elastic with a constant pulse wave propagation, even though many studies has evinced that the pulse wave propagation changes along the aortic centerline and in the coarcted region. Thus, the compressible strategy can be modified in order to take into account these changes via a pulse wave velocity function that varies along the centerline.

The validation of the model has been performed by a direct comparison of the peak-to-peak provided data, that has been measured by two different techniques (simultaneous and pullback). However, this measure, beside its variability enhanced by the adoption of two complete different protocols, could not as representative as a cycle averaged pressure gra-

dient which might be more informative of the deviation from a normal condition, a strategy that has been already adopted to evaluate patients with coronary stenosis. However, this required a time-varying curve of the measured pressure before and after the aortic coarctation. Nonethless these measurements can be used to further optimize the tuning process and modelling assumptions via a direct comparison between the time varying pressure waveforms measured and the one provided by the simulation.

The multi-scale model adopted in this work can be futher trained to explore and to evaluate different scenarios such as left ventricle hypertrophy and heart condition through the coupling of a lumped parameter description of the heart; cerebral perfusion and possible risks of cerebral hypertension via the coupling of a lumped description of the cerebral circulation or to evaluate the influence of the restored diameter on the pressure gradient, similarly to what has been presented in Chapter 7.

References

Absi, R. (2017). Revisiting the pressure-area relation for the flow in elastic tubes: Application to arterial vessels. *Series on Biomechanics*, 32, 47–59.

Agrawal, H., Bokowski, J. W., & Kenny, D. (2018). Coarctation of the aorta. *Visual Guide to Neonatal Cardiology*, (pp. 260).

Alastruey, J., Khir, A. W., Matthys, K. S., Segers, P., Sherwin, S. J., Verdonck, P. R., Parker, K. H., & Peiró, J. (2011). Pulse wave propagation in a model human arterial network: assessment of 1-d visco-elastic simulations against in vitro measurements. *Journal of biomechanics*, 44(12), 2250–2258.

Alastruey, J., Parker, K., Peiró, J., & Sherwin, S. (2008). Lumped parameter outflow models for 1-d blood flow simulations: effect on pulse waves and parameter estimation. *Communications in Computational Physics*, 4(2), 317–336.

Alastruey, J., Parker, K. H., Sherwin, S. J., et al. (2012a). Arterial pulse wave haemodynamics. In *11th International Conference on Pressure Surges* (pp. 401–442).: Virtual PiE Led t/a BHR Group Lisbon, Portugal.

Alastruey, J., Passerini, T., Formaggia, L., & Peiró, J. (2012b). Physical determining factors of the arterial pulse waveform: theoretical analysis and calculation using the 1-d formulation. *Journal of Engineering Mathematics*, 77(1), 19–37.

Alastruey, J., Xiao, N., Fok, H., Schaeffter, T., & Figueroa, C. A. (2016). On the impact of modelling assumptions in multi-scale, subject-specific models of aortic haemodynamics. *Journal of The Royal Society Interface*, 13(119), 20160073.

Amato, J. J., Rheinlander, H. F., & Cleveland, R. J. (1977). A method of enlarging the distal transverse arch in infants with hypoplasia and coarctation of the aorta. *The Annals of Thoracic Surgery*, 23(3), 261–263.

Antiga, L., Piccinelli, M., Botti, L., Ene-Iordache, B., Remuzzi, A., & Steinman, D. A. (2008). An image-based modeling framework for patient-specific computational hemodynamics. *Medical & biological engineering & computing*, 46(11), 1097.

Apter, J. T. (1967). Correlation of visco-elastic properties with microscopic structure of large arteries: Iv. thermal responses of collagen, elastin, smooth muscle, and intact artesries. *Circulation Research*, 21(6), 901–918.

Avila, L. S. (2006). *The VTK user's guide: updated for version 5*. Kitware.

Avolio, A. (1980). Multi-branched model of the human arterial system. *Medical and Biological Engineering and Computing*, 18(6), 709–718.

Azer, K. & Peskin, C. S. (2007). A one-dimensional model of blood flow in arteries with friction and convection based on the womersley velocity profile. *Cardiovascular Engineering*, 7(2), 51–73.

Barnard, A., Hunt, W., Timlake, W., & Varley, E. (1966). A theory of fluid flow in compliant tubes. *Biophysical journal*, 6(6), 717–724.

Batchelor, G. K. (2000). *An introduction to fluid dynamics*. Cambridge university press.

Baumgartner, H., Hung, J., Bermejo, J., Chambers, J. B., Evangelista, A., Griffin, B. P., Iung, B., Otto, C. M., Pellikka, P. A., & Quiñones, M. (2009). Echocardiographic assessment of valve stenosis: Eae/ase recommendations for clinical practice. *Journal of the American Society of Echocardiography*, 22(1), 1–23.

Bentall, H. & De Bono, A. (1968). A technique for complete replacement of the ascending aorta. *Thorax*, 23(4), 338–339.

Bessems, D., Rutten, M., & Van De Vosse, F. (2007). A wave propagation model of blood flow in large vessels using an approximate velocity profile function. *Journal of Fluid Mechanics*, 580, 145–168.

Blanco, P. J., Watanabe, S. M., Dari, E. A., Passos, M. A. R., & Feijóo, R. A. (2014). Blood flow distribution in an anatomically detailed arterial network model: criteria and algorithms. *Biomechanics and modeling in mechanobiology*, 13(6), 1303–1330.

Bodell, B. D., Taylor, A. C., & Patel, P. J. (2018). Thoracic Endovascular Aortic Repair: Review of Current Devices and Treatments Options. *Techniques in Vascular & Interventional Radiology*, 21(3), 137–145.

Boileau, E., Nithiarasu, P., Blanco, P. J., Müller, L. O., Fossan, F. E., Hellevik, L. R., Donders, W. P., Huberts, W., Willemet, M., & Alastruey, J. (2015). A benchmark study of numerical schemes for one-dimensional arterial blood flow modelling. *International journal for numerical methods in biomedical engineering*, 31(10), 1–33.

Bolster Jr, B. D., Atalar, E., Hardy, C. J., & McVeigh, E. R. (1998). Accuracy of arterial pulse-wave velocity measurement using mr. *Journal of Magnetic Resonance Imaging*, 8(4), 878–888.

Bonfanti, M., Balabani, S., Greenwood, J. P., Puppala, S., Homer-Vanniasinkam, S., & Díaz-Zuccarini, V. (2017). Computational tools for clinical support: a multi-scale compliant model for haemodynamic simulations in an aortic dissection based on multi-modal imaging data. *Journal of The Royal Society Interface*, 14(136), 20170632.

Brook, B. & Pedley, T. (2002). A model for time-dependent flow in (giraffe jugular) veins: uniform tube properties. *Journal of biomechanics*, 35(1), 95–107.

Brooke, B. S., Habashi, J. P., Judge, D. P., Patel, N., Loeys, B., & Dietz, H. C. I. (2008). Angiotensin II blockade and aortic-root dilation in marfan's syndrome. *New England Journal of Medicine*, 358(26), 2787–2795.

Brown, A. G., Shi, Y., Marzo, A., Staicu, C., Valverde, I., Beerbaum, P., Lawford, P. V., & Hose, D. R. (2012). Accuracy vs. computational time: translating aortic simulations to the clinic. *Journal of biomechanics*, 45(3), 516–523.

Brown, M. L., Burkhart, H. M., Connolly, H. M., Dearani, J. A., Cetta, F., Li, Z., Oliver, W. C., Warnes, C. A., & Schaff, H. V. (2013). Coarctation of the aorta: lifelong surveillance is mandatory following surgical repair. *Journal of the American College of Cardiology*, 62(11), 1020–1025.

Brüning, J., Hellmeier, F., Yevtushenko, P., Kühne, T., & Goubergrits, L. (2018). Uncertainty quantification for non-invasive assessment of pressure drop across a coarctation of the aorta using cfd. *Cardiovascular engineering and technology*, 9(4), 582–596.

Burattini, R. & Natalucci, S. (1998). Complex and frequency-dependent compliance of viscoelastic windkessel resolves contradictions in elastic windkessels. *Medical engineering & physics*, 20(7), 502–514.

by the Association for European Paediatric Cardiology (AEPC), E., Members, A. F., Baumgartner, H., Bonhoeffer, P., De Groot, N. M., de Haan, F., Deanfield, J. E., Galie, N., Gatzoulis, M. A., Gohlke-Baerwolf, C., et al. (2010). Esc guidelines for the management of grown-up congenital heart disease (new version 2010) the task force on the management of grown-up congenital heart disease of the european society of cardiology (esc). *European heart journal*, 31(23), 2915–2957.

Canchi, T., Kumar, S. D., Ng, E. Y. K., & Narayanan, S. (2015). A review of computational methods to predict the risk of rupture of abdominal aortic aneurysms. *BioMed research international*, 2015.

Čanić, S. & Kim, E. H. (2003). Mathematical analysis of the quasilinear effects in a hyperbolic model blood flow through compliant axi-symmetric vessels. *Mathematical Methods in the Applied Sciences*, 26(14), 1161–1186.

Caro, C. G., Pedley, T., & Schroter, R. (2012). *The mechanics of the circulation*. Cambridge University Press.

Cavalcante, J. L., Lima, J. A., Redheuil, A., & Al-Mallah, M. H. (2011). Aortic stiffness: current understanding and future directions. *Journal of the American College of Cardiology*, 57(14), 1511–1522.

Chaikof, E. L., Blankensteijn, J. D., Harris, P. L., White, G. H., Zarins, C. K., Bernhard, V. M., Matsumura, J. S., May, J., Veith, F. J., Fillinger, M. F., Rutherford, R. B., & Kent, K. (2016). Reporting standards for endovascular aortic aneurysm repair. *Journal of Vascular Surgery*, 35(5), 1048–1060.

Commission, I. E. et al. (2010). Medical electrical equipment—part 2-44: particular requirements for the basic safety and essential performance of x-ray equipment for computed tomography. *International Electrotechnical Commission (IEC)*, (pp. 60601–2).

Conrad, W. A. (1969). Pressure-flow relationships in collapsible tubes. *IEEE Transactions on Biomedical Engineering*, BME-16(4), 284–295.

Coogan, J. S., Chan, F. P., Taylor, C. A., & Feinstein, J. A. (2011). Computational fluid dynamic simulations of aortic coarctation comparing the effects of surgical-and stent-based treatments on aortic compliance and ventricular workload. *Catheterization and Cardiovascular Interventions*, 77(5), 680–691.

Cosentino, D., Capelli, C., Derrick, G., Khambadkone, S., Muthurangu, V., Taylor, A. M., & Schievano, S. (2015). Patient-specific computational models to support interventional procedures: a case study of complex aortic re-coarctation. *EuroIntervention*, 11(5), 669–672.

Courant, R., Friedrichs, K., & Lewy, H. (1967). On the partial difference equations of mathematical physics. *IBM journal of Research and Development*, 11(2), 215–234.

David, T. & Feindel, C. (1992). An aortic valve-sparing operation for patients with aortic incompetence and aneurysm of the ascending aorta. *The Journal of thoracic and cardiovascular surgery*, 103(4), 617–22.

Davies, R. R., Goldstein, L. J., Coady, M. A., Tittle, S. L., Rizzo, J. A., Kopf, G. S., & Elefteriades, J. A. (2002). Yearly rupture or dissection rates for thoracic aortic aneurysms: simple prediction based on size. *The Annals of Thoracic Surgery*, 73(1), 17 – 28.

Dehaki, M. G., Ghavidel, A. A., Givtaj, N., Omrani, G., & Salehi, S. (2010). Recurrence rate of different techniques for repair of coarctation of aorta: A 10 years experience. *Annals of Pediatric Cardiology*, 3(2), 123–126.

Della Corte, A., Bancone, C., Conti, C. A., Votta, E., Redaelli, A., Del Viscovo, L., & Cotrufo, M. (2012). Restricted cusp motion in right-left type of bicuspid aortic valves: A new risk marker for aortopathy. *The Journal of Thoracic and Cardiovascular Surgery*, 144(2), 360–369.e1.

Deriche, R. (1992). Recursively implementing the gaussian and its derivatives. In *Proc. Secound Int. Conf. On Image Processing* (pp. 263–267).

Di Martino, E., Guadagni, G., Fumero, A., Ballerini, G., Spirito, R., Biglioli, P., & Redaelli, A. (2016). Fluid–structure interaction within realistic three-dimensional models of the aneurysmatic aorta as a guidance to assess the risk of rupture of the aneurysm. *Medical Engineering and Physics*, 23(9), 647–655.

Dodge-Khatami, A., Backer, C. L., & Mavroudis, C. (2000). Risk factors for recoarctation and results of reoperation: A 40-year review. *Journal of Cardiac Surgery*, 15(6), 369–377.

Donati, F., Myerson, S., Bissell, M. M., Smith, N. P., Neubauer, S., Monaghan, M. J., Nordsletten, D. A., & Lamata, P. (2017). Beyond bernoulli: improving the accuracy and precision of noninvasive estimation of peak pressure drops. *Circulation: Cardiovascular Imaging*, 10(1), e005207.

Doyle, B. J. & Norman, P. E. (2016). Computational biomechanics in thoracic aortic dissection: today's approaches and tomorrow's opportunities. *Annals of biomedical engineering*, 44(1), 71–83.

Edwards, W. & Kerr, A. (1970). A safer technique for replacement of the entire ascending aorta and aortic valve. *The Journal of thoracic and cardiovascular surgery*, 59(6), 837–839.

El-Hamamsy, I. & Yacoub, M. H. (2012). Cellular and molecular mechanisms of thoracic aortic aneurysms. *Nat Rev Cardiol*, 6(12), 771–786.

Elefteriades, J. A. & Farkas, E. A. (2010). Thoracic aortic aneurysm: Clinically pertinent controversies and uncertainties. *Journal of the American College of Cardiology*, 55(9), 841–857.

Euler, L. (1844). Principia pro motu sanguinis per arterias determinando.opera postuma mathematica et physica anno 1844 detecta. *Ediderunt P.H. Fuss et N. Fuss Petropoli; Apund Eggers et Socios*, 2, 814–823.

Fahraeus, R. & Lindqvist, T. (1931). The viscosity of the blood in narrow capillary tubes. *American Journal of Physiology-Legacy Content*, 96(3), 562–568.

Fay, J. A. & Sonwalkar, N. (1996). A fluid mechanics hypercourse. *A Fluid Mechanics Hypercourse, by James A. Fay and Nishikant Sonwalkar. ISBN 0-262-56103-4. Cambridge, Massachusetts, USA: The MIT Press, May 1996.(Paper)*.

Fielden, S. W., Fornwalt, B. K., Jerosch-Herold, M., Eisner, R. L., Stillman, A. E., & Oshinski, J. N. (2008). A new method for the determination of aortic pulse wave velocity using cross-correlation on 2d pcmr velocity data. *Journal of Magnetic Resonance Imaging*, 27(6), 1382–1387.

Figueroa, C. A., Taylor, C. A., Chiou, A. J., Yeh, V., & Zarins, C. K. (2009). Magnitude and direction of pulsatile displacement forces acting on thoracic aortic endografts. *Journal of Endovascular Therapy*, 16(3), 350–358.

Fillinger, M. F., Raghavan, M. L., Marra, S. P., Cronenwett, J. L., & Kennedy, F. E. (2002). In vivo analysis of mechanical wall stress and abdominal aortic aneurysm rupture risk. *Journal of vascular surgery*, 36(3), 589–597.

Formaggia, L., Lamponi, D., Tuveri, M., & Veneziani, A. (2006). Numerical modeling of 1d arterial networks coupled with a lumped parameters description of the heart. *Computer Methods in Biomechanics and Biomedical Engineering*, 9(5), 273–288.

Fung, Y.-c. (2013). *Biomechanics: mechanical properties of living tissues*. Springer Science & Business Media.

Gallo, D., De Santis, G., Negri, F., Tresoldi, D., Ponzini, R., Massai, D., Deriu, M., Segers, P., Verhegghe, B., Rizzo, G., et al. (2012). On the use of in vivo measured flow rates as boundary conditions for image-based hemodynamic models of the human aorta: implications for indicators of abnormal flow. *Annals of biomedical engineering*, 40(3), 729–741.

Goubergrits, L., Riesenkampff, E., Yevtushenko, P., Schaller, J., Kertzscher, U., Berger, F., & Kuehne, T. (2015a). Is mri-based cfd able to improve clinical treatment of coarctations of aorta? *Annals of biomedical engineering*, 43(1), 168–176.

Goubergrits, L., Riesenkampff, E., Yevtushenko, P., Schaller, J., Kertzscher, U., Hennemuth, A., Berger, F., Schubert, S., & Kuehne, T. (2015b). MRI-based computational fluid dynamics for diagnosis and treatment prediction: Clinical validation study in patients with coarctation of aorta. *Journal of Magnetic Resonance Imaging*, 41(4), 909–916.

Grinberg, L., Cheever, E., Anor, T., Madsen, J. R., & Karniadakis, G. (2011). Modeling blood flow circulation in intracranial arterial networks: a comparative 3d/1d simulation study. *Annals of biomedical engineering*, 39(1), 297–309.

Gross, R. E. (1951). Treatment of certain aortic coarctations by homologous grafts: A report of nineteen cases. *Annals of Surgery*, 134(4), 753–768.

Grotenhuis, H. B., Westenberg, J. J., Steendijk, P., van der Geest, R. J., Ottenkamp, J., Bax, J. J., Jukema, J. W., & de Roos, A. (2009). Validation and reproducibility of aortic pulse wave velocity as assessed with velocity-encoded mri. *Journal of Magnetic Resonance Imaging: An Official Journal of the International Society for Magnetic Resonance in Medicine*, 30(3), 521–526.

Groth, K., Hove, H., Kyhl, K., Folkestad, L., Gaustadnes, M., Vejlstrup, N., Stochholm, K., R. Østergaard, J., Andersen, N., & Gravholt, C. (2015). Prevalence, incidence, and age at diagnosis in marfan syndrome. *Orphanet Journal of Rare Diseases*, 10.

Harris, K. C., Du, W., Cowley, C. G., Forbes, T. J., Kim, D. W., & On Behalf of the Congenital Cardiac Intervention Study Consortium (CCISC) (2014). A prospective observational multicenter study of balloon angioplasty for the treatment of native and recurrent coarctation of the aorta. *Catheterization and Cardiovascular Interventions*, 83(7), 1116–1123.

Hart, J. C. & Waldhausen, J. A. (1983). Reversed subclavian flap angioplasty for arch coarctation of the aorta. *The Annals of Thoracic Surgery*, 36(6), 715–717.

Hollander, E. H., Wang, J.-J., Dobson, G. M., Parker, K. H., & Tyberg, J. V. (2001). Negative wave reflections in pulmonary arteries. *American Journal of Physiology-Heart and Circulatory Physiology*, 281(2), H895–H902.

Huang, G. P., Yu, H., Yang, Z., Schwieterman, R., & Ludwig, B. (2018). 1d simulation of blood flow characteristics in the circle of willis using thinks. *Computer methods in biomechanics and biomedical engineering*, 21(4), 389–397.

Ibrahim, E.-S. H., Johnson, K. R., Miller, A. B., Shaffer, J. M., & White, R. D. (2010). Measuring aortic pulse wave velocity using high-field cardiovascular magnetic resonance: comparison of techniques. *Journal of Cardiovascular Magnetic Resonance*, 12(1), 26.

Itu, L., Sharma, P., Ralovich, K., Mihalef, V., Ionasec, R., Everett, A., Ringel, R., Kamen, A., & Comaniciu, D. (2013). Non-invasive hemodynamic assessment of aortic coarctation: Validation with in vivo measurements. *Annals of Biomedical Engineering*, 41(4), 669–681.

Ivanov, K., Kalinina, M., & Levkovich, Y. I. (1981). Blood flow velocity in capillaries of brain and muscles and its physiological significance. *Microvascular research*, 22(2), 143–155.

Jager, G. N., Westerhof, N., & Noordergraaf, A. (1965). Oscillatory flow impedance in electrical analog of arterial system:: Representation of sleeve effect and non-newtonian properties of blood. *Circulation research*, 16(2), 121–133.

Joh, J. H., Ahn, H.-J., & Park, H.-C. (2013). Reference diameters of the abdominal aorta and iliac arteries in the korean population. *Yonsei medical journal*, 54(1), 48–54.

Johnson, H. J., McCormick, M. M., & Ibanez, L. (2015). The itk software guide book 1: Introduction and development guidelines fourth edition updated for itk version 4.7. *Kitware, Inc.(January 2015)*.

Johnston, K., Rutherford, R. B., Tilson, M., Shah, D. M., Hollier, L., & Stanley, J. C. (1991). Suggested standards for reporting on arterial aneurysms. *Journal of Vascular Surgery*, 13(3), 452 – 458.

Joly, F., Soulez, G., Garcia, D., Lessard, S., & Kauffmann, C. (2018). Flow stagnation volume and abdominal aortic aneurysm growth: Insights from patient-specific computational flow dynamics of lagrangian-coherent structures. *Computers in biology and medicine*, 92, 98–109.

Jones, C. M., Baker-Groberg, S. M., Cianchetti, F. A., Glynn, J. J., Healy, L. D., Lam, W. Y., Nelson, J. W., Parrish, D. C., Phillips, K. G., Scott-Drechsel, D. E., et al. (2014). Measurement science in the circulatory system. *Cellular and molecular bioengineering*, 7(1), 1–14.

Juchems, M. S., Pless, D., Fleiter, T. R., Gabelmann, A., Liewald, F., Brambs, H. J., & Aschpoff, A. J. (2004). Blutflusssimulation mittels computational-fluid-dynamics an aus CT-daten rekonstruierten aortenaneurysmata vor und nach stent-graft implantation. *Fortschr Röntgenstr*, 177(1), 56–61. 56.

Juffermans, J. F., Nederend, I., van den Boogaard, P. J., ten Harkel, A. D., Hazekamp, M. G., Lamb, H. J., Roest, A. A., & Westenberg, J. J. (2019). The effects of age at correction of aortic coarctation and recurrent obstruction on adolescent patients: Mri evaluation of wall shear stress and pulse wave velocity. *European Radiology Experimental*, 3(1), 24.

Karmonik, C., Partovi, S., Müller-Eschner, M., Bismuth, J., Davies, M. G., Shah, D. J., Loebe, M., Böckler, D., Lumsden, A. B., & von Tengg-Kobligk, H. (2012). Longitudinal computational fluid dynamics study of aneurysmal dilatation in a chronic debakey type iii aortic dissection. *Journal of vascular surgery*, 56(1), 260–263.

Kilic, H., Yelgec, S., Salih, O., Akdemir, R., Karakurt, O., Cagirci, G., Yeter, E., Acikel, S., Dogan, M., Arslantas, U., et al. (2013). An invasive but simple and accurate method for ascending aorta–femoral artery pulse wave velocity measurement. *Blood pressure*, 22(1), 45–50.

Kim, H. J., Vignon-Clementel, I. E., Figueroa, C. A., LaDisa, J. F., Jansen, K. E., Feinstein, J. A., & Taylor, C. A. (2009). On coupling a lumped parameter heart model and a three-dimensional finite element aorta model. *Annals of biomedical engineering*, 37(11), 2153–2169.

Kumar, A. & Agarwal, S. (2014). Marfan syndrome: An eyesight of syndrome. *Meta Gene*, 2, 96 – 105.

Kwon, S., Feinstein, J. A., Dholakia, R. J., & LaDisa, J. F. (2014). Quantitfication of local hemodynamic alterations caused by virtual implantation of three commercially-available stents for the treatment of aortic coarctation. *Pediatric cardiology*, 35(4), 732–740.

LaDisa, J. F., Figueroa, C. A., Vignon-Clementel, I. E., Kim, H. J., Xiao, N., Ellwein, L. M., Chan, F. P., Feinstein, J. A., & Taylor, C. A. (2011). Computational simulations for aortic coarctation: representative results from a sampling of patients. *Journal of biomechanical engineering*, 133(9), 0910081–9.

Landes, G. (1943). Einige untersuchungen an elektrischen analogieschaltungen zum kreitslaufsystem. *Z Biol*, 101, 418–429.

Langley, S. M., Sunstrom, R. E., Reed, R. D., Rekito, A. J., & Gerrah, R. (2013). The neonatal hypoplastic aortic arch: Decisions and more decisions. *Seminars in Thoracic*

and Cardiovascular Surgery: Pediatric Cardiac Surgery Annual, 16(1), 43 – 51. Seminars in Thoracic and Cardiovascular Surgery: Pediatric Cardiac Surgery Annual 2013.

Laskey, W. K., Parker, H. G., Ferrari, V. A., Kussmaul, W. G., & Noordergraaf, A. (1990). Estimation of total systemic arterial compliance in humans. *Journal of Applied Physiology*, 69(1), 112–119.

Lederle FA, Johnson GR, Wilson SE, & et al (2000). The aneurysm detection and management study screening program: Validation cohort and final results. *Archives of Internal Medicine*, 160(10), 1425–1430.

Lee, J. & Smith, N. (2008). Development and application of a one-dimensional blood flow model for microvascular networks. *Proceedings of the Institution of Mechanical Engineers, Part H: Journal of Engineering in Medicine*, 222(4), 487–511.

Lehmann, E., Parker, J., Hopkins, K., Taylor, M., & Gosling, R. (1993). Validation and reproducibility of pressure-corrected aortic distensibility measurements using pulse-wave-velocity doppler ultrasound. *Journal of biomedical engineering*, 15(3), 221–228.

LeVeque, R. J. (1992). Numerical methods for conservation laws. *Birkha user Basel*.

Li, J. K. (2000). *The arterial circulation: physical principles and clinical applications*. Springer Science & Business Media.

Li, Z. & Kleinstreuer, C. (2016). Blood flow and structure interactions in a stented abdominal aortic aneurysm model. *Medical Engineering and Physics*, 27(5), 369–382.

Lin, E. & Alessio, A. (2009). What are the basic concepts of temporal, contrast, and spatial resolution in cardiac ct? *Journal of cardiovascular computed tomography*, 3(6), 403–408.

Lock, J. E., Bass, J. L., Amplatz, K., Fuhrman, B. P., & Castaneda-Zuniga, W. (1983). Balloon dilation angioplasty of aortic coarctations in infants and children. *Circulation*, 68(1), 109–116.

Lotfi, A., Simmons, A., & Barber, T. (2016). Evaluation of different meshing techniques for the case of a stented artery. *Journal of biomechanical engineering*, 138(3), 031005.

Lungu, A. (2015). *Mri Image Based Measurement, Modelling and Diagnostic Interpretation of Pressure and Flow in the Pulmonary Arteries: Application in puulmonary hypertension*. PhD thesis, University of Sheffield.

Lungu, A., Swift, A. J., Capener, D., Kiely, D., Hose, R., & Wild, J. M. (2016). Diagnosis of pulmonary hypertension from magnetic resonance imaging–based computational models and decision tree analysis. *Pulmonary circulation*, 6(2), 181–190.

Macgowan, C. K., Henkelman, R. M., & Wood, M. L. (2002). Pulse-wave velocity measured in one heartbeat using mr tagging. *Magnetic Resonance in Medicine: An Official Journal of the International Society for Magnetic Resonance in Medicine*, 48(1), 115–121.

Mao, S. S., Ahmadi, N., Shah, B., Beckmann, D., Chen, A., Ngo, L., Flores, F. R., lin Gao, Y., & Budoff, M. J. (2008). Normal thoracic aorta diameter on cardiac computed tomography in healthy asymptomatic adults: impact of age and gender. *Academic radiology*, 15(7), 827–834.

Matsumura, J. S., Cambria, R. P., Dake, M. D., Moore, R. D., Svensson, L. G., Snyder, S., Investigators, T. C. T., et al. (2008). International controlled clinical trial of thoracic endovascular aneurysm repair with the zenith tx2 endovascular graft: 1-year results. *Journal of vascular surgery*, 47(2), 247–257.

Matthys, K. S., Alastruey, J., Peiró, J., Khir, A. W., Segers, P., Verdonck, P. R., Parker, K. H., & Sherwin, S. J. (2007). Pulse wave propagation in a model human arterial network: assessment of 1-d numerical simulations against in vitro measurements. *Journal of biomechanics*, 40(15), 3476–3486.

Melis, A. (2017). *Gaussian process emulators for 1D vascular models.* PhD thesis, University of Sheffield.

Menon, A., Wendell, D. C., Wang, H., Eddinger, T. J., Toth, J. M., Dholakia, R. J., Larsen, P. M., Jensen, E. S., & LaDisa, J. F. (2012). A coupled experimental and computational approach to quantify deleterious hemodynamics, vascular alterations, and mechanisms of long-term morbidity in response to aortic coarctation. *Journal of Pharmacological and Toxicological Methods*, 65(1), 18–28.

Milewicz, D. M., Dietz, H. C., & Miller, D. C. (2005). Treatment of aortic disease in patients with marfan syndrome. *Circulation*, 111(11), 150–157.

Milišić, V. & Quarteroni, A. (2004). Analysis of lumped parameter models for blood flow simulations and their relation with 1d models. *ESAIM: Mathematical Modelling and Numerical Analysis*, 38(4), 613–632.

Milišić, V. & Quarteroni, A. (2004). Analysis of lumped parameter models for blood flow simulations and their relation with 1d models. *ESAIM: Mathematical Modelling and Numerical Analysis*, 38(4), 613–632.

Mohiaddin, R. H., Firmin, D. N., & Longmore, D. B. (1993). Age-related changes of human aortic flow wave velocity measured noninvasively by magnetic resonance imaging. *Journal of Applied Physiology*, 74(1), 492–497.

Mynard, J. P., Penny, D. J., & Smolich, J. J. (2013). Scalability and in-vivo validation of a multi-scale numerical model of the left coronary circulation. *American Journal of Physiology-Heart and Circulatory Physiology*.

Mynard, J. P. & Smolich, J. J. (2015). One-dimensional haemodynamic modeling and wave dynamics in the entire adult circulation. *Annals of biomedical engineering*, 43(6), 1443–1460.

Nakhleh, A., Rukhkyan, I., Wolfson, V., Rosner, I. A., Odeh, M., & Slobodin, G. (2013). Aortic wall thickness in patients without aortitis: a computed tomography-based study of 100 patients. In *ARTHRITIS AND RHEUMATISM*, volume 65 (pp. 364–364).: WILEY-BLACKWELL 111 RIVER ST, HOBOKEN 07030-5774, NJ USA.

Nodes, T. & Gallagher, N. (1982). Median filters: Some modifications and their properties. *IEEE Transactions on Acoustics, Speech, and Signal Processing*, 30(5), 739–746.

Nordon, I. M., Hinchliffe, R. J., Loftus, I. M., Morgan, R. A., & Thompson, M. M. (2011). Management of acute aortic syndrome and chronic aortic dissection. *Cardiovascular and interventional radiology*, 34(5), 890–902.

Oaks, W. & Paoletti, S. (2000). Polyhedral mesh generation. *Proceedings of the 9th International Meshing Round Table. New Orlean Louisiana: Sandia National Laboratories*, (pp. 57–67).

Ohki, T., Veith, F. J., Shaw, P., Lipsitz, E., Suggs, W. D., Wain, R. A., Bade, M., Mehta, M., Cayne, N., Cynamon, J., Valldares, J., & McKay, J. (2001). Increasing incidence of midterm and long-term complications after endovascular graft repair of abdominal aortic aneurysms: A note of caution based on a 9-year experience. *Annals of Surgery*, 234(3), 323–335.

O'Laughlin, M. P., Perry, S. B., Lock, J. E., & Mullins, C. E. (1991). Use of endovascular stents in congenital heart disease. *Circulation*, 83(6), 1923–1939.

Olufsen, M. S., Ottesen, J. T., Tran, H. T., Ellwein, L. M., Lipsitz, L. A., & Novak, V. (2005). Blood pressure and blood flow variation during postural change from sitting to standing: model development and validation. *Journal of Applied Physiology*.

Olufsen, M. S., Peskin, C. S., Kim, W. Y., Pedersen, E. M., Nadim, A., & Larsen, J. (2000). Numerical simulation and experimental validation of blood flow in arteries with structured-tree outflow conditions. *Annals of biomedical engineering*, 28(11), 1281–1299.

O'Rourke, M., Nichols, W. W., & Vlachopoulos, C. (2011). *McDonald's blood flow in arteries: theoretical, experimental and clinical principles*. CRC press.

Osher, S. & Sethian, J. A. (1988). Fronts propagating with curvature-dependent speed: algorithms based on hamilton-jacobi formulations. *Journal of computational physics*, 79(1), 12–49.

Otto, F. (1899). Die grundform des arteriellen pulses. *Zeitung fur Biologie*, 37, 483–586.

Pant, S., Fabrèges, B., Gerbeau, J.-F., & Vignon-Clementel, I. (2014). A methodological paradigm for patient-specific multi-scale cfd simulations: from clinical measurements to parameter estimates for individual analysis. *International journal for numerical methods in biomedical engineering*, 30(12), 1614–1648.

Pasta, S., Rinaudo, A., Luca, A., Pilato, M., Scardulla, C., Gleason, T. G., & Vorp, D. A. (2013). Difference in hemodynamic and wall stress of ascending thoracic aortic aneurysms with bicuspid and tricuspid aortic valve. *Journal of biomechanics*, 46(10), 1729–1738.

Payne, S. (2004). Analysis of the effects of gravity and wall thickness in a model of blood flow through axisymmetric vessels. *Medical and Biological Engineering and Computing*, 42(6), 799–806.

Pearson, G. D., Devereux, R., Loeys, B., Maslen, C., Milewicz, D., Pyeritz, R., Ramirez, F., Rifkin, D., Sakai, L., Svensson, L., Wessels, A., Van Eyk, J., & Dietz, H. C. (2008). Report of the national heart, lung, and blood institute and national marfan foundation working group on research in marfan syndrome and related disorders. *Circulation*, 118(7), 785–791.

Peiró, J. & Veneziani, A. (2009). *Cardiovascular mathematics. Chapter: Reduced models of the cardiovascular system, pages 347-394*. Springer.

Peric, M. (2004). Flow simulation using control volumes of arbitrary polyhedral shape. *ERCOFTAC bulletin*, 62, 25–29.

Prados, E., Camilli, F., & Faugeras, O. (2006). A viscosity solution method for shape-from-shading without image boundary data. *ESAIM: Mathematical Modelling and Numerical Analysis*, 40(2), 393–412.

Prasad, A., Xiao, N., Gong, X.-Y., Zarins, C. K., & Figueroa, C. A. (2013). A computational framework for investigating the positional stability of aortic endografts. *Biomechanics and modeling in mechanobiology*, 12(5), 869–887.

Press, W. H., Teukolsky, S. A., Vetterling, W. T., & Flannery, B. P. (2007). *Numerical recipes 3rd edition: The art of scientific computing*. Cambridge university press.

Project, C. A. (2013). 2nd CFD Challenge predicting patient-specific hemodynamics at rest and stress through an aortic coarctation. http://vascularmodel.org/miccai2013/.

Pythoud, F., Stergiopulos, N., Westerhof, N., & Meister, J. (1996). Method for determining distribution of reflection sites in the arterial system. *American Journal of Physiology-Heart and Circulatory Physiology*, 271(5), H1807–H1813.

Quarteroni, A. & Formaggia, L. (2004). Mathematical modelling and numerical simulation of the cardiovascular system. *Handbook of numerical analysis*, 12, 3–127.

Quarteroni, A. & Veneziani, A. (2003). Analysis of a geometrical multiscale model based on the coupling of ode and pde for blood flow simulations. *Multiscale Modeling & Simulation*, 1(2), 173–195.

Raghavan, M. L., Vorp, D. A., Federle, M. P., Makaroun, M. S., & Webster, M. W. (2000). Wall stress distribution on three-dimensionally reconstructed models of human abdominal aortic aneurysm. *Journal of vascular surgery*, 31(4), 760–769.

Ralovich, K., Itu, L. M., Vitanovski, D., Sharma, P., Ionasec, R. I., Mihalef, V., Krawtschuk, W., Zheng, Y., Everett, A. D., Pongiglione, G., Leonardi, B., Ringel, R. E., Navab, N., Heimann, T., & Comaniciu, D. (2015). Noninvasive hemodynamic assessment, treatment outcome prediction and follow-up of aortic coarctation from mr imaging. *Medical physics*, 42 5, 2143–56.

Ramirez, F. & Dietz, H. C. (2007). Marfan syndrome: from molecular pathogenesis to clinical treatment. *Current Opinion in Genetics & Development*, 17(3), 252 – 258. Genetics of disease.

Reddy, J. (2013). *An introduction to the finite element method*, volume 1221. McGraw-Hill New York, USA.

Reymond, P., Merenda, F., Perren, F., Rufenacht, D., & Stergiopulos, N. (2009). Validation of a one-dimensional model of the systemic arterial tree. *American Journal of Physiology-Heart and Circulatory Physiology*, 297(1), 208–222.

Rinaudo, A. & Pasta, S. (2014). Regional variation of wall shear stress in ascending thoracic aortic aneurysms. *Proceedings of the Institution of Mechanical Engineers, Part H: Journal of Engineering in Medicine*, 228(6), 627–638.

Roache, P. J. (1994). Perspective: a method for uniform reporting of grid refinement studies. *Journal of Fluids Engineering*, 116(3), 405–413.

Roger, V. L., Go, A. S., Lloyd-Jones, D. M., Adams, R. J., Berry, J. D., Brown, T. M., Carnethon, M. R., Dai, S., De Simone, G., Ford, E. S., et al. (2011). Heart disease and stroke statistics—2011 update: a report from the american heart association. *Circulation*, 123(4), e18–e209.

Rogers, W. J., Hu, Y.-L., Coast, D., Vido, D. A., Kramer, C. M., Pyeritz, R. E., & Reichek, N. (2001). Age-associated changes in regional aortic pulse wave velocity. *Journal of the American College of Cardiology*, 38(4), 1123–1129.

Romarowski, R. M., Lefieux, A., Morganti, S., Veneziani, A., & Auricchio, F. (2018). Patient-specific cfd modelling in the thoracic aorta with pc-mri–based boundary conditions: A least-square three-element windkessel approach. *International journal for numerical methods in biomedical engineering*, (pp. e3134).

Rosero, E. B., Peshock, R. M., Khera, A., Clagett, P., Lo, H., & Timaran, C. H. (2011). Sex, race, and age distributions of mean aortic wall thickness in a multiethnic population-based sample. *Journal of vascular surgery*, 53(4), 950–957.

Rydberg, J., Kopecky, K. K., Lalka, S. G., Johnson, M. S., Dalsing, M. C., & Persohn, S. A. (2001). Stent grafting of abdominal aortic aneurysms: Pre-and postoperative evaluation with multislice helical CT. *Journal of Computer Assisted Tomography*, 25(4).

Sarsam, M. & Yacoub, M. (1993). Remodeling of the aortic valve anulus. *The Journal of thoracic and cardiovascular surgery*, 105(3), 435–438.

Saxena, A. (2015). Recurrent coarctation: Interventional techniques and results. *World Journal for Pediatric and Congenital Heart Surgery*, 6(2), 257–265.

Seifert, B. L., DesRochers, K., Ta, M., Giraud, G., Zarandi, M., Gharib, M., & Sahn, D. J. (1999). Accuracy of doppler methods for estimating peak-to-peak and peak instantaneous gradients across coarctation of the aorta: an in vitro study. *Journal of the American Society of Echocardiography*, 12(9), 744–753.

Sethian, J. A. (1996). A fast marching level set method for monotonically advancing fronts. *Proceedings of the National Academy of Sciences*, 93(4), 1591–1595.

Shang, E. K., Nathan, D. P., Sprinkle, S. R., Vigmostad, S. C., Fairman, R. M., Bavaria, J. E., Gorman, R. C., Gorman III, J. H., Chandran, K. B., & Jackson, B. M. (2013). Peak wall stress predicts expansion rate in descending thoracic aortic aneurysms. *The Annals of Thoracic Surgery*, 95(2), 593–598.

Sheng, C., Sarwal, S., Watts, K., & Marble, A. (1995). Computational simulation of blood flow in human systemic circulation incorporating an external force field. *Medical and Biological Engineering and Computing*, 33(1), 8–17.

Sherwin, S., Franke, V., Peiró, J., & Parker, K. (2003). One-dimensional modelling of a vascular network in space-time variables. *Journal of Engineering Mathematics*, 47(3-4), 217–250.

Shi, Y., Lawford, P., & Hose, R. (2011). Review of zero-d and 1-d models of blood flow in the cardiovascular system. *Biomedical engineering online*, 10(1), 33.

Singh, S., Xu, X., Wood, N., Pepper, J., Izgi, C., Treasure, T., & Mohiaddin, R. (2016). Aortic flow patterns before and after personalised external aortic root support implantation in marfan patients. *Journal of Biomechanics*, 49(1), 100–111.

SMART SERVIER MEDICAL ART (2019). Illustrations, medical specialties. http://smart.servier.com.

Sotelo, J. A., Valverde, I., Beerbaum, P. B., Greil, G. F., Schaeffter, T., Razavi, R., Hurtado, D. E., Uribe, S., & Figueroa, C. A. (2015). Pressure gradient prediction in aortic coarctation using a computational-fluid-dynamics model: validation against invasive pressure catheterization at rest and pharmacological stress. *Journal of Cardiovascular Magnetic Resonance*, 17(1), Q78.

Spiegel, M., Redel, T., Zhang, Y. J., Struffert, T., Hornegger, J., Grossman, R. G., Doerfler, A., & Karmonik, C. (2011). Tetrahedral vs. polyhedral mesh size evaluation on flow velocity and wall shear stress for cerebral hemodynamic simulation. *Computer methods in biomechanics and biomedical engineering*, 14(01), 9–22.

Stergiopulos, N., Young, D., & Rogge, T. (1992). Computer simulation of arterial flow with applications to arterial and aortic stenoses. *Journal of biomechanics*, 25(12), 1477–1488.

Stewart, S. F., Day, S., Burgreen, G. W., Paterson, E. G., Manning, K. B., Hariharan, P., Deutsch, S., Giarra, M., Cheek, C., Reddy, V., et al. (2009). Preliminary results of fda's 'critical path'project to validate computational fluid dynamic methods used in medical device evaluation. *ASAIO J*, 55(2), 173.

Sun, Y.-H., Anderson, T. J., Parker, K. H., & Tyberg, J. V. (2000). Wave-intensity analysis: a new approach to coronary hemodynamics. *Journal of Applied Physiology*, 89(4), 1636–1644.

Sun, Z. & Chaichana, T. (2016). A systematic review of computational fluid dynamics in type b aortic dissection. *International journal of cardiology*, 210, 28–31.

Suradi, H. & Hijazi, Z. M. (2015). Current management of coarctation of the aorta. *Global Cardiology Science and Practice*, (pp.44).

Tahernia, A. (1993). Cardiovascular anomalies in marfan's syndrome: the role of echocardiography and beta-blockers. *Southern medical journal*, 86(3), 305–310.

Temam, R. (2001). *Navier-Stokes equations: theory and numerical analysis*. American Mathematical Soc.

Tieu, B. C., Ju, X., Lee, C., Sun, H., Lejeune, W., Recinos III, A., Brasier, A. R., & Tilton, R. G. (2011). Aortic adventitial fibroblasts participate in angiotensin-induced vascular wall inflammation and remodeling. *Journal of vascular research*, 48(3), 261–272.

Torok, R. D., Campbell, M. J., Fleming, G. A., & Hill, K. D. (2015). Coarctation of the aorta: management from infancy to adulthood. *World journal of cardiology*, 7(11), 765.

Treasure, T. (2013). Personalized external aortic root support. *Texas Heart Institute Journal*, 40(5), 549–552.

Treasure, T., Takkenberg, J. J. M., Golesworthy, T., Rega, F., Petrou, M., Rosendahl, U., Mohiaddin, R., Rubens, M., Thornton, W., Lees, B., & Pepper, J. (2014). Personalised external aortic root support (PEARS) in marfan syndrome: analysis of 1–9 year outcomes by intention-to-treat in a cohort of the first 30 consecutive patients to receive a

novel tissue and valve-conserving procedure, compared with the published results of aortic root replacement. *Heart*.

Valverde, I., Staicu, C., Grotenhuis, H., Marzo, A., Rhode, K., Shi, Y., Brown, A. G., Tzifa, A., Hussain, T., Greil, G., et al. (2011). Predicting hemodynamics in native and residual coarctation: preliminary results of a rigid-wall computational-fluid-dynamics model (rw-cfd) validated against clinically invasive pressure measures at rest and during pharmacological stress. *Journal of Cardiovascular Magnetic Resonance*, 13(1), P49.

Van de Vosse, F. N. & Stergiopulos, N. (2011). Pulse wave propagation in the arterial tree. *Annual Review of Fluid Mechanics*, 43, 467–499.

Van Leer, B. (1979). Towards the ultimate conservative difference scheme. v. a second-order sequel to godunov's method. *Journal of computational Physics*, 32(1), 101–136.

Vergara, C., Viscardi, F., Antiga, L., & Luciani, G. B. (2012). Influence of bicuspid valve geometry on ascending aortic fluid dynamics: A parametric study. *Artificial Organs*, 36(4), 368–378.

Versteeg, H. K. & Malalasekera, W. (2007). *An introduction to computational fluid dynamics: the finite volume method*. Pearson education.

Vignon-Clementel, I. E., Figueroa, C. A., Jansen, K. E., & Taylor, C. A. (2006a). Outflow boundary conditions for three-dimensional finite element modeling of blood flow and pressure in arteries. *Computer methods in applied mechanics and engineering*, 195(29-32), 3776–3796.

Vignon-Clementel, I. E., Figueroa, C. A., Jansen, K. E., & Taylor, C. A. (2006b). Outflow boundary conditions for three-dimensional finite element modeling of blood flow and

pressure in arteries. *Computer methods in applied mechanics and engineering*, 195(29-32), 3776–3796.

Vossschulte, K. (1961). Surgical correction of coarctation of the aorta by an "isthmusplastic" operation. *Thorax*, 16(4), 338–345.

Vulliémoz, S., Stergiopulos, N., & Meuli, R. (2002). Estimation of local aortic elastic properties with mri. *Magnetic Resonance in Medicine: An Official Journal of the International Society for Magnetic Resonance in Medicine*, 47(4), 649–654.

Warnes, C. A., Williams, R. G., Bashore, T. M., Child, J. S., Connolly, H. M., Dearani, J. A., del Nido, P., Fasules, J. W., Graham, T. P., Hijazi, Z. M., et al. (2008). Acc/aha 2008 guidelines for the management of adults with congenital heart disease: a report of the american college of cardiology/american heart association task force on practice guidelines (writing committee to develop guidelines on the management of adults with congenital heart disease) developed in collaboration with the american society of echocardiography, heart rhythm society, international society for adult congenital heart disease, society for cardiovascular angiography and interventions, and society of thoracic surgeons. *Journal of the American College of Cardiology*, 52(23), e143–e263.

Wendell, D. C., Samyn, M. M., Cava, J. R., Ellwein, L. M., Krolikowski, M. M., Gandy, K. L., Pelech, A. N., Shadden, S. C., & LaDisa, J. F. (2013). Including aortic valve morphology in computational fluid dynamic simulations: initial findings and application to aortic coarctation. *Medical engineering and physics*, 35(6), 12.

Westerhof, N., Bosman, F., De Vries, C. J., & Noordergraaf, A. (1969). Analog studies of the human systemic arterial tree. *Journal of biomechanics*, 2(2), 121–143.

Westerhof, N., Elzinga, G., & Sipkema, P. (1971). An artificial arterial system for pumping hearts. *Journal of applied physiology*, 31(5), 776–781.

Whitaker, R. T. & Xue, X. (2001). Variable-conductance, level-set curvature for image denoising. In *Proceedings 2001 International Conference on Image Processing (Cat. No. 01CH37205)*, volume 3 (pp. 142–145).: IEEE.

Willemet, M. & Alastruey, J. (2015). Arterial pressure and flow wave analysis using time-domain 1-d hemodynamics. *Annals of Biomedical Engineering*, 43, 190–206.

Wisotzkey, B. L., Hornik, C. P., Green, A. S., & Barker, P. C. (2015). Comparison of invasive and non-invasive pressure gradients in aortic arch obstruction. *Cardiology in the Young*, 25(7), 1348–1357.

Womersley, J. (1957). Oscillatory flow in arteries: the constrained elastic tube as a model of arterial flow and pulse transmission. *Physics in Medicine & Biology*, 2(2), 178.

Wright, J., Cruickshank, J., Kontis, S., Doré, C., & Gosling, R. (1990). Aortic compliance measured by non-invasive doppler ultrasound: description of a method and its reproducibility. *Clinical Science*, 78(5), 463–468.

Wyse, R., Robinson, P., Deanfield, J., Pedoe, D. T., & Macartney, F. (1984). Use of continuous wave doppler ultrasound velocimetry to assess the severity of coarctation of the aorta by measurement of aortic flow velocities. *Heart*, 52(3), 278–283.

Xiao, N., Alastruey, J., & Alberto Figueroa, C. (2014). A systematic comparison between 1-d and 3-d hemodynamics in compliant arterial models. *International journal for numerical methods in biomedical engineering*, 30(2), 204–231.

Yang, J., Pak, Y. E., & Lee, T.-R. (2016). Predicting bifurcation angle effect on blood flow in the microvasculature. *Microvascular research*, 108, 22–28.

Yang, X., Yu, H. C., Choi, Y., Lee, W., Wang, B., Yang, J., Hwang, H., Kim, J. H., Song, J., Cho, B. H., et al. (2014). A hybrid semi-automatic method for liver segmentation based on level-set methods using multiple seed points. *Computer methods and programs in biomedicine*, 113(1), 69–79.

Zamir, M., Sinclair, P., & Wonnacott, T. H. (1992). Relation between diameter and flow in major branches of the arch of the aorta. *Journal of biomechanics*, 25(11), 1303–1310.

Zhu, Y., Chen, R., Juan, Y.-H., Li, H., Wang, J., Yu, Z., & Liu, H. (2018). Clinical validation and assessment of aortic hemodynamics using computational fluid dynamics simulations from computed tomography angiography. *Biomedical engineering online*, 17(1), 53.

A

Appendix A

The characteristic analysis

This section shows how the system of hyperbolic equations 3.1 can be manipulated in order to introduce two new dependent variables, *the Riemann invariants*, which are of great importance for the setting of boundary conditions and interface conditions when solving the nonlinear system for an arterial network.

The system of hyperbolic equations 3.1 can be written in its conservative form[1] after few manipulations and assumptions such as a flat constant (in time and space) velocity profile ($\gamma_v = 9$ and $\alpha = 1$) and no external acting pressure ($P_ext = 0$)

$$\frac{\partial \mathbf{U}}{\partial t} + \frac{\partial \mathbf{F}(\mathbf{U})}{\partial z} = \mathbf{S}(\mathbf{U}) \tag{A.1}$$

where

$$\mathbf{U} = \begin{bmatrix} A \\ Au \end{bmatrix} \quad \mathbf{F}(\mathbf{U}) = \begin{bmatrix} Au \\ Au^2 + \gamma A^{3/2} \end{bmatrix} \quad \mathbf{S}(\mathbf{U}) = \begin{bmatrix} 0 \\ f_s \end{bmatrix} \tag{A.2}$$

$$\gamma = \frac{\beta}{3\rho\sqrt{A_0}} \quad f_s = -\frac{A}{\rho}\left[\frac{\partial P}{\partial A_0}\frac{\partial A_0}{\partial z} + \frac{\partial P}{\partial \beta}\frac{\partial \beta}{\partial z} + 2\mu(\gamma_v + 2)\frac{u}{A}\right]$$

F is the flux, **S** is the source term and **U** is the solution. If one defines the Jacobian of the flux as

$$\frac{\partial \mathbf{F}}{\partial \mathbf{U}} = \mathbf{H} = \begin{bmatrix} 0 & 1 \\ \frac{3}{2}\gamma\sqrt{A} - u^2 & 2u \end{bmatrix} \tag{A.3}$$

[1] The conservative form derives from expressing the conservation equations in a divergence form as:

$$\frac{d\xi}{dt} + \nabla \cdot f(\xi) = 0$$

where ξ is the conserved quantity.

Then the equation (A.1) can be written (in a non conservative form) as

$$\frac{\partial \mathbf{U}}{\partial t} + \mathbf{H}\frac{\partial \mathbf{U}}{\partial z} = \mathbf{S}(\mathbf{U}) \tag{A.4}$$

Under the assumption that $A > 0$, the square matrix $\mathbf{H}$ has two distinct real eigenvalues, thus the system of equations is said to be strictly hyperbolic A.1

$$\lambda_{1,2} = u \pm c, \quad c = \sqrt{\frac{3}{2}\gamma\sqrt{A}} = A^{\frac{1}{4}}\sqrt{\frac{\beta}{2\rho}} \tag{A.5}$$

c is the wavespeed. In most conditions for arterial flow, the wavespeed is more than one order of magnitude bigger than the local velocity ($u << c$, the blood flow is defined as subcritical), therefore $\lambda_1 < 0$ and $\lambda_2 > 0$. Since $\mathbf{H}$ has two distinct real eigenvalues, it can be written as a function of its diagonal matrix and right and left eigenvector matrices[2]

$$\mathbf{LHR} = \Lambda \tag{A.6}$$

$$\Lambda = \begin{bmatrix} \lambda_1 & 0 \\ 0 & \lambda_2 \end{bmatrix} \quad \mathbf{L} = \mathbf{R}^{-1} = \begin{bmatrix} \frac{c}{A} & 1 \\ -\frac{c}{A} & 1 \end{bmatrix}$$

Assuming a change of variable such that

[2]The matrix is diagonalizable, it mean that for the considered matrix A, it exists a matrix D such that

$$\Lambda = P^{-1}AP$$

where Λ is a diagonal matrix that contains the eigenvector of the matrix A while P is a matrix that contains the eigenvectors of the matrix A

$$\frac{\partial \mathbf{W}}{\partial \mathbf{U}} = \mathbf{L} \tag{A.7}$$

where $\mathbf{W} = [W_1, W_2]^T$ is the vector of the characteristic variables (*the Riemann invariants or variables*) of the hyperbolic system. Multiplying (A.1) by L and substituting (A.6) into (A.1), the final hyperbolic system becomes

$$\mathbf{L}\,\frac{\partial \mathbf{U}}{\partial t} + \Lambda \mathbf{L}\frac{\partial \mathbf{U}}{\partial z} = \mathbf{LS} \tag{A.8}$$

where Combining (A.7) and (A.8)

$$\frac{\partial \mathbf{W}}{\partial t} + \Lambda \frac{\partial \mathbf{W}}{\partial z} = \mathbf{LS} \tag{A.9}$$

In case where $\mathbf{S} = 0$ A.9 reduces to a system of decoupled ordinary diferrential equations (ODEs)

$$\frac{\partial W_i}{\partial t} + \lambda_i \frac{\partial W_i}{\partial z} = 0, i = 1, 2 \tag{A.10}$$

Where W_i are the invariant Riemann variables and it can be shown that along a certain path or *characteristic curves* $x = x(t)$ in space (x, t), they remains constant, these curves are described by the differential equations

$$\frac{dz}{dt} = \lambda_1, \frac{dz}{dt} = \lambda_2 \tag{A.11}$$

W_1 and W_2 are constant along two characteristic lines with a slope defines as $C_{1,2} =$

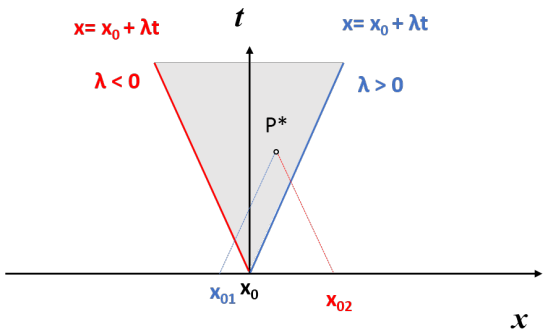

Figure A.1: Family of parallel characteristic curves with slope $\lambda \gtrless 0$ with a common origin at x_0. The initial condition $(x_0, t_0 = 0)$ propagates forwardly along the curve $x = x_0 \pm \lambda t$ with a velocity of λ. The Rienmann problem is solved by finding the solution at $P*$ as a contribution of two waves that has an origin at x_{01} and x_{02} and propagate along the dashed lines that propagate forward and backward.

$\frac{dx}{dt} = \lambda_{1,2} = u \pm c$. The initial value for W_1 and W_2 is propagated forward and backward and it is attenuated by the viscous dissipation effects, transmural pressure changes, wall distensibility or convective acceleration changes and other changes that are physically integrated in the hyperbolic system. The characteristic variables can be mathematically derived from the integration of (A.7) with respect to U

$$\frac{\partial \mathbf{W}}{\partial \mathbf{U}} = \mathbf{L} \tag{A.12}$$

$$\frac{\partial W_1}{\partial A} = \frac{c}{A} \rightarrow \int \partial W_1 = \int \frac{c}{A} \partial A \tag{A.13}$$

The value $W_{1,A}$ is then

$$W_{1,A} = \sqrt{\frac{\beta}{2\rho}} \int \frac{A^{1/4}}{A} \partial A = 4\sqrt{\frac{\beta}{2\rho}} (A^{\frac{1}{4}} - A_0^{\frac{1}{4}}) = 4(c - c_0) \tag{A.14}$$

where c_0 and u_0 are the reference velocity and wave speed at the initial area A_0. $W_{1,u}$ is derived as

$$\frac{\partial W_1}{\partial u} = 1 \rightarrow \int \partial W_1 = \int \partial u \tag{A.15}$$

$$W_{1,u} = u - u_0 \tag{A.16}$$

hence

$$W_1 = W_{1,u} + W_{1,A} = u - u_0 + 4(c - c_0) = u - u_0 + 4\sqrt{\frac{\beta}{2\rho}} (A^{\frac{1}{4}} - A_0^{\frac{1}{4}}) \tag{A.17}$$

and in a similar way W_2 is equal to

$$W_2 = W_{2,u} + W_{2,A} = u - u_0 - 4\sqrt{\frac{\beta}{2\rho}} (A^{\frac{1}{4}} - A_0^{\frac{1}{4}}) = u - u_0 - 4(c - c_0) \tag{A.18}$$

u_0 is a reference blood velocity. From proximal aorta to distal peripheral branches, W_1

solution propagates with a finite speed λ_1 in the positive (forward) z-direction along the vessel centerline; while W_2 solution propagates with a finite speed λ_2 in the negative (backward) z-direction along the vessel centerline from distal branches to proximal aorta. This mean that at any point of the 1D domain the changes in pressure or velocities can be decomposed into a combination of forward and backward travelling waves. For each point in the one-dimensional domain, the primitives variables (A, u) can be retrieved from

$$A = (\frac{W_2 - W_1}{4})^4 (\frac{\rho}{2\beta})^2, \quad u = \frac{W_1 + W_2}{2} \tag{A.19}$$

Permissions

Copyright Clearance Center

Confirmation Number: 11797792
Order Date: 03/11/2019

Customer Information

Customer: Massimiliano Mercuri
Account Number: 3001418753
Organization: Mr
Email: mmercuri1@sheffield.ac.uk
Phone: +33 789069787
Payment Method: Invoice

This is not an invoice

Order Details

Annual review of fluid mechanics

Billing Status: **N/A**

Order detail ID: 71849392
ISSN: 1545-4479
Publication Type: e-Journal
Volume:
Issue:
Start page:
Publisher: ANNUAL REVIEWS

Permission Status: Granted
Permission type: Republish or display content
Type of use: Thesis/Dissertation
Order License Id: 4545991056603

Requestor type	Academic institution
Format	Print, Electronic
Portion	image/photo
Number of images/photos requested	1
The requesting person/organization	Massimiliano Mercuri
Title or numeric reference of the portion(s)	Figure 1 of the article named: "Pulse Wave Propagation in the Arterial Tree" by Frans N. van de Vosse and Nikos Stergiopulos Annual Review of Fluid Mechanics, Vol. 43:467-499
Title of the article or chapter the portion is from	"Pulse Wave Propagation in the Arterial Tree", Annual Review of Fluid Mechanics, Vol. 43:467-499
Editor of portion(s)	Annual Review of Fluid Mechanics
Author of portion(s)	Frans N. van de Vosse and Nikos Stergiopulos
Volume of serial or monograph	Vol. 43:467-499
Page range of portion	1
Publication date of portion	2010
Rights for	Main product and any product related to main product

Duration of use	Life of current edition
Creation of copies for the disabled	no
With minor editing privileges	no
For distribution to	Worldwide
In the following language(s)	Original language of publication
With incidental promotional use	no
Lifetime unit quantity of new product	Up to 499
Title	Tuning of boundary conditions for haemodynamic simulation
Institution name	University of Sheffield
Expected presentation date	Jul 2019

Note: This item was invoiced separately through our **RightsLink service.** More info **$ 0.00**

Total order items: 1 **Order Total: $0.00**

Oggetto: RE: Contact SMART
Mittente: <webmaster@servier.com>
Data: 3/12/2019, 4:55 PM
A: <m.mercuri@therenva.com>

Dear Massimiliano,

Thanks for your message. You are totally free to use Servier Medical Art images as you want. No permission is required. Please use the following link (http://smart.servier.com/) to cite Servier Medical Art in your references. More information about the license can be found here: https://creativecommons.org/licenses/by/3.0/

Best regards,

Xavier GALLET
Servier International

-----Message d'origine-----
De : SMART [mailto:no-reply@smart.servier.com]
Envoyé : mardi 12 mars 2019 12:03
À : <FRcb DOM webmaster.com internet
Objet : Contact SMART

Question provenant du site SMART

Massimiliano Mercuri

m.mercuri@therenva.com

Copyright

Good morning,
I am a PhD student from the University of Sheffield I found your images very useful, so I wondered if I could use some of them for my thesis. If it is the case how would you like me to cite your site and which documentation do I need to prove that I received your permission to re-use?
Thanks
Massimiliano Mercuri

Oggetto: Re: Copyrights request
Mittente: Charles Molnar <Molnar@camosun.bc.ca>
Data: 3/13/2019, 12:31 AM
A: Massimiliano Mercuri <m.mercuri@therenva.com>, Jane Gair <GairJ@camosun.bc.ca>

Hi
I wonder if this helps? All the images are free of copyright and may be used without attribution.
Regards
Charlie

From: Massimiliano Mercuri <m.mercuri@therenva.com>
Sent: March 12, 2019 8:16:17 AM
To: Jane Gair; Charles Molnar
Subject: Copyrights request

Good Morning

I am Massimiliano Mercuri a PhD student from the University of Sheffield, I am about to submit my thesis to undertake the title.

I am writing to you because I was interested to use Figure 21.19 of chapter 21.4 Blood Flow and Blood Pressure regulation of the book Concepts of biology 1ST Candian Edition, so I would like to know how would you like to be referred and if you were able to provide some documentation where it is stated that I could you this Image (it is not very clear for me from how it is explained in the site, in any case I would like to be sure that you are happy with how I refer)

Hope to hear from you soon,

kind regards,

Massimiliano

SPRINGER NATURE LICENSE TERMS AND CONDITIONS

Aug 12, 2019

This Agreement between Mr -- Massimiliano Mercuri ("You") and Springer Nature ("Springer Nature") consists of your license details and the terms and conditions provided by Springer Nature and Copyright Clearance Center.

License Number	4646521142421
License date	Aug 12, 2019
Licensed Content Publisher	Springer Nature
Licensed Content Publication	Springer eBook
Licensed Content Title	An Automatic Method for Aortic Segmentation Based on Level-Set Methods Using Multiple Seed Points
Licensed Content Author	Massimiliano Mercuri, Andrew J. Narracott, DR Hose et al
Licensed Content Date	Jan 1, 2018
Type of Use	Thesis/Dissertation
Requestor type	academic/university or research institute
Format	print and electronic
Portion	figures/tables/illustrations
Number of figures/tables/illustrations	3
Will you be translating?	no
Circulation/distribution	>50,000
Author of this Springer Nature content	yes
Title	Tuning of boundary conditions for haemodynamic simulation
Institution name	University of Sheffield
Expected presentation date	Oct 2019
Portions	all Figures in the document
Requestor Location	Mr 30 Rue Legraverend Rennes Rennes, France 35000 France Attn: Mr
Total	0.00 EUR

Terms and Conditions

Springer Nature Customer Service Centre GmbH
Terms and Conditions

This agreement sets out the terms and conditions of the licence (the **Licence**) between you and **Springer Nature Customer Service Centre GmbH** (the **Licensor**). By clicking

'accept' and completing the transaction for the material (**Licensed Material**), you also confirm your acceptance of these terms and conditions.

1. Grant of License

1. 1. The Licensor grants you a personal, non-exclusive, non-transferable, world-wide licence to reproduce the Licensed Material for the purpose specified in your order only. Licences are granted for the specific use requested in the order and for no other use, subject to the conditions below.

1. 2. The Licensor warrants that it has, to the best of its knowledge, the rights to license reuse of the Licensed Material. However, you should ensure that the material you are requesting is original to the Licensor and does not carry the copyright of another entity (as credited in the published version).

1. 3. If the credit line on any part of the material you have requested indicates that it was reprinted or adapted with permission from another source, then you should also seek permission from that source to reuse the material.

2. Scope of Licence

2. 1. You may only use the Licensed Content in the manner and to the extent permitted by these Ts&Cs and any applicable laws.

2. 2. A separate licence may be required for any additional use of the Licensed Material, e.g. where a licence has been purchased for print only use, separate permission must be obtained for electronic re-use. Similarly, a licence is only valid in the language selected and does not apply for editions in other languages unless additional translation rights have been granted separately in the licence. Any content owned by third parties are expressly excluded from the licence.

2. 3. Similarly, rights for additional components such as custom editions and derivatives require additional permission and may be subject to an additional fee. Please apply to Journalpermissions@springernature.com/bookpermissions@springernature.com for these rights.

2. 4. Where permission has been granted **free of charge** for material in print, permission may also be granted for any electronic version of that work, provided that the material is incidental to your work as a whole and that the electronic version is essentially equivalent to, or substitutes for, the print version.

2. 5. An alternative scope of licence may apply to signatories of the STM Permissions Guidelines, as amended from time to time.

3. Duration of Licence

3. 1. A licence for is valid from the date of purchase ('Licence Date') at the end of the relevant period in the below table:

Scope of Licence	Duration of Licence
Post on a website	12 months
Presentations	12 months
Books and journals	Lifetime of the edition in the language purchased

4. Acknowledgement

4. 1. The Licensor's permission must be acknowledged next to the Licenced Material in print. In electronic form, this acknowledgement must be visible at the same time as the figures/tables/illustrations or abstract, and must be hyperlinked to the journal/book's homepage. Our required acknowledgement format is in the Appendix below.

5. Restrictions on use

5. 1. Use of the Licensed Material may be permitted for incidental promotional use and minor editing privileges e.g. minor adaptations of single figures, changes of format, colour and/or style where the adaptation is credited as set out in Appendix 1 below. Any other changes including but not limited to, cropping, adapting, omitting material that affect the meaning, intention or moral rights of the author are strictly prohibited.

5. 2. You must not use any Licensed Material as part of any design or trademark.

5. 3. Licensed Material may be used in Open Access Publications (OAP) before publication by Springer Nature, but any Licensed Material must be removed from OAP sites prior to final publication.

6. Ownership of Rights

6. 1. Licensed Material remains the property of either Licensor or the relevant third party and any rights not explicitly granted herein are expressly reserved.

7. Warranty

IN NO EVENT SHALL LICENSOR BE LIABLE TO YOU OR ANY OTHER PARTY OR ANY OTHER PERSON OR FOR ANY SPECIAL, CONSEQUENTIAL, INCIDENTAL OR INDIRECT DAMAGES, HOWEVER CAUSED, ARISING OUT OF OR IN CONNECTION WITH THE DOWNLOADING, VIEWING OR USE OF THE MATERIALS REGARDLESS OF THE FORM OF ACTION, WHETHER FOR BREACH OF CONTRACT, BREACH OF WARRANTY, TORT, NEGLIGENCE, INFRINGEMENT OR OTHERWISE (INCLUDING, WITHOUT LIMITATION, DAMAGES BASED ON LOSS OF PROFITS, DATA, FILES, USE, BUSINESS OPPORTUNITY OR CLAIMS OF THIRD PARTIES), AND
WHETHER OR NOT THE PARTY HAS BEEN ADVISED OF THE POSSIBILITY OF SUCH DAMAGES. THIS LIMITATION SHALL APPLY NOTWITHSTANDING ANY FAILURE OF ESSENTIAL PURPOSE OF ANY LIMITED REMEDY PROVIDED HEREIN.

8. Limitations

8. 1. ***BOOKS ONLY:***Where **'reuse in a dissertation/thesis'** has been selected the following terms apply: Print rights of the final author's accepted manuscript (for clarity, NOT the published version) for up to 100 copies, electronic rights for use only on a personal website or institutional repository as defined by the Sherpa guideline (www.sherpa.ac.uk/romeo/).

9. Termination and Cancellation

9. 1. Licences will expire after the period shown in Clause 3 (above).

9. 2. Licensee reserves the right to terminate the Licence in the event that payment is not received in full or if there has been a breach of this agreement by you.

Appendix 1 — Acknowledgements:

For Journal Content:
Reprinted by permission from [**the Licensor**]: [**Journal Publisher** (e.g. Nature/Springer/Palgrave)] [**JOURNAL NAME**] [**REFERENCE CITATION** (Article name, Author(s) Name), [**COPYRIGHT**] (year of publication)

For **Advance Online Publication papers:**
Reprinted by permission from [**the Licensor**]: [**Journal Publisher** (e.g. Nature/Springer/Palgrave)] [**JOURNAL NAME**] [**REFERENCE CITATION** (Article name, Author(s) Name), [**COPYRIGHT**] (year of publication), advance online publication, day month year (doi: 10.1038/sj.[JOURNAL ACRONYM].)

For Adaptations/Translations:
Adapted/Translated by permission from [**the Licensor**]: [**Journal Publisher** (e.g. Nature/Springer/Palgrave)] [**JOURNAL NAME**] [**REFERENCE CITATION** (Article name, Author(s) Name), [**COPYRIGHT**] (year of publication)

Note: For any republication from the British Journal of Cancer, the following credit line style applies:

Reprinted/adapted/translated by permission from [**the Licensor**]: on behalf of Cancer Research UK: : [**Journal Publisher** (e.g. Nature/Springer/Palgrave)] [**JOURNAL NAME**] [**REFERENCE CITATION** (Article name, Author(s) Name), [**COPYRIGHT]** (year of publication)

For **Advance Online Publication** papers:
Reprinted by permission from The [**the Licensor**]: on behalf of Cancer Research UK: [**Journal Publisher** (e.g. Nature/Springer/Palgrave)] [**JOURNAL NAME**] [**REFERENCE CITATION** (Article name, Author(s) Name), [**COPYRIGHT**] (year of publication), advance online publication, day month year (doi: 10.1038/sj.[JOURNAL ACRONYM])

For Book content:
Reprinted/adapted by permission from [**the Licensor**]: [**Book Publisher** (e.g. Palgrave Macmillan, Springer etc) [**Book Title**] by [**Book author**(s)] [**COPYRIGHT**] (year of publication)

Other Conditions:

Version 1.2

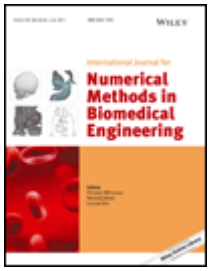

Title:	A systematic comparison between 1-D and 3-D hemodynamics in compliant arterial models
Author:	Nan Xiao, Jordi Alastruey, C. Alberto Figueroa
Publication:	INTERNATIONAL JOURNAL FOR NUMERICAL METHODS IN BIOMEDICAL ENGINEERING
Publisher:	John Wiley and Sons
Date:	Sep 24, 2013